TECHNISCHE
UNIVERSITÄT
WIEN
Vienna University of Technology

DISSERTATION

Computational non-equilibrium Dynamics in Solids: Solver for the far-from-equilibrium Boltzmann-equation

ausgeführt zum Zwecke der Erlangung des akademischen Grades des

Doktors der technischen Wissenschaften (Dr. techn.)

am Institut für Festkörperphysik der

Technischen Universität Wien

unter Anleitung von

Univ.-Prof. Dr. Karsten Held
(Technische Universität Wien, Wien)

und

Asst.-Prof. Dr. Marco Battiato
(Nanyang Technological University, Singapur)

durch

Dipl.-Ing. Michael Wais

Seyringer Straße 1-2-290 1210 Wien

Matrikelnummer 1026319

Wien, Juni 2020

Kurzfassung

Die vorliegende Dissertation beschäftigt sich mit der Entwicklung einer Simulationssoftware die in der Lage ist, die volle Boltzmann Transportgleichung (BTG) zu lösen. Das Ziel dahinter ist, neue Einsichten in das Zusammenspiel von Elektronentransport und Thermalisation in Festkörpern zu bekommen. Das Verständnis der Nichtgleichgewichtsdynamik von Elektronen in festen Körpern bildet die Basis für viele moderne Technologien wie zum Beispiel Mikroelektronik, Solarzellen oder Thermoelektrische Generatoren. Die meisten technologischen Anwendungen basieren auf Physik nahe am thermischen Gleichgewicht, ein gut verstandenes Forschungsgebiet. Die Entwicklung von Femtosekundenlasern hat das neue Forschungsfeld der starken Nichtgleichgewichtsphyisk eröffnet, welches das Potenzial für weiteren technologischen Fortschritt mit sich bringt. Nichtgleichgewichtseffekte könnten für neuartige Terahertz Strahler, ultraschnelle magnetische Schreibvorgänge oder Solarzellen effizienter als die Schokley-Queisser Grenze genutzt werden.

Wenn ein Femtosekundenlaserpuls von einem Festkörper absorbiert wird, werden die Elektronen zu höherenergetischen Zuständen angeregt. Diese hochenergetischen Elektronen unterlaufen einen komplizierten Prozess, bei dem die Elektronen untereinander, aber auch mit Phononen oder Verunreinigungen streuen. Gleichzeitig können sie durch ein elektrisches Feld beschleunigt werden und sich im Raum bewegen. Um Nichtgleichgewichtsexperimente korrekt verstehen und interpretieren zu können, sind wir deshalb gezwungen auf theoretische Modelle und Simulationen zurückzugreifen. Eine der Standardmethoden zur Beschreibung von Elektronentransport in Festkörpern ist die BTG.

Trotz ihrer fundamentalen Bedeutung für die Nichtgleichgewichtselektronendynamik wird die BTG üblicherweise nur mit starken Vereinfachungen oder für einfache Modellsysteme gelöst. Der Grund liegt in ihrer mathematischen Struktur, die es besonders schwierig macht, sie numerisch auszuwerten. Um dieses Problem zu lösen, wird zunächst ein vereinfachter Boltzmann Streuoperator, bei dem die Impulserhaltung vernachlässigt wird, untersucht. Die damit berechnete Thermalisationsdynamik eines optisch angeregten Mott-Isolators wird mit den Resultaten einer dynamischen Molekularfeldtheorie Rechnung im Nichtgleichgewicht verglichen. Im Hauptteil wird eine neue Methode zum numerischen Lösen der vollständigen BTG ausgearbeitet. Bei dieser Methode ist die Energie, der Impuls und die Teilchenanzahl dann exakt erhalten. In weiterer Folge wird diese Methode verwendet um die Thermalisationsdynamik von verschiedenen Nichtgleichgewichtsmodellsystemen und die dabei wirksamen, fundamentalen Prozesse, besser zu verstehen. Als Abschluss wird die Methode zur Simulation eines tatsächlich durchgeführten Experiments verwendet. Dabei werden einwandige Kohlenstoffnanoröhren unter Spannung mit Femtosekunden Laserpulsen beschossen. Die Messungen offenbaren eine Diskrepanz zwischen Photostrom und Terahertzemission, die wir numerisch reproduzieren und verstehen können.

Abstract

This thesis is dedicated to the development of a numerical solver for the full Boltzmann transport equation (BTE) and a better understanding of thermalization and transport dynamics in solids. Many modern technologies are based on non-equilibrium dynamics of electrons in solids, for example microelectronics, solar cells or thermoelectric generators. Most technological applications are however based on transport physics close to thermal equilibrium which is a mature and well understood field. The development of femtosecond lasers has created the whole new research area of strongly out-of-equilibrium dynamics with a wide range of interesting effects that have the potential for further technological advances. These strong non-equilibrium effects could be exploited for novel terahertz emitters, ultrafast magnetic recording or particularly efficient solar cells beyond the Schokley-Queisser limit.

When a femtosecond laser pulse hits a solid, it excites electrons to higher energy states. These high energetic electrons are subject to a complicated interplay of scatterings with other electrons, phonons or impurities while at the same time the electrons may be accelerated by electric fields and move to different positions in space. For a correct interpretation and understanding of strongly out-of-equilibrium transport and thermalization experiments one has to rely on theoretical models and simulations. One of the standard approaches to describe transport of electrons in solids is the BTE.

Although of fundamental importance for strongly out-of-equilibrium dynamics, the full BTE is usually only solved numerically with huge approximations or for oversimplified model systems. The reason lies in its inherent mathematical structure that makes it difficult to compute. To approach this problem we first introduce a simplified Boltzmann collision operator where the momentum conservation is neglected. We compare the resulting thermalization dynamics to results of non-equilibrium dynamical-mean-field theory for a photodoped Mott-insulator. In the main part we develop a novel numerical method to solve the full BTE that exactly conserves momentum, energy and particle density. We then apply it to several strongly out-of-equilibrium model systems to get a deeper insight into fundamental processes. Finally, we use the developed method to simulate an actual experiment where biased single-walled carbon-nanotubes are excited by a femtosecond laser pulse. We uncover a mysterious discrepancy of the measured photocurrent and terahertz emission that we can numerically reproduce and understand thanks to our simulation.

Acknowledgements

First and foremost I would like to thank my parents for supporting me throughout my whole life. Due to them I was in the fortunate position to live a rather sorrow-free life as a student where I only had to worry about exams and not so much about economic constraints. They have taught me never to give up which is definitely an asset for doing a PhD in physics. Without them this thesis would not exist and I would not be the person I am today.

My special thanks goes to Marco Battiato who has been co-supervising me for almost five years during my master thesis project and the PhD. He was the one dragging me into the research area of non-equilibrium dynamics which is a demanding, yet fascinating field. He also gave me the opportunity to visit him at the end of the world, Singapore, to work in his group for half a year. This stay turned out to be very beneficial for my work as well as for my personal development, although I struggled quite a lot to adapt to the harsh climate. I also want to thank him for the countless hours of scientific discussion which gave me a lot of new insights. He is definitely a jack-of-all-trades in science.

I am also especially grateful to Karsten Held who has been my main supervisor here in Vienna. He gave me the opportunity to work in a very independent way, allowing me to pursue my research even when it did not go into the main direction of his group. I always appreciated the scientific discussions and the support he gave me during the past five years.

I also want to thank all the people of the AG Held, the Toschi group and the Kunes group here in Vienna as well as the people of the Battiato group in Singapore for the nice company.

Last but not least I thank all my friends who supported me even when the times (and sometimes also I myself) were difficult. Life without friends would definitely be a dull thing.

Contents

1 Introduction **1**

2 Boltzmann Theory **5**
- 2.1 Phase-space and distribution function . . . 5
- 2.2 The transport term: Vlasov Equation . . . 8
- 2.3 The collision operator . . . 9
  - 2.3.1 Electron-electron collision operator . . . 10
  - 2.3.2 Electron-phonon collision operator . . . 12
  - 2.3.3 General collision operators . . . 13
  - 2.3.4 Difficulties in calculating the collision operator . . . 16
- 2.4 Relaxation time approximation and local equilibrium . . . 17

3 Boltzmann scattering without momentum conservation **21**
- 3.1 Model and derivation . . . 22
  - 3.1.1 Laser excitations . . . 25
- 3.2 Numerical implementation . . . 27
  - 3.2.1 Test of the code . . . 30
- 3.3 Thermalization dynamics of an excited, hypercubic Mott-insulator . . . 32
  - 3.3.1 Spectral density for QBE . . . 33
  - 3.3.2 Two time-scale relaxation dynamics . . . 34
  - 3.3.3 Coherent laser excitations . . . 41
  - 3.3.4 Population dynamics . . . 43
  - 3.3.5 Scattering strength . . . 43
  - 3.3.6 Three-step thermalization . . . 44

4 Transport numerics **47**
- 4.1 The Discontinuous Galerkin method . . . 47
- 4.2 Algorithm . . . 50
  - 4.2.1 Boundary conditions . . . 53

Die approbierte gedruckte Originalversion dieser Dissertation ist an der TU Wien Bibliothek verfügbar.
The approved original version of this doctoral thesis is available in print at TU Wien Bibliothek.
TU Bibliothek Your knowledge hub WIEN

4.3 Test cases 55

5 Scattering numerics **61**
5.1 Scattering Tensor 62
5.1.1 Basis and discretization 63
5.1.2 The scattering tensor 64
5.1.3 Calculation of the scattering tensor elements 65
5.1.4 Caveats of the method 70
5.2 Conservation symmetries and clean-up 71
5.2.1 Symmetries 71
5.2.2 Clean-up 74
5.3 Scattering rates 76
5.4 Non-equilibrium dynamics of model systems 79
5.4.1 Scattering rates 80
5.4.2 Particle-hole symmetric excitation: $\Delta = 0$ 83
5.4.3 Particle-hole symmetric excitation: $\Delta = 1$ 85
5.4.4 Particle-hole asymmetric excitation: $\Delta = 0$ 88
5.4.5 Particle-hole asymmetric excitation: $\Delta = 1$ 90
5.5 Numerical implementation 93
5.6 Joining scattering with transport 95

6 Dynamics in carbon-nanotubes **97**
6.1 Introduction to graphene and carbon-nanotubes 98
6.1.1 Graphene band-structure 98
6.1.2 From graphene to carbon-nanotubes 99
6.1.3 Excitons in carbon-nanotubes 103
6.2 Aligned CNTs as THz emitters 104
6.2.1 The experiment 106
6.2.2 The microscopic model 109
6.2.3 Scattering processes and amplitudes 110
6.2.4 Details of the simulation 114
6.2.5 Results and comparison of theory and experiment 116

7 Conclusion and outlook **121**

Appendices **123**

A Scattering amplitude for the Hubbard model **125**

B Applicability of the scattering rate equation **127**

Bibliography **131**

Curriculum Vitae **143**

Publication List **145**

Chapter 1

Introduction

Without non-equilibrium physics the world would be a boring place. Almost all phenomena encountered in daily life, including life itself, are based on the fact that the world is not in thermal equilibrium. There is actually no such thing as real equilibrium physics. An at least slightly out of equilibrium situation is always needed to measure any physical property in an experiment. One can think for example of a measurement of the electrical conductivity where one has to drive a current through the sample to obtain information on the system. Non-equilibrium situations are natural for interactions with the physical world, however the theoretical description of these phenomena belongs to the most demanding tasks in physics.

While currently most solid-state technologies are based on physics close to equilibrium, driving the solid strongly out-of-equilibrium shows a range of intriguing dynamical effects that have the potential for future technological use. Some examples are novel solar cells [1,2], giant spin injection in semiconductors [3,4], the ultrafast demagnetization [5–7] and novel opto-electronic terahertz-devices [8,9]. Strongly out-of-equilibrium situations in solids can be generated by femtosecond laser pulses [5,10–17]. These laser pulses can be very intense and therefore significantly alter the electronic population and even trigger metal-to-insulator transitions [18–20]. After an irradiation by a femtosecond laser the electrons scatter with each other, lattice vibrations, impurities and potential other quasi-particles in the system. At the same time, due to external fields or a broken translational symmetry at e.g. surfaces, the electrons may propagate in space. This interplay between thermalization through scatterings and transport takes place on the femto-, pico- and even nanosecond scale and is particularly hard to simulate [3,7,21–23].

Various different models and techniques have been developed to calculate the non-equilibrium dynamics in solids. The two most common ways to describe transport are the non-equilibrium Green's function formalism (NEGF) [24,25] and the so called Boltzmann equation [26–28][1] and its extensions [33, 34].

The NEGF methods introduce the many-particle Green's functions that describe the time-evolution of a test particle added to the particles already in the system. From the behavior of this test-particle one can extract information on the current state of the system. These methods include the full effect of the interaction potential (i.e. they are per se not restricted to weakly interacting particles) and coherent phenomena like quasi-particle renormalizations. This results in a huge computational cost so that either additional simplifications have to be made like the non-equilibrium dynamical-mean-field theory approach [35, 36] or only very simple model systems can be described.

The Boltzmann equation was historically introduced by Boltzmann in 1872 to describe classical gas dynamics [26]. Later it was extended to the description of quantum mechanical particles and counts as the basic transport theory in solids. When it is applied to quantum mechanical particles, coherence between the scattering events is lost but the leading order dynamical properties of the particles, stemming from quantum mechanics, are preserved. This simplification limits the range of applicability of the technique. Nevertheless, the success of the Boltzmann equation for the description of transport in solids is remarkable. It has been used to calculate basic response quantities such as the electrical or thermal conductivity and the Seebeck-coefficient as well as for transport through junctions between differently doped regions in semiconductors or entire heterostructures consisting of different materials [27, 37–41].

Although less numerically demanding than the NEGF methods, solving the complete Boltzmann equation numerically is a formidable challenge and usually heavy approximations are used [42–45]. The most prominent numerical methods to solve the Boltzmann equation are so-called Monte Carlo methods [46–49] or their extensions [50, 51]. They are particularly popular in the fields of semiconductor and plasma physics. However, due to the stochastic nature of these methods, they give only approximate solutions and introduce huge noise especially when they are used for transport.

Deterministic methods do not posses these shortcomings. However, they are considered computationally too demanding to solve the full Boltzmann equation when processes like electron-electron scatterings are included. Hence, they are only used for strongly simplified forms of the Boltzmann collision term [52, 53]. The most popular simplifications are the relaxation-time-approximation, restriction to lowest order electron-phonon scattering, restriction to parabolic dispersion relations and low electron-densities. Additionally, all the above mentioned methods, being deterministic or stochastic in nature, lack an

---

[1] When people talk about the Boltzmann equation for electrons the term quantum Boltzmann equation is also used [28–30]. However, sometimes quantum Boltzmann refers to extensions of the ordinary Boltzmann equation [31, 32]. Hence, we refer to it as Boltzmann equation in the following.

TU Bibliothek Your knowledge hub WIEN
Die approbierte gedruckte Originalversion dieser Dissertation ist an der TU Wien Bibliothek verfügbar.
The approved original version of this doctoral thesis is available in print at TU Wien Bibliothek.

exact conservation of one or several extensive, thermodynamic quantities like particle number, energy or momentum. This constitutes problems for the convergence in long-time thermalization simulations.

The aim of this thesis is to take one step towards a semi-deterministic Boltzmann solver including transport in combination with the full collision operators even for two-particle scatterings and without any restrictions on bandstructures or particle-densities. Additionally we put emphasis on the problem of the exact conservation of the extensive, thermodynamic quantities in order to make simulations possible that describe dynamics from the sub-picosecond scale up to nanoseconds. Furthermore we seek to get a deeper understanding on how the two most popular methods in the field of non-equilibrium dynamics, i.e. the Boltzmann-equation and the NEGF-methods, are connected.

The thesis is organized as follows:

- In chapter 2 we will give a basic introduction to the Boltzmann-transport-equation (BTE) and its theoretical foundations. The concept of quasi-particles and phase-space are introduced. Furthermore the two main parts of the BTE, the transport term and the collision term, are introduced for arbitrary particles and scatterings. Finally, the very famous relaxation-time approximation and local-equilibrium assumption of the BTE are discussed.

- In chapter 3 we investigate the Boltzmann collision operator for electron-electron interaction disregarding the momentum conservation. This approximation is similar to the simplification used in dynamical-mean-field theory (DMFT). We compare the solution of the simplified Boltzmann collision term and non-equilibrium DMFT and discuss the similarities and differences.

- In chapter 4 we use the discontinuous Galerkin finite-elements method to solve the transport part of the Boltzmann equation for a one-dimensional system. We explain the effect of different boundary conditions and discuss the stability of the code.

- In chapter 5 we develop the numerical method to solve the computationally most demanding part of the BTE, the collision operator. The numerical discretization scheme is introduced followed by a discussion on mathematical symmetries and how they affect the conservation of thermodynamic extensive quantities. The numerical implementation of the method is applied to two-dimensional, two-band systems (with and without bandgap). Furthermore we discuss how the scattering code can be joined with the transport code.

- In chapter 6 we discuss an experiment where aligned semiconducting carbon-nanotubes (CNTs) are illuminated with a femtosecond laser pulse under simultaneous presence of an external electric field. It is found that this setup is an unexpectedly efficient terahertz emitter. We solve the full BTE for an elaborate model of CNTs explaining the puzzling discrepancy in the scaling of the terahertz radiation amplitude and the measured photocurrent with the applied voltage.

Die approbierte gedruckte Originalversion dieser Dissertation ist an der TU Wien Bibliothek verfügbar.
The approved original version of this doctoral thesis is available in print at TU Wien Bibliothek.
TU Bibliothek WIEN Your knowledge hub

Chapter 2

Boltzmann Theory

In this chapter we introduce the basic theoretical foundations of the Boltzmann transport equation (BTE). The Boltzmann equation actually consists of two parts, the transport part and the collision part that are conceptually different. In the following the two parts are introduced independently and then combined to get the full Boltzmann equation. Although there exist very formal derivations of the BTE from the Bogoliubov-Born-Green-Kirkwood-Yvon-hierarchy [54–58] or alternative approaches [30], we chose here to show a straightforward, though less formal approach. We highlight how different types of scatterings (e.g. electron-electron, electron-phonon, phonon-phonon) are written as Boltzmann collision operators.

The chapter is organized as follows: At first, we introduce the concepts of phase-space and distribution function in quantum mechanics (section 2.1). Then we give a short introduction to the transport part of the Boltzmann equation (section 2.2). This is followed by an introduction to the Boltzmann collision operators (section 2.3) where we derive the collision operators from perturbation theory. Additionally this concept, which is well known for electron-electron and electron-phonon scattering, is extended to arbitrary scattering processes. Finally, we briefly discuss the famous relaxation-time approximation and local equilibrium assumption (section 2.4).

2.1 Phase-space and distribution function

The use of the Boltzmann equation for quantum mechanical many-body systems is closely related to the concept of the quasi-particle. The fundamental statement of this concept is, that even though the physical particles in the system interact through the strong and long-range Coulomb force the basic excitations of the system behave like almost independent particles which are called quasi-particles. Their dynamical behavior however can be strongly renormalized due to the interaction of the physical electrons in the system.

The reason for the success of the Boltzmann equation is that in most solids the basic excitations are quasi-particles.

Let us consider a system of N non-interacting quasi-electrons that is described by the time-independent Schrödinger equation

$$\sum_{i=1}^{N}\left(-\frac{\hat{\mathbf{p}}_i^2}{2m_e}+V(\hat{\mathbf{x}}_i)\right)|\psi\rangle=E\,|\psi\rangle \tag{2.1}$$

with the quasi-electron mass m_e, the momentum operator of the i-th electron $\hat{\mathbf{p}}_i$, the position operator of the i-th electron $\hat{\mathbf{x}}_i$, the energy E and the single particle potential $V(\cdot)$. As the particles are non-interacting, Eq. (2.1) separates into N independent single particle equations that all have the same structure,

$$\left(-\frac{\hat{\mathbf{p}}^2}{2m_e}+V(\hat{\mathbf{x}})\right)|\phi\rangle=\epsilon\,|\phi\rangle\ . \tag{2.2}$$

In a crystal the single-particle potential is periodic, i.e. $V(\hat{\mathbf{x}}+\mathbf{R}_l)=V(\hat{\mathbf{x}})$ where $\mathbf{R}_l$ is the vector pointing to the l-th unit cell in the Bravais lattice. This discrete translational symmetry gives rise to a quantum number, the crystal momentum $\mathbf{k}$. The momenta $\mathbf{k}$ can assume values that lie in the so-called first Brillouin-zone which is a unit cell of the reciprocal lattice centered around the Γ-point (i.e. $\mathbf{k}=0$). In case of a finite-size crystal, $\mathbf{k}$ is discrete while in case of an infinitely large crystal it becomes continuous. For a certain $\mathbf{k}$ the Schrödinger equation has several solutions which are labeled by another quantum number, the so-called band index n. Additionally we have the spin index σ[1]. Each eigenstate $|\phi_{n,k,\sigma}\rangle$ has then the eigenenergy $\epsilon_{n,\sigma}(\mathbf{k})$ that is called dispersion relation or quasi-particle energy alternatively.

One can construct wave-packet states that are centered at a certain position $\mathbf{x}_c$ in real space and $\mathbf{k}_c$ in momentum space. These states are only approximate eigenstates of the hamiltonian and consist of superpositions of the exact eigenstates $|\phi_{n,k,\sigma}\rangle$. As each particle can now be labeled with its real-space and reciprocal-space position it is convenient to introduce the so-called phase-space. This is the Cartesian product of real and momentum space. The volume of the total phase-space is then $V_{Ph}=V\times V_{BZ}$ with the volume of the crystal V and the volume of the Brillouin-zone V_{BZ}. From the construction of the wave-packet it follows that it occupies a finite volume in the phase-space, i.e. $V_{particle}=(2\pi)^d$ where d is the dimension of the system. This is a direct consequence of the uncertainty-principle which states, that a particle cannot have a definite position in real- and momentum-space simultaneously. As the wave-packets are no real eigenstates of the hamiltonian they are subject to an increase in real-space volume in time, i.e. they will spread. In Boltzmann theory it is assumed that the momentum-space volume of

---

[1] Here we assume that spin-orbit coupling is negligible, hence, the spin is a good quantum-number.

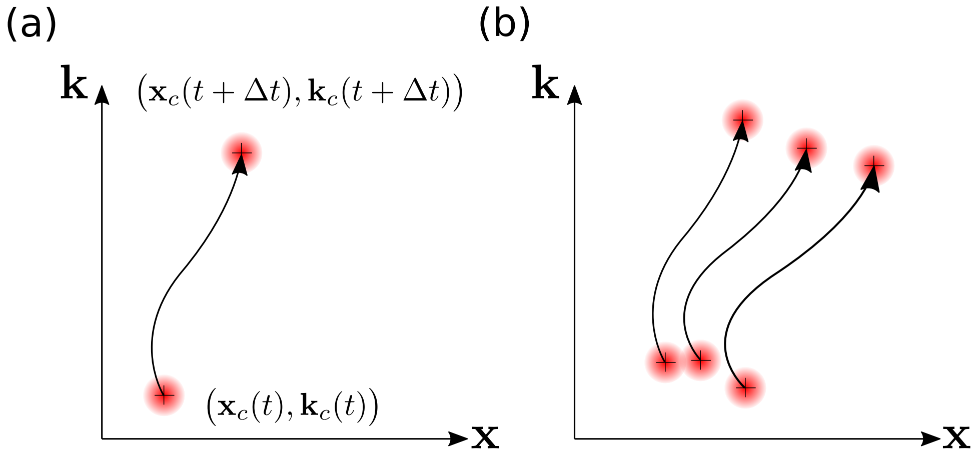
(a)
(b)
k
$\big(\mathbf{x}_c(t+\Delta t), \mathbf{k}_c(t+\Delta t)\big)$
$\big(\mathbf{x}_c(t), \mathbf{k}_c(t)\big)$
x
k
x

Figure 2.1: (a) Symbolic picture of the propagation of a wave-packet in the phase-space from time t to $t + \Delta t$. (b) Symbolic picture of several wave-packet trajectories. As they are solutions of the equations of motion Eqs. (2.3) they never cross.

the wave-packet is much smaller than the size of the first Brillouin-zone. Consequently, the real-space volume of the wave-packet is much larger than a crystal unit-cell. Under the assumption of a wave-packet that is strongly localized in momentum space, the time-dependent spread of the wave-packet in real-space can be neglected.

By the application of the time-evolution operator one can show that the center of the wave-packet $\big(\mathbf{x}_c, \mathbf{k}_c\big)$, to leading order, moves according to [27, 37, 38]

$$\frac{\partial \mathbf{x}_c(t)}{\partial t} = \frac{1}{\hbar}\nabla_{k_c}\epsilon_{n,\sigma}(\mathbf{k}_c) \equiv \mathbf{v}_{\mathbf{x}_c} \ , \tag{2.3a}$$

$$\frac{\partial \mathbf{k}_c(t)}{\partial t} = -\frac{e}{\hbar}\left(\mathbf{E}(\mathbf{x}_c, t) + \frac{1}{c}\frac{\partial \mathbf{x}_c(t)}{\partial t} \times \mathbf{H}(\mathbf{x}_c, t)\right) \equiv \mathbf{v}_{\mathbf{k}_c} \ , \tag{2.3b}$$

with the gradient with respect to momentum ∇_k, the absolute value of the electron charge e, the speed of light c, the real-space velocity $\mathbf{v}_{\mathbf{x}_c}$, the momentum-space velocity $\mathbf{v}_{\mathbf{k}_c}$, the external electric field $\mathbf{E}(\mathbf{x}_c, t)$ and the external magnetic field $\mathbf{H}(\mathbf{x}_c, t)$.

The Eqs. (2.3) are the so-called semi-classical equations of motion[2]. As they are first order differential equations a wave-packet with a certain position in the phase-space at time t propagates to a position at time $t + \Delta t$ that is uniquely determined by the integration of these equations of motion. As a consequence two trajectories of particles in the phase-space can never cross.

As we already know how the individual particle wave-packets evolve in time it is not always necessary to deal with the full N-particle wave-function $|\Psi_N(t)\rangle$. Instead, it may be sufficient to use the single-particle phase-space distribution function $f_{n,\sigma}(t, \mathbf{x}, \mathbf{k})$. It is defined as the probability that a wave-packet state with $(n, \sigma, \mathbf{x}_c = \mathbf{x}, \mathbf{k}_c = \mathbf{k})$ is occupied at time t. Using the distribution function is an approximation and will definitely not hold if quantum-effects like interference are relevant. However, in many real systems the particles scatter with phonons, impurities and each other which leads to a rapid decoherence. Therefore, in many cases it is completely sufficient and well justified to study the dynamics of a many-electron system using the distribution function instead of the wave-function.

---

[2] Note, that there can be additional velocity terms if the band has non-trivial Berry-curvature. These cases are not discussed here but can be found in e.g. Ref. [59].

Each wave packet occupies the phase-space volume $(2\pi)^d$, hence, the density-of-states in the phase-space is $\frac{1}{(2\pi)^d}$. With this knowledge we can write the number of particles $\mathrm{d}N_{n,\sigma}(t, \mathbf{x}, \mathbf{k})$ located in a phase-space volume-element $\mathrm{d}V_{ph} = \mathrm{d}^d x\ \mathrm{d}^d k$ as

$$\mathrm{d}N_{n,\sigma}(t, \mathbf{x}, \mathbf{k}) \equiv \mathrm{d}^d x\ \mathrm{d}^d k \frac{1}{(2\pi)^d} f_{n,\sigma}(t, \mathbf{x}, \mathbf{k}) \ . \tag{2.4}$$

The dynamic properties of each wave-packet are determined by its position in the phase-space and quantum numbers, i.e. by the set $(n, \sigma, \mathbf{x}, \mathbf{k})$. Therefore, with the distribution function and Eq. (2.4), extensive thermodynamic quantities $\Theta(t)$ and their corresponding currents $\mathbf{J}_\Theta(t, \mathbf{x})$ can be calculated according to

$$\Theta(t) = \sum_{n,\sigma} \int_V \mathrm{d}^d x \int_{V_{BZ}} \mathrm{d}^d k \frac{1}{(2\pi)^d} f_{n,\sigma}(t, \mathbf{x}, \mathbf{k}) \theta_{n,\sigma}(\mathbf{x}, \mathbf{k}) \ , \tag{2.5a}$$

$$\mathbf{J}_\Theta(t, \mathbf{x}) = \sum_{n,\sigma} \int_{V_{BZ}} \mathrm{d}^d k \frac{1}{(2\pi)^d} f_{n,\sigma}(t, \mathbf{x}, \mathbf{k}) \theta_{n,\sigma}(\mathbf{x}, \mathbf{k}) \mathbf{v}_{\mathbf{x}}(\mathbf{k}) \tag{2.5b}$$

where $\theta_{n,\sigma}(\mathbf{x}, \mathbf{k})$ is the single-particle contribution to $\Theta(t)$. Some examples of thermodynamic quantities and their currents are given in Tab. 2.1.

2.2 The transport term: Vlasov Equation

In a non-interacting system the total particle number of each species (n, σ) has to be conserved. Additionally, as the particle-motion is described by a first-order differential equation, a particle located at a certain position in phase-space can only smoothly move to a neighboring point. As a result of these properties, the particle density, or equivalently the distribution function, has to fulfill the continuity equation

$$\frac{\partial}{\partial t} f_{n,\sigma}(t, \mathbf{x}, \mathbf{k}) + \nabla \cdot \Big(\mathbf{v} f_{n,\sigma}(t, \mathbf{x}, \mathbf{k}) \Big) = 0 \ , \tag{2.6}$$

where $\nabla = (\nabla_{\mathbf{x}}, \nabla_{\mathbf{k}})^{\mathrm{T}}$ is the gradient in the full $2d$-dimensional phase-space and $\mathbf{v} = (\mathbf{v}_{\mathbf{x}}, \mathbf{v}_{\mathbf{k}})^{\mathrm{T}}$ is the total velocity.

As pointed out in section 2.1 an electron always occupies a volume of $(2\pi)^d$ in the phase space. In order for this property to hold for all times we further have to require

description	Θ	$\theta_{n,\sigma}(\mathbf{x},\mathbf{k})$
number of particles / particle current	N	1
charge / charge current	C	$-e$
spin / spin current	$\mathcal{S}$	σ
inner energy / inner energy current	E	$\epsilon_{n,\sigma}(\mathbf{k})$
total energy / total energy current	U	$\epsilon_{n,\sigma}(\mathbf{k}) - e\phi(\mathbf{x})$
entropy / entropy current	S	$\left(\epsilon_{n,\sigma}(\mathbf{k}) - \mu(\mathbf{x})\right)/T(\mathbf{x})$
heat / heat current	Q	$\epsilon_{n,\sigma}(\mathbf{k}) - \mu(\mathbf{x})$

Table 2.1: Different thermodynamic quantities, their associated symbols Θ and their corresponding single-particle contribution $\theta_{n,\sigma}(\mathbf{x},\mathbf{k})$ for Eqs. (2.5). $\phi(\mathbf{x})$ is the local electrical potential, $T(\mathbf{x})$ is the local temperature and $\mu(\mathbf{x})$ is the local chemical potential. Local temperature and chemical potential are closely related to the local equilibrium assumption which is introduced later.

incompressibility of the phase-space distribution function. This is equivalent to a vanishing divergence of the velocity field, i.e. $\nabla \cdot \mathbf{v} = 0$. The equations of motion given by Eqs. (2.3) indeed fulfill this requirement. We can therefore write Eq. (2.6) as

$$\frac{\partial}{\partial t} f_{n,\sigma}(t,\mathbf{x},\mathbf{k}) + \mathbf{v}_{\mathbf{x}} \cdot \nabla_{\mathbf{x}} f_{n,\sigma}(t,\mathbf{x},\mathbf{k}) + \mathbf{v}_{\mathbf{k}} \cdot \nabla_{\mathbf{k}} f_{n,\sigma}(t,\mathbf{x},\mathbf{k}) = 0 \ , \tag{2.7}$$

where it is easy to see that the left-hand side is the total time derivative of the distribution-function if we follow a wave-packet at its trajectory in the phase-space.

This equation is historically called Vlasov-equation [60, 61] and was first used in combination with the Maxwell-Equations for the description of plasmas. It describes the collision-less flow of particles if external fields are present.

2.3 The collision operator

The Vlasov equation (2.7) describes the motion of non-interacting quasi-particles where a part of the electron-electron interaction is already included in the dispersion relation $\epsilon_{n,\sigma}(\mathbf{k})$ of the quasi-particle. Additionally, there will be a residual short-range interaction between the quasi-particles that gives rise to scattering. In order to correctly describe this effect, the Vlasov equation Eq. (2.7) has to be modified by adding the so-called collision operators $\left(\frac{\partial f_{n,\sigma}}{\partial t}\right)_{\mathrm{col}}$,

$$\frac{\partial}{\partial t} f_{n,\sigma} + \mathbf{v}_{\mathbf{x}} \cdot \nabla_{\mathbf{x}} f_{n,\sigma} + \mathbf{v}_{\mathbf{k}} \cdot \nabla_{\mathbf{k}} f_{n,\sigma} = \sum_{\mathrm{col}} \left(\frac{\partial f_{n,\sigma}}{\partial t}\right)_{\mathrm{col}} \ . \tag{2.8}$$

The sum on the right-hand side runs over all possible scattering processes. This is the Boltzmann-equation as described in numerous textbooks [27, 37, 38]. The Boltzmann collision operator is also called quantum Fokker-Planck equation [28].

2.3.1 Electron-electron collision operator

In order to understand how to construct such a collision operator let us consider electron-electron scattering at first. We assume a system that is described by a Hamiltonian $\hat{H}$ consisting of a non-interacting part $\hat{H}_0$ and an interaction part $\hat{H}_{\text{e-e}}$,

$$\hat{H} = \underbrace{\sum_{n,\mathbf{k},\sigma} \epsilon_{n,\sigma}(\mathbf{k}) \hat{\psi}^\dagger_{n,\mathbf{k},\sigma} \hat{\psi}_{n,\mathbf{k},\sigma}}_{\hat{H}_0} + \underbrace{\frac{1}{2} \sum_{\substack{n_0 \dots n_3 \\ \sigma_0 \cdots \sigma_3 \\ \mathbf{k}_1, \mathbf{k}_2, \mathbf{q}}} V^{\text{e-e}}_{\substack{n_0 \dots n_3 \\ \sigma_0 \cdots \sigma_3}}(\mathbf{k}_0, \mathbf{k}_1, \mathbf{q}) \hat{\psi}^\dagger_{n_2,\mathbf{k}_0+\mathbf{q},\sigma_2} \hat{\psi}^\dagger_{n_3,\mathbf{k}_1-\mathbf{q},\sigma_3} \hat{\psi}_{n_1,\mathbf{k}_1,\sigma_1} \hat{\psi}_{n_0,\mathbf{k}_0,\sigma_0}}_{\hat{H}_{\text{e-e}}} \tag{2.9}$$

where we have used the creation (annihilation) operator $\hat{\psi}^\dagger_{n,\mathbf{k},\sigma}$ ($\hat{\psi}_{n,\mathbf{k},\sigma}$) that creates (annihilates) an electron in the state $(n, \mathbf{k}, \sigma)$[3]. $V^{\text{e-e}}_{\substack{n_0 \dots n_3 \\ \sigma_0 \cdots \sigma_3}}(\mathbf{k}_0, \mathbf{k}_1, \mathbf{q})$ is the matrix element of the interaction potential that may depend on the involved bands n_i as well as on the spins σ_i and momenta $\mathbf{k}_1$, $\mathbf{k}_2$, $\mathbf{q}$ in general. We can now calculate the time-evolution of a wave-function with two electrons in a state $|0, 1\rangle \equiv \hat{\psi}^\dagger_{n_0,\mathbf{k}_0,\sigma_0} \hat{\psi}^\dagger_{n_1,\mathbf{k}_1,\sigma_1} |\emptyset\rangle$ at time $t = 0$, where $|\emptyset\rangle$ is the state without electrons. The probability rate for a transition into another state $|2, 3\rangle$ at time t can be calculated in first-order time dependent perturbation theory as

$$\mathcal{W}_{0123} = \underbrace{\frac{2\pi}{\hbar} \left| \langle 2, 3 | \hat{H}_{\text{e-e}} | 0, 1 \rangle \right|^2}_{\equiv \frac{(2\pi)^{2d}}{V^2} w^{\text{e-e}}_{0123}} \delta_t(\epsilon_0 + \epsilon_1 - \epsilon_2 - \epsilon_3) \tag{2.10}$$

where $\epsilon_i \equiv \epsilon_{n_i,\sigma_i}(\mathbf{k}_i)$. The function $\delta_t(\cdot)$ is peaked at zero and becomes a delta-distribution in the limit $t \to \infty$. When this limit is performed Eq. (2.10) is known as Fermi's Golden Rule [62, 63]. We will call $\mathcal{W}_{0123}$ transition rate and $w^{\text{e-e}}_{0123}$ transition amplitude in this thesis.

An important property of the transition rate $\mathcal{W}_{0123}$ can be seen when the translation operator $\hat{T}_{\mathbf{R}_l}$ that shifts a wave-function by a Bravais-lattice vector $\mathbf{R}_l$, is used. From the Bloch-theorem it follows that $\hat{T}_{\mathbf{R}_l} \hat{\psi}^\dagger_{n,\mathbf{k},\sigma} = e^{i\mathbf{R}_l \cdot \mathbf{k}} \hat{\psi}^\dagger_{n,\mathbf{k},\sigma} \hat{T}_{\mathbf{R}_l}$. With this relation and the property $\hat{T}^{-1}_{\mathbf{R}_l} = \hat{T}^\dagger_{\mathbf{R}_l}$ we can write

$$\langle 2, 3 | \hat{H}_{\text{e-e}} | 0, 1 \rangle = \langle 2, 3 | \hat{T}^{-1}_{\mathbf{R}_l} \underbrace{\hat{T}_{\mathbf{R}_l} \hat{H}_{\text{e-e}} \hat{T}^{-1}_{\mathbf{R}_l}}_{= \hat{H}_{\text{e-e}}} \hat{T}_{\mathbf{R}_l} | 0, 1 \rangle \tag{2.11a}$$

$$= e^{i\mathbf{R}_l \cdot (\mathbf{k}_0 + \mathbf{k}_1 - \mathbf{k}_2 - \mathbf{k}_3)} \langle 2, 3 | \hat{H}_{\text{e-e}} | 0, 1 \rangle . \tag{2.11b}$$

---

[3] Note, that this is not a wave-packet state, but an eigenstate of the non-interacting Hamiltonian $\hat{H}_0$.

Die approbierte gedruckte Originalversion dieser Dissertation ist an der TU Wien Bibliothek verfügbar.
The approved original version of this doctoral thesis is available in print at TU Wien Bibliothek.
TU Bibliothek WIEN Your knowledge hub

In order for $\langle 2,3|\,\hat{H}_{\text{e-e}}\,|0,1\rangle$ to be non-zero it must hold that $\mathbf{R}_l\cdot(\mathbf{k}_0+\mathbf{k}_1-\mathbf{k}_2-\mathbf{k}_3)=2\pi z$ with an arbitrary integer number z. This is fulfilled if $(\mathbf{k}_0+\mathbf{k}_1-\mathbf{k}_2-\mathbf{k}_3)=\mathbf{G}$ where $\mathbf{G}$ is a reciprocal lattice vector. With this knowledge we can write Eq. (2.10) as

$$\mathcal{W}_{0123}=\frac{(2\pi)^{2d}}{V^2}w^{\text{e-e}}_{0123}\sum_{\mathbf{G}}\delta_{(\mathbf{k}_0+\mathbf{k}_1-\mathbf{k}_2-\mathbf{k}_3),\mathbf{G}}\;\delta_t(\epsilon_0+\epsilon_1-\epsilon_2-\epsilon_3) \tag{2.12}$$

where $\delta_{(\mathbf{k}_0+\mathbf{k}_1-\mathbf{k}_2-\mathbf{k}_3),\mathbf{G}}$ is the Kronecker-delta. The transition amplitude has the important properties

$$w^{\text{e-e}}_{0123}=w^{\text{e-e}}_{1023}\;, \tag{2.13a}$$

$$w^{\text{e-e}}_{0123}=w^{\text{e-e}}_{2301}\;, \tag{2.13b}$$

which follow directly from its definition Eq. (2.10) and the fermionic anti-commutation relations for creation and annihilation operators.

The time-evolution of the single-particle distribution function $f_{n,\sigma}(t,\mathbf{k})$[4] due to electron-electron collisions can now be calculated by the summation of all scattering rates that scatter electrons into the state $(n,\sigma,\mathbf{k})$ and subtraction of all scattering rates that scatter the electron away from $(n,\sigma,\mathbf{k})$. A scattering process only happens if both initial two single-electron states are occupied which has the probability $f_{n_0,\sigma_0}(\mathbf{k}_0)f_{n_1,\sigma_1}(\mathbf{k}_1)$ for a process $|0,1\rangle\rightarrow|2,3\rangle$. In case of Fermions the final two states additionally have to be unoccupied due to the Pauli-principle. This gives the additional probability $(1-f_{n_2,\sigma_2}(\mathbf{k}_2))(1-f_{n_3,\sigma_3}(\mathbf{k}_3))$ for this scattering. Altogether the resulting probability factor for the scattering is then $f_{n_0,\sigma_0}(\mathbf{k}_0)f_{n_1,\sigma_1}(\mathbf{k}_1)(1-f_{n_2,\sigma_2}(\mathbf{k}_2))(1-f_{n_3,\sigma_3}(\mathbf{k}_3))$ for the process $|0,1\rangle\rightarrow|2,3\rangle$.

The collision operator for electron-electron scattering thus eventually reads

$$\begin{aligned}\left(\frac{\partial f_{n_0,\sigma_0}(\mathbf{k}_0)}{\partial t}\right)_{\text{e-e}} =&\frac{(2\pi)^{2d}}{V^2}\frac{1}{2}\sum_{\mathbf{G}}\sum_{\substack{n_1,n_2,n_3\\ \sigma_1,\sigma_2,\sigma_3\\ \mathbf{k}_1,\mathbf{k}_2,\mathbf{k}_3}} w^{\text{e-e}}_{0123}\;\delta_{(\mathbf{k}_0+\mathbf{k}_1-\mathbf{k}_2-\mathbf{k}_3),\mathbf{G}}\;\delta_t(\epsilon_0+\epsilon_1-\epsilon_2-\epsilon_3)\\ &\times\Big[(1-f_{n_0,\sigma_0}(\mathbf{k}_0))(1-f_{n_1,\sigma_1}(\mathbf{k}_1))f_{n_2,\sigma_2}(\mathbf{k}_2)f_{n_3,\sigma_3}(\mathbf{k}_3)\\ &\quad -f_{n_0,\sigma_0}(\mathbf{k}_0)f_{n_1,\sigma_1}(\mathbf{k}_1)(1-f_{n_2,\sigma_2}(\mathbf{k}_2))(1-f_{n_3,\sigma_3}(\mathbf{k}_3))\Big]\;.\end{aligned} \tag{2.14}$$

The factor $\frac{1}{2}$ in front of the sums is needed to prevent double counting. The terms within the square brackets are called phase-space factor in the following and denoted as $\mathcal{P}(f_0,f_1,f_2,f_3)\equiv[(1-f_0)(1-f_1)f_2f_3-f_0f_1(1-f_2)(1-f_3)]$ with the abbreviation $f_i=f_{n_i,\sigma_i}(\mathbf{k}_i)$. Note that there are more formal ways to derive the phase-space factor we are not discussing within the scope of this introduction [28].

---

[4] As we are discussing a spatially homogeneous system we have dropped the real-space dependence

If the real-space volume V of the system is sufficiently large one can replace the sums over the momenta by integrals $\sum_{\mathbf{k}} \to \frac{V}{(2\pi)^d} \int_{V_{BZ}} \mathrm{d}^d\mathbf{k}$, the momentum-delta with a delta-distribution $\delta_{(\mathbf{k}_0+\mathbf{k}_1-\mathbf{k}_2-\mathbf{k}_3),\mathbf{G}} \to \frac{(2\pi)^d}{V}\delta(\mathbf{k}_0+\mathbf{k}_1-\mathbf{k}_2-\mathbf{k}_3+\mathbf{G})$ and for sufficiently large times t the function $\delta_t(\cdot)$ with a delta distribution $\delta(\cdot)$ to get the more common version

$$\begin{aligned}\left(\frac{\partial f_0}{\partial t}\right)_{\text{e-e}} = \frac{1}{2}\sum_{\mathbf{G}} \sum_{\substack{n_1,n_2,n_3\\ \sigma_1,\sigma_2,\sigma_3}} \iiint_{{V_{BZ}}^3} \mathrm{d}^d k_1 \mathrm{d}^d k_2 \mathrm{d}^d k_3 \; w^{\text{e-e}}_{0123}\; \delta(\mathbf{k}_0+\mathbf{k}_1-\mathbf{k}_2-\mathbf{k}_3+\mathbf{G}) \\ \times\, \delta(\epsilon_0+\epsilon_1-\epsilon_2-\epsilon_3)\mathcal{P}(f_0,f_1,f_2,f_3)\;. \end{aligned} \tag{2.15}$$

This is the collision term for electron-electron interaction that can be found in various textbooks [27, 28, 38].

The transition amplitude $w^{\text{e-e}}_{0123}$ as defined by Eq. (2.10) does not depend on the real-space volume V. Since the transition amplitude is volume-independent, also the collision operator Eq. (2.15) is volume-independent. Assuming that the volume used in the derivation is microscopically large but macroscopically small we can use the exact same collision operator for spatially non-homogeneous systems.[5] All the involved distribution functions then have to be evaluated at the same real-space position $\mathbf{x}$.

2.3.2 Electron-phonon collision operator

Consider a system with electron-phonon scattering to leading order. This interaction is described by the Fröhlich-Hamiltonian [64, 65] that reads

$$\hat{H}_{\text{e-ph}} = \sum_{\substack{\mathbf{k},\mathbf{q}\\ n_i,\sigma}} V^{\text{e-ph}}_{\substack{n_0,n_1\\ \sigma}}(\mathbf{k},\mathbf{q}) \left(\hat{\psi}^{\dagger}_{n_1,\mathbf{k},\sigma}\hat{\psi}_{n_0,\mathbf{k}-\mathbf{q},\sigma}\hat{a}_{n_2,\mathbf{q}} + \hat{\psi}^{\dagger}_{n_1,\mathbf{k}-\mathbf{q},\sigma}\hat{\psi}_{n_0,\mathbf{k},\sigma}\hat{a}^{\dagger}_{n_2,\mathbf{q}}\right) \tag{2.16}$$

where $V^{\text{e-ph}}_{\substack{n_0,n_1\\ \sigma}}(\mathbf{k},\mathbf{q})$ is the effective (spin-conserving) electron-phonon interaction potential and $\hat{a}^{\dagger}_{n_2,\mathbf{q}}$ ($\hat{a}_{n_2,\mathbf{q}}$) is the creation (annihilation) operator of a phonon with momentum $\mathbf{q}$ in the phonon-band n_2. In analogy with the electron-electron collision operator one can construct the electron-phonon collision operator as

---

[5] The volume used in the derivation would then be the real-space volume of the wave-packets.

$$\begin{aligned}\left(\frac{\partial f_0}{\partial t}\right)_{\text{e-ph}} = &\sum_{\mathbf{G}} \sum_{\substack{n_1,n_2\\ \sigma_1}} \left(1-\frac{1}{2}\delta_{n_0,n_1}\delta_{\sigma_0,\sigma_1}\right) \iint_{V_{BZ}{}^2} \mathrm{d}^d k_1 \mathrm{d}^d k_2 \; w_{012}^{\text{e-ph}} \; \delta(\mathbf{k}_1-\mathbf{k}_0+\mathbf{k}_2+\mathbf{G}) \\ &\times \delta(\epsilon_0-\epsilon_1-\omega_2)\Big[(1-f_0)f_1f_2 - f_0(1-f_1)(1+f_2)\Big] \\ &+\sum_{\mathbf{G}} \sum_{\substack{n_1,n_2\\ \sigma_1}} \left(1-\frac{1}{2}\delta_{n_0,n_1}\delta_{\sigma_0,\sigma_1}\right) \iint_{V_{BZ}{}^2} \mathrm{d}^d k_1 \mathrm{d}^d k_2 \; w_{012}^{\text{e-ph}} \; \delta(\mathbf{k}_1-\mathbf{k}_0-\mathbf{k}_2+\mathbf{G}) \\ &\times \delta(\epsilon_0-\epsilon_1+\omega_2)\Big[(1-f_0)f_1(1+f_2) - f_0(1-f_1)f_2\Big]\end{aligned} \tag{2.17}$$

with the phonon dispersion relation $\omega_2 \equiv \omega_{n_2}(\mathbf{k}_2)$ and the phonon distribution function $f_2 \equiv f_{n_2}(\mathbf{k}_2)$ which can be understood in the same sense as the electron dispersion relation and distribution function. For electrons or fermions in general, the term $(1-f)$ in the phase-space factor is the probability that a certain state is unoccupied and accounts for the Pauli-principle. In case of bosons we need a $(1+f)$ factor that can be interpreted as probability for stimulated- ($\propto f$) plus spontaneous- ($\propto 1$) emission. As can be seen Eq. (2.17) actually consists of two collision operators. The first operator (first two lines) describes the process where an electron in state 0 emits a phonon in state $(n_2, \mathbf{k}_2)$ and becomes an electron in state 1 and the time reversed version of this process. The second operator (third and fourth line) describes the situation where an electron in state 0 absorbs a phonon $(n_2, \mathbf{k}_2)$ and becomes an electron in state 1 and the time reversed version. The factor $\left(1-\frac{1}{2}\delta_{n_0,n_1}\delta_{\sigma_0,\sigma_1}\right)$ is needed to prevent double-counting.

2.3.3 General collision operators

The electron-electron collision operator Eq. (2.15) can be extended to higher order electron-boson or boson-boson scattering. This is done by modifying the phase-space factor to account for different particle types. For example the phase-space factor for the electron-boson scattering-case reads

$$\mathcal{P}_{\text{4-cons}}(f_0, f_1, f_2, f_3) = \left[(1-f_0)(1+f_1)f_2f_3 - f_0f_1(1-f_2)(1+f_3)\right] \;, \tag{2.18}$$

where f_1 and f_3 are bosonic distribution-functions. As above, the bosonic particles have $(1+f)$ terms in the phase-space factor in contrast to electrons which have $(1-f)$. The collision operator for particle-number conserving electron-phonon scattering then reads

$$\left(\frac{\partial f_0}{\partial t}\right)_{\text{e-ph-2}} = \sum_{\mathbf{G}} \sum_{\substack{n_1,n_2,n_3\\ \sigma_1,\sigma_2,\sigma_3}} \iiint_{V_{BZ}{}^3} \mathrm{d}^d k_1 \mathrm{d}^d k_2 \mathrm{d}^d k_3 \; w_{0123}^{\text{e-ph-2}} \\ \times \delta(\mathbf{k}_0 + \mathbf{k}_1 - \mathbf{k}_2 - \mathbf{k}_3 + \mathbf{G}) \delta(\epsilon_0 + \omega_1 - \epsilon_2 - \omega_3) \mathcal{P}_{\text{4-cons}}(f_0, f_1, f_2, f_3) \; . \tag{2.19}$$

Note that the $\frac{1}{2}$ pre-factor of Eq. (2.15) is not needed here as electrons and phonons are different particles, thus distinguishable.

If bosons are taken into account it is also possible that the total number of particles is not conserved in the scattering process. An example would be a process where one electron scatters into another state by absorbing two phonons. The collision operator for such a processes reads

$$\left(\frac{\partial f_0}{\partial t}\right)_{\text{e-ph-3}} = \sum_{\mathbf{G}} \sum_{\substack{n_1,n_2,n_3\\ \sigma_1,\sigma_2,\sigma_3}} \iiint_{V_{BZ}{}^3} \mathrm{d}^d k_1 \mathrm{d}^d k_2 \mathrm{d}^d k_3 \; w_{0123}^{\text{e-ph-3}} \\ \times \delta(\mathbf{k}_0 + \mathbf{k}_1 - \mathbf{k}_2 + \mathbf{k}_3 + \mathbf{G}) \delta(\epsilon_0 + \omega_1 - \epsilon_2 + \omega_3) \mathcal{P}_{\text{4-noncons}}(f_0, f_1, f_2, f_3) \; , \tag{2.20}$$

with

$$\mathcal{P}_{\text{4-noncons}}(f_0, f_1, f_2, f_3) = [(1 - f_0)(1 + f_1) f_2 (1 + f_3) - f_0 f_1 (1 + f_2) f_3] \; . \tag{2.21}$$

Note, that here the arguments of the delta-distributions have also changed to account for the correct energy- and momentum-conservation. As a matter of course the particle-number conserving electron-boson scattering and two-bosons absorption/emission are effective processes containing several elementary interactions (cf. Fig 2.2 below).

Like the electron-phonon scattering discussed in section 2.3.2 there can be further scatterings where one phonon is scattered into another state by absorbing a phonon. These processes are called anharmonic scatterings and are considered the leading order contribution in thermalization of phonon ensembles. The collision operator for theses cases has a similar form as the electron-phonon collision operator but of course with the bosonic phase-space factors.

Logically the previously discussed scatterings can be grouped into two types of collision operators, the three- and four-leg operators. The three-leg operator involves three different particle states, hence does not conserve the total particle number. As discussed above there are two types of four-leg operators, particle-number conserving and non-conserving, with slightly different structures. In order to keep track of the different scatterings, and the corresponding operators it is advisable to use Feynman diagrams as a simple visualization.

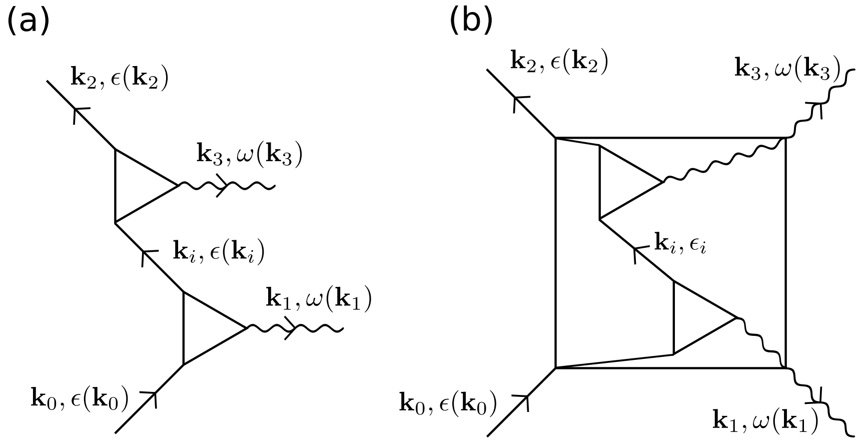
(a)
$\mathbf{k}_2, \epsilon(\mathbf{k}_2)$
$\mathbf{k}_3, \omega(\mathbf{k}_3)$
$\mathbf{k}_i, \epsilon(\mathbf{k}_i)$
$\mathbf{k}_1, \omega(\mathbf{k}_1)$
$\mathbf{k}_0, \epsilon(\mathbf{k}_0)$
(b)
$\mathbf{k}_2, \epsilon(\mathbf{k}_2)$
$\mathbf{k}_3, \omega(\mathbf{k}_3)$
$\mathbf{k}_i, \epsilon_i$
$\mathbf{k}_0, \epsilon(\mathbf{k}_0)$
$\mathbf{k}_1, \omega(\mathbf{k}_1)$

Figure 2.2: Illustration of electron-phonon scattering by Feynman-diagrams. (a) The consecutive repetition of the three-leg electron-phonon scattering in Boltzmann. Note that the intermediate electron $\mathbf{k}_i$ is limited to the energy $\epsilon(\mathbf{k}_i)$. (b) In order to include real two-phonon processes one has to implement the four-leg collision operator in Boltzmann.

However, there are some differences compared to the Feynman diagrams used in high-energy physics or in quantum many-body physics. The major difference is, that lines going into, or out of the diagram are always considered proper quasi-particle states. The corresponding propagator is already strongly renormalized and the energy is linked to the corresponding momentum by the dispersion relation.

This is illustrated by Fig. 2.2 that shows an example with electron-phonon scattering. When three-leg electron-phonon scattering is included, consecutive electron-phonon scatterings are taken into account in Boltzmann theory automatically. However, the intermediate electron in state $\mathbf{k}_i$ has to have the energy $\epsilon(\mathbf{k}_i)$. If for example the three-leg process is not possible at all because of momentum or energy conservation also the consecutive repetition of the diagram gives no contribution. In quantum field theory the intermediate electron can have any energy regardless of the momentum. Hence, there can be two-phonon processes even if the simple one-phonon process is not possible (at least in the Boltzmann-sense). In order to include such two-phonon processes in Boltzmann one has to describe them as four-leg operators.

Additionally, the phase information between consecutive scatterings is lost in Boltzmann theory.[6] Nevertheless, renormalizations because of phase-coherent scatterings can be included in the effective interaction potential that adjusts the strength of the corresponding scattering operator and in the renormalization of the dispersion relation.

With the Feynman diagrams in mind it is easy to set up some general rules for the construction of the corresponding collision operators:

---

[6] We will implicitly always assume that if we draw Feynman diagrams in the following.

- The momenta and energies corresponding to lines that go into (out of) the diagram get a positive (negative) sign in the delta distributions.
- The first term in the phase-space factor is the product of $(1-f)$ (fermions) or $(1+f)$ (bosons) factors for all lines that go out of the diagram and f factors for all lines that go into the diagram.
- The second term in the phase-space factor is subtracted from the first one and is constructed in the exact opposite way. It corresponds to the time-reversed diagram.
- If the tracked state (i.e. the state that is not integrated out) corresponds to a line going into the diagram one has to multiply the whole phase-space factor with (-1) to ensure the correct ordering of the two terms.

This way additional collision operators can be constructed.

2.3.4 Difficulties in calculating the collision operator

The integral of a four-leg collision operator is $3d$-dimensional for a d-dimensional system. In three dimensions the integral, hence, would be 9-dimensional. This already precludes most deterministic integration procedures, like the trapezoidal rule, as they scale badly with the dimension of the integral. The standard methods that are used for high-dimensional integrals are from the field of Monte-Carlo integration which are non-deterministic. The absolute accuracy of these methods scales with the inverse square-root of the number of points used, i.e. $\propto \frac{1}{\sqrt{N_{\mathrm{MC}}}}$ and is independent of the integral-dimension. Unfortunately, the demands regarding accuracy are relatively high for the scattering problem. If there is a finite error added to the actual value of the collision integral, the time derivative will change the total number of particles and the total energy in the system. Hence, it will eventually thermalize to a different equilibrium or not thermalize at all.

Furthermore, the integrand of a collision operator includes four delta-distributions in 3-dimensional systems, one per spatial dimension for momentum-conservation and one for energy-conservation. The momentum-deltas depend on the integration variables in a linear fashion, hence, they can be inverted analytically. The energy delta, however, depends on the integration variables (i.e. the momenta) only through the dispersion relations which can be arbitrary functions. If we consider the momentum that is not integrated as fixed, the energy-delta describes a $(3d-1)$-dimensional hypersurface in the $3d$ dimensional integration domain. In a similar way as the Fermi-surface it can have arbitrarily complicated shapes and even consist of several disconnected parts. This makes standard Monte-Carlo integration on the $3d$-dimensional integration domain impossible as the hypersurface will never be hit by a Monte-Carlo point by chance. The analytical reduction of the integral to an integration on the energy- and momentum-conserving subspace is only possible for some special cases like purely parabolic dispersion relations.

In addition to the difficulties discussed above the four-leg collision operator is a quartic operator in the distribution function f. If we want to project the whole Boltzmann equation onto a basis, as in finite-element discretization schemes, the collision operator would become a rank-five tensor. Given a finite number N_B of basis functions in the momentum space, we would have to evaluate the collision operator for all ${N_B}^5$ basis-function combinations. For a rather small basis-set consisting of $N_B = 100$ basis functions this would already give 10^{10} integrations. To describe a distribution function in the 3-dimensional momentum-space at room-temperature, $N_B = 100$ is often far from sufficient. We would rather need 100 basis-functions per dimension, i.e. $N_B = 10^6$ which makes a straight forward implementation of a finite-element scheme impossible on current computers or any machine in near future.

The above arguments are the reason why the full four-leg collision operator is usually not used in calculations, but only certain approximations. Summarizing, the main problems are

- The high dimensionality of the integral.
- The $d + 1$ delta-distributions inside the integral, where one of them depends on the integration variables through an arbitrary function.
- High accuracy requirements, in order to conserve the number of particles and the energy.
- The quartic structure of the four-leg operator that makes a projection onto a basis-set scale as ${N_B}^5$.

These issues will be discussed in more detail in chapter 5 where we will also explain how to tackle them.

2.4 Relaxation time approximation and local equilibrium

Due to the complicated mathematical structure of the full BTE it is very difficult to solve it numerically, especially if the full scattering is taken into account. Therefore, for standard transport calculations, several approximations are usually made. This thesis is dedicated to the solution of the full Boltzmann-transport-equation, nevertheless the relaxation-time approximation and the local equilibrium are introduced here as they are widely used and constitute the standard test-case.

The Fermi-Dirac (for fermions) and Bose-Einstein (for bosons) distributions are a fixed-point of the collision operators consistent with our knowledge from statistical physics. This means, if an external perturbation induces a non-equilibrium distribution, the collision operator ensures that the Fermi-Dirac or Bose-Einstein distribution is reestablished after the external perturbation has vanished. For non-equilibrium distributions that are sufficiently close to equilibrium one expects the non-equilibrium to decay to the thermal equilibrium exponentially with a time constant τ known as relaxation time. The collision operators for electron-scattering can then be approximated as

$$\left(\frac{\partial f(t,\mathbf{x},\mathbf{k})}{\partial t}\right)_{\text{col}} = -\frac{f(t,\mathbf{x},\mathbf{k}) - f_{\text{FD}}(\epsilon(\mathbf{k}),\mu,T)}{\tau_{\text{col}}(\mathbf{k},\mu,T)} \equiv -\frac{\delta f(t,\mathbf{x},\mathbf{k},\mu,T)}{\tau_{\text{col}}(\mathbf{k},\mu,T)} \ . \tag{2.22}$$

The Fermi-Dirac distribution $f_{\text{FD}}(\cdot,\cdot,\cdot)$ is defined as

$$f_{\text{FD}}(\epsilon,\mu,T) = \frac{1}{\exp\left(\frac{\epsilon-\mu}{k_B T}\right)+1} \ , \tag{2.23}$$

with the Boltzmann-constant k_B, the chemical potential μ and the temperature T. Note, that in the given version the relaxation-time depends on the momentum $\mathbf{k}$. This follows directly from the momentum-dependence of the original collision operators. However, often the approximation of a purely energy dependent $\tau(\epsilon(\mathbf{k}),\mu,T)$ or even constant $\tau(\mu,T)$ relaxation time is made in order to simplify calculations. It is important to keep in mind that the relaxation-times τ_{col} have to fulfill certain symmetries with respect to $\mathbf{k}$ in order to conserve the number of particles in the system. The energy conservation may be broken if the scatterings include dissipative processes like electron-phonon scatterings.

If the dynamics in a system is described by several different scattering mechanisms, the sum of the inverse relaxation-times gives the inverse of the total relaxation-time, i.e.

$$\frac{1}{\tau(\mathbf{k},\mu,T)} = \sum_{\text{col}} \frac{1}{\tau_{\text{col}}(\mathbf{k},\mu,T)} \ . \tag{2.24}$$

The relaxation-time approximation is often used in combination with another simplification, the so-called local equilibrium approximation. This approximation assumes that even in a spatially inhomogeneous system, the local distribution function resembles a Fermi-Dirac distribution. However, in order to account for the spatial inhomogeneity, the chemical potential and the temperature have to be position dependent, i.e. $\mu \to \mu(\mathbf{x})$ and $T \to T(\mathbf{x})$, i.e. we have Eq. (2.22) with $f_{\text{FD}}(\epsilon(\mathbf{k}),\mu(\mathbf{x}),T(\mathbf{x}))$. This is well-justified if the electron mean-free path, i.e. the path an electron can move without scattering, is short compared to the scale on which $T(\mathbf{x})$ and $\mu(\mathbf{x})$ change. Note, that δf still depends on $\mathbf{x}$

and **k** explicitly. In this regime it is advantageous to rewrite the Boltzmann-equation in terms of δf as defined in Eq. (2.22). Together with the relaxation-time approximation, the BTE becomes

$$\frac{\delta f}{\partial t} + \mathbf{v}_x \cdot \nabla_x(\delta f + f_{\mathrm{FD}}) + \mathbf{v}_k \cdot \nabla_k(\delta f + f_{\mathrm{FD}}) = -\frac{1}{\tau}\delta f \ . \tag{2.25}$$

In the stationary case the time-derivative of δf is zero and Eq. (2.25) becomes

$$\delta f = -\tau\Big(\mathbf{v}_x \cdot \nabla_x(\delta f + f_{\mathrm{FD}}) + \mathbf{v}_k \cdot \nabla_k(\delta f + f_{\mathrm{FD}})\Big) \ , \tag{2.26}$$

for which we can perform a fixed-point iteration to obtain δf. When we insert $\delta f = 0$ into the right-hand side of Eq. (2.26) we get the leading-order approximation of δf, i.e. the linear response of the system,

$$\delta f \approx -\tau\left(\mathbf{v}_x \cdot \left(\frac{\partial f_{\mathrm{FD}}}{\partial \mu}\nabla_x \mu + \frac{\partial f_{\mathrm{FD}}}{\partial T}\nabla_x T\right) + \mathbf{v}_k \cdot \frac{\partial f_{\mathrm{FD}}}{\partial \epsilon}\nabla_k \epsilon\right) \ . \tag{2.27}$$

With δf known, one can calculate response quantities, for example the electric current $\mathbf{J}_C$, according to Eq. (2.5). For the case of zero magnetic field and constant temperature this gives the famous Drift-Diffusion[7] equation [39],

$$\mathbf{J}_C = \sigma\left(\mathbf{E} + \frac{1}{e}\nabla\mu\right) \ , \tag{2.28}$$

with the electrical conductivity tensor $\sigma_{\alpha\beta}$,

$$\sigma_{\alpha\beta} = \frac{e^2}{\hbar^2}\sum_{n,\sigma}\int_{V_{BZ}} \mathrm{d}^d k \frac{\tau}{(2\pi)^d}(\nabla_{\mathbf{k}}\epsilon_{n,\sigma})_\alpha(\nabla_{\mathbf{k}}\epsilon_{n,\sigma})_\beta\left(-\frac{\partial f_{\mathrm{FD}}}{\partial \epsilon}\right) \ . \tag{2.29}$$

In the exact same way other response functions like the Seebeck coefficient, the thermal conductivity or the Hall coefficient can be calculated.

The transport equations and response functions obtained by the combination of relaxation time and local equilibrium approximation are vastly applied in physics and engineering. They are often referred to simply as Boltzmann transport theory even if they, more properly, are the perturbative expansion of Boltzmann with relaxation time and local equilibrium approximation. This leads to some confusion when it comes to discussions about the applicability of Boltzmann theory as often simply the approximations break down rather than Boltzmann transport theory itself.

---

[7] Here, the version with electrical field and chemical potential is shown. Instead of the chemical potential one can also write the equation in dependence of the particle density which is more common in the field of semiconductor physics.

Chapter 3

Boltzmann scattering without momentum conservation

In order to study the thermalization of systems out-of-equilibrium one has to solve the Boltzmann-equation Eq. 2.8. This, however, proves a very difficult task due to the involved nature of the collision operator as pointed out in section 2.3.4. One common, though severe, approximation for the collision-operator is the relaxation-time approximation briefly discussed in section 2.4. This simplification works well for simple transport calculations but gives poor results for the thermalization dynamics of strongly out-of-equilibrium systems.

One of the main complications of the collision operator is the simultaneous conservation of momentum and energy. In the field of non-equilibrium Green's functions (NEGF) one of the state-of-the-art methods is non-equilibrium DMFT (NEDMFT) [35,36] which becomes exact in the limit of infinite dimensions. In this limit it is sufficient to map the lattice problem onto a single impurity problem that is then solved. In the equations describing a single impurity the momentum $\mathbf{k}$ does not occur at all as it is a quantum-number that corresponds to the discrete translational invariance of the hamiltonian. In other words DMFT neglects the momentum dependence of the scattering.

In this section we will apply the DMFT approximation to the Boltzmann electron-electron collision operator and compare the corresponding thermalization dynamics to results obtained by NEDMFT. Remarkably, even in the Mott-insulating phase, the modified Boltzmann approach gives almost identical results, at least for some quantities. It can be shown that there is a deeper connection with the NEGF formalism from which this seemingly semi-classical collision-operator can be derived, even if there are no proper quasi-particles.

The chapter is organized as follows: At first, a simplified collision operator without momentum conservation is derived (section 3.1), then the numerical implementation of a solver for this collision operator is discussed (section 3.2) and finally the modified collision operator is used to describe the thermalization dynamics of a photo-excited Mott-insulator and the results are compared to NEDMFT (section 3.3).

The results shown in this chapter have been published in Ref. [66]. Some of the figures and parts of the text (marked by a black, vertical bar) are taken from this publication.

3.1 Model and derivation

For the entire chapter we will focus on a single band system with electron-electron interaction only. We are going to compare the results with NEDMFT that was applied to a Hubbard model [67] for a hypercubic lattice. In the Hubbard model, the Schrödinger equation is projected onto localized orbitals, the so-called Wannier orbitals. An orbital is located at each lattice site and the electrons are allowed to jump from one lattice site to another. Here we limit the hopping to the nearest neighbor only. If two electrons are located on the same site the system energy is increased by a factor U because of their electric repulsion. The corresponding Hamiltonian reads,

$$\hat{H} = \underbrace{-t \sum_{\langle i,j\rangle,\sigma} \hat{a}^\dagger_{i\sigma}\hat{a}_{j\sigma}}_{\hat{H}_0} + \underbrace{U \sum_i \hat{a}^\dagger_{i\uparrow}\hat{a}_{i\uparrow}\hat{a}^\dagger_{i\downarrow}\hat{a}_{i\downarrow}}_{\hat{H}_{e-e}} \tag{3.1}$$

with the hopping amplitude t, the on-site interaction U and the creation (annihilation) operator $\hat{a}^\dagger_{i\sigma}$ ($\hat{a}_{i\sigma}$) of an electron with spin σ at site i.

The non-interacting part $\hat{H}_0$ is diagonal when it is written with the new creation and annihilation operators,

$$\hat{\Psi}_{\mathbf{k}\sigma} \equiv \frac{1}{\sqrt{N}} \sum_j e^{i\mathbf{R}_j\cdot\mathbf{k}} \hat{a}_{j\sigma}, \tag{3.2a}$$

$$\hat{\Psi}^\dagger_{\mathbf{k}\sigma} \equiv \frac{1}{\sqrt{N}} \sum_j e^{-i\mathbf{R}_j\cdot\mathbf{k}} \hat{a}^\dagger_{j\sigma} \ . \tag{3.2b}$$

The quantity N is the total number of lattice sites[1] and the vector $\mathbf{R}_j$ points to the j-th lattice site. For the case $U \ll t$ the new operators describe proper quasi-particles for which we can apply Boltzmann-theory.

The Boltzmann equation Eq. (2.8) for a spatially homogeneous (i.e. $\nabla_{\mathbf{x}} f = 0$) single-band system with vanishing external electromagnetic fields (i.e. $\mathbf{E} = 0$ and $\mathbf{B} = 0$) and electron-electron interaction becomes

$$\begin{aligned}\frac{\partial}{\partial t} f_0 = \frac{1}{2} \sum_{\sigma_1,\sigma_2,\sigma_3} \sum_{\mathbf{G}} \iiint_{V_{BZ}{}^3} \mathrm{d}^d k_1 \mathrm{d}^d k_2 \mathrm{d}^d k_3 \; w^{\text{e-e}}_{0123} \; \delta(\mathbf{k}_0 + \mathbf{k}_1 - \mathbf{k}_2 - \mathbf{k}_3 + \mathbf{G}) \\ \times \delta(\epsilon_0 + \epsilon_1 - \epsilon_2 - \epsilon_3) \; \mathcal{P}(f_0, f_1, f_2, f_3)\end{aligned} \ . \tag{3.3}$$

---

[1] For now we consider a d-dimensional system. The limit $d \to \infty$ is performed in the end.

The factor $\frac{1}{2}$ in front of the sums is needed to prevent double counting. With the operators Eq. (3.2) and the fermionic anti-commutation relations we can calculate $w^{\text{e-e}}_{0123}$ as defined by Eq. (2.10) (see Appendix A),

$$w^{\text{e-e}}_{0123} = \frac{2\pi}{\hbar} \frac{U^2}{{V_{BZ}}^2} \delta_{\sigma_0,\bar{\sigma}_1} \delta_{\sigma_2,\bar{\sigma}_3} \ . \tag{3.4}$$

The two Kronecker-deltas represent the fact that only electrons of opposite spin may scatter with each other ($\bar{\sigma}_i \equiv -\sigma_i$) and that the total spin is conserved in the scattering event. This is a direct consequence of the single band and the local nature of the interaction that is used in the Hubbard-model.

In analogy to DMFT we give up momentum conservation also for the Boltzmann equation. That is, we remove the delta-distribution that ensures momentum conservation. To leave the order of magnitude and unit the same, we replace the delta-distribution with the inverse volume of the Brillouin-zone,

$$\sum_{\mathbf{G}} \delta(\mathbf{k}_0 + \mathbf{k}_1 - \mathbf{k}_2 - \mathbf{k}_3 + \mathbf{G}) \to \frac{1}{V_{BZ}} \ . \tag{3.5}$$

With the simplification Eq. (3.5) and the explicit form of the scattering amplitude $w^{\text{e-e}}_{0123}$ Eq. (3.4), the Boltzmann-equation Eq. (3.3) becomes

$$\begin{aligned} \frac{\partial}{\partial t} f_{\sigma_0}(\mathbf{k}_0) = \frac{2\pi}{\hbar} \frac{U^2}{{V_{BZ}}^3} \iiint_{{V_{BZ}}^3} &\mathrm{d}^d k_1 \mathrm{d}^d k_2 \mathrm{d}^d k_3 \ \delta(\epsilon_0 + \epsilon_1 - \epsilon_2 - \epsilon_3) \\ &\times \Big[(1 - f_{\sigma_0}(\mathbf{k}_0))(1 - f_{\bar{\sigma}_0}(\mathbf{k}_1)) f_\uparrow(\mathbf{k}_2) f_\downarrow(\mathbf{k}_3) \\ &\quad - f_{\sigma_0}(\mathbf{k}_0) f_{\bar{\sigma}_0}(\mathbf{k}_1)(1 - f_\uparrow(\mathbf{k}_2))(1 - f_\downarrow(\mathbf{k}_3)) \Big] \ . \end{aligned} \tag{3.6}$$

Analyzing the above equation we find that the sums over the spins have completely vanished due to the Kronecker-deltas in $w^{\text{e-e}}_{0123}$ and the fact that the integrand is symmetric with respect to exchange of the spins σ_2 and σ_3.

Furthermore, we observe that the integrand only depends on the momenta $\mathbf{k}_i$ through the distribution-functions. Hence, if the initial distribution-function at time $t = 0$ depends on $\mathbf{k}$ only through the dispersion relation $\epsilon(\mathbf{k})$ (i.e. when $f_\sigma(t = 0, \mathbf{k}) = \tilde{f}_\sigma(\epsilon(\mathbf{k}))$), the Boltzmann-equation without momentum-conservation (Eq. (3.6)) preserves that property. If we start from such a distribution, we may describe the system by a distribution function that only depends on the energy, i.e. $f_\sigma(\mathbf{k}) \to f_\sigma(\epsilon)$ for all times. Moreover, the integrand does not distinguish between spins. If the two spin distributions for spin up and spin down are equal at time $t = 0$ we can apply the same argument as above and describe the system with a single distribution function that depends only on the energy, i.e. $f_\sigma(\epsilon) \to f(\epsilon)$.

Now, the whole integrand in Eq. (3.6) depends on the momenta only through the dispersion relations $\epsilon(\mathbf{k})$. We can split each d-dimensional momentum integration into a

$d-1$ dimensional integration over the equal-energy shells and the momentum orthogonal to it or, equivalently, the energy, i.e. $\int \mathrm{d}^d k = \int \mathrm{d}k_\perp \int \mathrm{d}^{d-1} k_\parallel = \int \mathrm{d}\epsilon \int \mathrm{d}^{d-1} k_\parallel \frac{1}{|\nabla_{\mathbf{k}}\epsilon|}$. Using furthermore the fact that the normalized non-interacting density-of-states may be written as $A_0(\epsilon) = \frac{1}{V_{BZ}} \int \mathrm{d}^{d-1} k_\parallel \frac{1}{|\nabla \epsilon|}$ we can write the Boltzmann-equation without momentum-conservation eventually as

$$\begin{aligned}\frac{\partial}{\partial t} f(\epsilon_0) = \frac{2\pi}{\hbar} U^2 \iiint & \mathrm{d}\epsilon_1 \mathrm{d}\epsilon_2 \mathrm{d}\epsilon_3 \; A_0(\epsilon_1) A_0(\epsilon_2) A_0(\epsilon_3) \; \delta(\epsilon_0 + \epsilon_1 - \epsilon_2 - \epsilon_3) \\ & \times \Big[(1 - f(\epsilon_0))(1 - f(\epsilon_1)) f(\epsilon_2) f(\epsilon_3) \\ & \quad - f(\epsilon_0) f(\epsilon_1)(1 - f(\epsilon_2))(1 - f(\epsilon_3)) \Big] \; . \end{aligned} \tag{3.7}$$

This simplified version has several numerical advantages over the original Eq. (3.3):

- The integral is only 3-dimensional, regardless of the dimension of the system.
- There is only a single delta-distribution, and its argument depends on the integration variables only in a linear fashion.
- There is only a single distribution function due to spin-degeneracy.

Eq. (3.7) was derived from the Boltzmann equation. Hence, it is only a valid description if the interaction U is sufficiently smaller than the hopping t, i.e. $U \ll t$. This is also reflected by the occurrence of the density-of-states $A_0(\cdot)$ as in interacting systems with finite interaction there is strictly spoken no density-of-states. However, there exists an analogue quantity, the so-called spectral density $A(\epsilon)$ [68, 69]. When it is multiplied with an energy interval $\mathrm{d}\epsilon$, it gives the number of states that lie in this interval $\mathrm{d}\epsilon$ around the energy ϵ. It is calculated with

$$A(\omega) = -\frac{1}{\pi} \mathrm{Im} G^R(\omega) \; , \tag{3.8}$$

where $G^R(\omega)$ is the local, retarded Green's function that is defined as

$$G^R(t - t') = -i\Theta(t - t') \frac{1}{N} \sum_k \langle [\hat{\Psi}_{\mathbf{k}\sigma}(t), \hat{\Psi}^\dagger_{\mathbf{k}\sigma}(t')]_+ \rangle \; , \tag{3.9}$$

with the Heaviside-function $\Theta(\cdot)$ and the anti-commutator $[A, B]_+ \equiv AB + BA$. In case of larger U it is tempting to use Eq. (3.7) but replace the density-of-states by the spectral-density, $A_0(\cdot) \to A(\cdot)$. This will be a good approximation when the operators defined by Eq. (3.2) describe good quasi-particles. For the strongly interacting case this is not at all clear. The scattering rate in e.g. the upper Hubbard band is quite substantial, in particular at the low energy edge. However, we find that the above equation with the spectral density gives good agreement with results from non-equilibrium DMFT (NEDMFT) for the relaxation of an excited Mott-insulator (see section 3.3). A deeper reason for this unexpected result lies in the fact that a connection with NEDMFT exists.

From the non-equilibrium DMFT formalism we get, in principle, a time-dependent spectral density, $A(t,\epsilon)$. For NEGF there exists an analogue to the quasi-particle distribution function that is denoted as $F(t,\epsilon)$ (see Ref. [70] and Eq. (3.11) below) which will be called distribution function as well in the following. In equilibrium, $F(t,\epsilon)$ is given by a Fermi-Dirac distribution like the equilibrium quasi-particle distribution function. It can be shown that even for the case where $U \ll t$ does not hold, an equation with the same mathematical structure as the Boltzmann equation without momentum conservation Eq. (3.7) can be obtained for $F(t,\epsilon)$ if we require that the spectral-density is time-independent, i.e.

$$A(t,\epsilon) = A(0,\epsilon) \quad \forall t \; . \tag{3.10}$$

For the details of the derivation refer to Ref. [66]. For this simplified case, the distribution function can be calculated from the so-called lesser Green's function $G^<$ to leading order with the relation

$$F(t,\epsilon) = \frac{G^<(t,\epsilon)}{2\pi i A(0,\epsilon)} \; . \tag{3.11}$$

The obtained equation for the time-derivative of $F(t,\epsilon)$ reads [66]

$$\begin{aligned}\frac{\partial}{\partial t}F(\epsilon_0) = \underbrace{\frac{2\pi}{\hbar}U\bar{U}}_{\equiv\alpha} \iiint & \mathrm{d}\epsilon_1\mathrm{d}\epsilon_2\mathrm{d}\epsilon_3\; A(\epsilon_1)A(\epsilon_2)A(\epsilon_3)\;\delta(\epsilon_0+\epsilon_1-\epsilon_2-\epsilon_3) \\ & \times\Big[(1-F(\epsilon_0))(1-F(\epsilon_1))F(\epsilon_2)F(\epsilon_3) \\ & \quad - F(\epsilon_0)F(\epsilon_1)(1-F(\epsilon_2))(1-F(\epsilon_3))\Big] \; .\end{aligned} \tag{3.12}$$

This equation for F is structurally equivalent to Eq. (3.7), however, the interacting spectral density occurs instead of the density-of-states. Furthermore, a renormalized interaction $\bar{U}$ enters the pre-factor, reflecting the fact that we no longer describe the original quasi-particle occupation. It is not clear how to determine this renormalized interaction ab-initio, hence, we use it as a free parameter of the theory.

We will call Eq. (3.12) quantum Boltzmann equation (QBE) in the following.

3.1.1 Laser excitations

In order to describe the dynamics of a system within the Boltzmann without momentum-conservation framework we have to solve Eq. (3.12) starting from a non-equilibrium distribution. This non-equilibrium population has to be induced externally, which is usually achieved by irradiating the system under surveillance with an intense, femto-second laser pulse. In principle, we could calculate the excitation process with some other method like NEDMFT and then use the distribution function right after the laser pulse as starting distribution (i.e. $F_0(\cdot) \equiv F(t=0,\cdot)$).

Alternatively, we can also describe the excitation process within the Boltzmann framework. The electric field entering the semiclassical equations-of-motion Eq. (2.3) is limited to sufficiently low frequencies where the energy of a single photon is much smaller then the energetic distance to the next band. Electric fields with higher frequencies are not described through the semi-classical equations-of-motion, but rather through an additional collision term. The excitation (de-excitation) can be viewed as the absorption (emission) of a single photon, i.e. it is a three-leg process structurally equivalent to electron-phonon scattering as discussed in section 2.3.2. Here we assume a sufficiently high photon density so that we may describe them as a classical electric field. The corresponding collision term for the Boltzmann equation without momentum conservation reads

$$\left(\frac{\partial F(\epsilon_0)}{\partial t}\right)_{\text{col-laser}} = \int \mathrm{d}\epsilon_1 \, A(\epsilon_1) W_{\text{laser}}\left(\epsilon_0, \epsilon_1\right) \Big[(1-F(\epsilon_0))F(\epsilon_1) - F(\epsilon_0)(1-F(\epsilon_1))\Big] \, , \quad (3.13)$$

where $W_{\text{laser}}\left(\epsilon_0, \epsilon_1\right)$ is the transition rate due to the laser.

For the case of a laser field with a single frequency Ω that was switched on in the distant past we can calculate the transition rate with time-dependent perturbation theory as

$$W_{\text{laser}}\left(\epsilon_0, \epsilon_1\right) = I\left[\delta\left(\epsilon_0 - \epsilon_1 - \Omega\right) + \delta\left(\epsilon_0 - \epsilon_1 + \Omega\right)\right] \quad (3.14)$$

which is simply Fermi's golden rule. The two delta-distributions describe absorption and stimulated emission. The actual matrix element of the operator that couples the electric field is absorbed in the factor I together with the intensity of the field and the other constants. Due to the assumption of a classical electric field, the spontaneous photon emission term is neglected. This assumption is better justified for sunlight than for actual laser-pulses.

To mimic the effect of a solar photon we consider a laser pulse with a finite duration. As an approximation we can use Eq. (3.14) but with a time-dependent pre-factor that is proportional to the time-envelope function of the laser pulse, $I \to I(t)$. This is well justified if the envelope function changes slowly compared to the laser period $\tau = \frac{2\pi}{\Omega}$.

This argument does not strictly hold for femto-second laser-pulses as they often consist of few field-cycles only. Hence, we will also apply first-order, time-dependent perturbation theory directly. The laser field we use has the shape

$$\mathbf{E}(t) = \mathbf{n}E(t) = \mathbf{n}\underbrace{E_0 e^{-\left(\frac{t-t_0}{\sigma}\right)^2}}_{\equiv\sqrt{I(t)}} \sin(\Omega(t-t_0)) \quad (3.15)$$

Die approbierte gedruckte Originalversion dieser Dissertation ist an der TU Wien Bibliothek verfügbar.
The approved original version of this doctoral thesis is available in print at TU Wien Bibliothek.
TU Bibliothek WIEN Your knowledge hub

with the unit vector $\mathbf{n}$ that gives the polarization direction. If magnetic excitations are negligible, we can describe the coupling of the electric field to the system via the operator $-\hat{\mathbf{r}}$, hence, the perturbing potential reads $\hat{V}(t) = E(t)\hat{O}$ with $\hat{O} \equiv -\hat{\mathbf{r}} \cdot \mathbf{n}$. The probability to find the system that initially was in the state $|0\rangle$ at time $t = 0$, in the state $|1\rangle$ at time t reads

$$p_{01}(\epsilon_0, \epsilon_1, t) = \left| \langle 1| \hat{O} |0\rangle \int_0^t \mathrm{d}\tau E(\tau) e^{i(\epsilon_1 - \epsilon_0)\tau} \right|^2 \tag{3.16}$$

with the energies ϵ_0 (ϵ_1) of the initial (final) state ($\hbar = 1$). In the following we assume for simplicity that the transition matrix element is one, i.e. $\langle 1| \hat{O} |0\rangle = 1$ for all states. In analogy with the derivation of Fermi's golden rule we replace the transition rate in Eq. (3.13) with

$$W_{\text{laser}}(\epsilon_0, \epsilon_1, t) = \frac{\partial}{\partial t} p_{01}(\epsilon_0, \epsilon_1, t) \ . \tag{3.17}$$

The transition rate $W_{\text{laser}}(\epsilon_0, \epsilon_1, t)$ is now time-dependent and can become negative as well. The latter represents the coherent dynamics of electrons which are brought back to their original state after being excited. Such coherent processes are usually excluded in Boltzmann theory as they average to zero over longer timescales. On short timescales they can produce internal inconsistencies since they are associated with negative transition probabilities. This, in turn, could lead to negative populations. However, if the electron-electron scattering is much slower than the frequency of the coherent processes we can still employ Eq. (3.17) as an approximation since it is a valid (first-order) description if we only consider the (phase coherent) laser excitation between the states ϵ_0 and ϵ_1.

3.2 Numerical implementation

The QBE Eq. (3.12) consists of a three-dimensional integration and the energy-conserving delta-distribution. The delta could, in principle, be easily inverted analytically as it only depends on the integration variables in a linear fashion. The remaining two-dimensional integral is easily calculated by a standard numerical technique like Gauss-Integration or the Trapezoidal Rule. Eventually, the time-propagation can be calculated with an explicit time-stepping method, e.g. Forward-Euler or Runge-Kutta-4 which simply requires the evaluation of the scattering term at specific times.

Although numerically doable we chose another path here. We introduce a basis and project the distribution-function as well as the collision-operators onto this basis. The distribution-function then becomes a vector and the collision-operator becomes a tensor. In this way, applying the collision operator simply requires contracting the tensor with the distribution function vector. The tensor-elements are calculated for a certain spectral-density and stored. The time-propagation then reduces to a contraction of the tensor

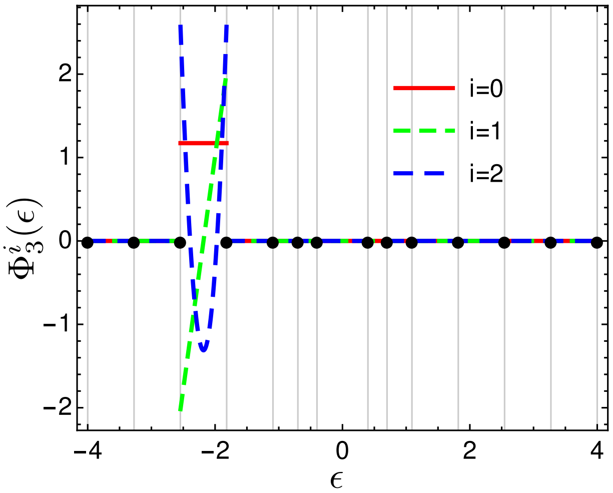

Figure 3.1: The basis functions $\Phi_I^i(\cdot)$ as defined by Eq. (3.18) for element $I = 3$ up to second polynomial order, $i \in [0, 2]$. The black dots and the vertical gray lines mark the element boundaries, the number of mesh elements is $N_E = 13$. The element size in this example is not uniform.

in every time-step. This method proves numerically advantageous when many different time-integrations are done for the same system, i.e. the same spectral-density $A(\cdot)$.

The discontinuous Galerkin basis (DG-basis) which will be more formally introduced in section 4.1 has several favorable properties for the collision-problem. First, each basis-function has a compact support, hence, it is only nonzero in a certain energy-range. In combination with the energy-conserving delta-function, this makes the projected collision operators sparse tensors. Second, the discontinuous nature of the basis-set allows for steep changes of the projected function. This is particularly advantageous for low-temperature Fermi-Dirac distributions.

In order to define the discontinuous Galerkin basis we split the energy domain into N_E elements where each element $I \in [1, N_E]$ has the lower (upper) boundary b_I (b_{I+1}). The basis functions we use are defined as

$$\Phi_I^i(x) = \begin{cases} \sqrt{\frac{2i+1}{b_{I+1}-b_I}} P_i\left(\frac{2x-b_{I+1}-b_I}{b_{I+1}-b_I}\right) & b_I \le x < b_{I+1} \\ 0 & \text{otherwise} \end{cases} , \tag{3.18}$$

where $P_i(y)$ is the Legendre-polynomial of order i at position y. We use Legendre-polynomials up to second polynomial order, i.e. $i \in [0, 2]$ (Fig. 3.1). It can be shown easily that the basis-set as defined by Eq. (3.18) is orthonormal with respect to the L^2-scalar product.

Using the expansion coefficients of the distribution function,

$$F_I^i(t) \equiv \int \mathrm{d}\epsilon \; \Phi_I^i(\epsilon) F(t, \epsilon) \; , \tag{3.19}$$

and the projection of the number 1 onto the basis,

$$1_I^i \equiv \int \mathrm{d}\epsilon \; \Phi_I^i(\epsilon) \ , \tag{3.20}$$

Eq. (3.12) becomes

$$\begin{aligned} \frac{\partial F_I^i(t)}{\partial t} = \alpha \sum_{\substack{j,k,m,n \\ J,K,M,N}} & \mathbb{S}_{IJKMN}^{ijkmn} \\ \times \Big(& \left(1_J^j - F_J^j(t)\right) \left(1_K^k - F_K^k(t)\right) F_M^m(t) F_N^n(t) \\ & - F_J^j(t) F_K^k(t) \left(1_M^m - F_M^m(t)\right) \left(1_N^n - F_N^n(t)\right) \Big), \end{aligned} \tag{3.21}$$

with the tensorial form of the collision operator that we will call scattering tensor in this thesis,

$$\begin{aligned} \mathbb{S}_{IJKMN}^{ijkmn} = \iiint & \mathrm{d}\epsilon_0 \mathrm{d}\epsilon_1 \mathrm{d}\epsilon_2 \mathrm{d}\epsilon_3 \; \Phi_I^i(\epsilon_0) \Phi_J^j(\epsilon_0) \Phi_K^k(\epsilon_1) \Phi_M^m(\epsilon_2) \Phi_N^n(\epsilon_3) \\ & \times A(\epsilon_1) A(\epsilon_2) A(\epsilon_3) \; \delta\left(\epsilon_0 + \epsilon_1 - \epsilon_2 - \epsilon_3\right) \ . \end{aligned} \tag{3.22}$$

The scattering tensor contains all the information about the system (i.e. the spectral-density) and is independent of time and distribution-function. It has two important properties,

$$\mathbb{S}_{IJKMN}^{ijkmn} = \mathbb{S}_{IJKNM}^{ijknm} \ , \tag{3.23a}$$

$$\mathbb{S}_{IJKMN}^{ijkmn} = \delta_{I,J} \; \mathbb{S}_{JJKMN}^{ijkmn} \ . \tag{3.23b}$$

The relation Eq. (3.23a) is irrespective of the basis used, whereas Eq. (3.23b) follows from the fact that the DG-basis functions are only non-zero within their corresponding element.

The collision-operator for laser excitations calculated with Fermi's golden rule (Eq. (3.13) and Eq.(3.14)) becomes,

$$\begin{aligned} \underset{IJK}{\mathbb{S}_{ijk}^{\text{laser}}} = \iint & \mathrm{d}\epsilon_0 \mathrm{d}\epsilon_1 \; A(\epsilon_1) \Phi_I^i(\epsilon_0) \Phi_J^j(\epsilon_0) \Phi_K^k(\epsilon_1) \\ & \times \left[\delta\left(\epsilon_0 - \epsilon_1 - \Omega\right) + \delta\left(\epsilon_0 - \epsilon_1 + \Omega\right)\right] \ , \end{aligned} \tag{3.24}$$

that also has the property $\underset{IJK}{\mathbb{S}_{ijk}^{\text{laser}}} = \delta_{I,J} \; \underset{JJK}{\mathbb{S}_{ijk}^{\text{laser}}}$. In case of the perturbation-theory laser excitation, the transition rate depends on time explicitly (see Eqs. (3.17) and (3.16)). The scattering-tensor method can still be applied when a scattering tensor for each time-step is calculated. Numerically, this is still advantageous as the laser field is only non-zero in a very short period, hence the number of tensors required is small.

The total Boltzmann equation without momentum conservation in the DG-basis can eventually be written as

$$\begin{aligned}\frac{\partial \mathbf{F}}{\partial t} =&\alpha\ \mathbb{S}\Big((\mathbf{1}-\mathbf{F}),(\mathbf{1}-\mathbf{F}),\mathbf{F},\mathbf{F}\Big) - \alpha\ \mathbb{S}\Big(\mathbf{F},\mathbf{F},(\mathbf{1}-\mathbf{F}),(\mathbf{1}-\mathbf{F})\Big)\\ &+ I(t)\ \mathbb{S}^{\text{laser}}\Big(\mathbf{1}-\mathbf{F},\mathbf{F}\Big) - I(t)\ \mathbb{S}^{\text{laser}}\Big(\mathbf{F},\mathbf{1}-\mathbf{F}\Big)\ ,\end{aligned} \tag{3.25}$$

in case Fermi's Golden Rule is used to describe the laser excitations.[2] In case we use first-order perturbation theory for the laser excitation, the equation is similar but without the factor $I(t)$ as it is already included in the time-dependent tensor. Eq. (3.25) is time-integrated using a Runge-Kutta-4 scheme starting from an initial distribution $\mathbf{F}(t=0,\cdot) \equiv \mathbf{F}_0(\cdot)$.

This code was implemented in *Mathematica 10.* The delta-distribution inside the tensors removes one of the integrations where we have chosen the ϵ_1-integration without loss of generality. For the actual calculation of the remaining integrals the standard built-in procedure *NIntegrate* was used. The tensors themselves were implemented using the built-in *SparseArray* class.

3.2.1 Test of the code

For an infinitesimal excitation of the equilibrium Fermi-Dirac at the energy ϵ_0 (i.e. $F = f_{\text{FD}} + \delta F$) we can calculate the time derivative from Eq. (3.12) as[3]

$$\begin{aligned}\frac{\partial}{\partial t}\delta F(\epsilon_0) \approx& -\delta F(\epsilon_0) \iiint \mathrm{d}\epsilon_1 \mathrm{d}\epsilon_2 \mathrm{d}\epsilon_3\ A(\epsilon_1)A(\epsilon_2)A(\epsilon_3)\ \delta(\epsilon_0+\epsilon_1-\epsilon_2-\epsilon_3)\\ &\times \Big[(1-f_{\text{FD}}(\epsilon_1))f_{\text{FD}}(\epsilon_2)f_{\text{FD}}(\epsilon_3) + f_{\text{FD}}(\epsilon_1)(1-f_{\text{FD}}(\epsilon_2))(1-f_{\text{FD}}(\epsilon_3))\Big]\\ \equiv& -\delta F(\epsilon_0)\ \frac{1}{\tau(\epsilon_0)}\ .\end{aligned} \tag{3.26}$$

This differential equation describes an exponential decay of the excitation with a decay-time of $\tau(\cdot)$. We can eliminate the ϵ_1-integration in Eq. (3.26) with the delta-distribution and then calculate the remaining two-dimensional integration with a standard numerical integration technique for a given $A(\cdot)$. Hence, we can directly determine the decay-time for a certain energy.

Additionally, we can use our code to simulate how a non-equilibrium distribution thermalizes. We use the fact that the decay-time can be directly calculated to test our code and the method applied. For the direct calculation of the decay-time we have assumed an

---

[2] Here we have used a symbolic way of writing the tensor contractions, where the rank-5 tensor takes four vectors and returns a vector.

[3] For a detailed derivation of a similar expression see section 5.3.

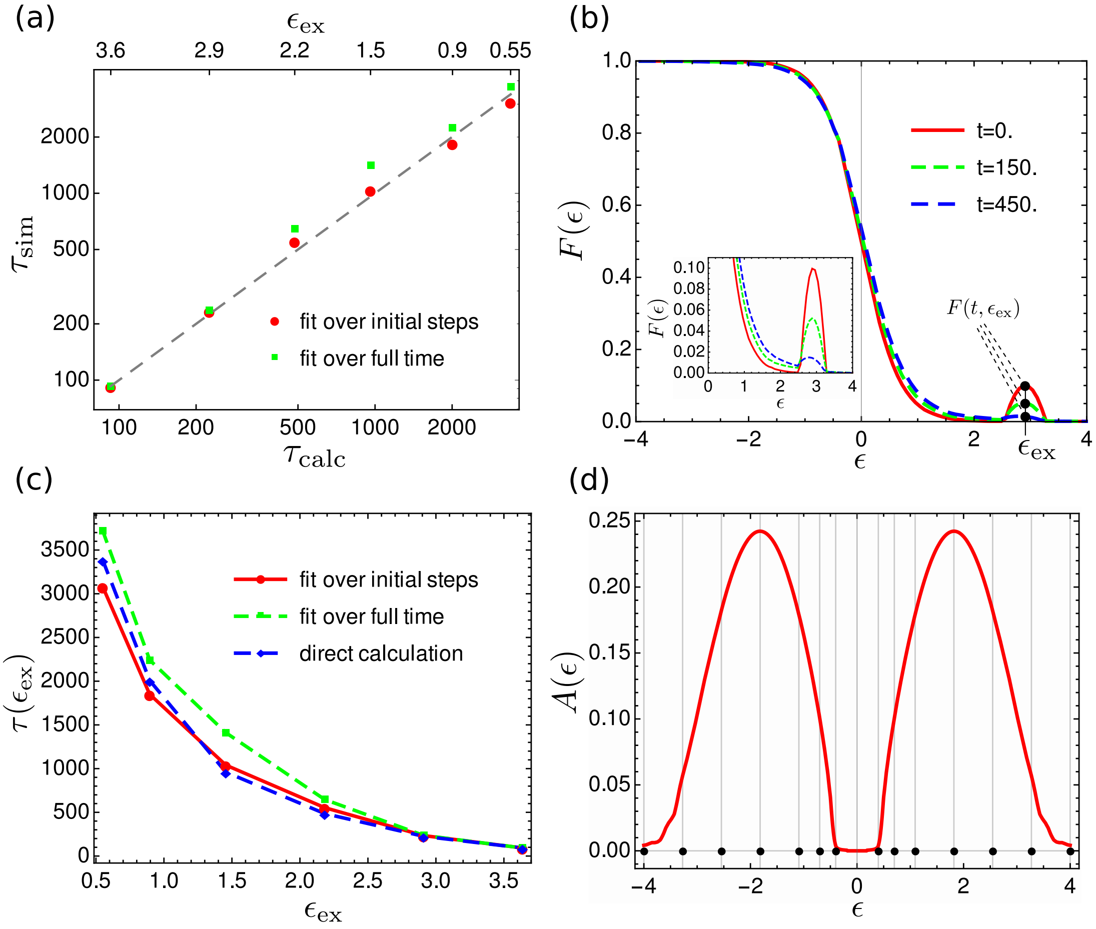

Figure 3.2: (a) The simulated decay-time τ_{sim} of a finite but small excitation (green: fit over full simulation-time; red: fit over first three time-steps) versus the decay-time τ_{calc} of an infinitesimal excitation directly calculated with Eq. (3.26). The inverse-temperature of the initial distribution was $\beta = 3$, the chemical potential $\mu = 0$ and the amplitude of the excitation $\delta F(0, \epsilon_{\text{ex}}) = 0.001$. (b) Thermalization of a distribution-function with a finite excitation at energy ϵ_{ex}. The amplitude of the excitation shown here is 100-times larger than the amplitude used for the decay-time calculation shown in (a). (c) Decay-times versus excitation energy for the two different fitting-procedures and the directly calculated result. (d) Spectral-density used for the calculation with the mesh on top.

Die approbierte gedruckte Originalversion dieser Dissertation ist an der TU Wien Bibliothek verfügbar.
The approved original version of this doctoral thesis is available in print at TU Wien Bibliothek.
TU Bibliothek Your knowledge hub WIEN

infinitesimal excitation with $\int \mathrm{d}\epsilon\ A(\epsilon)\delta F(\epsilon) \approx 0$ which we can achieve only approximately in the simulation due to the finite mesh-element size[4]. For each mesh-element with $\epsilon > 0$ we perform a simulation with an excitation that is peaked at the mesh-element center ϵ_{ex}. Then we fit an exponential-function of the shape $g(t) = c_1 + c_2\ \text{Exp}(-\frac{t}{\tau})$ to $F(t, \epsilon_{\text{ex}})$ in order to determine τ. We perform two different fits, (i) over the full simulation-time and (ii) over the first three time-steps yielding two different decay-times. The results are shown in Fig. 3.2.

The reason for the two different fittings is that for excitations close to the chemical potential of the initial Fermi-Dirac distribution the decay is not purely exponential. Hence, there is a certain ambiguity in determining the decay-time. The non-exponential decay is observed because of the finite mesh-element size as explained in the following: The amount of particles artificially injected by the excitation is proportional to the amplitude $\delta F(0, \epsilon_{\text{ex}})$ of the excitation and the mesh-element size. The distribution-function thermalizes to a new equilibrium accounting for the injected energy and particles (see inset Fig. 3.2b). The change of the distribution-function at its exponential tail depends on the number of injected particles and the energy, hence, it also depends on the amplitude of the excitation and the mesh-element size. Consequently, the ratio between the local change of the distribution-function and the change of the excitation itself is independent of the excitation amplitude $\delta F(0, \epsilon_{\text{ex}})$. The consequence is a non-exponential decay behavior occurring irrespective of the excitation-amplitude (assuming that we are still in the low perturbation regime).

3.3 Thermalization dynamics of an excited, hypercubic Mott-insulator

We use the quantum Boltzmann equation (QBE) introduced in the previous sections to simulate the excitation and relaxation of a hypercubic Mott-insulator. The results are compared to NEDMFT simulations of Ref. [71] and an unexpectedly good agreement between the conceptually different methods is found for the time-dependent particle-density. With the QBE we can simulate the laser excitation process with two different approximations introduced in section 3.1.1 and get more insight into the intriguing excitation dynamics also seen in NEDMFT. Due to the high cost of NEDMFT simulations, they can access only relatively short timescales. Since the QBE is numerically cheaper to calculate we can simulate the full thermalization which enables us to study the partial thermalization between the different Hubbard-bands occurring at an intermediate timescale.

---

[4] More precisely, the criteria under which Eq. (3.26) (see Appendix B) holds are only fulfilled approximately in the simulation due to the finite mesh-element size.

The following pages marked by a black, vertical line are taken from Ref. [66] and were mainly written by me, yet reviewed and slightly modified by my co-authors. The actual publication contains more theory about the connection of the QBE with non-equilibrium Green's functions which was not written by me and hence, only briefly summarized in section 3.1 above.

The term QPBE used in the following pages is an abbreviation of Quasi-particle-Boltzmann-equation and refers to Boltzmann for small interactions where clear quasi-particles can be identified (i.e. Eq. (3.7)). As in the previous section the term QBE stands for quantum Boltzmann equation and refers to the mathematically similar Eq. (3.12).

3.3.1 Spectral density for QBE

As described in the previous sections, our quantum Boltzmann equation is based on the assumption of a relatively rigid local density of states $A(\omega)$, with the Boltzmann equation describing the distribution function $F(\epsilon)$ with respect to this rigid density of states. This approximation is justified retrospectively by comparison to non-equilibrium DMFT results, where it is found to work under certain conditions. For our calculations we use the equilibrium spectral density $A(\epsilon)$ obtained from DMFT calculations for a certain chemical potential μ_0 and temperature T_0 and assume that its structure remains unchanged even when energy is pumped into the system, i.e.

$$A(\omega) = -\frac{1}{\pi}\mathrm{Im}G^R(\omega) \quad \forall t, \tag{3.27}$$

where $G^R(\omega)$ is the local retarded Green's function of a system with μ_0 and T_0.

The density of states used in the simulations corresponds to a Mott insulator with Hubbard bands and is shown in Fig. 3.3. Here, quasiparticles are not particularly well defined since the equilibrium DMFT self-energy [71] is 0.4 at the upper edge of the upper Hubbard band and – for generating the Mott gap – even larger (larger than the bandwidth) at its lower edge. Note, that the DMFT self-energy in the Mott-Hubbard bands remains finite also in the $U \to \infty$ limit, albeit it becomes slightly smaller and symmetric. Nonetheless the Boltzmann equation is found to produce meaningful results which demonstrates that the local Boltzmann equation does not have to be built on a quasiparticle approximation, as explained in Sec. 3.1.

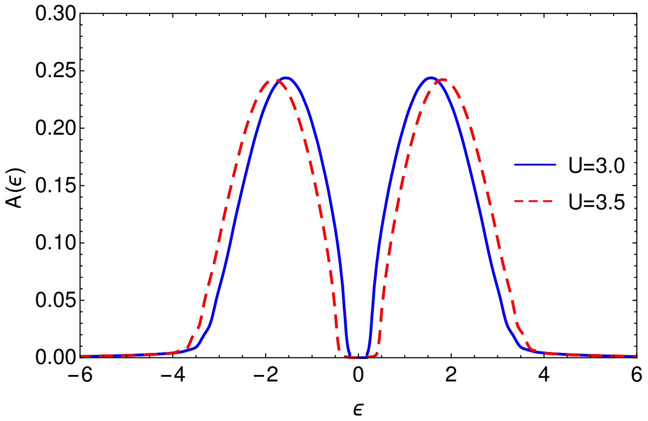

Figure 3.3: Spectral functions obtained from DMFT calculations for a hypercubic lattice at half-filling ($\mu = 0$), inverse temperature $\beta = 5$ and two different Hubbard-interactions U. For both interactions the system is in the Mott-insulating phase. (taken from Ref. [71])

3.3.2 Two time-scale relaxation dynamics

In this section we compare the dynamics obtained by the QBE to the non-equilibrium DMFT result for a hypercubic lattice at half-filling. The noninteracting density of states is $\rho_0(\epsilon) = \exp(-\epsilon^2/W^2)/\sqrt{\pi}W$ and we use $W = 1$ as the unit of energy ($1/W$ as the unit of time). We discuss Mott insulating systems with Hubbard-interactions $U = 3.0$ and $U = 3.5$ and set the initial inverse temperature to $\beta = 5$.

The excitations in the upper Hubbard band can be interpreted as double-occupancies of lattice-sites (doublons) while excitations in the lower Hubbard-band are empty sites (holons). We hence define the total doublon density $d(t)$ as

$$d(t) = \int_0^\infty \mathrm{d}\epsilon F(t,\epsilon)A(\epsilon) \tag{3.28}$$

in the Boltzmann approach. Note that this does not include virtual doublon excitations which are present in the Mott insulator even at zero temperature where $F(t,\epsilon) = 0$ for $\epsilon > 0$. If one counts both, up- and down-spin spectral functions there is also a factor of two compared to the usual double occupation because each doublon gives a peak in both, spin-up and -down, spectral functions. Since we discuss ratios of double occupations this factor two cancels anyhow.

As in Ref. [71] we excite the system with laser-pulses at different frequencies Ω and let it time-propagate until it is thermalized, i.e. until it has reached a Fermi-Dirac distribution again. We use a Gaussian time envelope centered at $t_0 = 6$ for the laser pulse as defined in Eq. (3.15), and a pulse width $\sigma = \sqrt{6}$. The strength of the laser pulse is adjusted such that the photo-induced doublon density at a given time $\tilde{t}$ right after the pulse is 0.01, i.e. $D(\tilde{t}) \equiv d(\tilde{t}) - d(0) = 0.01$. For the two different laser implementations a different strength of the laser pulse is needed to produce the same number of photo-doped doublons. We use $\tilde{t} = 15$ for the results given in Tab. 3.1, and $\tilde{t} = 12$ otherwise, in order to directly compare with time dependent data provided in Ref. [71].

Figure 3.4 shows that after the laser pulse has created a non-Fermi-Dirac population, the doublon density further increases until the system reaches its new equilibrium (marked by dashed lines). This means that during the thermalization process new doublons (and holons) have to be generated, hence electrons have to be excited across the Mott gap. The doublon-holon creation results from two different mechanisms: i) impact ionization and ii) multiple-scattering events. Case i) means that a doublon with an initial kinetic energy larger than the gap lowers its energy and excites another electron across the band-gap which generates one doublon and one holon [71, 72]. This process has been shown to be beneficial to the efficiency of correlated solar cells [1, 2]. The second thermalization process ii) means that a low energy doublon gains kinetic energy through several scatterings with other doublons and holons until its kinetic energy exceeds the gap size. Then it generates another doublon and a holon by lowering its kinetic energy. Excited holons undergo analogous processes. Within the Boltzmann description these are the only two processes that can lead to the generation of additional doublons. There are further processes in non-equilibrium DMFT related to the change of the spectral function. In particular, spectral weight is filled into the Mott-gap, similarly as upon increasing the temperature [73].

The two mechanisms i) and ii) take place on different timescales which can be seen if we try to fit a single-exponential decay $D_1(t) = a + b\exp[-t/\tau]$ to the doublon density $d(t)$ in a short time interval right after the pulse, i.e. for $t \in [12, 60]$. If there was only one thermalization mechanism the doublon curve would roughly follow the fitted function over the whole time range. However, this is not the case as can be seen in Fig. 3.4. The final value of the doublon density (dashed lines in Fig. 3.4) deviates significantly from the final value of the fitting function (arrows in Fig. 3.4). In accordance with Ref. [71] we find that the whole time evolution of the doublon density can be described by the sum of two exponential functions $D_2(t) = a + b\exp[-t/\tau] + c\exp[-t/\gamma]$. The two fitting parameters τ and γ represent the timescales on which the two different thermalization mechanisms described above take place. Here γ corresponds to the short timescale associated with impact ionization and τ to the long timescale associated with multiple

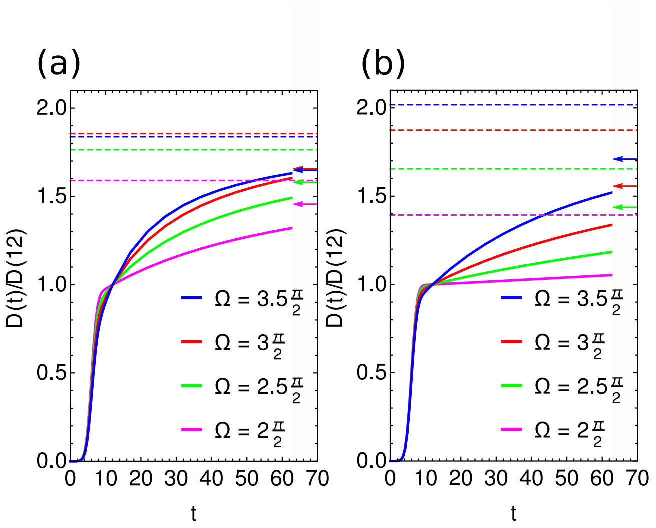

Figure 3.4: Normalized doublon density $D(t)/D(12)$ as a function of time for different laser frequencies (a) $U = 3.0$ and (b) $U = 3.5$. The dashed lines indicate the final value when the system has reached the new thermal equilibrium; the arrows give the final doublon density for a single exponential function fitted within the time interval $t \in [12, 60]$. Note that in a) the blue and red arrows lie almost on top of each other. In (b) there is no pink arrow as the fit was not possible within reasonable tolerance. Here Fermi's golden rule (section 3.1.1) was used for the laser excitation.

		DMFT			QBE						
U	Ω	γ	τ	τ/γ	γ	τ	τ/γ	γ	τ	τ/γ	α
3	$3.5\,\frac{\pi}{2}$	13	60	4.50	15	95	6.48	*11*	*70*	*6.37*	8
3	$3\,\frac{\pi}{2}$	15	61	4.09	18	91	5.01	*13*	*68*	*5.20*	8
3	$2.5\,\frac{\pi}{2}$	17	65	3.93	22	95	4.23	*16*	*76*	*4.84*	8
3.5	$3.5\,\frac{\pi}{2}$	44	376	8.55	39	231	5.88	*26*	*131*	*5.03*	5
3.5	$3\,\frac{\pi}{2}$	48	257	5.31	53	254	4.85	*32*	*167*	*5.18*	5

Table 3.1: Results for different interaction parameters U and laser frequencies Ω. The non-italic numbers in the QBE section are obtained from fits to the doublon density over the whole thermalization time and the italic ones are from fits within the interval $t \in [15, 60]$ with fixed final doublon value, i.e. as in Ref. [71] for non-equilibrium DMFT.

scattering events.

The two-time relaxation is already qualitatively consistent with DMFT. For a quantitative comparison, we note that the overall timescale for the evolution of the Boltzmann equation Eq. (3.12) is set by the constant α. As discussed above, α is treated as an adjustable parameter, as its ab-initio determination is difficult. Nevertheless, we can perform a non-trivial quantitative comparison between the Boltzmann approach and DMFT, by comparing the ratio between different timescales.

We choose integer-valued α for each value of U (independent of the laser frequency), such that the short timescale γ extracted from the fit roughly coincides with the short timescale γ_{DMFT} of Ref. [71]. The strategy of not fitting the timescales obtained from Ref. [71] more precisely, is motivated by the fact that the choice of $\tilde{t}$ and the fitting time range have a sizeable impact on the value of the time constants (see a more precise discussion below). This makes it meaningless to fit α with more than one significant digit. Interestingly, in spite of the limitations due to the fitting procedure, we clearly find that the second (longer) time scale τ shows the same order of magnitude as the DMFT result τ_{DMFT} (see Tab. 3.1), and the ratio $\frac{\tau}{\gamma}$ is almost independent of α for both DMFT and the Boltzmann approach.

As mentioned above, there is some freedom in the determination of the time constants listed in Tab. 3.1. First of all, the times γ and τ are extracted from fits of a sum of two exponential functions to the doublon curve over the whole time range. As can be seen in Fig. 3.4, impact ionization takes place on the same timescale as the laser excitation for the case $U = 3$. In other words, while the laser is switched on, the excited doublons immediately start to produce additional doublons through impact ionization. Since we

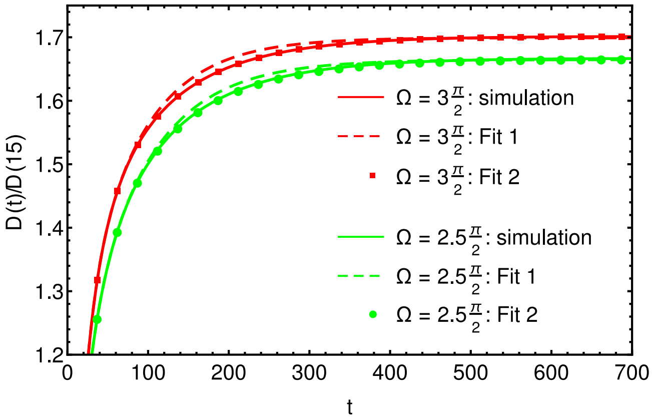

Figure 3.5: Normalized doublon density as a function of time for $U = 3.0$ and different laser frequencies Ω in a large time interval. The solid lines are the simulated doublon density, the dashed lines represent the double-exponential fit within the time interval $t \in [15, 60]$ and with fixed final doublon number. The dots indicate the double-exponential fit obtained from an even larger total simulated time $t \in [15, 1700]$.

further normalize the number of doublons to 0.01 at time $\tilde{t} = 12$ (or $\tilde{t} = 15$), to be consistent with the approach in Ref. [71], the details of the dynamics depend on the exact timing and shape of the laser as well as on the normalization time $\tilde{t}$. For $U = 3.5$ the laser and impact ionization timescales are well separated which makes the dynamics more independent of the exact laser shape and duration.

Furthermore, when comparing the times to the non-equilibrium DMFT results one should keep in mind that the non-equilibrium DMFT has only access to short times after the excitation (maximum time $t = 60$ in Ref. [71]). The final (equilibrium) doublon value was determined from the temperature corresponding to the total energy of the system, and the remaining constants were obtained from a fit in the time interval $t \in [15, 60]$. However, within the Boltzmann framework we can obtain the thermalization times τ and γ from fits of $D_2(t)$ to the doublon density over the full thermalization time (e.g. $t \in [15, 1700]$ for $U = 3.0$; "Fit 2" in Fig. 3.5). In order to estimate the error arising from the fact that non-equilibrium DMFT has only a limited time interval for the fit we perform a second fit analogous to the DMFT fit. That is, we assume that the constant a in D_2 is equal to the final doublon value, $a = D(t_{\max})$ and we obtain the other coefficients from fitting within $t \in [15, 60]$ ("Fit 1" in Fig. 3.5). All results are collected in Tab. 3.1 and the different fits are shown together with the simulated doublon densities in Fig. 3.5 for two laser frequencies. Some deviations are visible at intermediate times between $t = 100$ and $t = 300$.

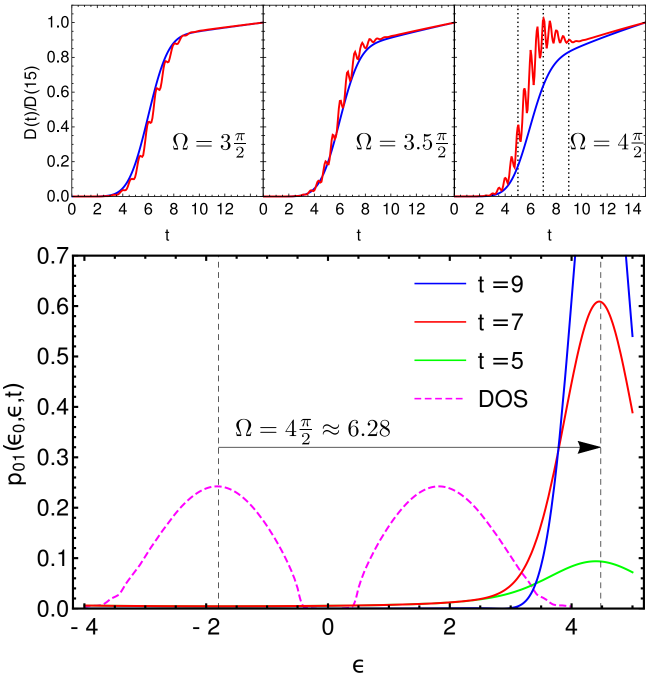

Figure 3.6: Upper panel: Time-dependent doublon density for QBE comparing Fermi's golden rule (blue lines) and first order perturbation theory (red lines) for the laser transition at different frequencies for $U = 3.5$. Lower panel: Transition probability p_{01} [Eq. (3.16)] from a specific initial state energy $\epsilon_0 = -1.8$, at different times (dashed lines in the right upper panel), for $\Omega = 6.28$ and $U = 3.5$. For the related non-equilibrium DMFT result see Fig. 2 of Ref. [71].

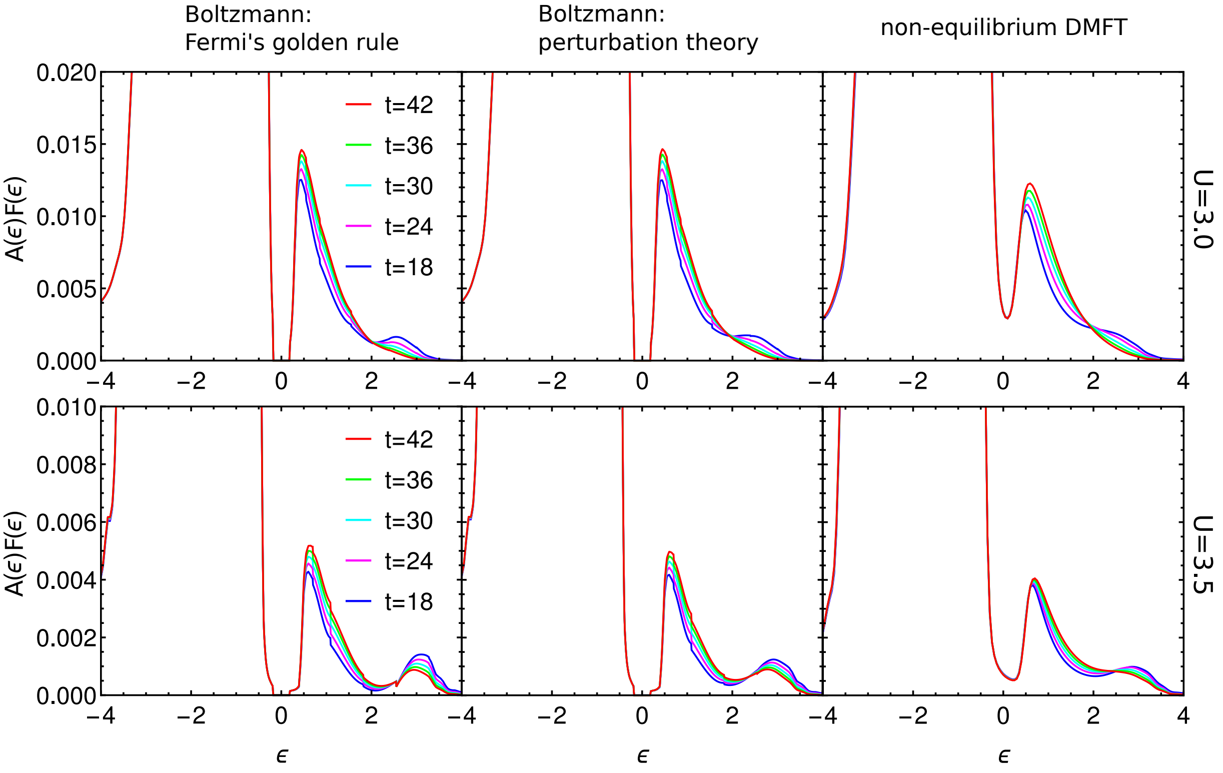

Figure 3.7: Electron population for $U = 3.0$ (first row) and $U = 3.5$ (second row) at different times. The figures in the first column are obtained from QBE simulations with the Fermi's golden rule laser transition, the figures in the second column are obtained from QBE simulations with first-order perturbation theory laser transitions and the figures in the third column show the photo-emission spectra obtained from the lesser component of the DMFT Green's function [71]. For $U = 3.0$ the number of photo-doped doublons after the laser pules is $D(12) = 0.0056$ and the laser frequency is $\Omega = 3.5\pi/2$, for $U = 3.5$ we have $D(12) = 0.0021$ and a laser frequency of $\Omega = 4\pi/2$ in accordance with Ref. [71]. For both U-values the initial inverse temperature is $\beta = 5$.

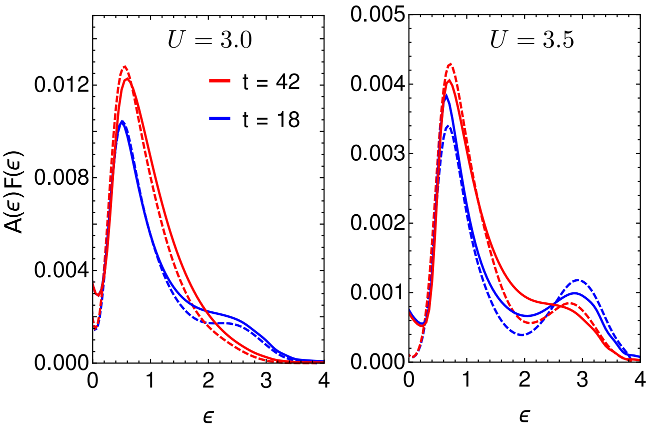

Figure 3.8: Electron population for $U = 3.0$ (left panel) and $U = 3.5$ (right panel) from QBE with laser transition in perturbation theory (dashed lines) and non-equilibrium DMFT (solid lines). Here, the Boltzmann distributions of the middle column of Fig. 3.7 were smoothed by convolution with a Gaussian with $\sigma = 0.14$ in order to resemble the smoothing inherent in the DMFT data.

The data in Tab. 3.1 in addition with the previous discussion shows that the doublon-relaxation timescales of non-equilibrium DMFT and QBE are similar within the numerical and methodological tolerance. This result may be unexpected given the fact that the validity of the QBE, which assumes a rigid spectrum, is not a priori clear for the description of strongly correlated systems.

3.3.3 Coherent laser excitations

When the first order perturbation theory laser is used to model the absorption process (section 3.1.1), there are some differences compared to the simpler implementation with Fermi's golden rule. First, we can observe that the excitation due to the laser field is not monotonic but oscillates with twice the laser frequency (upper panel Fig. 3.6). For smaller frequencies ($\Omega = 3\frac{\pi}{2}, 3.5\frac{\pi}{2}$) the doublon density roughly follows the prediction from Fermi's golden rule, whereas for higher frequencies ($\Omega = 4\frac{\pi}{2}$) we observe that the doublon density in the perturbation theory implementation first increases more strongly, but then decreases at the end of the laser pulse to approach the same value as given by the Fermi's golden rule implementation. That is, we have a maximum in $D(t)$ at $t \approx 7$ in Fig. 3.6 (upper right panel). This behavior gets more pronounced as the frequency increases, as was confirmed by an additional simulation at $\Omega = 4.5\frac{\pi}{2}$ (not shown). A similar effect was also observed in non-equilibrium DMFT simulations (compare upper right panel of Fig. 2 of Ref. [71]) and finite system simulations [74].

With the simpler Boltzmann approach, the physics behind this behavior can be understood. The laser frequency $\Omega = 4\frac{\pi}{2}$ is so large that only the outermost regions of the density of states are connected by direct transitions. In the Fermi's golden rule implementation only excitations from ϵ_0 to $\epsilon_0 + \Omega$ are possible. In contrast, in the perturbation theory implementation, transitions are possible into a broader energy range because of the finite time of the laser pulse. Generally speaking the energy integrated transition probability in Eq. (3.16) grows monotonically with time, making the energy-integrated transition rate (Eq. 3.17) always positive. However if we inspect the energy resolved quantities, we notice that, right after the laser pulse is switched on, the transition probability p_{01} given by Eq. (3.16) is very broad in energy as the laser field restricted to short times $[0, t]$ contains many frequency components. As the time passes the central peak height increases while the distribution gets narrower and the transition probability resembles more and more a Dirac-δ function that we would expect from Fermi's golden rule (see Fig. 3.6 lower panel). We observe, that the central peak grows during the whole duration of the laser pulse while the narrowing happens only for times where the time-envelope of the pulse has a negative slope (i.e. for times $t > 6$).

This narrowing effect implies that the transition rate (Eq. (3.17)) after being initially positive, becomes negative at later times on the tail of the peak, e.g. for $\epsilon = 3$ in Fig. 3.6 (lower panel). Therefore, after an initial excitation, the electrons that were excited at those energies will be returned to their original state in the lower band. For low frequency excitations, most of the allowed transitions will lie well within the upper Hubbard band. Therefore the excitation and de-excitation happening on the energy tails of the transitions will be heavily shadowed by the always positive transition rate at the central peak. However, for large laser frequencies, a larger fraction of the transitions will be happening only at the borders of the Hubbard bands. In this scenario transitions happening at the peak of the energy resolved transition rate will not be activated since they will fall outside of the density of states, and the excitation and de-excitatiton of electrons at the tail will be more evident.

Finally we emphasize that the choice of the laser implementation makes little difference on the overall thermalization dynamics (i.e. the relaxation times vary by less than 5%).

TU Bibliothek, WIEN Your knowledge hub
Die approbierte gedruckte Originalversion dieser Dissertation ist an der TU Wien Bibliothek verfügbar.
The approved original version of this doctoral thesis is available in print at TU Wien Bibliothek.

3.3.4 Population dynamics

In Fig. 3.7 we further compare the energy resolved electron population $F(\epsilon)A(\epsilon)$ at different times for Boltzmann with Fermi's golden rule laser transitions, Boltzmann with perturbation theory laser transitions, and non-equilibrium DMFT. The three methods give very similar electron-distributions and provide evidence for impact ionization, since high energy doublons (spectral weight at high energies in the upper Hubbard band) disappear while low energy doublons increase more strongly. However there are some differences that we will address in the following. First, we can see that the laser excitation around $\epsilon \approx 2.5$ for $U = 3.0$ or around $\epsilon \approx 3$ for $U = 3.5$ displays sharper features for Boltzmann with Fermi's golden rule laser transition than for the two other cases. This is because Fermi's golden rule assumes a sharp transition at the laser frequency Ω which is only well justified when the period of the laser frequency is short compared to the time-envelope of the pulse. Therefore we can see a smoothened laser excitation due to an energetic broadening of the laser-pulse for Boltzmann with laser transitions in first order perturbation theory, as well as for non-equilibrium DMFT.

Furthermore, one observes that the non-equilibrium DMFT distribution has a finite electron density within the gap. A part of this effect arises because the Mott-gap gets filled with electrons as the energy (or temperature) of the system increases. This is physics beyond the Boltzmann description, as it corresponds to a redistribution of spectral weight in the density of states which contradicts the assumption made in Eq. (3.10). However, it is important to note that is not the only reason for the presence of spectral weight within the bandgap in the computed non-equilibrium DMFT distribution. It is noteworthy that a finite electron density within the gap (see Ref. [71], not shown here) is reported even at $t = 0$. The latter is due to the fact that the calculation of the time-resolved photo-emission spectrum was performed by integration only over short time intervals: this results in a purely numerical broadening in the frequency space. Therefore, for a meaningful comparison we convolute the Boltzmann electron distributions with a Gaussian, where the width (σ) is chosen such that the electron density inside the gap is approximately the same as at $t = 0$ in the non-equilibrium DMFT case calculation (not shown here; $\sigma = 0.14$). For both cases ($U = 3.0$ and $U = 3.5$) the broadened electron distribution is much closer to the DMFT result (see Fig. 3.8).

3.3.5 Scattering strength

So far we have not discussed the role of the scattering pre-factor α that gives the strength of the interaction between excitations and has been used as a free parameter. If α were derived by taking the bare Hubbard interaction U for the vertex $w(\mathbf{k}_0, \mathbf{k}_1, \mathbf{k}_2, \mathbf{k}_3)$ in a QPBE, or for the vertex $\bar{U}$ in (3.12), we would get $\alpha_{\text{bare}} = \frac{2\pi}{\hbar}U^2$ (see section 3.1). The values we obtain for α in order to fit the time-scales differ significantly from this simple value. Not only the values are different from α_{bare}, also the dependency on U is reversed: α decreases with increasing U. The reason for this is that we have used a strongly renormalized spectral density which means that part of the interaction is already included in the density of states. The parameter α would then just be the residual interaction between excitations within this renormalized density of states. Another effect which is disregarded in the Boltzmann approach approach is the filling of the Mott-Hubbard gap due to the laser excitation. This effect is larger for intermediate U (i.e. small band-gaps) and gives rise to additional scattering channels via the in-gap states, leading to a larger α when trying to represent the dynamics in a Boltzmann approach. Indeed, full DMFT simulations yield the most rapid thermalization for intermediate values of U [75]. While this might explain the counterintuitive decrease of α, how to obtain the correct pre-factor for QBE for strongly interacting systems is left for further investigation.

3.3.6 Three-step thermalization

An advantage of the quantum Boltzmann equation compared to non-equilibrium DMFT is the possibility to simulate the whole thermalization process, not only a short time interval after the laser pulse. By studying the distribution function at different times during thermalization, one finds a third, intermediate characteristic timescale.

Right after the laser pulse, the system shows a strong deviation from its original Fermi-Dirac distribution (see Fig. 3.7). In a first step, as already discussed above, the highly excited electrons produce impact ionization until there are no electrons with sufficient energy any more. This happens in the case $U = 3.5$ and $\Omega = 3\frac{\pi}{2}$ over the characteristic timescale $\gamma = 53$ (see TABLE 3.1).

In a second step, the thermalization proceeds through scatterings that leave the doublon and holon numbers unchanged. One doublon (holon) can scatter with another doublon (holon) redistributing the energy within the upper (lower) Hubbard band, or one doublon can scatter with a holon which corresponds to an exchange of energy between the upper and lower Hubbard bands. These doublon- and holon-conserving scatterings are not affected by the gap, hence they take place on a much faster timescale than the long-time thermalization. Since the number of doublons remains unchanged, this additional time scale is not visible in the doublon dynamics shown in Fig. 3.5.

Only on a much longer time scale ($\tau = 254$ in the case $U = 3.5$ and $\Omega = 3\frac{\pi}{2}$, see Tab. 3.1) the system reaches a full thermalization. This requires the creation of high energy doublons (holons) through multiple scattering processes so that impact ionization can eventually thermalize the number of doublons (holons). These processes constitute the second, long time scale in Fig. 3.5.

We now systematically analyze this intermediate thermalization step by fitting two Fermi-Dirac functions within the lower and upper Hubbard band, respectively, to the distribution function $F(t,\epsilon)$ in every time step. Such independently thermalized distributions in the upper and lower band are common in semiconductor physics, and have also been observed in more strongly correlated insulators using non-equilibrium DMFT for the ionic Hubbard model [76]. The fit yields two chemical potentials μ, two inverse temperatures β and two (squared) deviations Δ from the Fermi-Dirac functions for the lower and upper bands

$$\Delta_{\text{lower}}(t) \equiv \int_{-\infty}^{-\frac{E_{\text{gap}}}{2}} \mathrm{d}\epsilon \left(F(t,\epsilon) - \frac{1}{e^{(\epsilon-\mu_{\text{lower}}(t))\beta_{\text{lower}}(t)}+1} \right)^2, \tag{3.29a}$$

$$\Delta_{\text{upper}}(t) \equiv \int_{\frac{E_{\text{gap}}}{2}}^{\infty} \mathrm{d}\epsilon \left(F(t,\epsilon) - \frac{1}{e^{(\epsilon-\mu_{\text{upper}}(t))\beta_{\text{upper}}(t)}+1} \right)^2. \tag{3.29b}$$

Figure 3.9 (a) shows that the deviation from a Fermi-Dirac distribution is largest directly after the laser pulse. It decays over a characteristic timescale of $\eta = 100$ and is essentially zero at $t = 400$. Because the system is particle-hole symmetric, the inverse temperatures in Fig. 3.9 (b) are equal at all times for both Hubbard bands but at $t = 400$ still lower than the equilibrium (long time) value. Even more obvious is the substantial difference in the two chemical potentials at this intermediate time in Fig. 3.9 (c). Let us stress once more that one cannot see the intermediate relaxation stage, where the upper and lower Hubbard bands are thermalizing independently, in the time dependence of the double occupation.

The third thermalization step, full thermalization between the bands (involving further doublon-holon generation), is clearly seen in Fig. 3.9(c) as the equalization of the two chemical potentials.

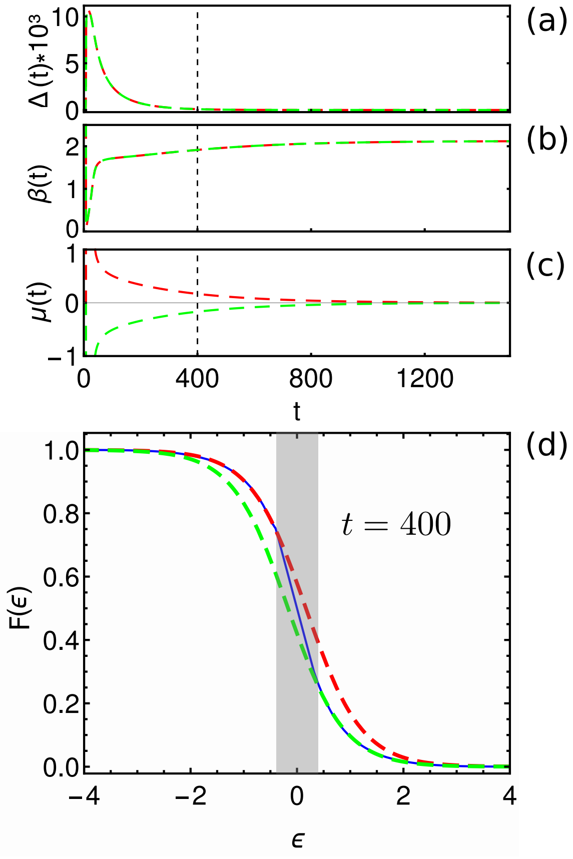

Figure 3.9: Fermi-Dirac fit to the non-equilibrium distribution function within the lower (red) and the upper (green) Hubbard-band. The interaction parameter for this case is $U = 3.5$ and the laser frequency is $\Omega = 3\frac{\pi}{2}$. The fitting error (a) [Eq. (3.29)] has almost vanished at time $t = 400$ (black, dashed line) whereas the inverse temperatures (b) are not yet thermalized and the chemical potentials (c) still differ significantly. Panel (d) shows the actual distribution function (blue, solid line) in comparison to the Fermi-Dirac fit in the lower (red) and upper (green) Hubbard band for $t = 400$. The gray area marks the gap of size $E_g = 0.8$.

Chapter 4

Transport numerics

The numerically most challenging part in solving the Boltzmann equation is the scattering as pointed out in section 2.3.4. Hence, most of the work done in the scope of this thesis is dedicated to the development of an algorithm to calculate the collision operator. However, many non-equilibrium experiments are performed with applied electric fields in order to obtain additional information during the thermalization process. Indeed, many intriguing physical effects may occur due to the interplay of transport and thermalization like for example terahertz (THz) emission [8, 9], ultrafast demagnetization [5–7] or giant spin injection in semiconductors [3, 4]. Therefore, we have also implemented a solver for the transport part (i.e. the Vlasov equation) for one-dimensional systems. In section 6.2 we apply the combined method (i.e. the solver for transport and scattering) to THz emission from carbon-nanotubes.

This chapter is organized as follows: We begin with an introduction to the discontinuous Galerkin method (section 4.1) where we put special emphasis on its application to the one-dimensional Vlasov equation. Then we discuss the details of our implementation, in particular the basis, how the different tensors simplify and how the boundary conditions are implemented (section 4.2). Finally, we apply the transport code to some test cases to show stability, error and overall functionality (section 4.3).

4.1 The Discontinuous Galerkin method

If one attempts to solve a partial differential equation numerically, a certain discretization scheme has to be used. The most popular one is probably finite-differences where a rectangular grid is introduced and the sought function is only known at the grid points. The biggest advantage of this method is its fairly easy implementation leading to codes that are straight forward to read and debug. However, it is difficult to account for non-rectangular domain boundaries and it is not possible to refine the grid only in a finite part of the domain. This lack of flexibility is the reason why finite-differences are rarely used for problems where the solution varies on different scales depending on the position in the domain.

The finite-element Galerkin methods [77] represent an important improvement over the standard finite-differences schemes. There, the domain is split into finite-size subdomains, i.e. "finite elements" and a special basis is introduced where each basis function has a compact support. Usually the basis functions are only non-zero on a small number of neighboring elements so that the local accuracy is governed by the local size of the elements. In general there is no restriction concerning the shape of the elements but often tetrahedrons (or their lower dimensional analogs) are used, which makes it easy to approximate arbitrary domain boundaries. The partial differential equation is then solved on the finite subspace spanned by the basis functions after reformulating the problem in the so-called weak formulation.

The discontinuous Galerkin method [77, 78] is an extension of standard finite-elements with a set of intriguing properties. Originally it was developed for convection dominated convection-diffusion problems as they occur for example in fluid dynamics, plasma physics, semiconductor physics or even meteorology. A general convection diffusion equation has the shape,

$$\frac{\partial f}{\partial t} + \nabla \cdot \mathbf{F}(f) + \beta \nabla^2 f = 0 \, , \tag{4.1}$$

where f is a density, $\mathbf{F}(\cdot)$ is a vectorial function depending on f describing the convective flow and $\nabla^2 f$ is the diffusive part. In order for the problem to be convection dominated the diffusion-parameter β has to be sufficiently small.

The Vlasov equation is a pure convection equation with a linear convective flow, i.e. $\beta = 0$ and $\mathbf{F}(f) = \mathbf{v} f$. Hence, it obviously falls into the class of convection dominated convection-diffusion problems. For illustration, we will discuss discontinuous Galerkin for the Vlasov equation of a one-dimensional system. In this case the phase-space is two-dimensional, one dimension for the real-space and one dimension for the momentum-space (Fig. 4.1). We denote the volume of the domain (i.e. the phase-space) with V_{Ph} in the following.

First, the space is split into non-overlapping, finite elements G_J where the index J labels the different elements. Then a basis is introduced, where each basis-function is only non-zero inside one element G_J. Inside its element the basis-function is usually a polynomial of a certain degree but in principle any function that is continuously differentiable can be used. There can also be an arbitrary number of basis-functions that are non-zero within the same element G_J as long as they are linearly independent. We will denote the basis-functions as Φ_J^j in the following where the index J labels the element and j the different basis-functions inside the element.

TU Bibliothek Your knowledge hub WIEN
Die approbierte gedruckte Originalversion dieser Dissertation ist an der TU Wien Bibliothek verfügbar.
The approved original version of this doctoral thesis is available in print at TU Wien Bibliothek.

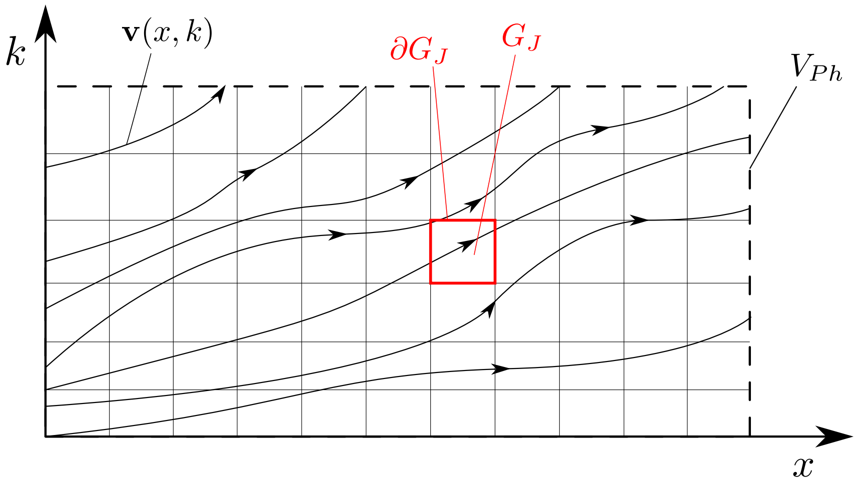

Figure 4.1: Two-dimensional phase-space domain V_{Ph} for a one-dimensional system. The full domain is split into a finite number of elements G_J with the boundaries ∂G_J. The lines with arrows illustrate the streamlines given by the velocity field $\mathbf{v}(x,k)$.

The next step is to reformulate the partial differential equation we want to solve in an integral form, i.e. in the weak formulation. The equation

$$\frac{\partial f}{\partial t} + \nabla \cdot (\mathbf{v} f) = 0 \tag{4.2}$$

also holds when it is multiplied with an arbitrary function of the solution space and integrated over the domain. As the basis-functions are obviously elements of the solution space we can write

$$\int_{V_{Ph}} \mathrm{d}V \; \Phi_J^j \left(\frac{\partial f}{\partial t} + \nabla \cdot (\mathbf{v} f) \right) = 0 \; . \tag{4.3}$$

The basis function is only non-zero within the element J, hence it is sufficient to perform the integration only on G_J and not V_{Ph}. With partial integration and the Gauss-theorem we can write,

$$\int_{G_J} \mathrm{d}V \; \Phi_J^j \frac{\partial f}{\partial t} - \int_{G_J} \mathrm{d}V \; (\nabla \Phi_J^j) \cdot \mathbf{v} f + \int_{\partial G_J} \mathrm{d}A \; \Phi_J^j \mathbf{n} \cdot \mathbf{F}_N(f) = 0 \; . \tag{4.4}$$

Here, we have introduced the so-called numerical flux $\mathbf{F}_N(\cdot)$. The quantity $\mathbf{n}$ is a normalized vector pointing outwards of the element J and stands normal to the surface ∂G_J. From the straight-forward application of the Gauss-theorem we would actually have to use $\mathbf{F}_N(\cdot) = \mathbf{v} f$. However, the solution f in the solution space spanned by the basis-function is not continuous at the element boundaries. Therefore a straight forward calculation of the flux is not possible and we need an expression for the so-called numerical flux. There are several different schemes to the construct $\mathbf{F}_N(\cdot)$ where some examples are the upwind-flux, the Godunov-flux, the Engquist-Osher-flux or the Lax-Friedrichs-flux [78].

For a linear flux of the form $\mathbf{F}(f) = \mathbf{v}f$ all mentioned fluxes coincide with the definition of the upwind flux that is

$$\mathbf{F}_N(f) = \begin{cases} \mathbf{v}f^- & \text{if} \quad \mathbf{n}\cdot\mathbf{v} > 0 \\ \mathbf{v}f^+ & \text{if} \quad \mathbf{n}\cdot\mathbf{v} < 0 \end{cases} , \tag{4.5}$$

where f^- (f^+) means that f is evaluated inside the current (neighboring) element.

The distribution function can be expanded in the basis-functions as well,

$$f(t,x,k) = \sum_{I,i} f_I^i(t)\Phi_I^i(x,k) , \tag{4.6}$$

where one should note that the time-dependence of f enters into the expansion coefficients $f_I^i(t)$ and the phase-space coordinates enter into the basis-functions $\Phi_I^i(x,k)$. When the expansion Eq. (4.6) is inserted into Eq. (4.4) we obtain an ordinary first-order linear differential equation for the coefficients f_I^i,

$$\sum_{I,i}\left[\frac{\partial f_I^i}{\partial t}\underbrace{\int_{G_J}\mathrm{d}V\ \Phi_J^j\Phi_I^i}_{\equiv M_{JI}^{ji}} - f_I^i\underbrace{\int_{G_J}\mathrm{d}V\ (\nabla\Phi_J^j)\cdot\mathbf{v}\Phi_I^i}_{\equiv T_{JI}^{ji}} + f_I^i\underbrace{\int_{\partial G_J}\mathrm{d}A\ \Phi_J^j\mathbf{n}\cdot\mathbf{F}_N(\Phi_I^i)}_{\equiv F_{JI}^{ji}}\right] = 0\ . \tag{4.7}$$

The introduced tensor M_{JI}^{ji} is called mass-matrix and is always diagonal in the element indices JI which makes it computationally cheap to invert. Finally, we can rewrite Eq. (4.7) as

$$\frac{\partial\mathbf{f}}{\partial t} = M^{-1}\left(T - F\right)\mathbf{f} , \tag{4.8}$$

which can be solved by any time-integration method as forward Euler or Runge-Kutta starting from an initial distribution $\mathbf{f}_0$.

4.2 Algorithm

As already discussed above, the phase-space of a one-dimensional system is two-dimensional (denoted as $1D \times 1D$-case in the following) consisting of the real-space position x and the momentum k. If the studied system is homogeneous in real-space, we can describe it approximately with a distribution function depending on the momentum only (denoted as $1D$-case in the following). Therefore we have implemented a solver for both cases, the purely k-dependent $1D$-case described by the equation

$$\frac{\partial}{\partial t}f_{n,\sigma} + \frac{q}{\hbar}E\frac{\partial f_{n,\sigma}}{\partial k} = 0 , \tag{4.9}$$

and the momentum- and position-dependent $1D \times 1D$-case,

$$\frac{\partial}{\partial t}f_{n,\sigma} + \frac{q}{\hbar}E\frac{\partial f_{n,\sigma}}{\partial k} + \frac{1}{\hbar}\frac{\partial\epsilon_{n,\sigma}}{\partial k}\frac{\partial f_{n,\sigma}}{\partial x} = 0 . \tag{4.10}$$

Die approbierte gedruckte Originalversion dieser Dissertation ist an der TU Wien Bibliothek verfügbar.
The approved original version of this doctoral thesis is available in print at TU Wien Bibliothek.
TU Bibliothek Your knowledge hub WIEN

There is no coupling between the transport equations of different bands n or spins σ, hence, these quantum numbers will be dropped in the following. For the algorithm we restrict ourselves to spatially uniform electric fields for simplicity.

As explained in section 4.1 the domain of the problem is split into finite-size elements that can have, in principle, arbitrary shapes. For the purely $1D$-case the domain is a line and the only possible element shape is a line-interval. We split the domain into N_E elements where each element $I \in [1, N_E]$ has the lower (upper) boundary b_I (b_{I+1}). We choose so-called nodal basis-functions of first order for the implementation of the transport code,

$$\Phi_I^i(y) = \begin{cases} \theta_I^i(y) & \text{if } b_I \leq x < b_{I+1} \\ 0 & \text{otherwise} \end{cases} , \tag{4.11}$$

with

$$\theta_I^i(y) = \begin{cases} \frac{b_{I+1}-y}{b_{I+1}-b_I} & \text{if } j = 1 \\ \frac{y-b_I}{b_{I+1}-b_I} & \text{if } j = 2 \end{cases} . \tag{4.12}$$

For each element J there exist two basis-functions where the first one has a value of one at the left boundary of the element and then decays linearly to zero at the other side of the element. The second function has the same shape but is one at the right boundary of the element. Note that these basis functions are not orthogonal. However, they have the advantage that the calculation of the flux-matrix F (see Eq. (4.7)) becomes very easy as shown below. Furthermore, we can determine the approximate expansion coefficients quickly by simply taking the values of the original function at the node-positions b_I. Note that this procedure does not give the proper expansion coefficients regarding the L^2-Norm.

The $1D \times 1D$ phase-space is a two-dimensional, rectangular domain. The elements could have arbitrary shapes e.g. triangular, rectangular or even more complicated ones. However, we can make a special choice that simplifies our future work. The $1D$-basis Eq. (4.11) can be used to cover the momentum space $\Phi_J^j(k)$ with corresponding mesh-nodes $b_J^k; J \in [1, N_E^k]$. The same basis can also be used to cover the real-space $\varphi_I^i(x)$[1] with mesh-nodes $b_I^x; I \in [1, N_E^x]$. A basis $\mathit{\Phi}(x,k)$ of the product space is then given by the products of all combinations of these $1D$-basis functions for position and momentum:

$$\mathit{\Phi}_{H(I,J)}^{h(i,j)}(x,k) \equiv \varphi_I^i(x)\Phi_J^j(k) . \tag{4.13}$$

The combined index $H(I,J)$ $(h(i,j))$ is a bijective map between the two element- (node-) indices $\{I,J\}$ $(\{i,j\})$ of the respective $1D$-bases and the elements (nodes) of the $1D \times 1D$ domain. The elements of the $1D \times 1D$ space are the Euclidean products of the line-elements of the $1D$-bases, i.e. have rectangular shape.

---

[1] We denote the $1D$-basis for real-space with φ instead of Φ but it is defined in the same way as Eq. (4.11).

The distribution-function is expanded in the bases introduced above,

$$f(t,k) \rightarrow \sum_{I,i} f_I^i(t)\Phi_I^i(k) \quad \text{for } 1D \tag{4.14a}$$

$$f(t,x,k) \rightarrow \sum_{\substack{i,j \\ I,J}} f_{IJ}^{ij}(t)\varphi_I^i(x)\Phi_J^j(k) \quad \text{for } 1D \times 1D\ . \tag{4.14b}$$

We project the dispersion relation $\epsilon(k)$ onto the basis $\Phi_J^j(k)$ as well. As we have restricted ourselves to a linear basis, the real-space velocity (i.e. the derivative of the dispersion relation) is constant within each mesh-element.

The next step is to setup the matrices M, T and F as defined by Eq. (4.7). As the $1D$-case is rather trivial we will show the explicit matrices only for the $1D \times 1D$-case.

Due to the fact that we have chosen non-orthogonal basis-functions calculating the inverse of the mass-matrix M^{-1} is non-trivial. The inversion of a $n \times n$ matrix scales as $O(n^3)$ for simple Gauss-elimination. Here, n would be the total number of basis functions. This would result in huge computational cost for large systems. However, we can use the fact that the DG-basis functions are only overlapping within the same mesh-element to order the basis-functions in a way, so that the mass-matrix becomes block-diagonal. The individual blocks are two(four)-dimensional for the $1D$-($1D \times 1D$-)case. Hence, the inversion consists of N_E inversions of small, fixed-size matrices, where N_E is the total number of mesh elements. This reduces the computational cost of the inversion to $O(N_E)$. For the $1D \times 1D$ case the mass matrix reads

$$M_{H(IJ)L(MN)}^{h(ij)l(mn)} = \delta_{I,M}\delta_{J,N} \int \mathrm{d}x\ \varphi_I^i(x)\varphi_I^m(x) \int \mathrm{d}k\ \Phi_J^j(k)\Phi_J^n(k)\ . \tag{4.15}$$

After the calculation of the inverse mass matrix we have to setup the remaining T- and F-matrices. The T-matrix actually consists of the sum of two matrices,

$$\begin{aligned} T_{H(IJ)L(MN)}^{h(ij)l(mn)} =& \delta_{I,M}\delta_{J,N}\Bigg(\int \mathrm{d}x\ \frac{\partial \varphi_I^i(x)}{\partial x} \varphi_I^m(x) \int \mathrm{d}k\ \frac{1}{\hbar}\frac{\partial \epsilon}{\partial k} \Phi_J^j(k)\Phi_J^n(k) \\ &+ \int \mathrm{d}x\ \frac{q}{\hbar} E\ \varphi_I^i(x)\varphi_I^m(x) \int \mathrm{d}k\ \frac{\partial \Phi_J^j(k)}{\partial k} \Phi_J^n(k) \Bigg) \end{aligned} . \tag{4.16}$$

Due to the ordering of the basis-functions the T-matrix is block-diagonal in the same way as the mass matrix.

The numerical flux Eq. (4.5) couples only neighboring elements and as a consequence the F-matrix is sparse, yet not block-diagonal as the M- or T- matrix. Following the definition of the flux-matrix Eq. (4.7) and the numerical flux Eq. (4.5) we have to perform a case-distinction for every side of the elements. The flux can be split into two flux-matrices, one that describes the flux in real-space direction F_x and one in momentum-direction F_k;

$F = F_x + F_k$. The different matrices read

$$F_{x\,H(IJ)L(MN)}^{\;h(ij)l(mn)} = \begin{cases} \delta_{J,N}\left[\delta_{I,M}\delta_{i,2}\delta_{m,2} - \delta_{(I-1),M}\delta_{i,1}\delta_{m,2}\right] \int \mathrm{d}k \frac{1}{\hbar}\frac{\partial\epsilon}{\partial k}\Phi_J^j(k)\Phi_J^n(k) & \left(\frac{\partial\epsilon}{\partial k}\right)_J > 0 \\ \delta_{J,N}\left[\delta_{(I+1),M}\delta_{i,2}\delta_{m,1} - \delta_{I,M}\delta_{i,1}\delta_{m,1}\right] \int \mathrm{d}k \frac{1}{\hbar}\frac{\partial\epsilon}{\partial k}\Phi_J^j(k)\Phi_J^n(k) & \left(\frac{\partial\epsilon}{\partial k}\right)_J < 0 \end{cases}, \tag{4.17}$$

and

$$F_{k\,H(IJ)L(MN)}^{\;h(ij)l(mn)} = \begin{cases} \delta_{I,M} \int \mathrm{d}x \frac{q}{\hbar} E \varphi_I^i(x)\varphi_I^m(x) \left[\delta_{J,N}\delta_{j,2}\delta_{n,2} - \delta_{(J-1),N}\delta_{j,1}\delta_{n,2}\right] & E > 0 \\ \delta_{I,M} \int \mathrm{d}x \frac{q}{\hbar} E \varphi_I^i(x)\varphi_I^m(x) \left[\delta_{(J+1),N}\delta_{j,2}\delta_{n,1} - \delta_{J,N}\delta_{j,1}\delta_{n,1}\right] & E < 0 \end{cases}. \tag{4.18}$$

4.2.1 Boundary conditions

In the discontinuous Galerkin method the boundary conditions enter into the flux-matrix F. For the calculation of the T- and M-matrix it is sufficient to know the distribution-function inside the simulation domain. The flux, however, couples the distribution function values of neighboring elements. When an element touches a boundary, one of its sides will not have any corresponding neighbor within the simulation domain and it is a priori not clear how to deal with the flux at these positions. This freedom is used to implement different boundary conditions.

The flux-matrix in real-space direction Eq. (4.17) has terms $\propto \delta_{(I-1),M}\delta_{i,1}\delta_{m,2}$ and $\propto \delta_{(I+1),M}\delta_{i,2}\delta_{m,1}$ which are responsible for the coupling of neighboring elements. The index I corresponds to the real-space element where the flux is calculated and the index M labels the real-space element of the discretized distribution-function responsible for the flux. The small indices correspond to the different basis-functions inside the elements. As we use nodal basis-functions the flux through a side of an element involves only one of the two basis-functions of the corresponding element (only one basis-function is non-zero at a element-boundary). In this paragraph and in the following, we are only explicitly discussing the boundary conditions for the flux in real-space direction. All findings also apply for the momentum-space flux.

Following the definition of the basis-functions strictly, it follows that $I, M \in [1, N_E^x]$, hence, the Kronecker-Delta $\delta_{(I-1),M}$ evaluates to zero at the left boundary ($I = 1$) and the Kronecker-Delta $\delta_{(I+1),M}$ evaluates to zero at the right boundary ($I = N_E^x$). This corresponds to pure outflow boundary conditions meaning that particles can move out of the system at the boundary and no new particles come in. For a real physical system this could make sense under some circumstances but in most cases this will not represent a realistic situation.

Another possibility for the boundary would be a periodic index, i.e.

$$M = 0 \quad \rightarrow \quad M = N_E^x \; , \tag{4.19a}$$

$$M = N_E^x + 1 \quad \rightarrow \quad M = 1 \; . \tag{4.19b}$$

Implementing a periodic index represents periodic boundary conditions, i.e. when a particle at the boundary moves further into the boundary direction it is transported to the opposite side of the domain. From theory we know that the crystal-momentum k is limited to the first Brillouin-zone (BZ) and all the physically relevant quantities are periodic with k. Therefore we always use periodic boundary conditions for the momentum-direction (i.e. for the index N in Eq. (4.18))[2].

For the real-space direction periodic boundary conditions rarely make sense. The most natural boundary conditions are the so-called inflow-boundary conditions. They assume that electrons with a certain distribution enter the simulated material from the boundaries. In most cases this distribution will be a Fermi-Dirac with the chemical potential and temperature of the neighboring material, but there is no general limitation on the shape of the distribution. This can be achieved by a matrix L_x (R_x) representing just the flux through the left (right) real-space boundary,

$$L_x{}^{h(ij)n}_{H(IJ)N} = \begin{cases} -\delta_{I,1}\delta_{i,1}\delta_{J,N} \int \mathrm{d}k \frac{1}{\hbar}\frac{\partial \epsilon}{\partial k} \Phi_J^j(k)\Phi_J^n(k) & \left(\frac{\partial \epsilon}{\partial k}\right)_J > 0 \\ 0 & \left(\frac{\partial \epsilon}{\partial k}\right)_J < 0 \end{cases} , \tag{4.20}$$

$$R_x{}^{h(ij)n}_{H(IJ)N} = \begin{cases} 0 & \left(\frac{\partial \epsilon}{\partial k}\right)_J > 0 \\ \delta_{I,N_E^x}\delta_{i,2}\delta_{J,N} \int \mathrm{d}k \frac{1}{\hbar}\frac{\partial \epsilon}{\partial k} \Phi_J^j(k)\Phi_J^n(k) & \left(\frac{\partial \epsilon}{\partial k}\right)_J < 0 \end{cases} . \tag{4.21}$$

The boundary-flux matrices have to be contracted with the projection of the distribution function at the left (right) boundary $f_L{}^n_N$ ($f_R{}^n_N$) that streams into the domain. Note, that these functions and their projections are elements of the momentum-space only. When inflow boundary conditions are used, outflow boundary conditions have to be used in the setup process of the flux-matrix F. With the new terms added, Eq. (4.8) reads

$$\frac{\partial \mathbf{f}}{\partial t} = M^{-1}\left(T - F\right)\mathbf{f} - M^{-1}L_x\,\mathbf{f_L} - M^{-1}R_x\,\mathbf{f_R} \; . \tag{4.22}$$

A third possibility would be reflective boundary conditions. They represent the situation where particles which reach the real-space boundary, are reflected and stay within the simulated material. This could happen when there is a strong band mismatch or, if a quasi-particle is described that does not exist within the other material, e.g. an exciton. For simplicity, we assume here that the dispersion relation is symmetric with respect to the gamma-point and a monotonous function of the momentum for $k > 0$. If these conditions are fulfilled, every energy of a particle corresponds to exactly two momenta that are exactly the opposite of each other and have opposite velocities, i.e. $\epsilon(k) = \epsilon(-k)$; $v_x(k) = -v_x(-k)$. We require these properties also for the projected dispersion relation which means that also the k-mesh has to be symmetric around the gamma-point. The implementation is similar to the inflow boundary conditions using the boundary-flux matrices. However, they are not contracted with a fixed vector but with the mirrored projection of the distribution function at that boundary,

---

[2] Of course, this is only correct if there is no band-crossing at the BZ-boundary.

$$f_{L}{}_{N}^{n} = \delta_{n,1}\ f^{1,2}_{1,(N_E^k-N+1)} + \delta_{n,2}\ f^{1,1}_{1,(N_E^k-N+1)}\ , \tag{4.23}$$

$$f_{R}{}_{N}^{n} = \delta_{n,1}\ f^{2,2}_{N_E^k,(N_E^k-N+1)} + \delta_{n,2}\ f^{2,1}_{N_E^k,(N_E^k-N+1)}\ . \tag{4.24}$$

The inflow boundary condition can also be combined with the reflective boundary condition assuming that particles stream in at one side and are reflected at the other one. This is achieved by the corresponding assignments of the boundary vectors $f_{L}{}_{N}^{n}$ and $f_{R}{}_{N}^{n}$.

4.3 Test cases

We test the code with several simple examples for which the behavior is known. In the $1D$-case (i.e. without real-space dependence) we setup a system with periodic boundary conditions as the Brillouin-zone is always periodic. The initial distribution at time $t = 0$ is a simple Gaussian function centered at $k = 0$ (Fig. 4.2). The charge is negative and the electric field positive. Hence, the distribution function is shifted towards negative momenta as time progresses (Fig. 4.2a and Fig. 4.2c). The electric field is irrespective of momentum which results in a rigid shift of the initial distribution. As we have employed periodic boundary conditions, after a certain time $t = T$ (or all integer multiples of this time, i.e. $t = nT$; $n \in \mathbb{N}$) the initial distribution is reestablished. This is of course only true as we did not include any scattering here. Note, that the dispersion relation of the band has no influence on the transport in the $1D$-case and it does not occur in the underlying equations.

The discretization error results in so-called numerical dissipation [78] broadening the curves in Fig. 4.2b. This effect gets weaker when the number of basis functions is increased. In order to show the effect of the numerical dissipation we have performed simulations with two different meshes where the distribution is propagated till a time $t = 10T$ (Fig. 4.2).

With the $1D \times 1D$ code we study several different cases. First, we discuss inflow boundary-conditions in real-space and periodic boundary-conditions in momentum-space at different electric fields (Fig. 4.3). For the electrons entering the domain from the boundaries we assume a Fermi-Dirac distribution with a chemical potential $\mu = -0.5$

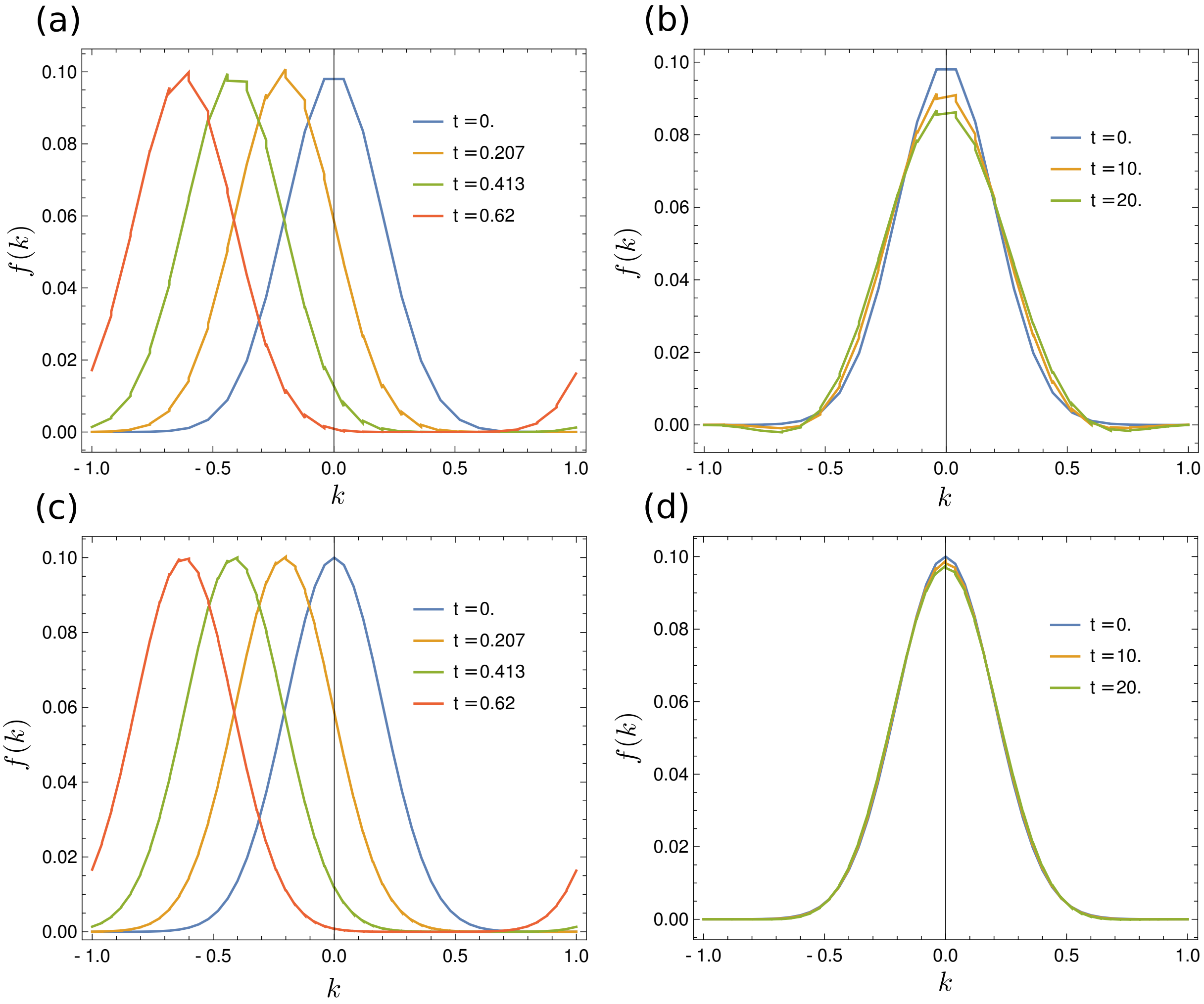

Figure 4.2: Test case calculated with the $1D$ code for periodic boundary conditions and two different meshes: $N_E = 25$ (a) and (b); $N_E = 50$ (c) and (d). The initial distribution function is a Gaussian centered at $k = 0$. The electric field is $E = 1$ and the charge $q = -1$. (a) and (c) show the initial movement which is a rigid shift of the initial population. (b) and (d) show the distribution after several periods ($T = 2$; t = 5T = 10; t = 10T = 20).

and an inverse temperature $\beta = 20$. The dispersion relation inside the domain is $\epsilon(k) = -\cos(\pi k)$ with the first Brillouin zone $k \in [-1, 1]$. As initial condition we assume that there are no electrons within the simulation domain, i.e. $f(t = 0, x, k) = 0$.

Electrons with $k > 0$ have positive real-space velocities and electrons with $k < 0$ have negative ones. As a consequence, only electrons with positive momentum stream in from the left boundary at $x = 0$ while the electrons coming from the right boundary at $x = 10$ have negative momentum. After a certain time the distribution function in the domain does not change any more and a steady state is reached. In case of $E = 0$ the steady state distribution function is just a Fermi-Dirac with the same temperature and chemical potential as the boundary distribution that streams into the system. For moderate electric fields ($E = 0.03$ in Fig. 4.3) the particles are shifted towards smaller k-values during their journey through the domain. This results in a steady state distribution that for each real-space position resembles a momentum-shifted Fermi-Dirac with locally different chemical potentials (at least for sufficiently small fields). When the electric field is very strong ($E = 0.1$ in Fig. 4.3) all the electrons entering from the left side are decelerated until they revert their velocity and leave the domain through the left side from which they have originally entered. The electrons entering the system from the right side get shifted to smaller k as well which results in an acceleration.

Another instructive example is shown in Fig.4.4. There, the setup of the system is similar to the previous example but with the boundary distributions set to zero (i.e. pure outflow boundary conditions). The initial distribution is a Gaussian centered at $k = 0.5$ and $x = 5$. For the field $E = 0$ the electrons stay at their momenta which all have positive, but different velocities. Hence, the electron distribution gets dispersed while moving out of the system. If the electric field is strong enough (here $E = 0.8$) one can observe so-called Bloch-oscillations. The electrons start moving in positive x-direction and are shifted to smaller k-values at the same time. Once the momenta become negative, also the velocities becomes negative. As a consequence one can show, that after a certain time T each electron gets back to its original position in the phase-space, i.e. after the time T the initial distribution function is reestablished. Note that a proper Bloch-oscillation is only observable if no particles leak out of the system during this one period, i.e. the real-space domain must be large enough.

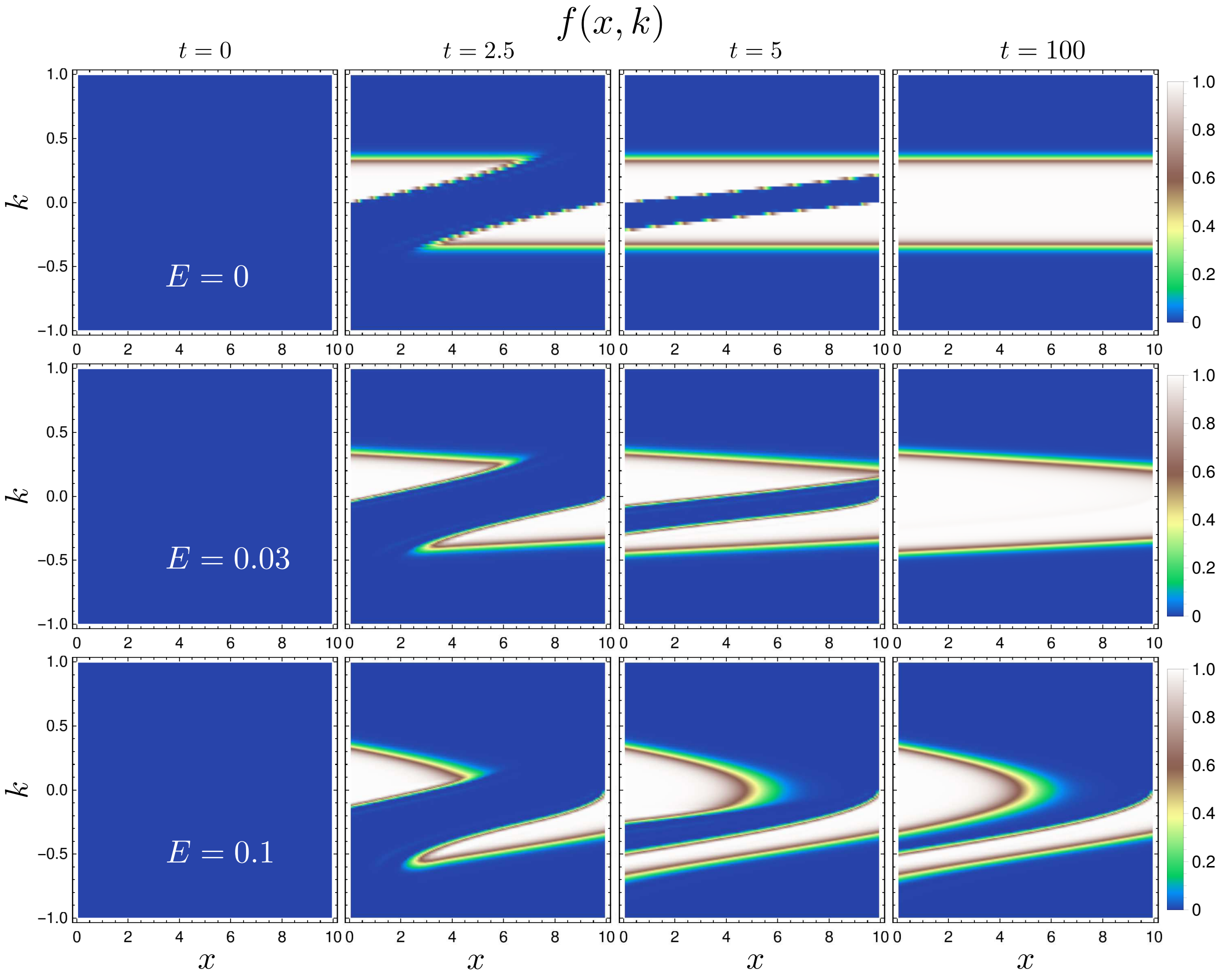

Figure 4.3: Example for the $1D \times 1D$ code with inflow boundary-conditions in x-direction and periodic boundary-conditions in k-direction at different fields E. The distribution function at the boundaries are Fermi-Dirac distributions with $\mu = -0.5$ and $\beta = 20$, the dispersion relation of the band is $\epsilon(k) = -\cos(\pi k)$, the charge is $q = -1$ and the initial distribution function is zero. The number of mesh-elements is $N_E^x = 40$ and $N_E^k = 80$.

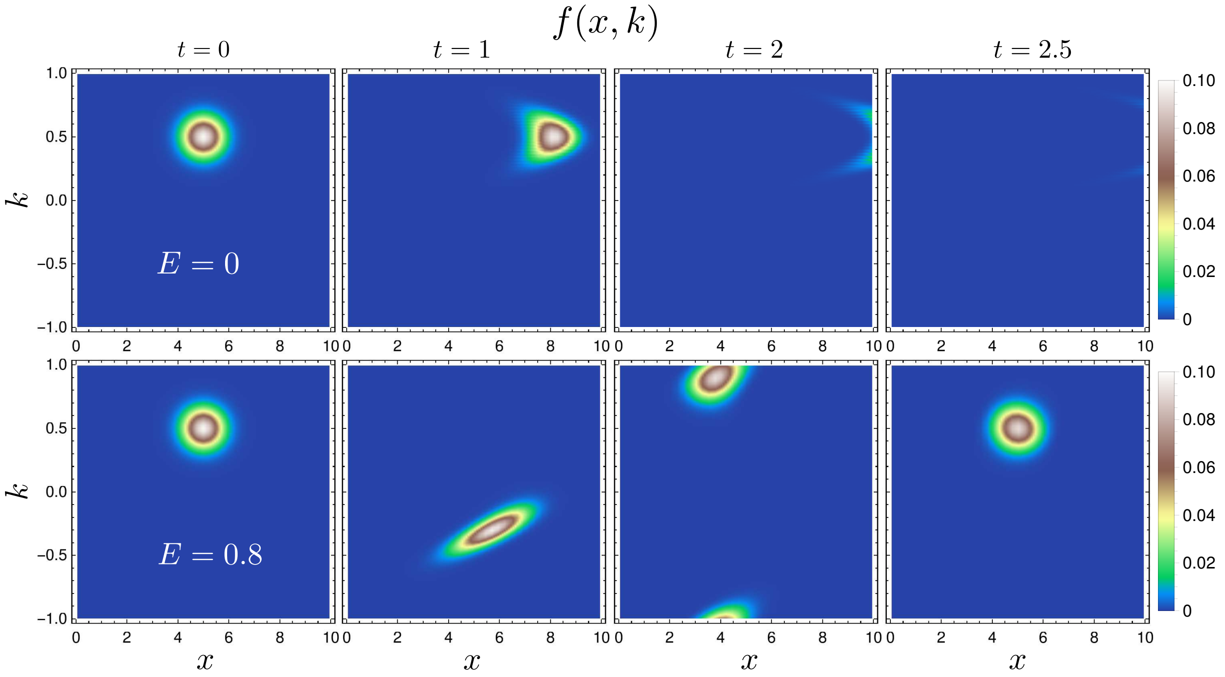

Figure 4.4: Example for the behavior of electrons at different fields in the $1D \times 1D$ case. The band- and mesh-properties are the same as in Fig. 4.3. In the x-direction we use outflow boundary-conditions, in the k-direction periodic boundary-conditions. For $E = 0$ the electrons in the system move into the x-direction as they have finite and positive velocities until they leave it. In case of $E = 0.8$ the electrons propagate through the phase-space until they reach their initial position after a time $T = \frac{2}{E} = 2.5$.

Chapter 5

Scattering numerics

In this chapter we develop a numerical method to calculate the Boltzmann collision operators (see section 2.3). As already mentioned in section 2.3.4 calculating the collision operators is a demanding task, especially for four-leg processes. This requires several methodological developments that are introduced in this chapter. For brevity we explicitly discuss the different aspects of the method for the electron-electron scattering process only. The basic ideas can be directly extended to other four-leg and three-leg scatterings. Also the treatment of different kinds of quasi-particles like electrons, phonons or excitons is possible within the framework we are presenting. We have implemented scattering for one-dimensional ($1D$) and two-dimensional ($2D$) systems. When we discuss specific details of the scattering we stick to the $2D$-case in the following as many intriguing details become trivial for the $1D$-case.

The overall method resembles the simplified method introduced in section 3.2 that was used to calculate the Boltzmann scattering without momentum conservation. However, the scheme introduced in this chapter is a lot more sophisticated as it includes scattering between different bands, different scattering processes and simultaneous momentum- and energy- conservation up to machine precision.

Within the standard Boltzmann framework, all collision operators are local in real-space. This means, that all distribution-functions occurring are evaluated at the same real-space position. Hence, we neglect a (potential) real-space dependence of the distribution-functions for the discussion of the scattering algorithm.

The chapter is organized in the following way: In section 5.1 we introduce a basis and project the collision operator onto it which yields a mathematical object we call scattering tensor. We present a numerical procedure to calculate the tensor elements and discuss its limitations. This is followed by a discussion about the symmetries of the scattering tensor and how these symmetries are linked to particle, momentum and energy conservations. We also present a scheme on how to enforce these symmetries in the tensor (section 5.2). The scattering tensor can also be used to calculate scattering rates of particles in equilibrium systems which is explained in section 5.3. In section 5.4 we apply the introduced method to non-equilibrium thermalization dynamics in $2D$-systems. In section 5.5 we present some details on the numerical implementation and finally, we discuss how to join the scattering code with the transport code (section 5.6).

The method introduced in this chapter was published in Ref. [79]. This chapter was written first and provides more detailed information than the publication for which the text was shrunk and slightly modified by the co-authors. Hence, in this chapter only those sections are marked with a vertical, black bar that are exactly the same as in the publication. Single sentences will also be identical to sentences in Ref. [79] in the other parts of this chapter.

5.1 Scattering Tensor

As prototypical collision operator we use electron-electron scattering where an electron of band n_0 scatters with an electron of band n_1 to end up in the bands n_2 and n_3 (or the time-reversed process; $n_0 + n_1 \leftrightarrow n_2 + n_3$). The collision integral that gives the distribution-function change in band n_0 due to this process is

$$\begin{aligned}\left(\frac{\partial f_0}{\partial t}\right)_{n_0+n_1\leftrightarrow n_2+n_3} = {} & w^{\text{e-e}}_{n_0n_1n_2n_3} \sum_{\mathbf{G}} \iiint_{V_{BZ}{}^3} \mathrm{d}^d k_1 \mathrm{d}^d k_2 \mathrm{d}^d k_3 \; \delta(\mathbf{k}_0 + \mathbf{k}_1 - \mathbf{k}_2 - \mathbf{k}_3 + \mathbf{G}) \\ & \times \delta(\epsilon_0 + \epsilon_1 - \epsilon_2 - \epsilon_3) \left[(1-f_0)(1-f_1)f_2f_3 - f_0f_1(1-f_2)(1-f_3)\right] \;, \end{aligned} \tag{5.1}$$

with $f_i \equiv f_{n_i}(\mathbf{k}_i)$ and $\epsilon_i \equiv \epsilon_{n_i}(\mathbf{k}_i)$. The spin indices σ_i are absorbed into the band indices n_i for brevity. The scattering amplitude $w^{\text{e-e}}_{n_0n_1n_2n_3}$ is proportional to the transition matrix element squared (see section 2.3.1). It depends, in principle, on all the involved electron states, i.e. their momenta $\mathbf{k}_i$ and their bands n_i. We assume that the dependence of the scattering amplitude on the momenta is weak compared to the contribution from the phase-space which is a good approximation in many cases [80][1]. Therefore, we neglect the momentum dependence of $w^{\text{e-e}}_{n_0n_1n_2n_3}$ and write it in front of the integral in Eq. (5.1). Nevertheless, the method developed in this chapter can be easily extended to momentum dependent scattering amplitudes which are then used as additional input for the method.

Note, that if we want to calculate the full scattering we need to sum over all different band-contributions and multiply the sum with a global pre-factor of $\frac{1}{2}$ to prevent double-

---

[1] In fact, the scattering amplitude is indeed momentum independent for a local interaction as e.g. in the Hubbard model (see Appendix A).

Die approbierte gedruckte Originalversion dieser Dissertation ist an der TU Wien Bibliothek verfügbar.
The approved original version of this doctoral thesis is available in print at TU Wien Bibliothek.
TU Bibliothek WIEN Your knowledge hub

counting (see Eq. (2.15)),

$$\left(\frac{\partial f_0}{\partial t}\right)_{\text{e-e}} = \frac{1}{2}\sum_{n_1,n_2,n_3}\left(\frac{\partial f_0}{\partial t}\right)_{n_0+n_1\leftrightarrow n_2+n_3} . \tag{5.2}$$

5.1.1 Basis and discretization

When we attempt to calculate the collision operators numerically we have to discretize them using a certain scheme. In analogy to finite-element methods we project the collision operators as well as the distribution functions onto a basis. We choose the discontinuous Galerkin (DG)-type basis for that purpose. For the $1D$-case we use the definition Eq. (3.18).

For the $2D$-case we use the two-dimensional equivalent of the $1D$-basis. We split the two-dimensional domain of each band n into $N_E(n)$ non-overlapping triangles that are labeled with a capital index, $I \in [1, N_E(n)]$. The I-th triangle of band n is denoted $T_{\underset{n}{I}}$. Each DG-basis function is non-zero only within a single triangle. Within their corresponding triangle (or element), the basis functions consist of two-dimensional, orthonormal polynomials up to linear order. In two dimensions this gives three linearly independent basis functions per element (Fig. 5.1) while in one dimension a locally linear DG basis has two basis functions per element. The definition of the $2D$ basis-functions reads

$$\Phi^i_{\underset{n}{I}}(\mathbf{k}) = \begin{cases} \mathcal{P}^i_{\underset{n}{I}}(\mathbf{k}) & \text{if } \mathbf{k} \in T_{\underset{n}{I}} \\ 0 & \text{otherwise} \end{cases} , \tag{5.3}$$

with

$$\mathcal{P}^i_{\underset{n}{I}}(\mathbf{k}) = \begin{cases} \gamma^0_{\underset{n}{I}} & \text{if } i = 0 \\ \beta^1_{\underset{n}{I}} k_y + \gamma^1_{\underset{n}{I}} & \text{if } i = 1 \\ \alpha^2_{\underset{n}{I}} k_x + \beta^2_{\underset{n}{I}} k_y + \gamma^2_{\underset{n}{I}} & \text{if } i = 2 \end{cases} . \tag{5.4}$$

Let us stress, that a possible real-space dependence is not taken into account in this section, therefore the basis functions only depend on the momentum. In section 5.6 we will extend the method to position dependent problems. The above definition Eq. 5.4 contains six unknown coefficients per element that are determined by requiring the basis to be orthonormal, i.e.

$$\int \mathrm{d}^2k\ \Phi^i_{\underset{n}{I}}(\mathbf{k})\Phi^j_{\underset{n}{J}}(\mathbf{k}) = \delta_{I,J}\delta_{i,j} . \tag{5.5}$$

Note, that the numerical values of the coefficients of a certain basis-function depend on the exact position and shape of the corresponding triangle.

We project the distribution functions onto the subspace spanned by the basis,

$$f^i_{\underset{n}{I}}(t) \equiv \int \mathrm{d}^dk\ f_n(t,\mathbf{k})\Phi^i_{\underset{n}{I}}(\mathbf{k}) , \tag{5.6}$$

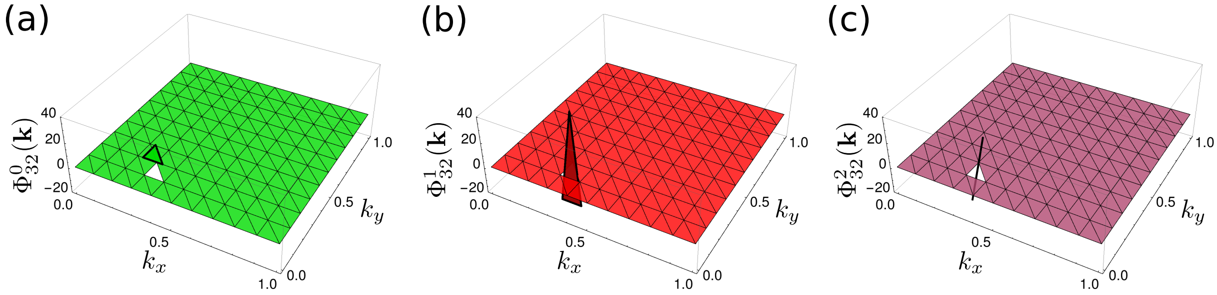

Figure 5.1: All three linear-independent basis functions for the element $I = 32$; (a) $\Phi^0_{32}(\mathbf{k})$, (b) $\Phi^1_{32}(\mathbf{k})$, (c) $\Phi^2_{32}(\mathbf{k})$. For a definition see Eq. (5.3)

and for later convenience we define

$$1^{i}_{\underset{n}{I}} \equiv \int \mathrm{d}^d k \; \Phi^{i}_{\underset{n}{I}}(\mathbf{k}) \; . \tag{5.7}$$

As pointed out in section 2.1 extensive thermodynamic quantities like total energy or particle number can be calculated once the distribution-function is known. If the real-space integration and the summation over all bands in Eq. (2.5) is not performed, we get the corresponding density contributed by band n,

$$\Theta_n(t) = \int_{V_{BZ}} \mathrm{d}^d k \frac{1}{(2\pi)^d} f_n(t, \mathbf{k}) \theta_n(\mathbf{k}) \; , \tag{5.8}$$

where $\theta_n(\mathbf{k})$ is the single-particle contribution ($\theta_n(\mathbf{k}) = 1$ for particle density, $\theta_n(\mathbf{k}) = \epsilon_n(\mathbf{k})$ for energy density, etc.; see TABLE 2.1). Using the basis introduced above, Eq. (5.8) becomes

$$\Theta_n(t) = \frac{1}{(2\pi)^d} \sum_{I,i} f^{i}_{\underset{n}{I}}(t) \theta^{i}_{\underset{n}{I}} \; , \tag{5.9}$$

where $\theta^{i}_{\underset{n}{I}}$ is the expansion coefficient of the single-particle contribution,

$$\theta^{i}_{\underset{n}{I}}(t) \equiv \int \mathrm{d}^d k \; \theta_n(\mathbf{k}) \Phi^{i}_{\underset{n}{I}}(\mathbf{k}) \; . \tag{5.10}$$

5.1.2 The scattering tensor

When we project Eq.(5.1) onto the basis and apply Eq. (5.6) and (5.7) we get

$$\begin{aligned}\left(\frac{\partial f^{i}_{\underset{n_0}{I}}}{\partial t}\right)_{n_0+n_1\leftrightarrow n_2+n_3} &\equiv \int \mathrm{d}^d k \; \Phi^{i}_{\underset{n_0}{I}}(\mathbf{k}_0) \left(\frac{\partial f_0}{\partial t}\right)_{n_0+n_1\leftrightarrow n_2+n_3} = \\ &= w^{\text{e-e}}_{n_0 n_1 n_2 n_3} \sum_{\substack{j,k,m,n \\ J,K,M,N}} (\mathbb{S}_{n_0+n_1\leftrightarrow n_2+n_3})^{ijkmn}_{\underset{n_0 n_1 n_2 n_3}{IJKMN}} \Big((1^{j}_{\underset{n_0}{J}} - f^{j}_{\underset{n_0}{J}})(1^{k}_{\underset{n_1}{K}} - f^{k}_{\underset{n_1}{K}}) f^{m}_{\underset{n_2}{M}} f^{n}_{\underset{n_3}{N}} \\ &\qquad - f^{j}_{\underset{n_0}{J}} f^{k}_{\underset{n_1}{K}} (1^{m}_{\underset{n_2}{M}} - f^{m}_{\underset{n_2}{M}})(1^{n}_{\underset{n_3}{N}} - f^{n}_{\underset{n_3}{N}}) \Big) ,\end{aligned} \tag{5.11}$$

with the scattering tensor:

$$(\mathbb{S}_{n_0+n_1\leftrightarrow n_2+n_3})^{ijkmn}_{\substack{IJKMN\\n_0n_1n_2n_3}} = \sum_{\mathbf{G}} \iiiint \mathrm{d}^dk_0\mathrm{d}^dk_1\mathrm{d}^dk_2\mathrm{d}^dk_3\ \Phi^{i}_{\substack{I\\n_0}}(\mathbf{k}_0)\Phi^{j}_{\substack{J\\n_0}}(\mathbf{k}_0)\Phi^{k}_{\substack{K\\n_1}}(\mathbf{k}_1)\Phi^{m}_{\substack{M\\n_2}}(\mathbf{k}_2)\Phi^{n}_{\substack{N\\n_3}}(\mathbf{k}_3)$$
$$\times\, \delta(\mathbf{k}_0+\mathbf{k}_1-\mathbf{k}_2-\mathbf{k}_3+\mathbf{G})\ \delta\left(\epsilon_0+\epsilon_1-\epsilon_2-\epsilon_3\right)\ . \tag{5.12}$$

In $2D$, this tensor consists of a 8-dimensional integration and contains all the information about the scattering system. For each scattering process (e.g. $n_0+n_1\leftrightarrow n_2+n_3$) we get as many tensors as the process has legs where each of the tensors describes the effect of the scattering on one of the involved bands. This is only strictly true if all the bands are different. When some of the legs belong to the same band, one has to be careful not to double count. In the following we will drop the process-label and denote the scattering tensor only with $\mathbb{S}^{ijkmn}_{\substack{IJKMN\\n_0n_1n_2n_3}}$ for brevity.

In general, the basis of each band can have a different number of elements. In order to understand the scaling of the scattering tensor we will assume here that the meshes of all bands consist of the same number of elements N_E. In a straight forward estimation the number of tensor elements scales with the number of mesh elements as $N_{SC}\propto {N_E}^5$. However, in the DG-basis each basis function has a compact support and the elements, where they are non-zero, are non-overlapping. This strongly improves the effective scaling for the following reason: The integration domain of the scattering tensor is $4d$-dimensional for a system of dimension d. The integral contains $d+1$ delta-distributions limiting the effective integration to the $4d-(d+1)=3d-1$ dimensional subspace that conserves energy and momentum. Each dimension is covered by a number of basis function that is $\propto {N_E}^{\frac{1}{d}}$ (which is only true due to their compact support), hence the effective scaling (counting only non-zero tensor elements) of the scattering tensor is

$$N_{SC}^{\text{4-leg}} \propto \left({N_E}^{\frac{1}{d}}\right)^{3d-1} = {N_E}^{3-\frac{1}{d}}\ , \tag{5.13}$$

for four-leg processes and

$$N_{SC}^{\text{3-leg}} \propto \left({N_E}^{\frac{1}{d}}\right)^{2d-1} = {N_E}^{2-\frac{1}{d}}\ , \tag{5.14}$$

for the three-leg processes.

5.1.3 Calculation of the scattering tensor elements

Calculating the tensor elements of the scattering tensors is a numerically demanding task. The integrals are high dimensional and they contain delta-distributions. The momentum-deltas can be analytically inverted as they simply depend on the integration variables in

TU Bibliothek WIEN Your knowledge hub
Die approbierte gedruckte Originalversion dieser Dissertation ist an der TU Wien Bibliothek verfügbar.
The approved original version of this doctoral thesis is available in print at TU Wien Bibliothek.

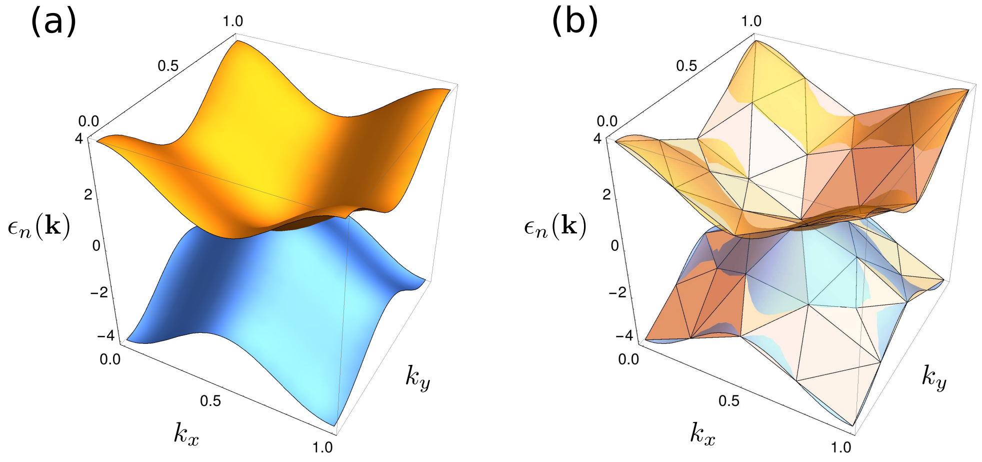

Figure 5.2: (a) Example of a $2D$ bandstructure consisting of two bands. (b) The bandstructure of (a) but locally linearized with the opaque original bands on top. A rather coarse mesh is used to highlight the effect of the local linearization.

a linear fashion. The energy-delta, however, describes a complicated hypersurface that depends on the exact shape of the dispersion-relations similar to Fermi-surfaces but in a higher dimensional space.

We solve this problem by local linearization of the dispersion relations. As each DG-basis function is only non-zero within one element, the actual integration domain for a tensor element $\mathbb{S}^{ijkmn}_{\substack{IJKMN\\n_0n_1n_2n_3}}$ is not $V_{BZ}\times V_{BZ}\times V_{BZ}\times V_{BZ}$ but rather $T_{\substack{J\\n_0}}\times T_{\substack{K\\n_1}}\times T_{\substack{M\\n_2}}\times T_{\substack{N\\n_3}}$, i.e. the product of the triangles (that are the elements) where the basis functions are non-zero. As all the momenta inside the integral are limited to their triangles, we can approximate the corresponding dispersion relations with their linearized versions, i.e.

$$\epsilon_{n_0}(\mathbf{k}_0)|_{\mathbf{k}_0\in T_{\substack{J\\n_0}}} \to \bar{\epsilon}_{\substack{J\\n_0}}(\mathbf{k}_0) \equiv \mathbf{u}_{\substack{J\\n_0}}\cdot\mathbf{k}_0 + t_{\substack{J\\n_0}} \ , \tag{5.15}$$

and equivalently for the other momenta. The three coefficients $u^{\mathrm{x}}_{\substack{J\\n_0}}$, $u^{\mathrm{y}}_{\substack{J\\n_0}}$ and $t_{\substack{J\\n_0}}$ are fixed by the requirement that the linearized dispersion $\bar{\epsilon}_{\substack{J\\n_0}}(\mathbf{k}_0)$ is equal to the original dispersion $\epsilon_{n_0}(\mathbf{k}_0)$ at the three nodes of the triangle $T_{\substack{J\\n_0}}$. When the linearization is done in that fashion, the locally linearized dispersions form a globally continuous function (Fig. 5.2). This is particularly important for the combination of the scattering method with transport as the semiclassical equations of motion require a continuous dispersion and are ill-defined otherwise.

Now that the energy-conserving delta-distribution only contains a function that depends linearly on the momenta, it can be (at least in principle) inverted analytically. In the following, we discuss step-by-step how to invert all the deltas and how to calculate the resulting integrals with a special version of the Monte-Carlo integration technique. As a first step, we invert the momentum-conserving delta in Eq. (5.12) with respect to $\mathbf{k}_1$ without loss of generality, which gives

$$\begin{aligned}\mathbb{S}^{ijkmn}_{\underset{n_0n_1n_2n_3}{IJKMN}} = \delta_{I,J} \sum_{\mathbf{G}} \int_{\underset{n_0}{T_J}} \mathrm{d}^2k_0 \int_{\underset{n_2}{T_M}} \mathrm{d}^2k_2 \int_{\underset{n_3}{T_N}} \mathrm{d}^2k_3\ \Omega\Big((\mathbf{k}_2 + \mathbf{k}_3 - \mathbf{k}_0 - \mathbf{G}) \in \underset{n_1}{T_K}\Big) \\ \times \mathcal{P}^i_{\underset{n_0}{J}}(\mathbf{k}_0) \mathcal{P}^j_{\underset{n_0}{J}}(\mathbf{k}_0) \mathcal{P}^k_{\underset{n_1}{K}}(\mathbf{k}_2 + \mathbf{k}_3 - \mathbf{k}_0 - \mathbf{G}) \mathcal{P}^m_{\underset{n_2}{M}}(\mathbf{k}_2) \mathcal{P}^n_{\underset{n_3}{N}}(\mathbf{k}_3) \\ \times \delta\left(\bar{\epsilon}_{\underset{n_0}{J}}(\mathbf{k}_0) + \bar{\epsilon}_{\underset{n_1}{K}}(\mathbf{k}_2 + \mathbf{k}_3 - \mathbf{k}_0 - \mathbf{G}) - \bar{\epsilon}_{\underset{n_2}{M}}(\mathbf{k}_2) - \bar{\epsilon}_{\underset{n_3}{N}}(\mathbf{k}_3)\right)\ ,\end{aligned} \tag{5.16}$$

with the function $\Omega(\cdot)$ that we define to be 1 if the statement inside is true and 0 otherwise. In Eq. (5.16) we have already changed the integration domains of the integrals to the triangles corresponding to the basis functions inside. As the momenta of the integrals are restricted to their triangles, we may also replace the basis functions $\Phi^i_{\underset{n}{I}}(\cdot)$ with the polynomials $\mathcal{P}^i_{\underset{n}{I}}(\cdot)$ (see Eq. (5.3)). In Eq. (5.16) we have also used the property

$$\mathbb{S}^{ijkmn}_{\underset{n_0n_1n_2n_3}{IJKMN}} = \delta_{I,J}\ \mathbb{S}^{ijkmn}_{\underset{n_0n_1n_2n_3}{JJKMN}}\ , \tag{5.17}$$

that follows from the local nature of the DG basis.

With the definition of the linerized dispersion Eq. (5.15) the energy-conserving delta in Eq.(5.16) reads,

$$\delta\left(\left(\underset{n_0}{\mathbf{u}_J} - \underset{n_1}{\mathbf{u}_K}\right) \cdot \mathbf{k}_0 + \left(\underset{n_1}{\mathbf{u}_K} - \underset{n_2}{\mathbf{u}_M}\right) \cdot \mathbf{k}_2 + \left(\underset{n_1}{\mathbf{u}_K} - \underset{n_3}{\mathbf{u}_N}\right) \cdot \mathbf{k}_3 + \underset{n_0}{t_J} + \underset{n_1}{t_K} - \underset{n_2}{t_M} - \underset{n_3}{t_N} - \underset{n_1}{\mathbf{u}_K} \cdot \mathbf{G}\right). \tag{5.18}$$

For the following let us assume that $\left(\underset{n_1}{u^x_K} - \underset{n_2}{u^x_M}\right) \neq 0$[2]. When this requirement is fulfilled we can invert the energy-delta with respect to k^x_2, which gives

$$\begin{aligned}\mathbb{S}^{ijkmn}_{\underset{n_0n_1n_2n_3}{IJKMN}} = \delta_{I,J} \sum_{\mathbf{G}} \int_{\underset{n_0}{T_J}} \mathrm{d}^2k_0 \int_{\underset{n_2}{L^{[a,b]}_M}} \mathrm{d}k^y_2 \int_{\underset{n_3}{T_N}} \mathrm{d}^2k_3\ \Omega\Big((\mathbf{k}_2 + \mathbf{k}_3 - \mathbf{k}_0 - \mathbf{G}) \in \underset{n_1}{T_K}\Big)\Big|_{k^x_2=\xi} \\ \times \Omega(\mathbf{k}_2 \in \underset{n_2}{T_M})\Big|_{k^x_2=\xi} \frac{1}{\left|\underset{n_1}{u^x_K} - \underset{n_2}{u^x_M}\right|} \mathcal{P}^i_{\underset{n_0}{J}}(\mathbf{k}_0) \mathcal{P}^j_{\underset{n_0}{J}}(\mathbf{k}_0) \mathcal{P}^k_{\underset{n_1}{K}}(\mathbf{k}_2 + \mathbf{k}_3 - \mathbf{k}_0 - \mathbf{G})\Big|_{k^x_2=\xi} \\ \times \mathcal{P}^m_{\underset{n_2}{M}}(\mathbf{k}_2)\Big|_{k^x_2=\xi} \mathcal{P}^n_{\underset{n_3}{N}}(\mathbf{k}_3)\ ,\end{aligned} \tag{5.19}$$

---

[2] One can also use any other vector-component of the momentum-prefactors occurring in Eq. (5.18) as long as it is non-zero.

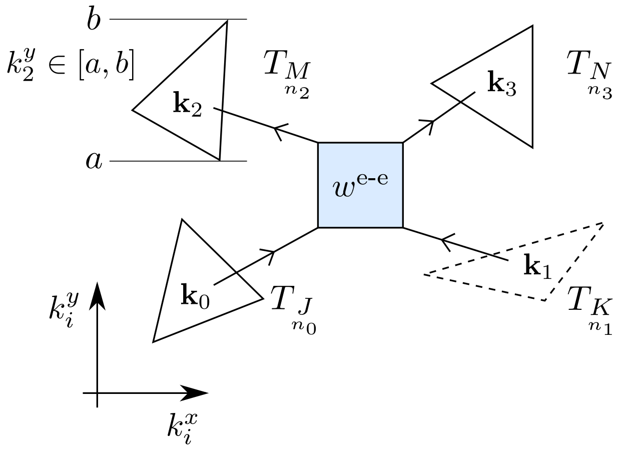

Figure 5.3: Schematic picture of the electron-electron scattering process for the elements (triangles) $T_{\underset{n_0}{J}}$, $T_{\underset{n_1}{K}}$, $T_{\underset{n_2}{M}}$, $T_{\underset{n_3}{N}}$. The integration of $\mathbf{k}_1$ is removed due to the inversion of the momentum-conserving delta (dashed triangle). The k_2^x-integration is fixed by the inversion of the energy-conserving delta. The remaining integration variables are $\mathbf{k}_0$, $\mathbf{k}_3$, and k_2^y.

with

$$\xi = \frac{1}{u^x_{\underset{n_1}{K}} - u^x_{\underset{n_2}{M}}} \Bigg(t_{\underset{n_2}{M}} + t_{\underset{n_3}{N}} - t_{\underset{n_0}{J}} - t_{\underset{n_1}{K}} + \mathbf{u}_{\underset{n_1}{K}} \cdot \mathbf{G} - \left(\mathbf{u}_{\underset{n_0}{J}} - \mathbf{u}_{\underset{n_1}{K}} \right) \cdot \mathbf{k}_0 - \left(u^y_{\underset{n_1}{K}} - u^y_{\underset{n_2}{M}} \right) k_2^y \\ - \left(\mathbf{u}_{\underset{n_1}{K}} - \mathbf{u}_{\underset{n_3}{N}} \right) \cdot \mathbf{k}_3 \Bigg) \,. \tag{5.20}$$

In Eq. (5.19) the integration domain is $T_{\underset{n_0}{J}} \times T_{\underset{n_3}{N}} \times L^{[a,b]}_{\underset{n_2}{M}}$ where $L^{[a,b]}_{\underset{n_2}{M}}$ is a line interval from a to b, where a (b) is the minimum (maximum) k_2^y-value in the corresponding triangle (Fig. 5.3). Furthermore, another Ω-function is introduced in Eq. (5.19) to ensure that only contributions are counted for which the momentum $\mathbf{k}_2$ lies inside its triangle.

The integral Eq. (5.19) contains a smooth integrand (except for the Ω-functions) and can be readily calculated with Monte-Carlo. For that purpose we generate a number N_{MC} of sets of random points $\underset{\alpha}{\mathbf{k}_0} \in T_{\underset{n_0}{J}}$, $\underset{\alpha}{\mathbf{k}_3} \in T_{\underset{n_3}{N}}$ and $\underset{\alpha}{k_2^y} \in L^{[a,b]}_{\underset{n_2}{M}}$. The scattering tensor components are then calculated according to

$$\mathbb{S}^{ijkmn}_{\substack{IJKMN\\ n_0 n_1 n_2 n_3}} = \delta_{I,J} \frac{T_{\underset{n_0}{J}} \times T_{\underset{n_3}{N}} \times L^{[a,b]}_{\underset{n_2}{M}}}{N_{\text{MC}} \left| u^x_{\underset{n_1}{K}} - u^x_{\underset{n_2}{M}} \right|} \sum_{\mathbf{G}} \sum_{\alpha=1}^{N_{\text{MC}}} \Omega\Big((\underset{\alpha}{\mathbf{k}_2} + \underset{\alpha}{\mathbf{k}_3} - \underset{\alpha}{\mathbf{k}_0} - \mathbf{G}) \in T_{\underset{n_1}{K}} \Big) \Big|_{\underset{\alpha}{k_2^x} = \xi_\alpha} \\ \times \Omega(\underset{\alpha}{\mathbf{k}_2} \in T_{\underset{n_2}{M}}) \Big|_{\underset{\alpha}{k_2^x} = \xi_\alpha} \mathcal{P}^i_{\underset{n_0}{J}}(\underset{\alpha}{\mathbf{k}_0}) \mathcal{P}^j_{\underset{n_0}{J}}(\underset{\alpha}{\mathbf{k}_0}) \mathcal{P}^k_{\underset{n_1}{K}}(\underset{\alpha}{\mathbf{k}_2} + \underset{\alpha}{\mathbf{k}_3} - \underset{\alpha}{\mathbf{k}_0} - \mathbf{G}) \Big|_{\underset{\alpha}{k_2^x} = \xi} \mathcal{P}^m_{\underset{n_2}{M}}(\underset{\alpha}{\mathbf{k}_2}) \Big|_{\underset{\alpha}{k_2^x} = \xi_\alpha} \mathcal{P}^n_{\underset{n_3}{N}}(\underset{\alpha}{\mathbf{k}_3}) \,. \tag{5.21}$$

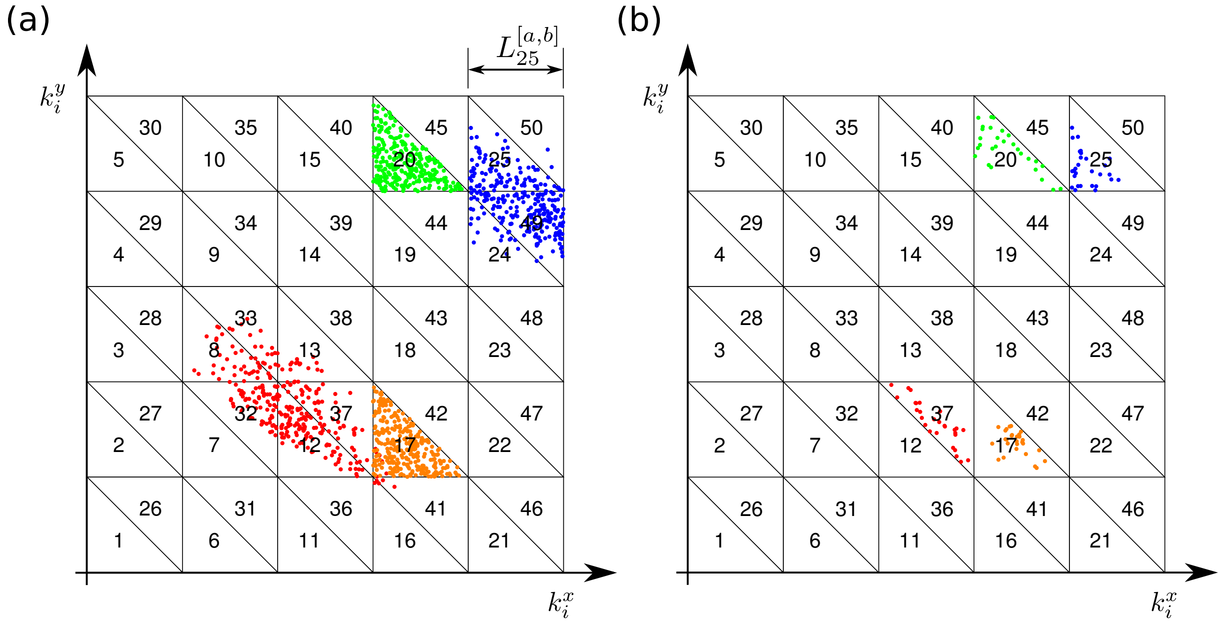
(a)
$L_{25}^{[a,b]}$
k_i^y
30 35 40 45 50
5 10 15 20 25
29 34 39 44 49
4 9 14 19 24
28 33 38 43 48
3 8 13 18 23
27 32 37 42 47
2 7 12 17 22
26 31 36 41 46
1 6 11 16 21
k_i^x
(b)
k_i^y
30 35 40 45 50
5 10 15 20 25
29 34 39 44 49
4 9 14 19 24
28 33 38 43 48
3 8 13 18 23
27 32 37 42 47
2 7 12 17 22
26 31 36 41 46
1 6 11 16 21
k_i^x

Figure 5.4: Triangular mesh of a single band with the element numbering on top for a $2D$-system. (a) Energy- and momentum-conserving Monte-Carlo point-sets for the scattering $\underset{n_0}{J}+\underset{n_0}{K} \leftrightarrow \underset{n_0}{M}+\underset{n_0}{N}$ with the elements $J = 25$ (blue), $K = 37$ (red), $M = 20$ (green), $N = 17$ (orange) ($N_{\mathrm{MC}} = 300$). The effective integration domain here is $T_{20} \times T_{17} \times L_{25}^{[a,b]}$. (b) The same point-sets as in (a) but only those where all momenta lie within their corresponding triangles (i.e. the accepted Monte-Carlo point-sets; $N_{\mathrm{acc}} = 28$).

Above, we have made the assumption $\left(\underset{n_1}{u_K^x} - \underset{n_2}{u_M^x}\right) \neq 0$ which was necessary for the inversion of the energy-delta. This does not hold in general, hence, the algorithm has to decide which momentum component to use for the inversion. We exclude scatterings where all the momentum pre-factors are zero as this would give an infinite expression. We discuss this case in section 5.1.4. Our method always uses the momentum where the corresponding prefactor has the largest absolute-value for the inversion. To understand why this is reasonable, we study the scattering-tensor elements for the case $i = j = k = m = n = 0$. With the definition of the basis functions Eq. (5.4), Eq. (5.21) becomes

$$\begin{aligned}\underset{n_0 n_1 n_2 n_3}{\mathbb{S}_{IJKMN}^{00000}} = \delta_{I,J} \frac{\underset{n_0}{T_J} \times \underset{n_3}{T_N} \times \underset{n_2}{L_M^{[a,b]}}}{N_{\mathrm{MC}}\left|\underset{n_1}{u_K^x} - \underset{n_2}{u_M^x}\right|} \underset{n_0}{\gamma_J^0}\underset{n_0}{\gamma_J^0}\underset{n_1}{\gamma_K^0}\underset{n_2}{\gamma_M^0}\underset{n_3}{\gamma_N^0} \\ \times \underbrace{\sum_{\mathbf{G}} \sum_{\alpha=1}^{N_{\mathrm{MC}}} \Omega\Big((\underset{\alpha}{\mathbf{k}_2} + \underset{\alpha}{\mathbf{k}_3} - \underset{\alpha}{\mathbf{k}_0} - \mathbf{G}) \in \underset{n_1}{T_K}\Big)\Big|_{\underset{\alpha}{k_2^x} = \xi_\alpha} \Omega(\underset{\alpha}{\mathbf{k}_2} \in \underset{n_2}{T_M})\Big|_{\underset{\alpha}{k_2^x} = \xi_\alpha}}_{N_{\mathrm{acc}}} .\end{aligned} \tag{5.22}$$

In Eq. (5.22) the only factors that depend on the momentum that was chosen for the inversion are $L^{[a,b]}_{\underset{n_2}{M}}$, $\left|u^x_{\underset{n_1}{K}} - u^x_{\underset{n_2}{M}}\right|$ and the number of accepted Monte-Carlo points N_{acc} (see Fig. 5.4). If the mesh contains only triangles that have approximately the same area and that are well conditioned[3], the line-element $L^{[a,b]}_{\underset{n_2}{M}}$ is almost independent of the chosen inversion. As the actual value of the scattering tensor element does not depend on the method used for its calculation, it must hold that if the factor $\left|u^x_{\underset{n_1}{K}} - u^x_{\underset{n_2}{M}}\right|$ is largest of all possible inversions, also the expectation value of the number of accepted Monte-Carlo points is the largest. This, in turn, makes the Monte-Carlo error the smallest.

5.1.4 Caveats of the method

The method to calculate the scattering tensor elements presented in the previous section has some caveats. The first one is, that it is essentially a standard Monte-Carlo method. Therefore, in order to get a decent precision for the individual tensor elements the number of Monte-Carlo points N_{MC} must be rather high. However, since the number of total scatterings (i.e. all combinations of basis functions) is high, the single integrals do not need a very high precision for the overall dynamics to give reasonably precise results. Yet, another problem arises: For the overall dynamics the precision of the individual scatterings does not matter so much but, as each scattering is not calculated exactly, the conservation of energy, particle number and momentum is broken and subject to a Monte-Carlo error. We find that these errors make the long-time convergence impossible as the system loses or gains particles/energy/momentum in ever time-step. The required number of Monte-Carlo points necessary to reduce this error sufficiently would exceed the computational capabilities. Fortunately one can show that the conservation of extensive quantities is linked to symmetries between different tensors-elements. If these symmetries are enforced on the tensor-elements during calculation, our method conserves all quantities up to machine precision. This topic is addressed in section 5.2.

Another problem arises due to the local linearization of the dispersion relation: In order to invert the energy-conserving delta, at least one pre-factor of the momenta in Eq. (5.18) has to be non-zero. However, for a scattering where all the involved legs correspond to the same element (i.e. $J = K = M = N$ and $n_0 = n_1 = n_2 = n_3$), this requirement is automatically violated and the corresponding scattering-tensor element diverges. This effect does not only happen for scatterings within the same element but for all scatterings where all involved linearized dispersion relations lie in the same plane. This is due to the fact that the momentum conservation is a linear equation in dependence of momentum. When the linearized dispersions of the different legs have the same functional form for certain elements, the energy-conservation equation degenerates and becomes equivalent to the momentum-conservation equation (up to a multiplicative factor). The two delta-distributions then have their zero-points at the same positions in the integration-domain which gives a divergence. We neglect such element-combinations as the algorithm would yield a too large, unphysical scattering. A proper finite-size scaling is hence necessary.

---

[3] That means that all sides have approximately the same length.

5.2 Conservation symmetries and clean-up

5.2.1 Symmetries

As mentioned above, a problem of using Monte-Carlo integration for the tensor elements is the conservation of extensive quantities such as particle number, energy or momentum. The precision requirements on these quantities are much higher than on the overall dynamics. Therefore we would like to conserve these quantities exactly.

The total change of an extensive quantity $\frac{\mathrm{d}}{\mathrm{d}t}\Theta_{\underset{n_0}{J}}$ in one element $T_{\underset{n_0}{J}}$ due to the electron-electron scattering process $n_0 + n_1 \leftrightarrow n_2 + n_3$ reads

$$\begin{aligned}\frac{\mathrm{d}}{\mathrm{d}t}\Theta_{\underset{n_0}{J}} &= \int_{T_{\underset{n_0}{J}}} \mathrm{d}^2k_0\; \theta_{n_0} \left(\frac{\partial f_0}{\partial t}\right)_{n_0+n_1\leftrightarrow n_2+n_3} \\ &= w^{\text{e-e}}_{n_0n_1n_2n_3} \sum_{\substack{i,j,k,m,n\\ K,M,N}} \theta^i_{\underset{n_0}{J}}\, (\mathbb{S}_{n_0+n_1\leftrightarrow n_2+n_3})^{ijkmn}_{\underset{n_0n_1n_2n_3}{JJKMN}} \Big((1^j_{\underset{n_0}{J}} - f^j_{\underset{n_0}{J}})(1^k_{\underset{n_1}{K}} - f^k_{\underset{n_1}{K}}) f^m_{\underset{n_2}{M}} f^n_{\underset{n_3}{N}} \\ &\qquad\qquad - f^j_{\underset{n_0}{J}} f^k_{\underset{n_1}{K}} (1^m_{\underset{n_2}{M}} - f^m_{\underset{n_2}{M}})(1^n_{\underset{n_3}{N}} - f^n_{\underset{n_3}{N}}) \Big)\,,\end{aligned} \tag{5.23}$$

with the projection of the single-particle contribution $\theta^i_{\underset{n_0}{J}}$ (see Eq. (5.10)).

As above, we will drop the process-label and denote the scattering tensor only with $\mathbb{S}^{ijkmn}_{\underset{n_0n_1n_2n_3}{JJKMN}}$ in the following. Furthermore, we will assume that all four bands that are involved in the scattering process are different (i.e. $n_0 \neq n_1 \neq n_2 \neq n_3$). For the cases where some of the bands are the same one can derive the corresponding equations in the same way as explained below.

We can now choose a specific set of elements J, K, M, N and study the change of the extensive quantity within theses elements due to scattering processes only between them. The time-derivative of the extensive quantity may be split into two different contributions: One that comes from electrons scattered into the element ($\frac{\mathrm{d}}{\mathrm{d}t}\Theta_{\underset{n_0}{J\leftarrow}}$) and one that comes from electrons scattered away from the element ($\frac{\mathrm{d}}{\mathrm{d}t}\Theta_{\underset{n_0}{J\rightarrow}}$); $\frac{\mathrm{d}}{\mathrm{d}t}\Theta_{\underset{n_0}{J}} = \frac{\mathrm{d}}{\mathrm{d}t}\Theta_{\underset{n_0}{J\leftarrow}} + \frac{\mathrm{d}}{\mathrm{d}t}\Theta_{\underset{n_0}{J\rightarrow}}$. Each possible scattering has to conserve the extensive quantity, hence, we do not only get a

Die approbierte gedruckte Originalversion dieser Dissertation ist an der TU Wien Bibliothek verfügbar.
The approved original version of this doctoral thesis is available in print at TU Wien Bibliothek.
TU Bibliothek WIEN Your knowledge hub

conservation equation for the total change of the extensive quantity but also for the two components stemming from electrons scattered into and out of the elements, i.e.

$$\frac{\mathrm{d}}{\mathrm{d}t}\underset{n_0}{\Theta_{J\rightarrow}}+\frac{\mathrm{d}}{\mathrm{d}t}\underset{n_1}{\Theta_{K\rightarrow}}+\frac{\mathrm{d}}{\mathrm{d}t}\underset{n_2}{\Theta_{M\leftarrow}}+\frac{\mathrm{d}}{\mathrm{d}t}\underset{n_3}{\Theta_{N\leftarrow}}=0\ , \tag{5.24}$$

$$\frac{\mathrm{d}}{\mathrm{d}t}\underset{n_0}{\Theta_{J\leftarrow}}+\frac{\mathrm{d}}{\mathrm{d}t}\underset{n_1}{\Theta_{K\leftarrow}}+\frac{\mathrm{d}}{\mathrm{d}t}\underset{n_2}{\Theta_{M\rightarrow}}+\frac{\mathrm{d}}{\mathrm{d}t}\underset{n_3}{\Theta_{N\rightarrow}}=0\ . \tag{5.25}$$

In Eq. (5.23) the part containing the projected distribution functions (i.e. the phase space factor) consists of two terms which represent the scattering into the current element $[(\underset{n_0}{1^j_J}-\underset{n_0}{f^j_J})(\underset{n_1}{1^k_K}-\underset{n_1}{f^k_K})\underset{n_2}{f^m_M}\underset{n_3}{f^n_N}]$ and away from it $[-\underset{n_0}{f^j_J}\underset{n_1}{f^k_K}(\underset{n_2}{1^m_M}-\underset{n_2}{f^m_M})(\underset{n_3}{1^n_N}-\underset{n_3}{f^n_N})]$. Hence, if we want to calculate the conservation equations Eq. (5.24) and Eq. (5.25) we have to use only one part of the phase-space in each term. Eq. (5.24) then becomes

$$\begin{aligned}0=\sum_{i,j,k,m,n}\Bigg[&\underset{n_0}{\theta^i_J}\left(\mathbb{S}^{ijkmn}_{\underset{n_0n_1n_2n_3}{JJKMN}}+\mathbb{S}^{ijknm}_{\underset{n_0n_1n_3n_2}{JJKNM}}\right)\left(-\underset{n_0}{f^j_J}\underset{n_1}{f^k_K}(\underset{n_2}{1^m_M}-\underset{n_2}{f^m_M})(\underset{n_3}{1^n_N}-\underset{n_3}{f^n_N})\right)\\&+\underset{n_1}{\theta^i_K}\left(\mathbb{S}^{ikjmn}_{\underset{n_1n_0n_2n_3}{KKJMN}}+\mathbb{S}^{ikjnm}_{\underset{n_1n_0n_3n_2}{KKJNM}}\right)\left(-\underset{n_1}{f^k_K}\underset{n_0}{f^j_J}(\underset{n_2}{1^m_M}-\underset{n_2}{f^m_M})(\underset{n_3}{1^n_N}-\underset{n_3}{f^n_N})\right)\\&+\underset{n_2}{\theta^i_M}\left(\mathbb{S}^{imnjk}_{\underset{n_2n_3n_0n_1}{MMNJK}}+\mathbb{S}^{imnkj}_{\underset{n_2n_3n_1n_0}{MMNKJ}}\right)\left((\underset{n_2}{1^m_M}-\underset{n_2}{f^m_M})(\underset{n_3}{1^n_N}-\underset{n_3}{f^n_N})\underset{n_0}{f^j_J}\underset{n_1}{f^k_K}\right)\\&+\underset{n_3}{\theta^i_N}\left(\mathbb{S}^{inmjk}_{\underset{n_3n_2n_0n_1}{NNMJK}}+\mathbb{S}^{inmkj}_{\underset{n_3n_2n_1n_0}{NNMKJ}}\right)\left((\underset{n_3}{1^n_N}-\underset{n_3}{f^n_N})(\underset{n_2}{1^m_M}-\underset{n_2}{f^m_M})\underset{n_0}{f^j_J}\underset{n_1}{f^k_K}\right)\Bigg]\ .\end{aligned} \tag{5.26}$$

Note, that the sum in Eq. (5.26) only runs over the small indices, i.e. the indices corresponding to the different basis functions inside the elements. Interestingly, all the partial phase-space factors occurring in Eq. (5.26) are the same (except for the signs). This partial phase-space factor actually consists of several terms of different powers of the distribution function,

$$\underset{n_0}{f^j_J}\underset{n_1}{f^k_K}(\underset{n_2}{1^m_M}-\underset{n_2}{f^m_M})(\underset{n_3}{1^n_N}-\underset{n_3}{f^n_N})=\underbrace{\underset{n_0}{f^j_J}\underset{n_1}{f^k_K}\underset{n_2}{1^m_M}\underset{n_3}{1^n_N}}_{\propto\,\mathbf{f}^2}\underbrace{-\underset{n_0}{f^j_J}\underset{n_1}{f^k_K}\underset{n_2}{f^m_M}\underset{n_3}{1^n_N}-\underset{n_0}{f^j_J}\underset{n_1}{f^k_K}\underset{n_2}{1^m_M}\underset{n_3}{f^n_N}}_{\propto\,\mathbf{f}^3}+\underbrace{\underset{n_0}{f^j_J}\underset{n_1}{f^k_K}\underset{n_2}{f^m_M}\underset{n_3}{f^n_N}}_{\propto\,\mathbf{f}^4}\ . \tag{5.27}$$

Since these terms scale with different powers of the distribution function vector $\mathbf{f}$, Eq. (5.26) must hold for each of them separately. Therefore we may apply the variational principle for the projected distribution-function components. This gives the conservation equation for the quantity Θ_n, obtained from Eq. (5.26) and the term $\propto\ \mathbf{f}^4$, which reads

$$\begin{aligned}0=\sum_i\Bigg[&\underset{n_0}{\theta^i_J}\left(\mathbb{S}^{ijkmn}_{\underset{n_0n_1n_2n_3}{JJKMN}}+\mathbb{S}^{ijknm}_{\underset{n_0n_1n_3n_2}{JJKNM}}\right)+\underset{n_1}{\theta^i_K}\left(\mathbb{S}^{ikjmn}_{\underset{n_1n_0n_2n_3}{KKJMN}}+\mathbb{S}^{ikjnm}_{\underset{n_1n_0n_3n_2}{KKJNM}}\right)\\&-\underset{n_2}{\theta^i_M}\left(\mathbb{S}^{imnjk}_{\underset{n_2n_3n_0n_1}{MMNJK}}+\mathbb{S}^{imnkj}_{\underset{n_2n_3n_1n_0}{MMNKJ}}\right)-\underset{n_3}{\theta^i_N}\left(\mathbb{S}^{inmjk}_{\underset{n_3n_2n_0n_1}{NNMJK}}+\mathbb{S}^{inmkj}_{\underset{n_3n_2n_1n_0}{NNMKJ}}\right)\Bigg]\ .\end{aligned} \tag{5.28}$$

We have now obtained a relation between several tensor elements that is independent of the distribution functions. It can be shown easily that if Eq. (5.28) holds, all the other equations that stem from the lower-order contributions in Eq. (5.26) (i.e. the terms that are $\propto \mathbf{f}^3$ and $\propto \mathbf{f}^2$) are automatically fulfilled as well. We have used Eq. (5.24) as a starting point for the derivation. When instead Eq. (5.25) is used, we arrive at the exact same relation.

When the scattering tensor elements fulfill Eq. (5.28), the extensive quantity $\Theta = \sum_n \Theta_n$ is conserved exactly in the scattering process. It is interesting to note that Eq. (5.28) couples only tensor elements which are certain permutations (eight in total) of the index triples $\{J, j, n_0\}, \{K, k, n_1\}, \{M, m, n_2\}, \{N, n, n_3\}$. In a $2D$-system with basis functions up to linear order (i.e. three basis functions per element) this means that 24 tensor elements are coupled by the conservation equations. Furthermore, the conservation equations do not couple different groups of these 24 tensor elements which makes them independent subspaces when it comes to the enforcement of the symmetries.

There are more symmetries in the tensors than the symmetries that stem from conserved quantities. It is easy to see from the definition of the tensor, that it is symmetric in the last two index triples, i.e.

$$\mathbb{S}^{ijkmn}_{\substack{JJKMN\\ n_0n_1n_2n_3}} = \mathbb{S}^{ijknm}_{\substack{JJKNM\\ n_0n_1n_3n_2}} \ . \tag{5.29}$$

Note, that this symmetry depends on the specific scattering process described by the tensor. For example a four-leg process where three legs go into the vertex and only one comes out does not have this symmetry in general. Furthermore, the tensors show symmetry in the first two, small indices,

$$\mathbb{S}^{ijkmn}_{\substack{JJKMN\\ n_0n_1n_2n_3}} = \mathbb{S}^{jikmn}_{\substack{JJKMN\\ n_0n_1n_2n_3}} \ , \tag{5.30}$$

which is a general symmetry independent of the specific scattering process. As discussed above, the conservation symmetries Eq. (5.28) couple only tensor elements inside blocks of 24 elements in a $2D$-system. The symmetry in the last two index-triples Eq. (5.29) does not interfere with this block-structure as it only affects tensor elements inside these blocks as well. However, the symmetry Eq. (5.30) does couple several different blocks. Hence, taking all symmetries together, in a $2D$-system a number of $N_{\text{coupled}} = 3^5 \times 8 = 1944$ scattering tensor elements are coupled by the symmetries. Still, the symmetries can be restored in these blocks of N_{coupled} elements independently.

There is yet another symmetry that follows from the definition of the scattering tensors and the basis Eq. (5.4). From the fact that the basis functions are orthonormal and the definition Eq. (5.7) it directly follows that

$$\Phi^0_{\substack{I\\ n}}(\mathbf{k}) = \gamma^0_{\substack{I\\ n}} \overset{!}{=} \frac{1}{1^0_{\substack{I\\ n}}} \ . \tag{5.31}$$

With this relation it is easy to show that

$$\underset{n_0}{1^0_J}\ \underset{n_0n_1n_2n_3}{\mathbb{S}^{0jkmn}_{JJKMN}} = \underset{n_1}{1^0_K}\ \underset{n_1n_0n_2n_3}{\mathbb{S}^{0kjmn}_{KKJMN}} = \underset{n_2}{1^0_M}\ \underset{n_2n_3n_0n_1}{\mathbb{S}^{0mnjk}_{MMNJK}} = \underset{n_3}{1^0_N}\ \underset{n_3n_2n_0n_1}{\mathbb{S}^{0nmjk}_{NNMJK}} \,. \tag{5.32}$$

Again, this symmetry depends on the scattering process under consideration. If the tensors fulfill the symmetries Eq. (5.32) and Eq. (5.29), particle conservation in the scattering process directly follows. This can be easily proven when the above symmetries are inserted in the equation for particle-conservation (Eq. (5.28) with $\underset{n_0}{\theta^i{}_J} = \underset{n_0}{1^i{}_J} = \delta_{i,0}\underset{n_0}{1^0_J}$),

$$\begin{aligned} 0 = \Bigg[& \underset{n_0}{1^0_J} \left(\underset{n_0n_1n_2n_3}{\mathbb{S}^{0jkmn}_{JJKMN}} + \underset{n_0n_1n_3n_2}{\mathbb{S}^{0jknm}_{JJKNM}} \right) + \underset{n_1}{1^0_K} \left(\underset{n_1n_0n_2n_3}{\mathbb{S}^{0kjmn}_{KKJMN}} + \underset{n_1n_0n_3n_2}{\mathbb{S}^{0kjnm}_{KKJNM}} \right) \\ & - \underset{n_2}{1^0_M} \left(\underset{n_2n_3n_0n_1}{\mathbb{S}^{0mnjk}_{MMNJK}} + \underset{n_2n_3n_1n_0}{\mathbb{S}^{0mnkj}_{MMNKJ}} \right) - \underset{n_3}{1^0_N} \left(\underset{n_3n_2n_0n_1}{\mathbb{S}^{0nmjk}_{NNMJK}} + \underset{n_3n_2n_1n_0}{\mathbb{S}^{0nmkj}_{NNMKJ}} \right) \Bigg] \,. \end{aligned} \tag{5.33}$$

According to the symmetries Eq. (5.32) and Eq. (5.29) all the terms in the above equation are equal, hence it is automatically fulfilled.

5.2.2 Clean-up

As long as the symmetry-equations that correspond to physically conserved quantities are fulfilled exactly, the numerical scattering conserves these quantities exactly as well. As explained in section 5.1.3 we use a special Monte-Carlo technique to calculate the tensors and therefore the tensor-elements are subject to a finite Monte-Carlo error. A solution to this problem is to restore the broken symmetries in the tensor after the calculation.

One strategy would be calculating only some of the tensor-elements using the Monte-Carlo routine and determining the remaining elements from the symmetry equations. This leads to the problem of finding the best inversion of the equations. This procedure was, indeed, implemented and tested. Nevertheless, we stick with another method that proved to be more stable and easier to implement which we will explain in the following.

The symmetry-equations derived in the previous section are all linear and homogeneous equations in the tensor-elements. We may write these equations as a scalar product of two vectors, the first one representing the i-th equation ($\mathbf{v}_i$, $i \in [1, N_{\text{sym}}]$ where N_{sym} is the number of symmetry-equations), the second one being a vector representation of the involved tensor-elements ($\mathbb{S}_v$). The system of symmetry-equations is fulfilled if the scalar product of those vectors vanishes (i.e. $\mathbf{v}_i \cdot \mathbb{S}_v = 0 \quad \forall i$). The vectors $\mathbf{v}_i$ and $\mathbb{S}_v$ are elements of a N_{coupled}-dimensional vector space $\mathcal{S}$ where N_{coupled} denotes the number of tensor-elements coupled by the equations. The vectors $\mathbf{v}_i$ form a basis of a N_{sym}-dimensional subspace $\mathcal{V}$ of $\mathcal{S}$; $\mathcal{V} \subset \mathcal{S}$. All vectors that lie in the space orthogonal to $\mathcal{V}$

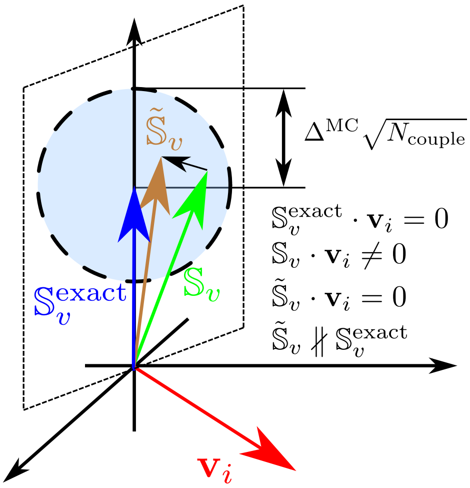
$\tilde{\mathbb{S}}_v$
$\Delta^{\mathrm{MC}}\sqrt{N_{\mathrm{couple}}}$
$\mathbb{S}_v^{\mathrm{exact}} \cdot \mathbf{v}_i = 0$
$\mathbb{S}_v \cdot \mathbf{v}_i \neq 0$
$\tilde{\mathbb{S}}_v \cdot \mathbf{v}_i = 0$
$\tilde{\mathbb{S}}_v \nparallel \mathbb{S}_v^{\mathrm{exact}}$
$\mathbb{S}_v^{\mathrm{exact}}$
$\mathbb{S}_v$
$\mathbf{v}_i$

Figure 5.5: Schematic picture of the vector representation of the equation-vectors $\mathbf{v}_i$, the involved scattering-tensor elements $\mathbb{S}_v$, the exact tensor $\mathbb{S}_v^{\mathrm{exact}}$, the monte-carlo calculated tensor $\mathbb{S}_v$, the cleaned-up tensor $\tilde{\mathbb{S}}_v$ and their mutual relations. In this illustration the total space is three-dimensional (i.e. $N_{\mathrm{couple}} = 3$) and the subspace orthogonal to the $\mathbf{v}_i$ is two-dimensional (i.e. $N_{\mathrm{couple}} - N_{\mathrm{sym}} = 2$; dashed plane).

fulfill the conservation equations, hence, the exact tensor is an element of that space as well; $\mathbb{S}_v \in (\mathcal{S} \setminus \mathcal{V})$.

As an example we consider one of the symmetry-equations for the last two index-triples (Eq. (5.29)) of the element-combination $\{J, n_0\}$, $\{K, n_1\}$, $\{M, n_2\}$, $\{N, n_3\}$. The corresponding vectors are

$$\mathbf{v}_1 = \begin{pmatrix} 1 \\ -1 \\ 0 \\ \vdots \\ 0 \end{pmatrix}, \quad \mathbb{S}_v = \begin{pmatrix} \mathbb{S}^{00000}_{\substack{JJKMN \\ n_0 n_1 n_2 n_3}} \\ \mathbb{S}^{00000}_{\substack{JJKNM \\ n_0 n_1 n_3 n_2}} \\ \mathbb{S}^{10000}_{\substack{JJKMN \\ n_0 n_1 n_2 n_3}} \\ \vdots \\ \mathbb{S}^{22222}_{\substack{NNMKJ \\ n_3 n_2 n_1 n_0}} \end{pmatrix}, \tag{5.34}$$

for which the symmetry equation is obtained if the scalar-product is zero,

$$0 \overset{!}{=} \mathbf{v}_1 \cdot \mathbb{S}_v = \mathbb{S}^{00000}_{\substack{JJKMN \\ n_0 n_1 n_2 n_3}} - \mathbb{S}^{00000}_{\substack{JJKNM \\ n_0 n_1 n_3 n_2}} \quad \rightarrow \quad \mathbb{S}^{00000}_{\substack{JJKMN \\ n_0 n_1 n_2 n_3}} = \mathbb{S}^{00000}_{\substack{JJKNM \\ n_0 n_1 n_3 n_2}} . \tag{5.35}$$

In the following we will denote the vector representing the Monte-Carlo calculated scattering-tensor as $\mathbb{S}_v$ and the exact tensor as $\mathbb{S}_v^{\mathrm{exact}}$. We define the absolute Monte-Carlo error of the j-th tensor-elements as Δ_j^{MC} and the maximum Monte-Carlo error as

$\Delta^{\mathrm{MC}} \equiv \max|_j \left(|\Delta_j^{\mathrm{MC}}|\right)$. It is easy to see that

$$|\mathbb{S}_v - \mathbb{S}_v^{\mathrm{exact}}|^2 = \sum_{j=1}^{N_{\mathrm{coupled}}} (\Delta_j^{\mathrm{MC}})^2 \leq (\Delta^{\mathrm{MC}})^2 N_{\mathrm{coupled}} \ . \tag{5.36}$$

Assuming that all the components of $\mathbb{S}_v$ have equal importance for the dynamics we may argue, that every other $\tilde{\mathbb{S}}_v$ lying within a sphere with radius $\Delta^{\mathrm{MC}}\sqrt{N_{\mathrm{coupled}}}$ around the exact tensor $\mathbb{S}_v^{\mathrm{exact}}$ is as good as $\mathbb{S}_v$. Therefore, we may project the Monte-Carlo calculated tensor $\mathbb{S}_v$ onto the part of the error-sphere that lies in the subspace $(\mathcal{S} \setminus \mathcal{V})$ to obtain a vector $\tilde{\mathbb{S}}_v : \quad \tilde{\mathbb{S}}_v \cdot \mathbf{v}_i = 0 \ \ \forall i$ (see Fig. 5.5).

Calculating the projection of the tensor onto $(\mathcal{S} \setminus \mathcal{V})$ is equivalent to orthogonalizing it to the subspace $\mathcal{V}$. For that purpose we define a set of vectors ξ_i,

$$\xi_i = \begin{cases} \mathbf{v}_i & \text{if } i \in [1, N_{\mathrm{sym}}] \\ \mathbb{S}_v & \text{if } i = N_{\mathrm{sym}} + 1 \end{cases} \ . \tag{5.37}$$

The vectors ξ_i span a $(N_{\mathrm{sym}} + 1)$-dimensional subspace[4] and they are, in general, non-orthogonal vectors. A fully orthogonal set of vectors χ_i that spans the same subspace can be obtained by the so-called Gram-Schmidt [81, 82] procedure. The Gram-Schmidt algorithm to calculate the χ_i reads,

$$\chi_1 = \xi_1 \ , \tag{5.38}$$

$$\chi_i = \xi_i - \sum_{j=1}^{i-1} \frac{\xi_i \cdot \chi_j}{\chi_j \cdot \chi_j} \chi_j \quad \forall i \in [2, N_{\mathrm{sym}} + 1] \ . \tag{5.39}$$

The last vector of the orthogonalized vector set is the sought tensor within the Monte-Carlo error-sphere that fulfills all symmetries exactly (Fig. 5.5b), i.e.

$$\tilde{\mathbb{S}}_v = \chi_{N_{\mathrm{sym}}+1} \ . \tag{5.40}$$

5.3 Scattering rates

With the scattering tensors we can calculate how a non-equilibrium distribution relaxes to a new equilibrium. However, it is also quite interesting to study the scattering rates of particles in a system close to equilibrium. In fact, many physically relevant quantities like the macroscopic transport coefficients contain these scattering rates in one way or another. Additionally, as will be discussed later, we need the equilibrium scattering rates if we want to determine the scattering strengths by comparison to thermalization experiments.

---

[4] This is only true if all the vectors are linearly independent.

TU Bibliothek, Your knowledge hub, WIEN
Die approbierte gedruckte Originalversion dieser Dissertation ist an der TU Wien Bibliothek verfügbar.
The approved original version of this doctoral thesis is available in print at TU Wien Bibliothek.

The scattering tensors contain the whole information of the scattering channels and how the available phase-space affects each of them. Hence, they also contain the equilibrium scattering rates already. In order to show how they are related to the scattering tensors we first have to define what we call the equilibrium scattering rate $\lambda_n(\mathbf{k})$. For that purpose we write the distribution-function as a Fermi-Dirac distribution[5] $f_{\mathrm{FD}}(\epsilon_n(\mathbf{k}), \mu, \beta)$ plus an excitation $\delta f_n(\mathbf{k})$,

$$f_n(t, \mathbf{k}) = f_{\mathrm{FD}}(\epsilon_n(\mathbf{k}), \mu, \beta) + \delta f_n(t, \mathbf{k}) \ , \tag{5.41}$$

where we assume that $\delta f_n(\mathbf{k})$ is small. For the following we will consider the prototypical case of electron-electron scattering within one band. All results can be easily extended to other scattering processes.

The time derivative of the distribution function due to electron-electron scattering within the same band reads

$$\begin{aligned}\frac{\partial f_0}{\partial t} = \ & w^{\text{e-e}}_{0123} \, \frac{1}{2} \sum_{\mathbf{G}} \iiint \mathrm{d}^d k_1 \mathrm{d}^d k_2 \mathrm{d}^d k_3 \ \delta(\mathbf{k}_0 + \mathbf{k}_1 - \mathbf{k}_2 - \mathbf{k}_3 + \mathbf{G}) \\ & \times \delta(\epsilon_0 + \epsilon_1 - \epsilon_2 - \epsilon_3) \left[(1 - f_0)(1 - f_1) f_2 f_3 - f_0 f_1 (1 - f_2)(1 - f_3)\right] \ .\end{aligned} \tag{5.42}$$

When we insert Eq. (5.41) into the above equation we get

$$\begin{aligned}\frac{\partial(\delta f_0)}{\partial t} = \ & w^{\text{e-e}}_{0123} \, \frac{1}{2} \sum_{\mathbf{G}} \iiint \mathrm{d}^d k_1 \mathrm{d}^d k_2 \mathrm{d}^d k_3 \ \delta_{\mathbf{k}} \delta_{\epsilon} \\ & \times \Big[(1 - f_{\mathrm{FD}_0})(1 - f_{\mathrm{FD}_1}) f_{\mathrm{FD}_2} f_{\mathrm{FD}_3} - f_{\mathrm{FD}_0} f_{\mathrm{FD}_1} (1 - f_{\mathrm{FD}_2})(1 - f_{\mathrm{FD}_3}) \\ & \quad - \delta f_0 \Big((1 - f_{\mathrm{FD}_1}) f_{\mathrm{FD}_2} f_{\mathrm{FD}_3} + f_{\mathrm{FD}_1} (1 - f_{\mathrm{FD}_2})(1 - f_{\mathrm{FD}_3}) \Big) \\ & \quad - \delta f_1 \Big((1 - f_{\mathrm{FD}_0}) f_{\mathrm{FD}_2} f_{\mathrm{FD}_3} + f_{\mathrm{FD}_0} (1 - f_{\mathrm{FD}_2})(1 - f_{\mathrm{FD}_3}) \Big) \\ & \quad + \delta f_2 \Big((1 - f_{\mathrm{FD}_0})(1 - f_{\mathrm{FD}_1}) f_{\mathrm{FD}_3} + f_{\mathrm{FD}_0} f_{\mathrm{FD}_1} (1 - f_{\mathrm{FD}_3}) \Big) \\ & \quad + \delta f_3 \Big((1 - f_{\mathrm{FD}_0})(1 - f_{\mathrm{FD}_1}) f_{\mathrm{FD}_2} + f_{\mathrm{FD}_0} f_{\mathrm{FD}_1} (1 - f_{\mathrm{FD}_2})) \Big) \\ & \quad + \ \cdots \end{aligned} \ , \tag{5.43}$$

where we have just written the terms of leading order in δf. The second line in Eq. (5.43) is just the electron-electron phase-space factor evaluated with Fermi-Dirac distributions. One can show that the Fermi-Dirac distribution is a fixed point of the collision integral, hence, this term equals zero. The term in the third line is $\propto \delta f(\mathbf{k}_0)$. The momentum $\mathbf{k}_0$ is not an integration variable of the integrals and therefore the term $\delta f(\mathbf{k}_0)$ can be written

---

[5] Of course only if the studied band is fermionic. In case of bosons we would have to use a Bose-Einstein distribution instead.

TU Bibliothek, WIEN Your knowledge hub
Die approbierte gedruckte Originalversion dieser Dissertation ist an der TU Wien Bibliothek verfügbar.
The approved original version of this doctoral thesis is available in print at TU Wien Bibliothek.

in front of the integrals. With all the remaining terms grouped together in the function $\mathcal{R}_0$ we can write Eq. (5.43) as

$$\frac{\partial(\delta f_0)}{\partial t} = \; - \delta f_0 \; \lambda_0 + \mathcal{R}_0 \; , \tag{5.44}$$

with

$$\lambda_0 \equiv w^{\text{e-e}}_{0123} \, \frac{1}{2} \sum_{\mathbf{G}} \iiint \mathrm{d}^d k_1 \mathrm{d}^d k_2 \mathrm{d}^d k_3 \; \delta_{\mathbf{k}} \delta_\epsilon \Big((1 - f_{\mathrm{FD}_1}) f_{\mathrm{FD}_2} f_{\mathrm{FD}_3} + f_{\mathrm{FD}_1} (1 - f_{\mathrm{FD}_2})(1 - f_{\mathrm{FD}_3}) \Big) \; . \tag{5.45}$$

Eq. (5.44) describes an exponentially decaying excitation δf_0 if the term $\mathcal{R}_0$ is negligible. One can show (see Appendix B) that this is indeed the case when the excitation δf is asymptotically equivalent to adding (or removing) a single particle at a momentum $\mathbf{k}_0$. Then $\lambda(\mathbf{k}_0)$ as defined by Eq. (5.45) can be interpreted as the scattering rate of this particle (or hole). Interestingly, for the scattering rate it does not make a difference if we add or remove a particle as the scattering rate is irrespective of the sign of the excitation δf.

The discretized version of the scattering rate is obtained by projection onto the basis functions, $\lambda_I^i \equiv \int \mathrm{d}^d k \lambda(\mathbf{k}) \Phi_I^i(\mathbf{k})$. Together with the discretized versions of the Fermi-Dirac distributions $[f_{\mathrm{FD}}]_I^i$ the scattering rate can be written as

$$\begin{aligned} \lambda_I^i = w^{\text{e-e}}_{0123} \, \frac{1}{2} \sum_{\substack{k,m,n \\ K,M,N}} \sum_{\mathbf{G}} \iiiint & \mathrm{d}^d k_0 \mathrm{d}^d k_1 \mathrm{d}^d k_2 \mathrm{d}^d k_3 \; \delta_{\mathbf{k}} \; \delta_\epsilon \; \Phi_I^i(\mathbf{k}_0) \Phi_K^k(\mathbf{k}_1) \Phi_M^m(\mathbf{k}_2) \Phi_N^n(\mathbf{k}_3) \\ & \times \Big((1_K^k - [f_{\mathrm{FD}}]_K^k) [f_{\mathrm{FD}}]_M^m [f_{\mathrm{FD}}]_N^n + [f_{\mathrm{FD}}]_K^k (1_M^m - [f_{\mathrm{FD}}]_M^m)(1_N^n - [f_{\mathrm{FD}}]_N^n) \Big) \; , \end{aligned} \tag{5.46}$$

which has a mathematical structure similar to a scattering tensor that is contracted with projections of the Fermi-Dirac distributions. In order to bring Eq. (5.46) to a form that involves the full scattering tensor we exploit the fact that the number one can be written as $1 = \sum_J^j 1_J^j \Phi_J^j(\mathbf{k}_0)^6$ for arbitrary momentum $\mathbf{k}_0$. When we insert this relation into

---

[6] Note, that this relation is exactly true also for a finite number of basis functions as we use a modal DG-basis.

Eq. (5.46) we obtain

$$\begin{aligned}
\lambda_I^i =& w_{0123}^{\text{e-e}} \, \frac{1}{2} \sum_{\substack{j,k,m,n \\ J,K,M,N}} \sum_{\mathbf{G}} \iiiint \mathrm{d}^d k_0 \mathrm{d}^d k_1 \mathrm{d}^d k_2 \mathrm{d}^d k_3 \; \delta_{\mathbf{k}} \; \delta_{\epsilon} \; \Phi_I^i(\mathbf{k}_0) \Phi_J^j(\mathbf{k}_0) \Phi_K^k(\mathbf{k}_1) \Phi_M^m(\mathbf{k}_2) \Phi_N^n(\mathbf{k}_3) \\
& \times \Big(1_J^j (1_K^k - [f_{\text{FD}}]_K^k) [f_{\text{FD}}]_M^m [f_{\text{FD}}]_N^n + 1_J^j [f_{\text{FD}}]_K^k (1_M^m - [f_{\text{FD}}]_M^m)(1_N^n - [f_{\text{FD}}]_N^n) \Big) \\
=& w_{0123}^{\text{e-e}} \, \frac{1}{2} \sum_{\substack{j,k,m,n \\ J,K,M,N}} \mathbb{S}_{IJKMN}^{ijkmn} \\
& \times \Big(1_J^j (1_K^k - [f_{\text{FD}}]_K^k) [f_{\text{FD}}]_M^m [f_{\text{FD}}]_N^n + 1_J^j [f_{\text{FD}}]_K^k (1_M^m - [f_{\text{FD}}]_M^m)(1_N^n - [f_{\text{FD}}]_N^n) \Big)
\end{aligned} \tag{5.47}$$

which is the contraction of the scattering tensor with a certain phase-space factor evaluated with projections of the equilibrium distributions. Using Eq. (5.47) we can now calculate equilibrium scattering rates directly from the scattering tensor $\mathbb{S}_{IJKMN}^{ijkmn}$.

5.4 Non-equilibrium dynamics of model systems

The following section was published in Ref. [79] and is therefore marked by a black, vertical bar.

In this section we discuss several prototypical non-equilibrium thermalizations and highlight different aspects of the dynamics in order to show the full capabilities of the method.

We describe a 2D system, with two electronic bands with the following dispersion relations

$$\epsilon_2(\mathbf{k}) \equiv 2t\cos(2\pi k_x) + 2t\cos(2\pi k_y) + 4t + \frac{\Delta}{2} \; , \tag{5.48a}$$

$$\epsilon_1(\mathbf{k}) \equiv -\epsilon_2(\mathbf{k}) \; , \tag{5.48b}$$

with the band-gap Δ and the tight-binding hopping $t = 1/2$ (see Fig. 5.6). Here, we have used a rescaled first Brillouin-zone that occupies the domain $[0,1] \times [0,1]$ instead of $[-\frac{\pi}{2}, \frac{\pi}{2}] \times [-\frac{\pi}{2}, \frac{\pi}{2}]$. In this notation the Γ-point is $\mathbf{k}_\Gamma = (0.5, 0.5)^{\mathrm{T}}$.

We will study the thermalization of an excited system for two different initial strongly out-of-equilibrium distributions and two different band-gaps ($\Delta = 0$ and $\Delta = 2t \equiv 1$). We include all possible electron-electron scatterings which are shown in TABLE 5.1. Notice that the scattering $1 + 1 \leftrightarrow 2 + 2$ will result in an empty phase space, as there

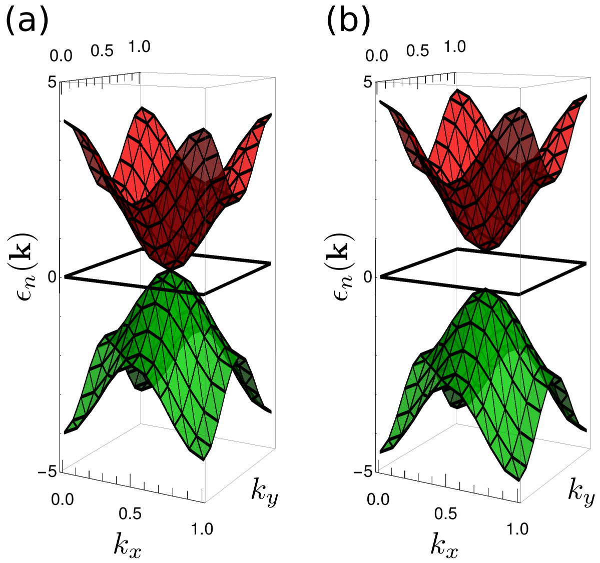

Figure 5.6: Locally linearized band-structure used for thermalization calculations with band-gaps (a) $\Delta = 0$ and (b) $\Delta = 1$. For each band we use the same mesh consisting of $N_E = 200$ triangles resulting in $N_B = 200 \times 3 \times 2 = 1200$ basis functions in total.

are no transitions that can satisfy energy conservation. For simplicity we assume, that all scattering processes have the same scattering amplitude $w^{\text{e-e}}$. The value of the scattering amplitude simply determines the global timescale, hence, without loss of generality we choose $w^{\text{e-e}} = 1$. Furthermore we do not consider spin in our calculations, i.e. we only have one electron-distribution per band.

For all studied cases, we use Fermi-Dirac distributions with $\mu = 0$ and $\beta = 3$ with additional band resolved excitations $\delta f_n(\mathbf{k})$ as the initial distributions,

$$f_2(\mathbf{k}, t = 0) = f_{\text{FD}}(\epsilon_2(\mathbf{k}), \mu, \beta) + \delta f_2(\mathbf{k}) \ , \tag{5.49a}$$

$$f_1(\mathbf{k}, t = 0) = f_{\text{FD}}(\epsilon_1(\mathbf{k}), \mu, \beta) + \delta f_1(\mathbf{k}) \ . \tag{5.49b}$$

These may arise e.g. from a laser excitation at momentum $\mathbf{k}$ which would lead to $\delta f_2(\mathbf{k}) = -\delta f_1(\mathbf{k})$.

5.4.1 Scattering rates

Before discussing the full thermalization process, it is instructive to get a preliminary idea of the scattering processes. The dynamics of a scattering process is mainly dictated by the phase space factor, which changes during strongly out-of-equilibrium dynamics. It

process	description
$1+1 \leftrightarrow 1+1$	scattering within band 1
$2+2 \leftrightarrow 2+2$	scattering within band 2
$1+2 \leftrightarrow 1+2$	scattering between band 1 and 2
$1+1 \leftrightarrow 1+2$	Auger emission
$2+2 \leftrightarrow 2+1$	impact excitation

Table 5.1: All possible electron-electron scattering processes for a two-band system; the process $1+1 \leftrightarrow 2+2$ is energetically forbidden.

is in general hard to visualize the internal structure of the scattering tensors which closely resembles the phase space factor, as they are high dimensional functions. Nonetheless often looking at scattering rates close to equilibrium can be an effective driver of intuition even further away from equilibrium.

With Eq. (5.47) we can calculate the scattering rates of a single electron (or hole) added to the equilibrium system (i.e. $\delta f_1(\cdot) \to 0$; $\delta f_2(\cdot) \to 0$ in Eq. (5.49)). As the band-structure is particle-hole symmetric, we only discuss the scattering rates of an electron added to the upper band (band 2).

In general, for the gap-less ($\Delta = 0$) system, the scattering rates for all the scattering channels become higher with increasing energy (Fig. 5.7). The level-lines roughly follow the equal-energy lines of the dispersion indicating that the scattering rates mainly depend on the energy of an excitation and not on the momentum explicitly. An exception is the scattering rate of an electron in the upper band due to Auger-process (i.e. the process $1+1 \leftrightarrow 1+2$) which decreases with increasing energy. Impact excitation ($2+2 \leftrightarrow 2+1$) is the strongest process, leading to a quick particle tranfer between the bands. Obviously scattering within the lowest band ($1+1 \leftrightarrow 1+1$) does not contribute to the decay of an excitation in band 2, and the associated scattering rates are identically 0 (they have been plotted for completeness and consistency).

The situation is different for the gapped ($\Delta = 1$) system (Fig. 5.8). The scattering rates (except Auger-emission) still increase with increasing energy. The total scattering rate, however, is not anymore approximately only energy dependent (the equal-rate lines in the total rate in Fig. 5.8 do not follow anymore the equal-energy lines). This indicates a momentum-dependence beyond the dependence through the dispersion-relations. This behavior mainly stems from impact excitation ($2+2 \leftrightarrow 2+1$).

Furthermore, we observe that impact excitation is now weaker (relative to the other processes) compared to the gap-less system. This is due to the fact that an electron has to be excited across the gap when impact excitation is performed. The larger the

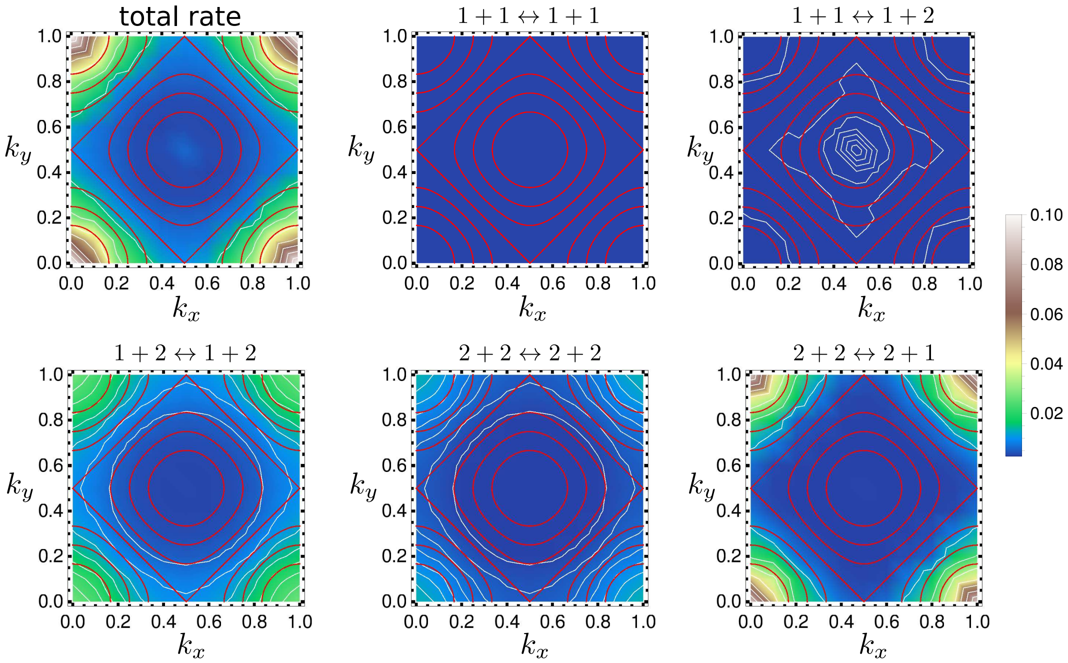

Figure 5.7: Equilibrium scattering rates $\lambda_2(\mathbf{k})$ of an electrons in the upper band (band 2) for the different processes (band gap $\Delta = 0$, temperature $T = \frac{1}{6t} \equiv \frac{1}{3}$). On top the equal-energy lines (red) are plotted as well as the equal-scattering-rate lines (white).

gap, the smaller the region within the upper bands where electrons have enough energy (relative to the Γ-point energy) to excite an electron from the lower band. The allowed phase space for the other relevant processes (i.e. $2+2 \leftrightarrow 2+2$ and $1+2 \leftrightarrow 1+2$) is not affected by the gap at all. Yet these two processes are weakened compared to the gap-less system since there are fewer thermally excited electrons (and holes) as scattering partners as the gap $\Delta = 1$ is larger than the fixed temperature $T = \frac{1}{3}$.

Let us stress that the structure of the scattering rates entirely comes from the scattering phase-space and not from transition matrix elements (which we have assumed to be momentum independent).

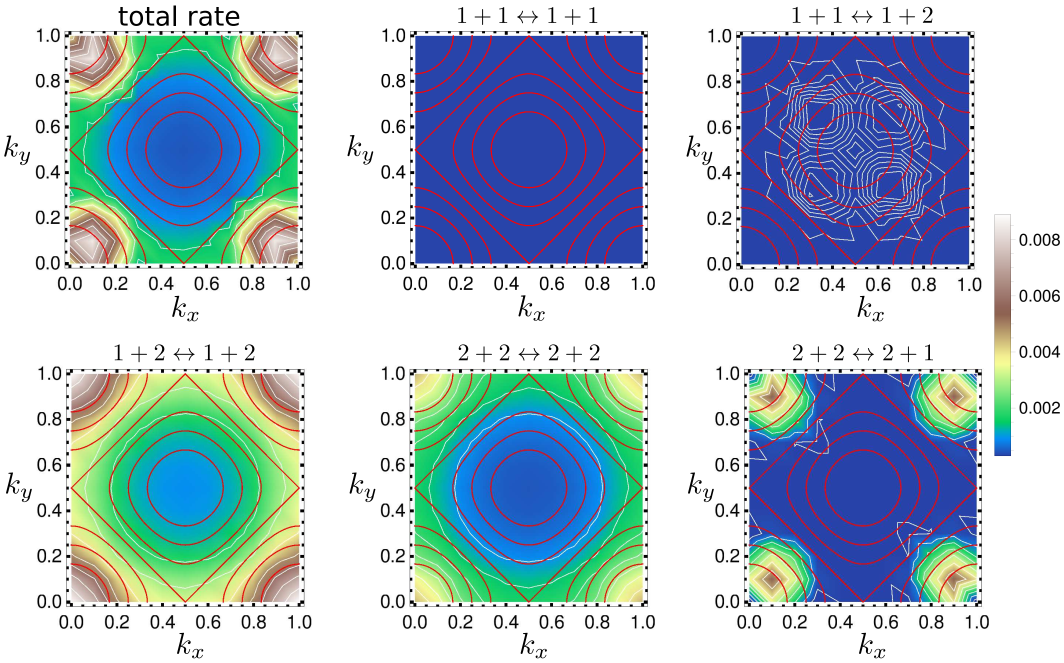

Figure 5.8: Same as Fig. 5.7 but for the band gap $\Delta = 1$. Note the order of magnitude difference in the color scale.

5.4.2 Particle-hole symmetric excitation: $\Delta = 0$

We now compute the full time propagation, in the presence of the above mentioned scattering channels, of some initial non-equilibrium distributions for the two considered model systems.

First, we study the thermalization of a particle-hole symmetric excitation that depends on the momentum only through the dispersion relations,

$$\delta f_2(\mathbf{k}) = \alpha \times \exp\left(\frac{-(\epsilon_2(\mathbf{k}) - \epsilon_c)^2}{2\sigma^2}\right) , \tag{5.50a}$$

$$\delta f_1(\mathbf{k}) = -\delta f_2(\mathbf{k}) \tag{5.50b}$$

with $\alpha = 0.1$, $\sigma = 0.5$ and $\epsilon_c = 4t + \frac{\Delta}{2}$. This type of excitation is similar to the excitation generated by a laser at an energy $\hbar\omega = 2\epsilon_c$ that is resonant with the transition between the center van-Hove singularities of the two $2D$ bands.

We calculate the time-propagation for this setup which is shown in Fig. 5.9 for the system with band gap $\Delta = 0$. The band structure and the initial distributions are

Die approbierte gedruckte Originalversion dieser Dissertation ist an der TU Wien Bibliothek verfügbar.
The approved original version of this doctoral thesis is available in print at TU Wien Bibliothek.
TU Bibliothek Your knowledge hub WIEN

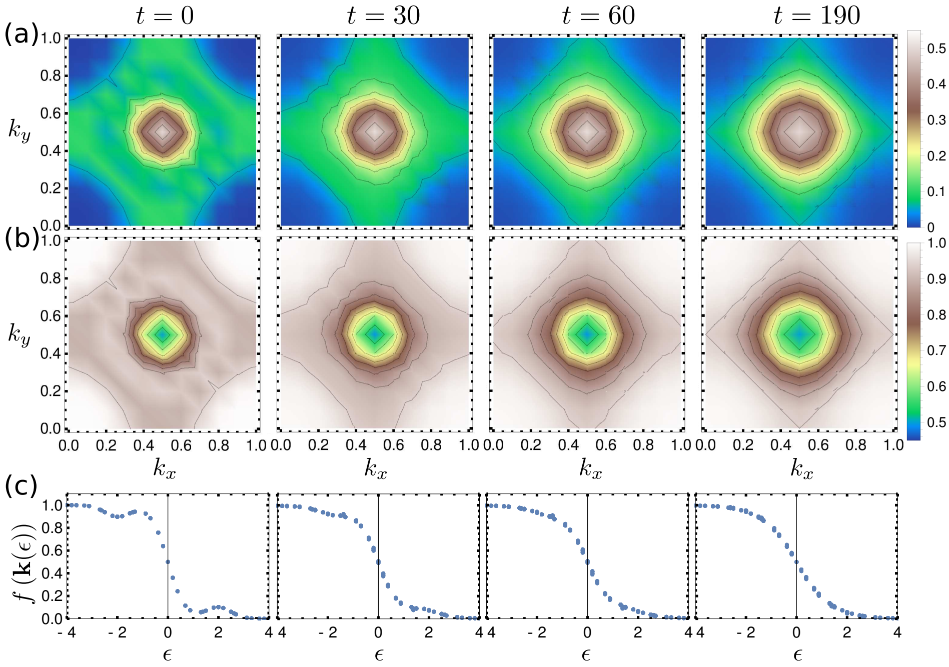

Figure 5.9: Distrubution function $f(\mathbf{k}, t)$ of band 2 (a) and band 1 (b) (band gap $\Delta = 0$) for different times. (c) Distribution function as a function of energy for different times. The initial distribution was a Fermi-Dirac distribution with $\mu = 0$, $\beta = 3$ and an excitation (Eq. (5.50)) that only depends on the energy.

particle-hole symmetric. As the electron-electron collision operators do not break it, the particle-hole symmetry is maintained at all times.

During the thermalization process the high-energetic electrons (or holes) of the initial excitations are transferred towards the Γ-point ($\mathbf{k}_\Gamma = (0.5, 0.5)^{\mathrm{T}}$), losing energy in the process. As the total energy is conserved, additional electrons have to be brought up from the lower band to compensate for this energy loss. Eventually, the system thermalizes to a new Fermi-Dirac with a higher temperature than the initial (see time $t = 190$ in Fig. 5.9).

The approach to the equilibrium distribution is more easily recognized when the distribution function is plotted versus energy, i.e. plotting all $f(\mathbf{k}(\epsilon), t)$ for a given ϵ and t (see Fig. 5.9c). Note, since the dispersion-relations cannot be inverted globally, we get several different distribution-function values for every energy (stemming from different points in the Brillouin-zone). In principle, far from equilibrium, there is no guarantee that these points will form a curve, as in general the population depends on $\mathbf{k}$ only through the energy solely at equilibrium (this is for instance evident in Fig. 5.12c below, where at early times the population plotted as a function of energy does not fall on a line, yet after the thermalization has taken place, a Fermi-Dirac distribution is recovered). As we are studying a case where the initial excitation was only dependent on the energy, the population has this characteristic at the initial timestep ($t = 0$ case in Fig. 5.9c). Interestingly, even though the scattering operators are explicitly momentum dependent, the population preserves this characteristic throughout the whole thermalization process. This is due to the fact that the scattering rates for this configuration have shown negligible explicit momentum dependence (as shown in section 5.4.1 and Fig. 5.7).

5.4.3 Particle-hole symmetric excitation: $\Delta = 1$

We now address the thermalization dynamics of the system with gap $\Delta = 1$, which shows important qualitative differences compared to the gap-less case. The first difference is that the time needed to thermalize is about one order of magnitude larger than for the system with zero gap. As pointed out in section 5.4.1 due to the larger gap there are fewer thermally excited carriers leading to a reduced strength of the processes $1+1 \leftrightarrow 1+1$, $1+2 \leftrightarrow 1+2$ and $2+2 \leftrightarrow 2+2$. However, the reduced number of thermal carriers alone cannot explain the large difference in the thermalization time. It mainly originates from the fact that the available phase-space for the Auger process and impact excitation is strongly reduced by the band gap. These are the only processes that may change the number of particles in the bands. In order to reach equilibrium the bands need to transfer particles among each other (which can happen only through the scatterings $1+1 \leftrightarrow 1+2$ and $2+2 \leftrightarrow 2+1$). Hence, a complete thermalization can happen only over the time-scales of impact excitation and Auger processes.

This leads yet to another very important effect: the thermalization happens in two distinct steps. The scatterings within the bands ($1+1 \leftrightarrow 1+1$, $2+2 \leftrightarrow 2+2$) and between the bands ($1+2 \leftrightarrow 1+2$) are faster than the remaining impact excitation ($2+2 \leftrightarrow 2+1$) and Auger process($1+1 \leftrightarrow 1+2$). As a result the two bands will first undergo an initial partial thermalization, during which they can redistribute energy within each band individually but there is not yet a sizeable number of particles exchanged between the bands. In oder words, the two bands act as two thermodynamic objects that can transfer energy but not particles.

The distribution-functions of the two bands will therefore form two individual Fermi-Dirac distributions with different chemical potentials but the same temperature for times $t \gtrsim 100$. This is visualized in Fig. 5.11. In Fig. 5.11a we plot the fitting with Fermi-Dirac distributions of the energy resolved population separately for the two bands. At earlier times the fitting error (Fig. 5.11d) is too large, showing that the distribution is still far from equilibrium. However, within several tens of time units the two bands already look internally thermalized (as the fitting error drastically decreases in Fig. 5.11d). Within this time the two bands also reach the same temperature because the bands can exchange energy through the process $1+2 \leftrightarrow 1+2$ which is not affected by the band gap (notice that this process is shadowed in this case by the fact that since the excitation is particle-hole symmetric, the population remains particle-hole symmetric throughout the whole dynamics, making the temperature trivially identical).

Nonetheless one can clearly see how a global thermalization has not been reached yet within the first several hundreds of time units. The two individual Fermi-Diracs have chemical potentials that lie below (above) zero for the upper (lower) band. As time progresses, the two chemical potentials, however, approach each other, due to Auger process and impact excitation scatterings on a scale of 2000 time units. One can also observe how the temperature of the two bands decreases. Eventually both chemical potentials equalize and the system reaches global thermal equilibrium where it can be described with a single Fermi-Dirac distribution for both bands (see time $t = 1990$ in Figs. 5.10 and 5.11).

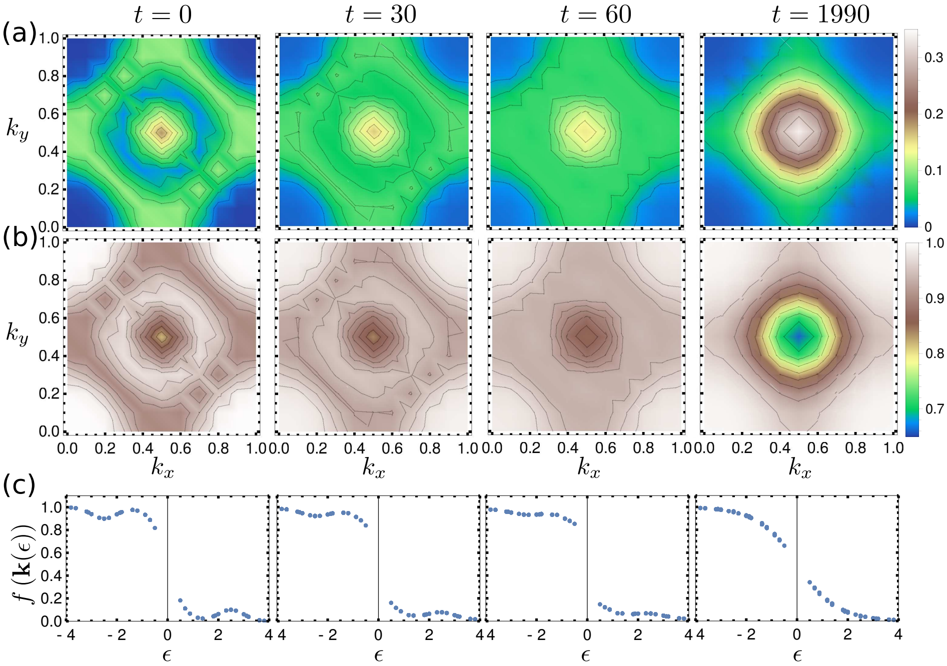

Figure 5.10: Same as Fig. 5.9 but for a band gap of $\Delta = 1$. Note the much longer thermalization time.

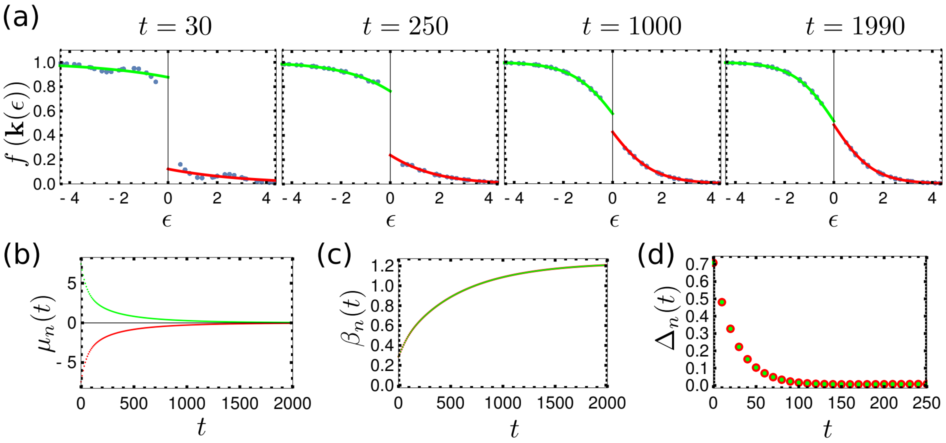

Figure 5.11: (a) Distribution function in dependence of the energy for different times with a Fermi-Dirac fit for the upper- (red) and lower- (green) band. (b) Chemical potentials, (c) inverse temperatures and (d) squared deviation of the Fermi-Dirac fits in dependence of time.

5.4.4 Particle-hole asymmetric excitation: $\Delta = 0$

In this section we will discuss a case where the excitation breaks particle-hole symmetry and is momentum asymmetric. We use the same band-structures as in the previous sections (which are particle-hole symmetric) but a different excitation (which is now not particle-hole symmetric and also **k**-dependent),

$$\delta f_2(\mathbf{k}) = \alpha \sum_{\mathbf{G}} \exp\left(\frac{-(\mathbf{k}-\mathbf{k}_c-\mathbf{G})^2}{2\sigma^2}\right) , \tag{5.51a}$$

$$\delta f_1(\mathbf{k}) = 0 , \tag{5.51b}$$

with $\alpha = 0.2$, $\sigma = 0.1$ and $\mathbf{k}_c = (0.8, 0.8)$. The sum over all reciprocal lattice vectors is needed to ensure that the distribution function is periodic at the borders of the first Brillouin-zone.

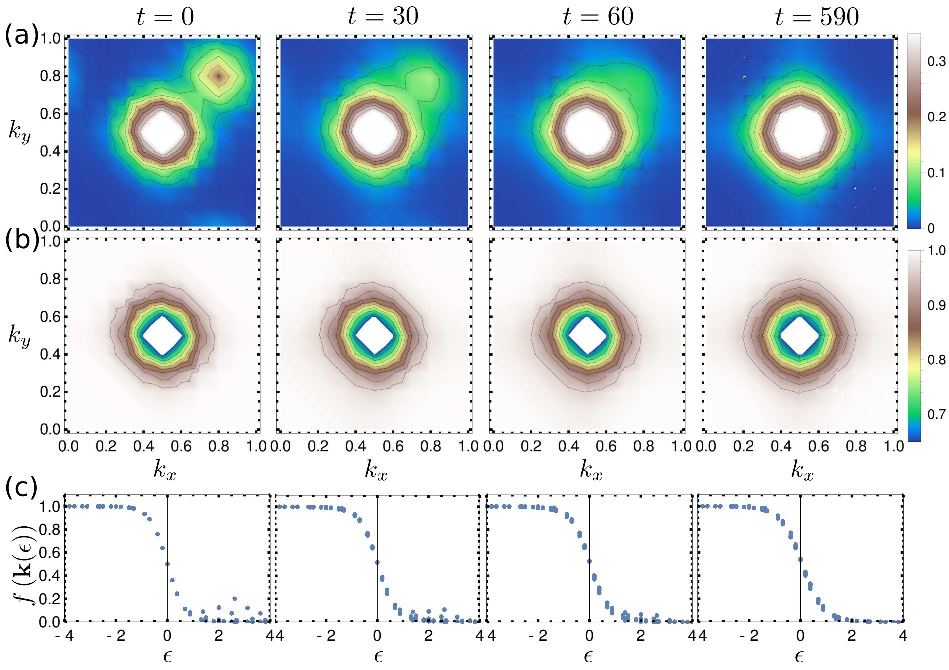

Figure 5.12: Distrubution function $f(\mathbf{k}, t)$ of band 2 (a) and band 1 (b) (band gap $\Delta = 0$) for different times. (c) The distribution function in dependence of the energy for different times. The initial distribution was a Fermi-Dirac with $\mu = 0$, $\beta = 3$ and an excitation that explicitly depends on the momentum.

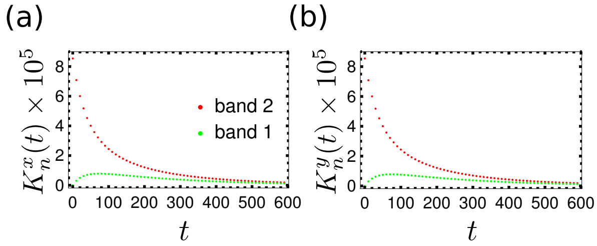

Figure 5.13: Total momentum density (red, upper band; green, lower band) in dependence of time for the x- (a) and y- (b) momentum component (gap $\Delta = 0$).

First, we discuss the case with zero band gap (Fig. 5.12). As seen in the previous sections, the electrons are redistributed by the scatterings towards the Γ-point during the thermalization process and electrons are excited from the lower band to the upper band to compensate for the energy loss. In contrast to the case discussed in the previous sections the distribution function in dependence of the energy (Fig. 5.12c) now clearly shows that the population is not a function of energy only. This is a consequence of starting with a distribution function centered around $\mathbf{k}_c = (0.8, 0.8)^{\mathrm{T}}$ which even has a net lattice momentum. To achieve a full thermalization towards a Fermi-Dirac (which has no net momentum), momentum needs to be dissipated. Since no electron-phonon scatterings have been included, this can happen only through two different electronic processes. (i) The electrons in the upper band scatter with each other ($2+2 \leftrightarrow 2+2$) and perform umklapp processes reducing the total momentum. (ii) The electrons of the upper band scatter with electrons of the lower band ($1+2 \leftrightarrow 1+2$) where they transfer momentum from the upper to the lower band and/or dissipate momentum through umklapp processes. The electrons of the lower band will then as well scatter with each other ($1+1 \leftrightarrow 1+1$) and dissipate momentum through further umklapp processes (Fig. 5.13).

We calculate the total momentum density by integrating over the population (see also section. 5.1.1)

$$\mathbf{K}_n(t) = \int_{V_{BZ}} \mathrm{d}^2k \frac{1}{(2\pi)^2} f_n(t, \mathbf{k}) \left(\mathbf{k} - (0.5, 0.5)\right) \ , \tag{5.52}$$

and plot the results in Fig. 5.13. We can see how the momentum of the upper band is partially reduced by umklapp and partially transferred to the lower band. The total momentum in the lower band shows an initial increase due to the direct transfer from the other band. Eventually both tend to decay to a situation with a vanishing total momentum. Interestingly, one can observe how the dissipation slows down considerably with time. The reason is that when the population decays closer to the Γ-point, fewer and fewer electrons are still close enough to the edge of the Brillouin zone to perform umklapp.

5.4.5 Particle-hole asymmetric excitation: $\Delta = 1$

We now simulate the thermalization process of the gapped system ($\Delta = 1$; Fig. 5.14) with the same initial distribution (Eq. (5.51)). As in the gap-less system, the initial momentum has to be dissipated in order to thermalize the system. In principle, the processes $2+2 \leftrightarrow 2+2$, $1+2 \leftrightarrow 1+2$ and $1+1 \leftrightarrow 1+1$ are not affected by the gap, hence, one might expect that the momentum exchange between the upper and lower band and the dissipation should be as fast as in the gap-less system. However, this is not the case (Fig. 5.15a). The reason is again the smaller number of thermally excited carriers. Since they involve two electrons, the strengths of the scattering processes relevant for momentum dissipation depend on the number of carriers in the band, both the ones that are thermally present and the excited ones.

The time-dependence of the total momentum in x-direction (i.e. $K^x(t) = K^x_1(t) + K^x_2(t)$) can be well described with a double-exponential function ($g(t) = a + b \times \mathrm{Exp}(-\frac{t}{\tau^I}) + c \times \mathrm{Exp}(-\frac{t}{\tau^{II}})$; with $\tau^I \leq \tau^{II}$)(Fig. 5.15a). The two times obtained from the fit are $\tau_K^I = 194$ and $\tau_K^{II} = 597$. We attribute the two different timescales to the strong energy dependence of the scattering rates. The short time τ_K^I reflects the momentum dissipation of the initial high-energy carriers while the larger time τ_K^{II} is the average dissipation time of the low energetic electrons closer to the Γ-point (note that only Umklapp processes contribute to the momentum dissipation).

After a time $t = 3 \times \tau_K^{II} \approx 1800$ a large part of the momentum has already decayed and the purely energy dependent representation is justified again. Therefore, for times $t \gtrsim 3 \times \tau_K^{II}$ it makes sense to perform Fermi-Dirac fits within each band. As we can see from the time-dependent chemical potentials $\mu_n(t)$ and inverse temperatures $\beta_n(t)$, the system undergoes the same step of partial thermalization as in the previous section where the upper and lower bands are populated according to Fermi-Dirac distributions with the same temperature but different chemical potentials. With increasing time, the chemical potentials approach each other until they equalize and the system reaches global equilibrium. We can estimate the time it takes for global thermalization from single exponential fits (i.e. with $y(t) = a + b \times \mathrm{Exp}(-\frac{t}{\tau})$) to $\mu_n(t)$ and $\beta_n(t)$ within the time interval $t \in [4000, 5990]$. We get $\tau_{\mu_1} = 2564$, $\tau_{\mu_2} = 2554$, $\tau_{\beta_1} = 3207$ and $\tau_{\beta_2} = 3182$. The two different times we get from the two bands for each quantity are identical within the tolerance; $\tau_{\beta_1} \approx \tau_{\beta_2} \equiv \tau_\beta$, $\tau_{\mu_1} \approx \tau_{\mu_2} \equiv \tau_\mu$. As expected, chemical

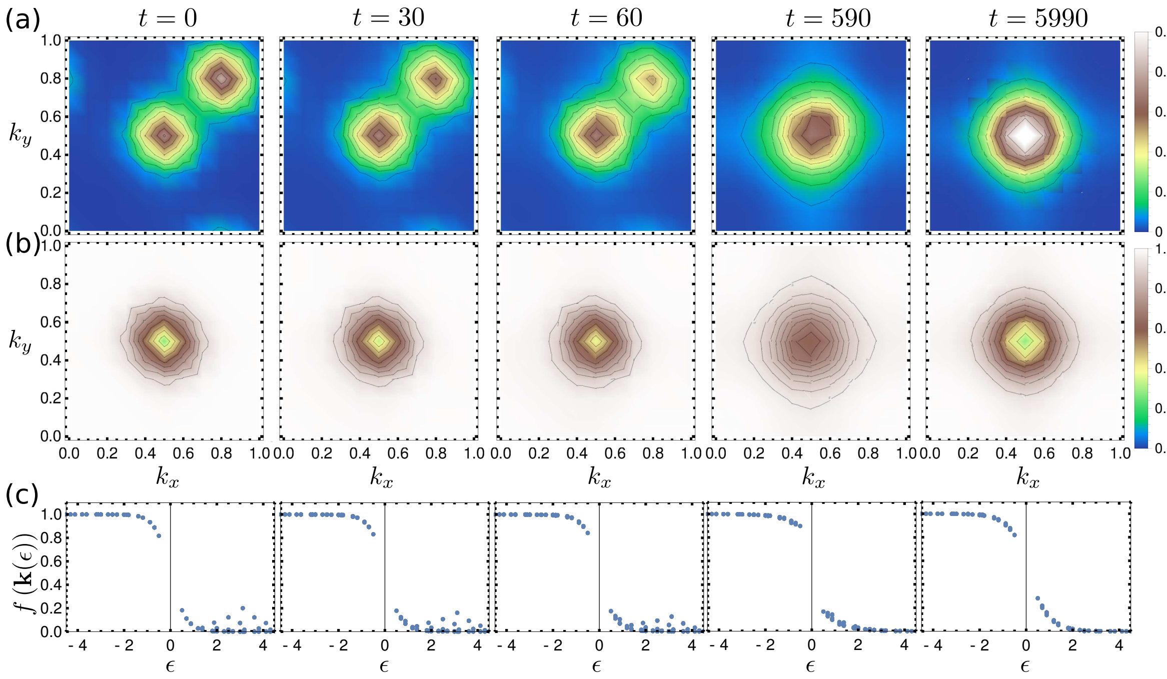

Figure 5.14: Same as Fig. 5.12 but for a band gap of $\Delta = 1$. Note the much longer thermalization time.

potential and inverse temperature thermalize on similar timescales albeit not identical.

It is interesting to study the particle density in dependence of time. In analogy to the momentum density, the band resolved particle density can be calculated with the relation

$$N_n(t) = \int_{V_{BZ}} \mathrm{d}^2 k \frac{1}{(2\pi)^2} f_n(t, \mathbf{k}) \ . \tag{5.53}$$

From the scattering rates Fig. 5.8 we see, that some of the initial electrons may directly perform impact excitation (i.e. the process $2+2 \leftrightarrow 2+1$). These initial, high energy electrons rapidly change the particle number in the upper band (Fig. 5.15b). After the initial electrons have decayed to lower energies, the low energetic electrons must perform several scatterings to gain again enough energy for the process $2+2 \leftrightarrow 2+1$ leading to a much longer timescale for total thermalization. Similar to the momentum density, the particle density follows a double exponential function. From a fit over the whole timescale we get $\tau^{I}_{N_2} = 178$ and $\tau^{II}_{N_2} = 2479$. The scattering rate of the process $2+2 \leftrightarrow 2+1$ is around $\lambda_{\text{impact}} = 0.0055$ at its maximum, leading to a lifetime of $\tau_{\text{impact}} = 1/\lambda_{\text{impact}} = 182$ which is approximately $\tau^{I}_{N_2}$. The larger thermalization time $\tau^{II}_{N_2}$ reflects the long-time thermalization of the system and is approximately the same

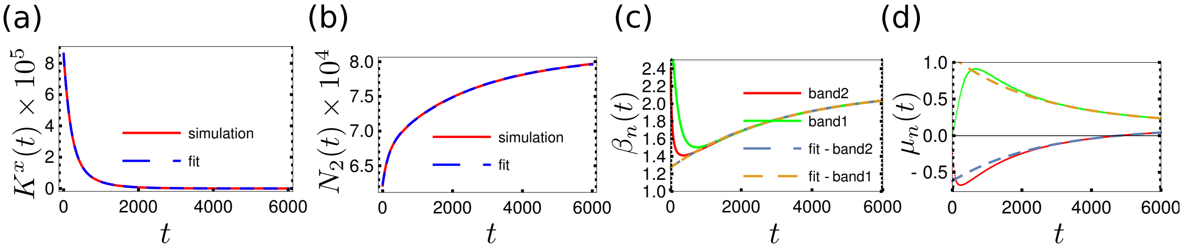

Figure 5.15: (a) Total momentum density in x-direction (red) with double-exponential fit (blue) on top, (b) particle density of the upper band (red) with double-exponential fit (blue) on top, (c) inverse temperatures and chemical potentials (d) of Fermi-Dirac fits to the upper (red) and lower (green) band with single-exponential fits (dashed, fitting-interval $t \in [4000, 5990]$)on top.

as the time constant τ_μ determined from the fitting of the time-dependence of chemical potentials.

Summarizing, the case of the gapped system with explicitly momentum dependent initial distribution reveals dynamics on several timescales. First, the initial, finite momentum is dissipated, i.e. the electrons that were added in a finite region in momentum space are distributed symmetrically over the whole Brillouin-zone. This process takes place on two timescales, one for high energetic electrons (τ_K^I) and one for long-time dissipation (τ_K^{II}). The high energetic electrons of the upper band also perform impact excitation which quickly increases the number of particles in the upper band ($\tau_{N_2}^I$). Then the upper and lower band behave like two separately thermalized systems with different chemical potentials. Only high-energetic electrons or holes, which are few at that time, may perform processes that lead to a particle transfer between the subsystems. Moreover, after a high energetic electron has brought up an electron through impact excitation, both electrons end up with low energy. They need to undergo further several scatterings to get enough kinetic energy to perform another impact excitation. This determines the timescale on which the chemical potentials of the upper and lower band equilibrate ($\tau_\mu \approx \tau_{N_2}^{II}$), reaching full thermalization. The timescales can be set in relation to each other giving $\tau_{N_2}^I < \tau_K^I < \tau_K^{II} < \tau_\mu$.

5.5 Numerical implementation

Several parts of the algorithm were implemented and tested in *Mathematica 10*. The full scattering code was then completely implemented in *MATLAB R2017b* in an object oriented fashion. The main idea was to limit the development effort to a manageable amount as the scheme introduced in this chapter had to be developed and tested. The program design was already done with a future port to *C++* in mind as the computational capabilities of *MATLAB*, being a script language, are limited. We will not give a detailed explanation of all the classes and their properties and methods here as this would go beyond the scope of this thesis. As a substitute, the code itself contains comments where necessary and small descriptions within each class that explain the details. TABLE 5.2 gives an overview of the classes and their main purpose.

class	purpose
Mesh2D	contains a triangulation of the simulation domain
DGSpace2Dtypes	represents different basis-functions
function2D	contains a discretized function
Band2D	like function2D but with additional methods for bands
BandStructure2D	contains several Band2D instances
multFunction2D	contains the distribution-functions for all bands
time_function2D	contains a multFunction2D instance for each timestep
scTens3chBasic2D	scattering tensor for 3-leg processes
scTens4chBasic2D	scattering tensor for 4-leg processes
ScTensFull2D	object that combines all the scattering tensors
linker_all	needed internally by ScTensFull2D for band-assignment
Vlasov1D	transport only in momentum space; only for 1D
Vlasov1Dx1D	transport in full phase-space; only for 1D

Table 5.2: Overview of the different classes and their purpose for the $2D$-case.

In Fig. 5.16 we show a schematic flow of a simulation. The first step is to setup a mesh where one has to specify the momentum-space simulation domain (usually the first Brillouin-zone) and the desired resolution. This determines the total number of mesh-elements used for the triangulation of the domain. Then one has to setup the bandstructure of the system. The *Band2D* class needs a *Mesh2D* instance and the dispersion-relation (either as analytical or numerical function) as input. During the initialization it generates a locally linearized but continuous version of the dispersion. In the *BandStructure2D* class the different bands are stored together to represent the whole system bandstructure.

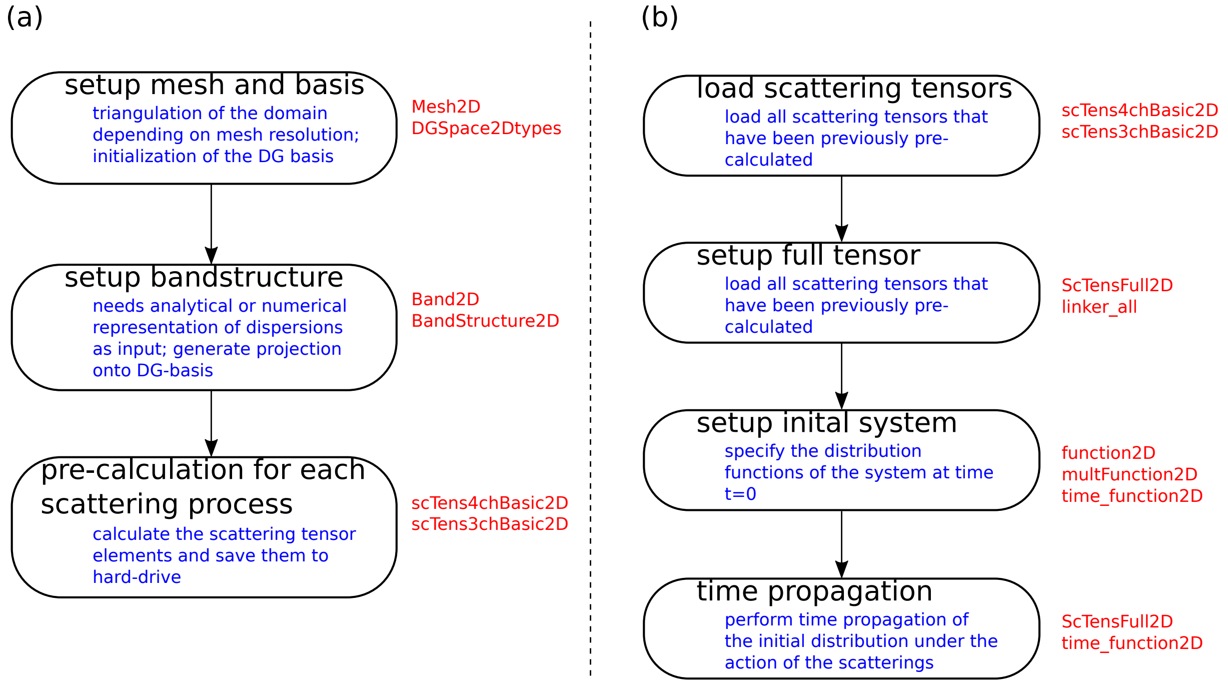
(a)
setup mesh and basis
triangulation of the domain depending on mesh resolution; initialization of the DG basis
Mesh2D
DGSpace2Dtypes
setup bandstructure
needs analytical or numerical representation of dispersions as input; generate projection onto DG-basis
Band2D
BandStructure2D
pre-calculation for each scattering process
calculate the scattering tensor elements and save them to hard-drive
scTens4chBasic2D
scTens3chBasic2D
(b)
load scattering tensors
load all scattering tensors that have been previously pre-calculated
scTens4chBasic2D
scTens3chBasic2D
setup full tensor
load all scattering tensors that have been previously pre-calculated
ScTensFull2D
linker_all
setup inital system
specify the distribution functions of the system at time t=0
function2D
multFunction2D
time_function2D
time propagation
perform time propagation of the initial distribution under the action of the scatterings
ScTensFull2D
time_function2D

Figure 5.16: (a) Program flow for the pre-calculation and (b) the time propagation of a $2D$ system. The classes that are mainly involved at each stage are denoted in red outside the boxes.

The next step is the actual pre-calculation of the scattering-tensors. We have implemented two different scattering-process classes, *scTens3chBasic2D* for 3-leg processes and *scTens4chBasic2D* for 4-leg processes. Each instance of these classes represents a full scattering process, e.g. there is one *scTens4chBasic2D*-object for the process $n_0{+}n_1 \leftrightarrow n_2{+}n_3$. The object contains a scattering-tensor for each leg, i.e. for the given example these would be $(\mathbb{S}_{n_0+n_1\leftrightarrow n_2+n_3})^{ijkmn}_{\substack{IJKMN\\ n_0n_1n_2n_3}}$, $(\mathbb{S}_{n_0+n_1\leftrightarrow n_2+n_3})^{ikjmn}_{\substack{IKJMN\\ n_1n_0n_2n_3}}$, $(\mathbb{S}_{n_0+n_1\leftrightarrow n_2+n_3})^{imnjk}_{\substack{IMNJK\\ n_2n_3n_0n_1}}$ and $(\mathbb{S}_{n_0+n_1\leftrightarrow n_2+n_3})^{inmjk}_{\substack{INMJK\\ n_3n_2n_0n_1}}$. The pre-calculated tensor-elements are saved to the hard-drive during pre-calculation. The generated tensors are already symmetrized, i.e. fulfill the conservation equations exactly.

Once all scattering-processes are pre-calculated we can perform time-propagations. For that we first need to load the scattering-tensors into the RAM. Then all the individual scattering-process objects have to be combined in an instance of the class *ScTensFull2D* that represents the total collision-operator of the system. As a next step we need to setup the initial configuration of the system, i.e. the distribution-functions at time $t = 0$. The discretized functions are combined in a *multFunction2D* instance which serves as starting point for the time-propagation.

The *ScTensFull2D*-instance performs the actual time-propagation starting from the initial-distribution using a Runge-Kutta4 scheme. At the end we get a *time_function2D*-instance back that contains the distribution-functions of the system for each time-step.

All the above mentioned classes have been implemented for $1D$-case[7] as well. The use is exactly as in the $2D$-case. In case of a calculation with transport (see section 5.6) in momentum-space, additionally an instance of the class *Vlasov1D* must be initialized for each band participating in transport. This object can be used in the same way as a scattering-process object and must be added to the *ScTensFull2D*-instance.

5.6 Joining scattering with transport

In chapter 4 we have discussed the transport part of the Boltzmann equation and how to solve it numerically for one-dimensional systems. In this chapter we have introduced a numerical scheme capable of calculating the full, momentum conserving collision operators for momentum dependent distribution-functions. The scattering algorithm has been introduced for two-dimensional systems, however, we have implemented it for one- as well as two-dimensional setups.

This section is dedicated to the combination of both schemes (i.e. transport and scattering) in order to solve the full Boltzmann equation numerically, at least in one-dimension. The generalization to higher dimensions is straightforward.

In the chapter about transport we have distinguished between the full transport in one-dimension taking real-space as well as momentum-space into account ($1D \times 1D$-case), and transport for problems where we have dropped the real-space dependencies ($1D$-case).

The $1D$-case can be easily joined with scattering. The discretized distribution-function time-derivative is the sum of the time-derivative stemming from transport and the time-derivatives stemming from all the collisions,

$$\frac{\partial f^i_{I_{n_0}}}{\partial t} = \left(\frac{\partial f^i_{I_{n_0}}}{\partial t}\right)_{\text{transport}} + \frac{1}{2}\sum_{n_1,n_2,n_3}\left(\frac{\partial f^i_{I_{n_0}}}{\partial t}\right)_{n_0+n_1\leftrightarrow n_2+n_3} . \tag{5.54}$$

In the above equation we have only summed the electron-electron scatterings. If there are other scattering-types they are added in the same way. The implementation of the time propagation for the equation above is straightforward and it was applied to the non-equilibrium dynamics in semi-conducting carbon-nanotubes which can be seen as a prototypical, real $1D$-system (see chapter 6).

---

[7] Note, that we use the term $2D$ ($1D$) for a two- (one-) dimensional momentum space. Again, the term $1D \times 1D$ means one dimension in momentum-space and one dimension in real-space.

The $1D \times 1D$-case is more complicated. For the transport implementation we have used a product basis,

$$\underset{n_0}{\varPhi^{aj}_{AJ}}(x,k) \equiv \varphi^a_A(x)\underset{n_0}{\Phi^j_J}(k) \ , \tag{5.55}$$

$$f_{n_0}(t,x,k) \rightarrow \sum_{\substack{aj\\AJ}} \underset{n_0}{f^{aj}_{AJ}}(t)\ \underset{n_0}{\varPhi^{aj}_{AJ}}(x,k) = \sum_{\substack{aj\\AJ}} \underset{n_0}{f^{aj}_{AJ}}(t)\ \varphi^a_A(x)\underset{n_0}{\Phi^j_J}(k) \ . \tag{5.56}$$

When we use this discretization for the collision operator Eq. (5.11) in the same way as the purely momentum dependent basis in section 5.1.2 we get

$$\begin{aligned}\left(\frac{\partial \underset{n_0}{f^{ai}_{AI}}}{\partial t}\right)_{n_0+n_1\leftrightarrow n_2+n_3} &\equiv \int \mathrm{d}^d x \int \mathrm{d}^d k_0\ \varphi^a_A(\mathbf{x})\underset{n_0}{\Phi^i_I}(\mathbf{k}_0)\left(\frac{\partial f_0}{\partial t}\right)_{n_0+n_1\leftrightarrow n_2+n_3} = \\ &= w^{\text{e-e}}_{n_0n_1n_2n_3} \sum_{\substack{b,c,d,e\\B,C,D,E}} \sum_{\substack{j,k,m,n\\J,K,M,N}} \mathbb{L}^{abcde}_{ABCDE}\left(\mathbb{S}_{n_0+n_1\leftrightarrow n_2+n_3}\right)^{ijkmn}_{\substack{IJKMN\\n_0n_1n_2n_3}} \\ &\Big((\underset{n_0}{1^{bj}_{BJ}} - \underset{n_0}{f^{bj}_{BJ}})(\underset{n_1}{1^{ck}_{CK}} - \underset{n_1}{f^{ck}_{CK}})\underset{n_2}{f^{dm}_{DM}}\underset{n_3}{f^{en}_{EN}} - \underset{n_0}{f^{bj}_{BJ}}\underset{n_1}{f^{ck}_{CK}}(\underset{n_2}{1^{dm}_{DM}} - \underset{n_2}{f^{dm}_{DM}})(\underset{n_3}{1^{en}_{EN}} - \underset{n_3}{f^{en}_{EN}})\Big),\end{aligned} \tag{5.57}$$

where we have introduced the so-called local tensor $\mathbb{L}^{abcde}_{ABCDE}$,

$$\mathbb{L}^{abcde}_{ABCDE} \equiv \int \mathrm{d}^d x\ \varphi^a_A(\mathbf{x})\varphi^b_B(\mathbf{x})\varphi^c_C(\mathbf{x})\varphi^d_D(\mathbf{x})\varphi^e_E(\mathbf{x}) \ . \tag{5.58}$$

The local tensor is diagonal in the element-indices due to the compact support of the DG-basis functions, i.e.

$$\mathbb{L}^{abcde}_{ABCDE} = \delta_{A,B}\delta_{A,C}\delta_{A,D}\delta_{A,E}\ L^{abcde}_{AAAAA} \ . \tag{5.59}$$

With the full $1D \times 1D$-discretization of the collision operators Eq. (5.57) and transport we again can calculate the time derivative of the distribution-functions as

$$\frac{\partial \underset{n_0}{f^{ai}_{AI}}}{\partial t} = \left(\frac{\partial \underset{n_0}{f^{ai}_{AI}}}{\partial t}\right)_{\text{transport}} + \frac{1}{2}\sum_{n_1,n_2,n_3}\left(\frac{\partial \underset{n_0}{f^{ai}_{AI}}}{\partial t}\right)_{n_0+n_1\leftrightarrow n_2+n_3} \ . \tag{5.60}$$

Due to lack of time, the $1D \times 1D$ scattering code was not joined with transport within the scope of this thesis and is left for future work.

TU Bibliothek, WIEN Your knowledge hub
Die approbierte gedruckte Originalversion dieser Dissertation ist an der TU Wien Bibliothek verfügbar.
The approved original version of this doctoral thesis is available in print at TU Wien Bibliothek.

Die approbierte gedruckte Originalversion dieser Dissertation ist an der TU Wien Bibliothek verfügbar.
The approved original version of this doctoral thesis is available in print at TU Wien Bibliothek.
TU Bibliothek WIEN Your knowledge hub

Chapter 6

Dynamics in carbon-nanotubes

Low dimensional materials are a fascinating field of research. Many intriguing effects emerge due to the reduced dimensionality like suppressed screening, strong excitonic effects or mass-less quasi-electrons. The increasing need for miniaturization of information processing structures in modern electronics has triggered huge interest in low dimensional materials and even large, single molecules as possible candidates for small transistors.

A prototypical two-dimensional ($2D$) material is graphene which has been extensively studied in recent years. One reason for the huge interest in this special material lies in its unique band-structure which consists of cones around the Fermi-level leading to Dirac-like physics. Understanding graphene forms the basis to understand the one-dimensional ($1D$) carbon-nanotubes (CNTs) which are essentially rolled graphene-sheets.

The strongly out-of-equilibrium physics in CNTs is still under discussion in the scientific community. The reason lies in the complicated interplay of many different quasi-particles and bands which requires a unified picture using concepts of several fields like DFT, many-body physics, transport and non-equilibrium thermalization dynamics.

In this chapter we will give a short introduction to graphene and carbon nanotubes. Then we will discuss an experiment that uses aligned single-walled carbon nanotubes (SWCNTs) to produce terahertz (THz) radiation. Then we explain how we model this experiment and calculate the dynamics with our Boltzmann solver.

The chapter is organized as follows: We give short introduction to graphene and carbon-nanotubes, in particular how the nanotube bandstructure can be deduced from graphene (Introduction to graphene and carbon-nanotubes, section 6.1). Then we discuss the experiment where terahertz emission is measured after an excitation of aligned carbon-nanotubes with a femtosecond laser pulse (Aligned CNTs as THz emitters; section 6.2). In that section we also discuss how to model the CNTs theoretically. Then we use our Boltzmann code to numerically calculate the complex dynamics produced by the model which gives results consistent with experimental findings. Through the simulation we gain deeper insight into the origin of the discrepancy between the dependence of the terahertz amplitude and the photocurrent on the applied voltage.

The results shown in this chapter have been published in Ref. [83]. Some of the figures and parts of the text (marked by a black, vertical bar) are taken from this publication.

6.1 Introduction to graphene and carbon-nanotubes

This section should give a (very) quick introduction to graphene and carbon-nanotubes without claim of completeness. It is broadly based on Refs. [84–87] and we encourage the interested reader to consult the excellent references to learn more about the fascinating field of carbon-nanotubes.

6.1.1 Graphene band-structure

Graphene is a $2D$-material that entirely consists of carbon-atoms. Carbon has six electrons where two of them fill the first electron shell and cannot form bonds with other atoms. The remaining four electrons in the second shell determine the chemical properties of carbon, i.e. how it may bind with other atoms. Atomic carbon may bind to three other carbon atoms by sp^2 hybrid orbitals where all the atoms lie within the same plane. When we assume that we have a lattice where each carbon binds to three other carbons and further assume that the distance between two neighboring carbons is always the same, we obtain a honeycomb structure given the triangular orientation of the sp^2 bonds.

The corresponding unit-cell is orthorhombic with an angle between the lattice basis-vectors of $\varphi = \frac{\pi}{3}$. Each unit-cell contains two carbon atoms (Fig. 6.1) where the first one (A) is located at the origin of the unit-cell and the second atom (B) at $\mathbf{r}_B = a_{\text{cc}} \frac{\mathbf{a}_1+\mathbf{a}_2}{|\mathbf{a}_1+\mathbf{a}_2|}$. The carbon-bond length is about $a_{\text{cc}} \approx 1.42\text{Å}$ and the lattice parameter is $a \equiv |\mathbf{a}_1| = |\mathbf{a}_2| = \sqrt{3}a_{\text{cc}}$.

As graphene is a $2D$-material, the localized sp^2 orbitals form σ-(anti-)bonding bands. Each atom in the unit-cell contributes three orbitals resulting in six bands where three of them are σ-bonding and three are σ-anti-bonding. The three bonding bands are completely filled by the six electrons per unit-cell, leaving the three anti-bonding bands completely empty.

The sp^2 orbitals consist of superpositions of the atomic $2s$, $2p_x$ and $2p_y$ orbitals. The remaining p_z-orbitals of the carbon-atoms form two more bands, one π-bonding and one π-anti-bonding. In a tight-binding model with next-neighbor hopping one can calculate

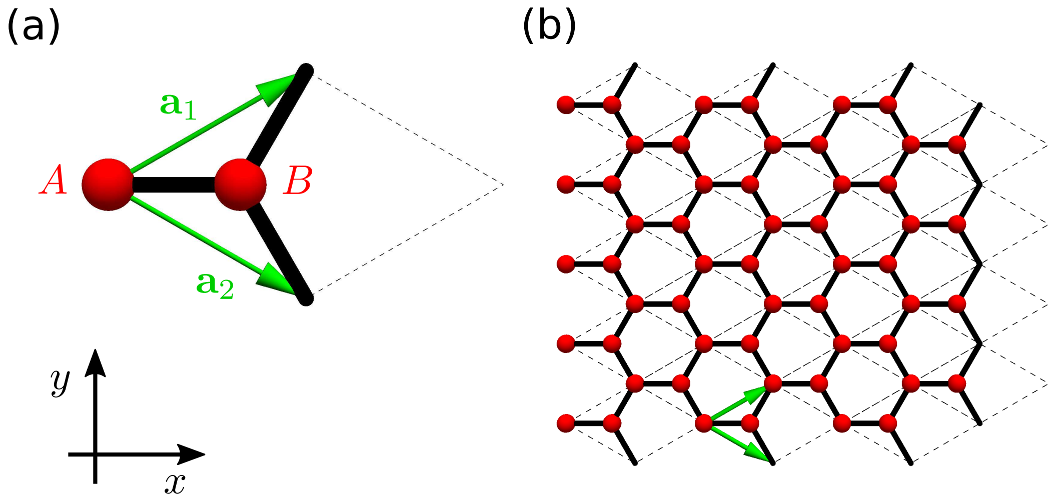

Figure 6.1: (a) Graphene unit-cell with the two carbon atoms A and B and the lattice vectors $\mathbf{a}_1$ and $\mathbf{a}_2$. (b) Graphene sheet composed of several unit-cells.

the dispersion relations of the two π-bands as [84]

$$\epsilon_\pm(\mathbf{k}) = \pm\gamma_0\sqrt{1 + 4\cos\left(\frac{\sqrt{3}k_x a}{2}\right)\cos\left(\frac{k_y a}{2}\right) + 4\cos^2\left(\frac{k_y a}{2}\right)}\,, \tag{6.1}$$

with $\gamma_0 \approx 2.9$eV (Fig. 6.2a). The first Brillouin-zone has a hexagonal shape (Fig. 6.2b) with the two bands touching at its edges. The two electrons per unit-cell, that are left after filling the σ-bonding bands, completely fill the lower band (at zero temperature). Therefore, the chemical potential lies exactly at $\mu = 0$ for undoped graphene[1]. The σ-bonding and σ-anti-bonding bands are energetically well separated ($\approx \pm 4$eV) which is the reason why usually only the π-bands are taken into account in transport calculations.

A remarkable property of the two π-bands is that they are touching at the K- and the K'-points in the Brillouin-zone (Fig. 6.2a). In the area around these special points, the dispersion relation has the shape of two cones touching at their tips. In the area around each of these points one can describe the system with an effective Hamiltonian that has the same shape as the Dirac-Hamiltonian from relativistic quantum mechanics and the electrons behave as particles with zero rest-mass. This has been the subject of extensive research as it poses a well controlled test-case for relativistic effects emerging from the Dirac equation, even winning Geim and Novoselov the Nobel price in 2010 [88–90].

6.1.2 From graphene to carbon-nanotubes

Carbon-nanotubes (CNTs) are carbon-structures resembling cylinders. Their diameter is of the order of nm while the length can range from several nm to several μm. Most

---

[1] Due to particle-hole symmetry this obviously also holds for finite temperature.

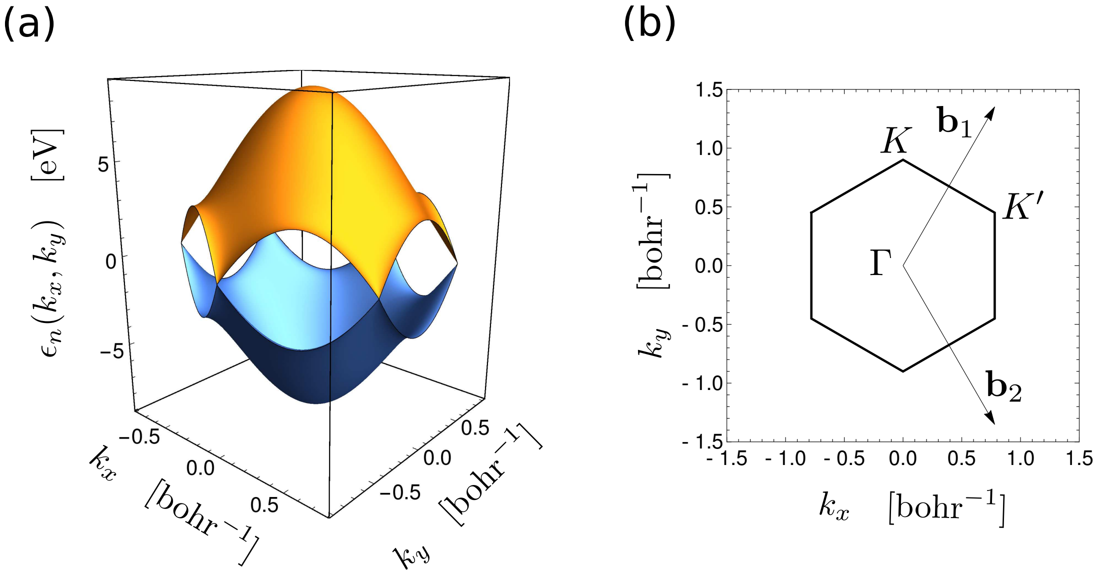

Figure 6.2: (a) Dispersion relation $\epsilon(k_x, k_y)$ of the two π-bands around the Fermi-level calculated within the tight-binding approximation with next-neighbor hopping. (b) Hexagonal first Brillouin-zone of graphene including the reciprocal lattice vectors $\mathbf{b}_1$ and $\mathbf{b}_2$.

production processes easily lead to CNTs that are much longer than their diameter, hence they can be seen as quasi-one-dimensional materials. A CNT is essentially a rolled graphene-sheet. Therefore, the physical properties of carbon-nanotubes can be deduced on an approximate level from graphene. To produce a physically stable CNT, the graphene must be rolled in such a way that the honey-comb structure smoothly covers the surface of the (fictive) cylinder it is rolled on. Hence, one can classify a CNT by its so-called chiral vector $\mathbf{C}_h$ which is a vector that points from the origin of one graphene unit-cell to the origin of another one (Fig. 6.3). It is defined as $\mathbf{C}_h = n\mathbf{a}_1 + m\mathbf{a}_2$ where $n, m \in \mathbb{N}_0$. In order to make the integer set (n, m) unique, the convention is that $n \geq m$. A certain type of cabon-nanotubes is then called (n, m)-CNT. The CNT can be constructed, at least theoretically, by rolling the graphene in the direction of $\mathbf{C}_h$. The circumference of the tube must be $|\mathbf{C}_h|$ which is equivalent to requiring that the graphene honey-combs smoothly cover the whole cylinder surface. Depending on the integers (n, m) that specify the carbon-nanotubes, we can group them into three classes, the armchair- $(n = m)$, zigzag- $(m = 0)$ and chiral- $(n \neq m \neq 0)$ tubes.

When we draw a vector in the graphene sheet that is orthogonal to the chiral vector and points from the origin of the chiral vector to the next nearest origin of another unit-cell we obtain the so-called translational vector $\mathbf{T}$. It points into the longitudinal direction of the carbon-nanotube and its length is the CNT unit-cell size, i.e. the lattice constant $a_{\mathrm{CNT}} = |\mathbf{T}|$.

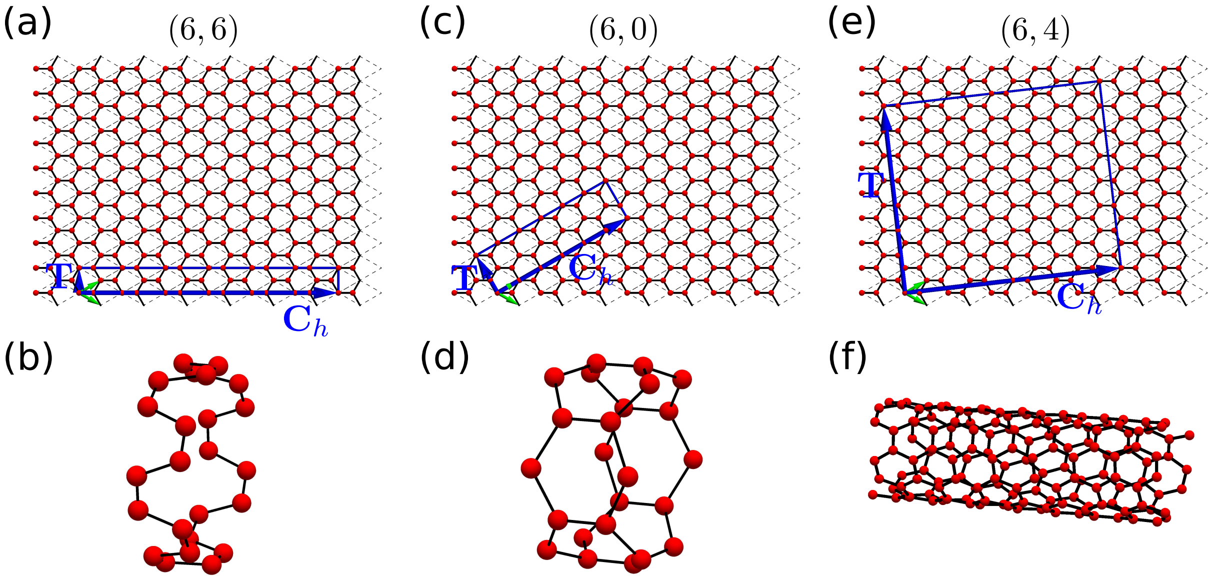

Figure 6.3: Graphene sheets with the chiral- ($\mathbf{C}_h$) and translational- ($\mathbf{T}$) vectors and the corresponding CNT unit-cells for the (a),(b) armchair-, (c),(d) zigzag- and (e),(f) chiral-CNTs.

In order to understand the physics of CNTs we can treat them in an approximate sense as graphene-sheets with Born-von Karman boundary conditions in the direction of the chiral-vector. Those graphene-quasi-particle states that fulfill the boundary-conditions, namely those with $\psi_{n,\mathbf{k}}(\mathbf{r}+\mathbf{C}_h) = \psi_{n,\mathbf{k}}(\mathbf{r})$, are also proper quasi-particle states of the carbon-nanotube. As the states also fulfill the Bloch-theorem we get

$$\psi_{n,\mathbf{k}}(\mathbf{r}+\mathbf{C}_h) = e^{i\mathbf{C}_h\cdot\mathbf{k}}\psi_{n,\mathbf{k}}(\mathbf{r}) \overset{!}{=} \psi_{n,\mathbf{k}}(\mathbf{r}) \ . \tag{6.2}$$

Eq. (6.2) implies that momentum $\mathbf{k}$ must fulfill the condition

$$2\pi z = \mathbf{C}_h \cdot \mathbf{k} \equiv |\mathbf{C}_h| k_\perp \quad \rightarrow \quad k_\perp = \frac{2\pi}{|\mathbf{C}_h|} z \ , \tag{6.3}$$

where z is an arbitrary integer. This means that only certain values are allowed for the momentum parallel to the chiral vector ($k_\perp$). We can define the so-called cutting lines,

$$\mathbf{L}_z(k) \equiv k\frac{\mathbf{T}}{|\mathbf{T}|} + \frac{2\pi}{|\mathbf{C}_h|} z \frac{\mathbf{C}_h}{|\mathbf{C}_h|} \tag{6.4}$$

where the $\mathbf{L}_z(\cdot)$-lines describe all valid momenta of graphene-eigenstates that fulfill the CNT boundary conditions. The momentum k is the momentum in the longitudinal direction of the carbon-nanotube, i.e. it is equivalent to the electron-momentum in a $1D$-picture.

Die approbierte gedruckte Originalversion dieser Dissertation ist an der TU Wien Bibliothek verfügbar.
The approved original version of this doctoral thesis is available in print at TU Wien Bibliothek.
TU Bibliothek WIEN Your knowledge hub

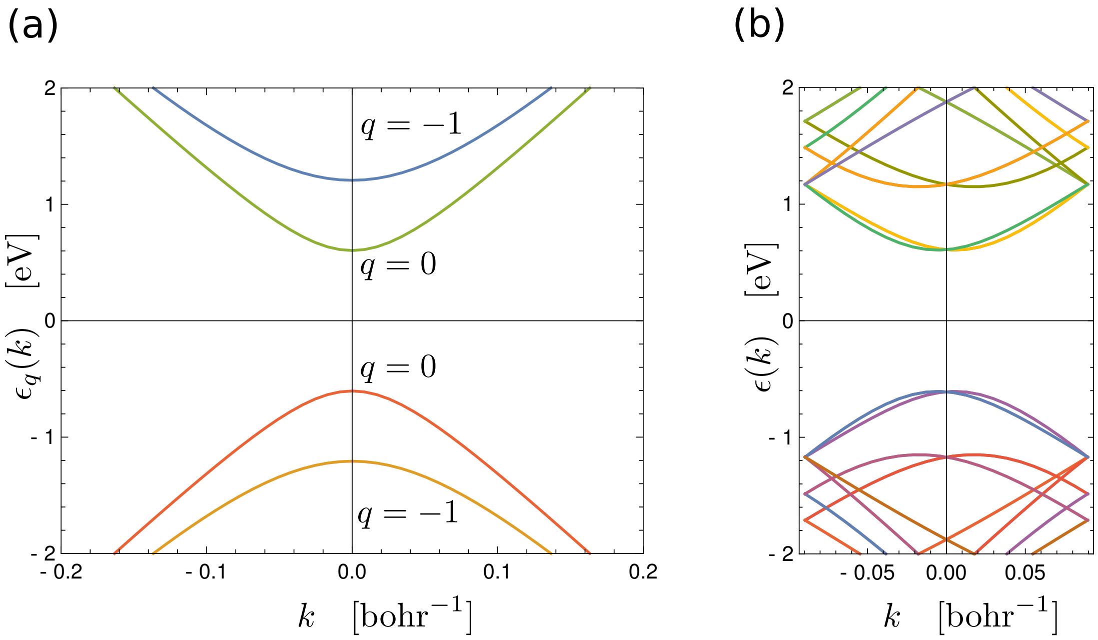

Figure 6.4: Band-structure of (6,4)-CNTs. (a) Obtained by evaluating the graphene band-structure (see Eq. (6.1)) along the cutting lines in the vicinity of one cone (see Eq. (6.5)) and (b) from the full application of the zone-folding scheme (including the bands stemming from both cones). Note that the momentum k in (a) and (b) is not equivalent.

The graphene band-structure around the Fermi-level resembles cones. Depending on the chiral vector (i.e. the type of CNT), the carbon-nanotube is either metallic (when there is a $\mathbf{L}_z(\cdot)$-line cutting through the center of the cones) or semi-conducting (when no $\mathbf{L}_z(\cdot)$-line is cutting through the center of the cones).

The electrons in metallic carbon-nanotubes cannot be described by a straightforward Boltzmann treatment using the bands obtained in this way. The reason is that the dispersion relation at the Fermi-level is linear which leads to perfect nesting in Boltzmann scattering. This means, that the expression for the scattering diverges as the first-order time-dependent perturbation theory used in the derivation of the Boltzmann scattering term is not sufficient any more. In order to describe the dynamics in such a case, we need to use different quasi-particles as fundamental excitations. In case of metallic CNTs the electrons around the Fermi-level cannot be described as independent quasi-electrons (as in Fermi-liquid theory), but as so-called Tomonaga-Luttinger liquid [91, 92]. We will not deal with metallic CNTs within the scope of this thesis.

As already mentioned above, around the Fermi-level the dispersion relation of graphene consists of two double-cones located at $\mathbf{K}$ and $\mathbf{K}'$. They determine the transport properties of graphene, hence, they are also the most relevant part of the dispersion relation for carbon-nanotubes. When we are just interested in the electrons sufficiently close to the Fermi-level, we may approximate the CNT dispersion relation with the graphene dispersion-relation evaluated along the cutting-lines only around the **K** (or equivalently **K**′) position. For semi-conducting carbon-nanotubes, this gives [84]

$$\epsilon_q^{\pm}(k) = \pm\frac{\sqrt{3}a}{2}\gamma_0\sqrt{\left(\frac{2\pi}{|\mathbf{C}_h|}\right)^2\left(q+\xi\frac{1}{3}\right)^2+k^2}\,, \tag{6.5}$$

with the integer $q \in \mathbb{Z}_0$ (Fig. 6.4a) labeling the discrete momenta perpendicular to the tube direction. The factor $\xi = \pm 1$ depends on the type of carbon nanotube. If there exists an integer l so that $n - m = 3l + 1$ it is $\xi = +1$ and if there exists an integer l so that $n - m = 3l - 1$ it is $\xi = -1$. Let us stress, that this approximation only holds in the vicinity of the **K**-point and does not reflect the full carbon-nanotube band-structure.

Here we want to note that there are different representations of the carbon-nanotube band-structures. Depending on the type of CNT, the $1D$ lattice parameter a_{CNT} can be much larger than in graphene, leading to CNT unit-cells that may contain hundreds of carbon atoms (Fig. 6.3f). The size of the $1D$ Brillouin-zone is $\frac{2\pi}{a_{\text{CNT}}}$ which, in turn, is much smaller than in graphene. A proper CNT band-structure within the smaller first Brillouin zone can be constructed by folding the dispersions obtained from graphene, into the small $1D$ Brillouin zone. The full procedure is called zone-folding. Within the scope of this introduction we will not explain this procedure and the different representations here, but refer to Ref. [86]. In the representation obtained by proper zone-folding, the number of emerging bands is much higher compared to the simpler approximation Eq. (6.5) (see Fig. (6.4)b). Many of these bands show degeneracies at the Brillouin-zone boundaries. They are protected by the numerous additional symmetries stemming from the fact that the CNT is composed of a rolled graphene layer that has translational invariance with respect to the smaller graphene lattice vectors. In (chiral) CNTs these translational symmetries become screw symmetries. Additionally, the bands get a non-trivial topology and additional quantum numbers [93]. When the Boltzmann-method is applied to such a band-structure, all these additional quantum-numbers must be conserved in the scatterings leading to very complicated scattering tensors.

For the Boltzmann-method it is more natural to think in terms of the graphene band-structure along the cutting-lines as in Eq. (6.5). Hence, we will stick to these band-structures (Fig. 6.4a) and not use the fully zone-folded bands.

6.1.3 Excitons in carbon-nanotubes

The electronic screening in carbon-nanotubes is weaker than in two- or three-dimensional materials due to their one-dimensional nature. A consequence of the enhanced electron-electron interaction is the occurrence of strong excitonic effects [94–96]. An exciton is a quasi-particle that can be understood as a bound electron-hole pair.

As the exciton is a composite quasi-particle consisting of two particles, its wave function depends on two spatial coordinates. One is associated with the center-of-mass and one with the relative position of the constituents. In a similar way as a hydrogen atom in vacuum, the relative motion of the particles leads to a set of energetically separated orbitals. The center-of-mass motion, however, yields an energetic continuum depending on a continuous center-of-mass momentum. The total energy is then the sum of the orbital energy and the center-of-mass energy. In complete analogy to a free hydrogen atom, the exciton band-structure in CNTs consists of many different bands corresponding to the different orbitals. Their momentum k is associated with the motion of their center-of-mass along the tube. However, in CNTs there are more degrees of freedom [94]. Electrons in any of the conduction bands may bind with holes in any of the valence bands. Additionally, the bands of the electron and the hole may belong both to the $\mathbf{K}$ or the $\mathbf{K}'$ cone of graphene or they may be any combination of both (e.g. the electron stems from a $\mathbf{K}$ conduction band while the hole stems from a $\mathbf{K}'$ valence band). This leads to many exciton-bands with different energetic shapes and different symmetries. Furthermore, depending on the symmetry of the wave function, the spins may form a singlet or triplet state. The exact binding energy of an exciton depends on the type of the carbon-nanotube and the type of exciton, but the order of magnitude is around $E_B \approx 300\text{meV}$ [95].

Only few of the excitons are optically active. The spin is conserved in an optical excitation, hence only spin-singlet excitons can be optically generated. Furthermore, the exciton has to have odd symmetry under reflections about the tube axis to be optically active. An electric field polarized in direction of the tube-axis couples via an operator with odd symmetry about tube-axis reflections to the Hamiltonian of the system. In the absorption process, the exciton is generated, hence, the final state contains one more exciton than the initial state. It is then easy to see, that the transition matrix element between initial and final state is only non-zero if the generated exciton has odd symmetry.

An example of different exciton bands for (6,5)-CNTs can be found in Ref. [96] where the dispersion relations are calculated with the Bethe-Salpeter equation.

6.2 Aligned CNTs as THz emitters

The following section consists mainly of the publication Ref. [83] and its supplementary material (marked by a vertical bar on the left side of the pages). The text and its structure have been slightly modified to better fit the scope of the thesis. The work Ref. [83] was a collaboration with experimentalists who synthesized the sample and performed the measurements while we have done the microscopic modeling, the simulation using our

Boltzmann code and the interpretation of the results.

The advent of modern low-dimensional semiconductor materials has opened up exciting possibilities for developing novel optoelectronic devices, utilizing their uniquely tunable optical properties which arise from unconventional degrees of freedom such as chirality, valley index, layer number, and twist angle. In particular, single-wall carbon nanotubes (SWCNTs) provide ideal one-dimensional (1D) semiconductors whose properties depend on the chirality and diameter [97]. Recent seminal advances in enriching chiralities [98] and achieving alignment [99] on a macroscopic scale promise large-scale applications of SWCNT transistors, light-emitting diodes, and photodetectors. Furthermore, the 1D nature of SWCNTs implies a highly restricted phase space for scattering, which in turn leads to ultrahigh carrier mobilities, suitable for high-frequency devices including terahertz (THz) emitters [8, 9]. Therefore, aligned and single-chirality SWCNT films are promising candidates for attaining electronic, THz, and optoelectronic functions on the same platform.

However, characteristic of low-dimensional semiconductors is their enormously enhanced exciton binding, compared to their bulk counterparts. The typical exciton binding energies of semiconducting SWCNTs exceed 300 meV [95, 97, 100, 101], as compared to 1-10 meV in typical bulk semiconductors. This means that excitons in these semiconductors are very difficult to ionize, casting serious doubt about their abilities to generate THz radiation in response to an external electric field because excitons are charge-neutral particles. Namely, to produce THz radiation efficiently, one needs to photogenerate charged free carriers that can be accelerated by an external field. From this point of view, undoped low-dimensional semiconductors with huge exciton binding energies do not seem to be promising as optically excited THz emitters.

Here, we report on our finding that a photoconductive antenna (PCA) made from a film of aligned single-chirality semiconducting SWCNTs is an unexpectedly efficient THz emitter. Without any optimization, we demonstrate that the produced THz intensities are only one order of magnitude lower than a state-of-the-art GaAs PCA. Furthermore, the CNT-based THz emitter can be easily fabricated on a variety of flexible substrates and is expected to be applied to compact THz analysis systems and wearable optoelectronics. The THz intensity is resonantly enhanced through an interband exciton resonance, indicating the importance of excitons in the THz generation process. To explain these observations, we developed a detailed microscopic model describing the strongly out-of-equilibrium dynamics and complex interplay of free carriers, excitons, photons, and phonons. We took into account all energy and momentum conserving scattering processes with realistic band dispersions. Through this, we shed light on a range of long-standing issues in SWCNT ultrafast dynamics. Importantly, we show

TU Bibliothek Your knowledge hub WIEN
Die approbierte gedruckte Originalversion dieser Dissertation ist an der TU Wien Bibliothek verfügbar.
The approved original version of this doctoral thesis is available in print at TU Wien Bibliothek.

that E_{22} excitons autoionize into free carriers right after the laser excitation. We find multiexciton generation through exciton impact generation to be efficient at high bias. This process explains the nonlinear bias dependence of the simultaneously measured DC photocurrent.

6.2.1 The experiment

We fabricated a dipole-type PCA structure (Fig. 6.5a) on top of a highly-aligned and chirality-enriched (6,5) SWCNT film deposited on a sapphire substrate (for more details see Supplementary Material of Ref. [83]). The nanotube alignment direction was aligned with the dipole gap during the fabrication process, so the applied DC electric field was parallel to the nanotube alignment direction (Fig. 6.5a). The electrodes attached on the PCA structure were used to apply the DC bias and to measure the generated photocurrent at the same time (Fig. 6.5a). A separate low-temperature (LT)-GaAs PCA switch was used to detect the generated THz radiation in a transmission configuration (Fig. 6.5a). We used an optical parametric oscillator as the wavelength-tunable excitation source or pump.

We excited the aligned SWCNTs around the E_{22} exciton resonance for (6,5) SWCNTs. Despite the fact that uncharged excitons are excited, a strong THz signal immediately appeared (Fig. 6.5b). The THz signal reversed its sign when the polarity of the applied biased was switched, confirming that the THz radiation is associated with a transient current parallel to the SWCNTs. We then probed the dependence of both THz emission and photocurrent on the pump laser photon energy (Fig. 6.5c), as well as its polarisation (Fig. 6.5d). Both closely follow the behavior of the E_{22} exciton absorption, which peaks at 2.14 eV and gets excited only by light polarized parallel to the nanotube axis. This further confirms that the THz generation process is initially triggered by the generation of excitons.

Figure 6.6a and 6.6b show the THz emission amplitude, as well as its spectrum, for our SWCNT device relative to that of a LT-GaAs-based PCA. After considering the losses due to absorbance and reflectance (see Supplementary Material of Ref. [83]), the emission efficiency (per thickness and absorbed power) of the SWCNT-based PCA is comparable within an order of magnitude to that of the LT-GaAs PCA. This is an excellent achievement for a prototype unoptimized device compared to the well-established THz emitter based on a conventional LT-GaAs PCA.

We also carried out pump-intensity- and bias-dependent measurements. At a fixed pump intensity, both THz amplitude and photocurrent showed direct proportionality to

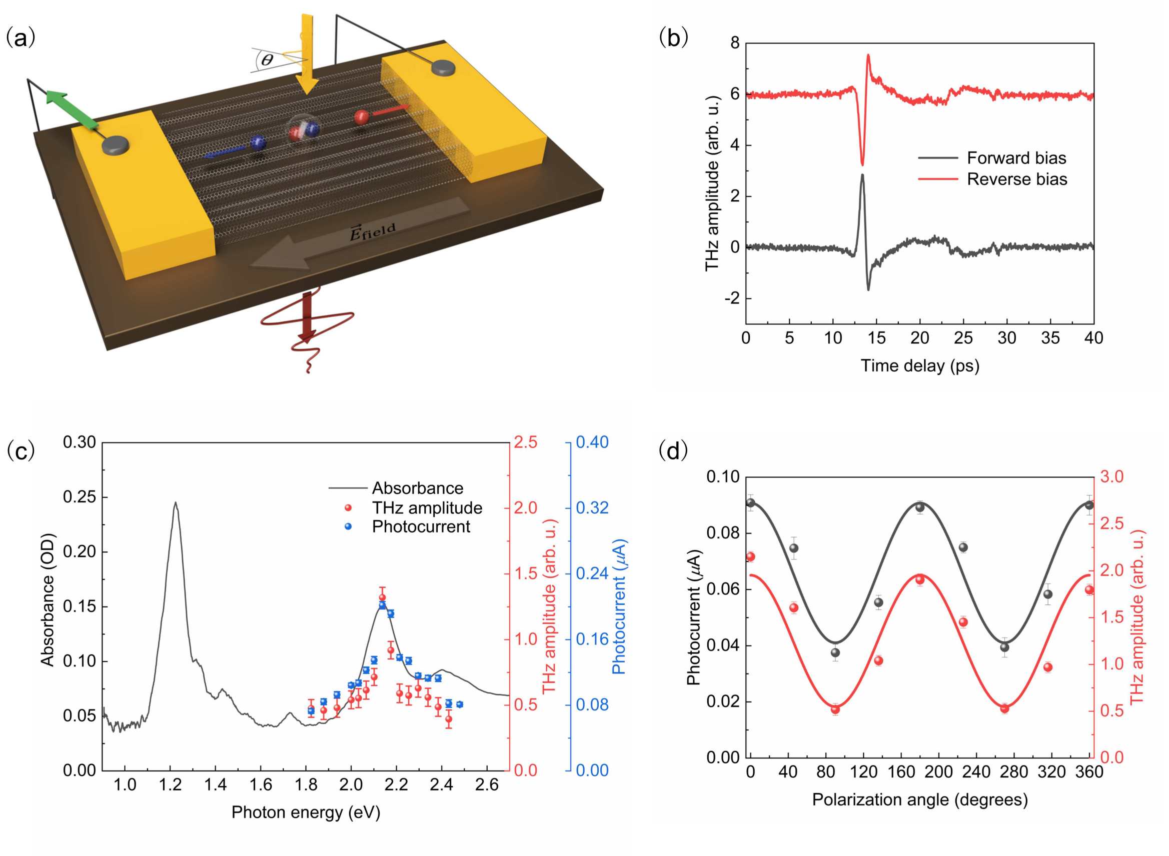

Figure 6.5: Schematic diagram of (a) CNT-based photoconductive antenna switch and experimental set-up. The CNTs are aligned with the direction of applied electric field. (b) THz emission waveforms at forward and reverse biases. (c) Absorbance spectrum for (6,5) CNT film plotted with the THz emission amplitude (red spheres) and photocurrent (blue spheres) as a function of photon energy. (d) THz amplitude and photocurrent as a function of angle between excitation femtosecond (fs) laser polarization and CNT alignment.

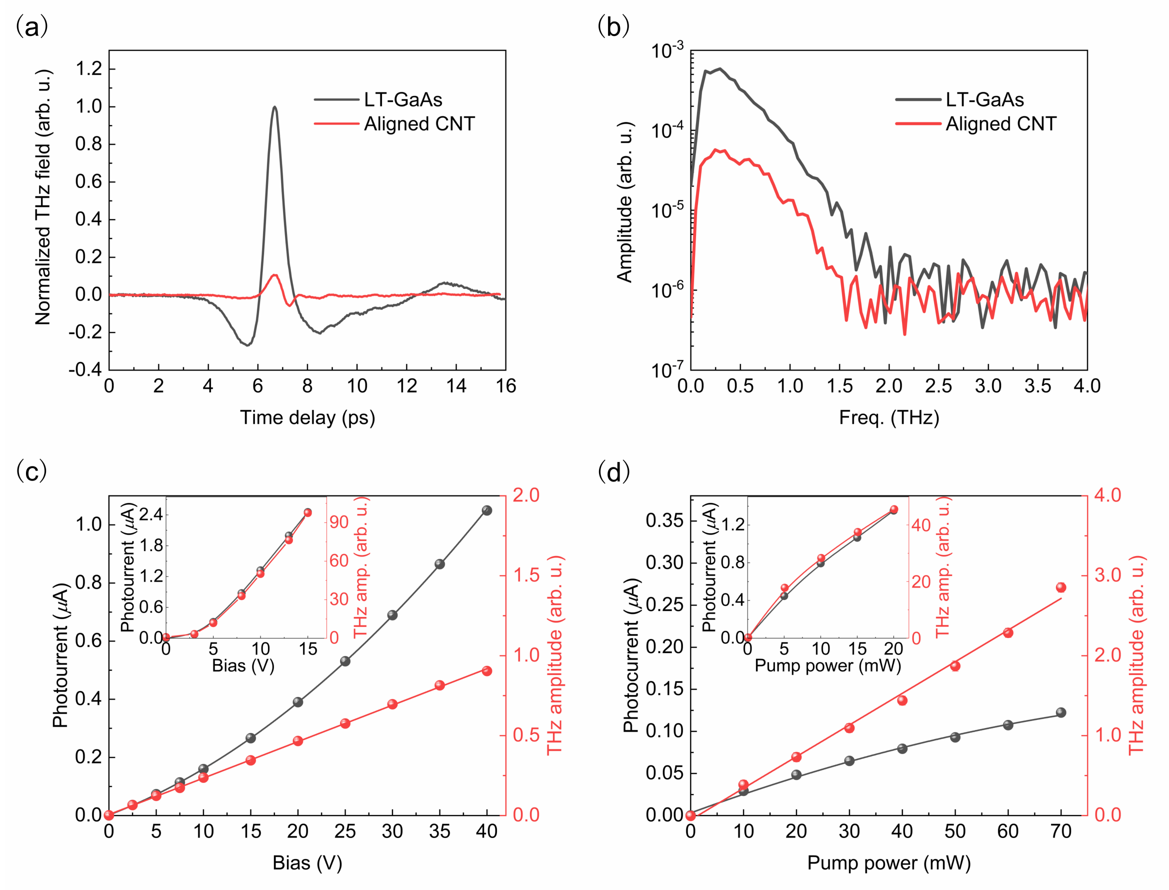

Figure 6.6: Relative THz emission from CNT-based PCA and LT-GaAs-based PCA in (a) time and (b) frequency domains. Bias (c) and pump power (d) dependence of photocurrent and THz emission from CNTs compared to same data from LT-GaAs-based PCA (insets).

the absorbance, with no apparent changes in the THz waveforms and spectra (see Supplementary Material of Ref. [83] for details). However, we observed striking differences between THz emission and photocurrent in their pump power and bias dependences. As shown in Fig. 6.6c and 6.6d, the THz amplitude shows a linear dependence on both the pump power and bias, whereas the photocurrent saturates at high pump powers and increases superlinearly with the bias. This is in direct contrast with the LT-GaAs device wherein both THz emission and photocurrent always show the same behavior. This difference in the bias dependence of THz and photocurrent suggests the emergence of new mechanisms for generating charged carriers in SWCNTs compared to typical PCAs.

6.2.2 The microscopic model

Quasiparticle-bandstructures

To provide a microscopic picture, we need to be able to accurately study the thermalization dynamics of several types of quasiparticles (electrons, excitons, photons, and phonons) within realistic band structure and in the presence of an external electric field. Describing the thermalization dynamics is particularly challenging: it requires full computation of far out-of-equilibrium scattering processes. The most critical complication is the precise accounting of energy and momentum selectivity of scattering events, which become exceptionally restrictive in 1D, and lead to critical deviation from typical Fermi liquid behaviors. Commonly used approximations [102–105] either irreparably break the predictive power over the thermalization dynamics, particularly the ability to describe metastable states and many-timescales dynamics, or only allow for lower order processes.

We explicitly treated four electron bands [84], three phonon [106]/defect bands (ac: acoustic phonon, op: optical phonon, Imp: impurity/defect), three exciton bands [94,95], and a photon band (see Fig. 6.7a).

For the exciton bands we take the dispersions from Ref. [94]. To contain the numerical cost, we include the lowest energetic, bright E_{22} mode (E_{22}), the lowest energetic, bright E_{11} mode (E_{11}) and the lowest energetic, dark singlet E_{11} mode (dE_{11}). Since [94] does not provide absolute energies, but relative positions to the E_{11} Γ-point, we place the bottom of both the E_{11} and E_{22} exciton bands by fitting with our experimental absorption spectrum (Fig. 6.5c).

For the electron bands we include two valence (e_1, e_2) and two conduction (e_3, e_4) bands, and we use the tight-binding dispersion-relations of graphene within the zone-folding approximation [107]. The energetic position of the electron bands is deduced from the position of the exciton bands and the exciton binding energy $E_B = 0.37\text{eV}$ [95]. That is at the Γ-point the bands are chosen such as $\epsilon_{e_4}(0) - \epsilon_{e_1}(0) = \epsilon_{E_{22}}(0) + E_B$ and $\epsilon_{e_3}(0) - \epsilon_{e_2}(0) = \epsilon_{E_{11}}(0) + E_B$.

Carbon-nanotubes have a variety of different acoustic and optical phonon modes [106]. In order to keep the computational cost manageable we only use two phonon bands, one acoustic (ac) resembling the 2nd A-branch of Fig. 3 in Ref. [106] and one optical (op), Einstein-like phonon with an energy of $\epsilon_{\text{op}} = 0.1\text{eV}$. Additionally one flat phonon-like band at zero energy (Imp) is used to mimic the effect of impurities.

6.2.3 Scattering processes and amplitudes

We took into account fifty two scattering channels, including both three-leg scatterings (i.e., two particles in and one out) and four-leg scatterings (i.e., two particles in and two out, or three in and one out), as shown in Fig. 6.7c. Within the Boltzmann equation, we also took account of the fact that quasiparticles are subject to an external electric field due to the bias, which induces an acceleration proportional to the quasiparticle charge. The electric field E is calculated from the external voltage U with $E = \frac{U}{l\epsilon}$ with the length of the CNT sample $l = 6\ \mu m$ and the dielectric constant $\epsilon = 2$.

Due to the lack of spatial resolution at this stage of implementation of the numerical solver, the physical extraction of accelerated quasiparticles from the SWCNTs into the metallic leads was included via an effective population decay term.

The 52 scattering processes (TABLE 6.1) can be grouped into 5 families, including all possible combinations of band indices. Below we briefly discuss each type of scattering.

Laser

We treat the laser excitation within the Boltzmann-scattering framework. The direct excitation (one photon absorbed and one exciton created) is a 2-leg process which has a 0 dimensional phase space for 1D systems (this does not happen in higher dimensions). This means that the excitation is allowed to happen only at exactly one k, and cannot contribute to a finite change in exciton number. Therefore the leading order must be a 3-leg process: specifically, we use a three-leg process where one photon is destroyed and one exciton plus an excitation in the impurity-band is generated. This is equivalent to an absorption process where momentum conservation is broken.

To simulate the effect of a laser pulse we assume a constant photon distribution $f_{h\nu}(k) = \alpha \left(\mathrm{Exp}[-\frac{(k-k_m)^2}{2\sigma^2}] + \mathrm{Exp}[-\frac{(k+k_m)^2}{2\sigma^2}]\right)$ with $k_m = 3.5667 \times 10^{-5}$ bohr^{-1} and $\sigma = 1.6667 \times 10^{-6}$ bohr^{-1}. For numerical convenience we apply the time profile to

Laser-absorption	Autoionization	Electron-phonon	Exciton-phonon	Exciton impact-gen
$E_{22} + Imp \leftrightarrow h\nu$	$e_1 + E_{22} \leftrightarrow e_3$	$e_1 + ac \leftrightarrow e_1$	$E_{11} + ac \leftrightarrow E_{11}$	$e_2 + Imp + dE_{11} \leftrightarrow e_2$
	$e_2 + E_{22} \leftrightarrow e_3$	$e_1 + op \leftrightarrow e_1$	$E_{11} + op \leftrightarrow E_{11}$	$e_3 + Imp + dE_{11} \leftrightarrow e_3$
	$e_2 + E_{22} \leftrightarrow e_4$	$e_2 + ac \leftrightarrow e_2$	$dE_{11} + ac \leftrightarrow dE_{11}$	$e_3 + Imp + dE_{11} \leftrightarrow e_4$
	$e_1 + E_{11} \leftrightarrow e_3$	$e_2 + op \leftrightarrow e_2$	$dE_{11} + op \leftrightarrow dE_{11}$	$e_1 + Imp + dE_{11} \leftrightarrow e_2$
	$e_2 + E_{11} \leftrightarrow e_3$	$e_3 + ac \leftrightarrow e_3$	$E_{22} + ac \leftrightarrow E_{22}$	$e_2 + Imp \leftrightarrow dE_{11} + e_2$
	$e_2 + E_{11} \leftrightarrow e_4$	$e_3 + op \leftrightarrow e_3$	$E_{22} + op \leftrightarrow E_{22}$	$e_3 + Imp \leftrightarrow dE_{11} + e_3$
	$e_1 + dE_{11} \leftrightarrow e_3$	$e_4 + ac \leftrightarrow e_4$	$E_{11} + ac \leftrightarrow dE_{11}$	$e_4 + Imp \leftrightarrow dE_{11} + e_3$
	$e_2 + dE_{11} \leftrightarrow e_3$	$e_4 + op \leftrightarrow e_4$	$E_{11} + op \leftrightarrow dE_{11}$	$e_2 + Imp \leftrightarrow dE_{11} + e_1$
	$e_2 + dE_{11} \leftrightarrow e_4$	$e_1 + ac \leftrightarrow e_2$	$dE_{11} + ac \leftrightarrow E_{11}$	
		$e_2 + ac \leftrightarrow e_1$	$dE_{11} + op \leftrightarrow E_{11}$	
		$e_1 + op \leftrightarrow e_2$	$E_{22} + ac \leftrightarrow E_{11}$	
		$e_2 + op \leftrightarrow e_1$	$E_{22} + op \leftrightarrow E_{11}$	
		$e_3 + ac \leftrightarrow e_4$	$E_{11} + ac \leftrightarrow E_{22}$	
		$e_4 + ac \leftrightarrow e_3$	$E_{11} + op \leftrightarrow E_{22}$	
		$e_3 + op \leftrightarrow e_4$	$E_{22} + ac \leftrightarrow dE_{11}$	
		$e_4 + op \leftrightarrow e_3$	$E_{22} + op \leftrightarrow dE_{11}$	
			$dE_{11} + ac \leftrightarrow E_{22}$	
			$dE_{11} + op \leftrightarrow E_{22}$	

Table 6.1: All 52 scattering processes grouped into five families as described in the text.

the scattering-amplitude $w^{E_{22}\,+\,Imp\,\leftrightarrow\,h\nu}(t) = \text{Exp}[-\frac{(t-t_c)^2}{2{\sigma_t}^2}]$ (for the center-time we use $t_c = 0.5ps$ and for the temporal broadening $\sigma_t = 0.1$ps). These parameters correspond to a laser center-frequency of $\hbar\omega = 2.14$eV and an energetic broadening of $\sigma_{en} = 0.1$eV. As amplitude we choose $\alpha = 10^{-3}$ a.u. which produces a small number of excitons.

We do not include the generation of free electron-hole pairs by laser absorption.

Exciton autoionization

An exciton can break up into an electron and a hole, for instance $E_{11} \leftrightarrow e_3 + h_1$. However since we treat all the bands within the electronic picture and we do not directly describe holes, the hole generated by the exciton autoionization process has to be written as an electron removal in the valence band, i.e. $e_1 + E_{11} \leftrightarrow e_3$.

The time reversed process of exciton autoionization is the binding of an electron and a hole into an exciton. As we are studying small excitations (to preserve the validity of the approximate statistical factor for excitons) and the case of chemical potential in the middle of the bandgap (see more later), such processes becomes negligible, as they are quadratic in the excitation density.

Ref. [108] reports that the dissociation of E_{22} excitons into free carriers competes with exciton-thermalization, which means that they must act on similar timescales. Their ratio controls the ratio of produced free carriers and produced E_{11} and dE_{11} excitons. We have chosen an exciton autoionization scattering amplitude ($w = 9.3 \times 10^{-6}$ a.u.) that leads to an autoionization lifetime of 0.1ps. With this strength ratio, each laser excited E_{22} exciton generates around 0.6 low energy excitons and 0.4 free electrons. This ratio is the free carrier yield of the laser excitation, which does not influence the qualitative picture of our results, but simply the absolute values.

Electron-phonon scatterings

Electron-phonon scatterings are fundamental as they lead to momentum dissipation (otherwise the electric field would indefinitely accelerate carriers). We include all scattering combinations among the bands that are energetically allowed. Notice that scatterings like $e_1 + ac \leftrightarrow e_2$ are not the time reversal to $e_2 + ac \leftrightarrow e_1$ and both must be explicitly included.

It is difficult to find data to estimate the scattering lifetime of electrons in semiconducting carbon nanotubes, as most of the experiments probe the excitonic system. In Ref. [109] they estimate that the most effective electron-phonon scattering leads to an electron lifetime of around 50fs, irrespectively on the metallicity or non-metallicity of the CNTs. We hence use a scattering amplitude that leads to an average electron-phonon scattering lifetime of 50fs ($w = 4.84 \times 10^{-6}$ a.u.).

Exciton-phonon scatterings

Exciton-phonon scatterings are included following similar considerations as in the case of electron-phonon scatterings.

The decay of E_{22} excitons to the bottom of the E_{11} and dE_{11} excitonic bands happens through exciton-phonon scatterings. Ref. [110, 111] reports a decay rate of excited E_{22} excitons of the order of one to two hundred femtoseconds, and a similar timescale for the transfer of population to low energy excitonic states E_{11}. This is comparable to experimental results in Ref. [112]. We use exciton-phonon scattering amplitudes ($w_{op} = 60.5 \times 10^{-6}$ a.u. for optical phonons) which leads to exciton scattering with one phonon every around 40fs. It requires around ten scatterings to dissipate the energy difference E_{22}-E_{11}, leading to a thermalisation time of around 400fs. We use a weaker scattering amplitude for acoustic phonons ($w_{ac} = 4.84 \times 10^{-6}$ a.u.) to reduce numerical cost. They have anyhow a minor effect (they merely smooth the spikes in the excitonic population). Note that these scattering amplitudes should be interpreted as rescaled scattering amplitudes, since we are explicitly considering fewer excitonic bands compared to real CNTs.

Impurity assisted exciton impact generation

Electrons accelerated to high energies can scatter, lose energy and create an exciton in the process. Such exciton impact generation can be the effect of a number of slightly different scattering channels. We found that the direct process is not allowed due to simultaneous energy and momentum conservation, in agreement with Ref. [113]. In Ref. [113] they propose impact generation facilitated by a previous electronic transition into a higher energetic band. We here propose a direct impurity (or phonon) assisted transition. The impurity/phonon acts as a breaking of the momentum conservation making impact-excitation allowed as soon as energetically possible. Such process has a larger phase space compared to the one proposed in Ref. [113]. However we warn against making conclusions on the precise scattering channel for exciton impact generation, since our simulations would provide qualitatively similar results for both alternative hypotheses (assuming the scattering amplitudes are properly rescaled). We include only the processes that generate excitons in the dE_{11} band, as it is the most relevant band due to its lowest energy and largest phase-space for the process. Our simulations show that direct exciton impact generation into higher energy exciton bands have importantly smaller phase space and negligibly contribute to the population dynamics compared to other processes like scattering with phonons.

The strength of this process controls the ratio between the non-linear vs linear component in the photocurrent in our calculations. In Ref. [113] they calculate the life-time due to impact exciton generation and show that it varies on several orders of magnitude. It plateaus around 0.1-1ps and several values are also around 2fs. The scattering rate ($w_{ac} = 48.4 \times 10^{-6}$ a.u.) has been chosen such as one electron with energy above the threshold generates one exciton by impact generation approximately every 1ps in agreement with the majority of the data shown in Ref. [113].

We report that we have found that the semi-quantitative theoretical behavior of the dynamics for both unbiased (to be compared to older experimental results) and biased (to be compared to the experimental results in this work) CNTs closely follows experimental results even if we moderately modify the scattering rates used in this work. Apart from testing variations of the parameters, we have not attempted a proper fitting due to the numerical cost. This proves that the proposed scenario is robust with respect to its parameters in explaining a rather large range of experimental findings.

Electron-electron scatterings

Similarly to the case of binding of free carriers into excitons, electron-electron scatterings are quadratic in the excitation density, negligibly contribute to the thermalisation, and have not been included in the presented numerical calculations.

6.2.4 Details of the simulation

Carrier extraction from CNTs

As mentioned above we are not explicitly describing the spatial distribution of quasi-particles. Nevertheless the extraction of carriers from the CNTs into the metallic leads plays an important role in the switching off of the current. Moreover a single electron can only perform few exciton impact generations before being removed from the system. We model this process with a decay term of the free carriers populations

$$\left(\frac{\partial f_n(k)}{\partial t}\right)_{\text{extr.}} = -\frac{1}{\tau_{\text{extr.}}}\left(f_n(k) - f_{n-eq.}(k)\right) \quad n \in \{e_1, \dots, e_4\} \tag{6.6}$$

where $\tau_{\text{extr.}}$ is the characteristic time the electron stays in the carbon-nanotube and $f_{n-eq.}(\cdot)$ is the equilibrium distribution of band n, i.e. the initial distribution.

The maximum velocity in our carbon nanotubes is approximately $v_{max} \approx 1\mu\text{m/ps}$. The length of CNTs is of the order of μm, hence, it takes a carrier in the middle of a tube around 1ps to reach the end or the leads and be able to recombine when moving at maximum speed. However in reality the electrons would take longer to reach the end of the CNTs due to scatterings. We use an extraction time $\tau = 5\text{ps}$ to mimic this timescale.

Notice that an alternative scenario to the switching off of the current can be envisioned. Carriers could also recombine at the CNT's edge. Thanks to the trapping at the defect that is the edge of the CNT, electrons and holes can come closer together and more easily recombine. If that happens the carriers do not need to reach the edge of the sample, but just the edge of the CNT they are generated in. This implies that the switching off of the current would happen more or less 5 times faster. Notice that this would make the negative peak following the main positive one in the theoretical data in Fig. 6.8a five times narrower and 5 times higher leading to a better fit of the experiments. However, we decided to not include this latest scenario in our treatment, even if it would have made the comparison better. The reason is that the discrepancy could as well be explained simply by the detector's response. Therefore, we felt

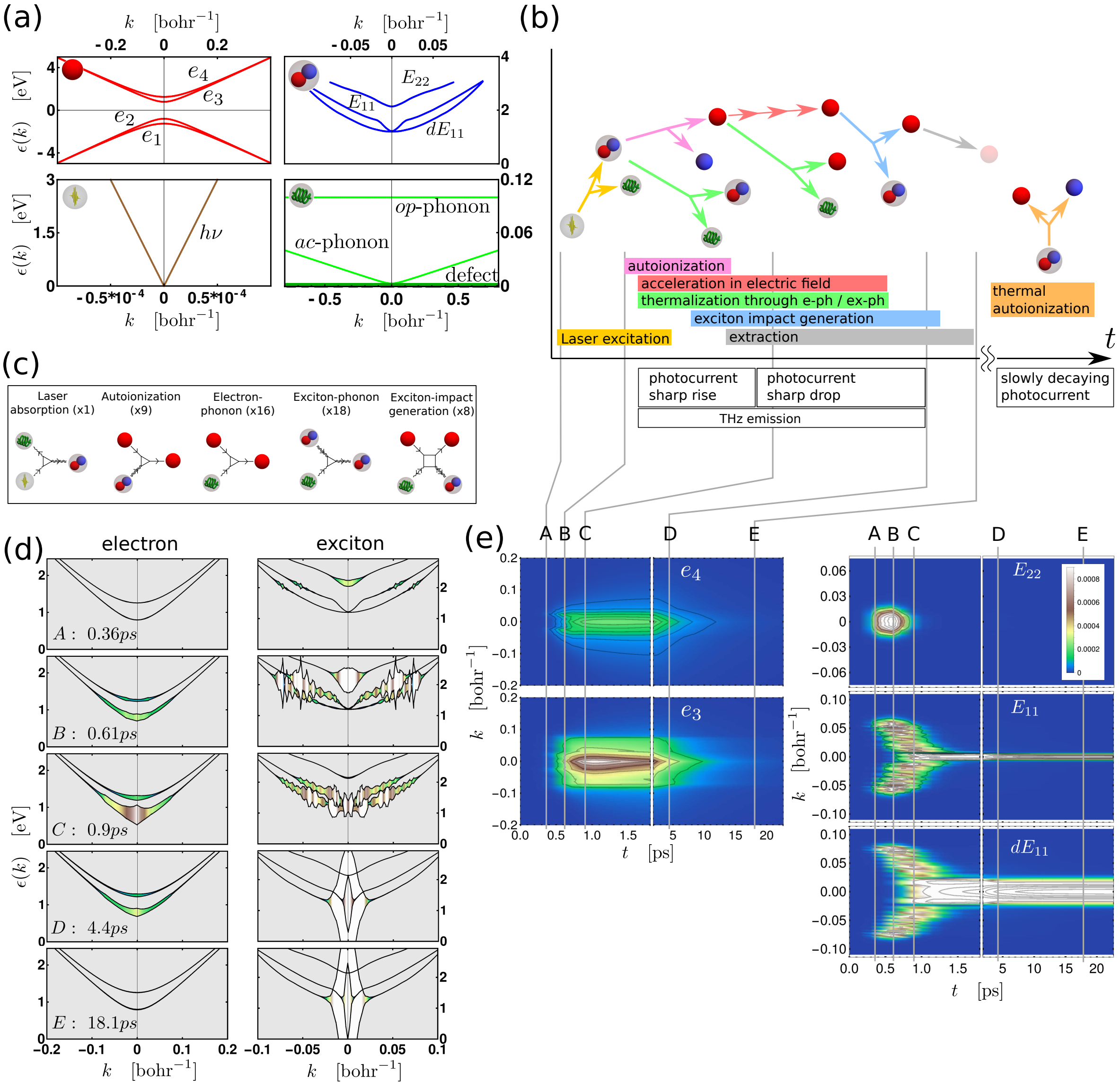

Figure 6.7: (a) Dispersions of the bands of all the included quasiparticles. (b) Qualitative description of the most influential scattering processes at different timescales. (c) Schematic representation of all the types of the 52 scatterings included in the modeling. (d) Time snapshots of the populations displayed over the dispersion: the thickness of the color bar as well as its colorscale represent the $k-$resolved population. The time propagation of the population in the remaining bands is calculated but not shown here. (e) Band resolved density plot of the quasiparticle population $f_n(k, t)$ for two of the electronic bands and all the excitonic bands.

Die approbierte gedruckte Originalversion dieser Dissertation ist an der TU Wien Bibliothek verfügbar.
The approved original version of this doctoral thesis is available in print at TU Wien Bibliothek.
TU Bibliothek Your knowledge hub WIEN

we do not have enough support from the experiments to make a reliable statement on that microscopic mechanism and we opted to include only the simplest and more straightforward scenario (recombination at the metallic leads).

Initial configuration

For the initial setup we choose Fermi-Dirac distributions for the electron-bands $e_{1\ldots4}$ with $\mu = 0$ and $\beta = 35\text{eV}^{-1}$ ($T \approx 330\text{K}$). A temperature higher than room temperature has been chosen, since, even if the experiments are done at room temperature, it is expected that the sample will heat up during the excitation process. Nonetheless our numerical simulations show a negligible effect of temperature on the dynamics.

For the two phonon-bands we choose Bose-Einstein distributions with the same μ and β as the electrons. As we are only describing two phonon bands we keep their distribution-function fixed for the whole simulation time in order to account for the higher lattice heat capacity.

We have treated impurities as a phonon-band. However it can be shown that to produce the proper statistical factor for impurity scattering, we have to impose a distribution-function $f_{Imp} = 0$. This impurity distribution-function is kept zero for the whole simulation.

Calculation of THz radiation

For a 1D-system the electric current is calculated within the Boltzmann-framework with

$$I(t) = \frac{1}{2\pi} \sum_{n=e_1}^{e_4} \int \mathrm{d}k \frac{\partial \epsilon_n(k)}{\partial k} q_n f_n(k,t) \ . \tag{6.7}$$

It can be shown that a time-dependent current emits radiation with an electric field that is proportional to the first time-derivative of the current,

$$E_{THz}(t) \propto \frac{\partial I(t)}{\partial t} \ . \tag{6.8}$$

which was used to calculate the THz radiation in the simulation.

6.2.5 Results and comparison of theory and experiment

The schematic diagram in Fig. 6.7b describes the processes occurring at different timescales, and Figs. 6.7d-6.7e show the populations of each band at selected time steps *A*-*E*. The laser excitation generates optically active E_{22} excitons (Fig. 6.7dA). They partially decay through scatterings with phonons [110, 111] into bright and dark

E_{11} excitons with similar energy but larger momentum (Fig. 6.7dB). These quasiparticles are unaffected by the electric field and eventually decay to the bottom of the excitonic bands through scatterings with phonons (Fig. 6.7dC). A fraction of the excitons autoionize into electron-hole pairs in the conduction (valence) bands (Fig. 6.7dB) through spontaneous dissociation [108]. The free carriers are then accelerated by the electric field and shift in k (Fig. 6.7dC), inducing a rapid rise in current, which, in turn, generates THz radiation (Fig. 6.8a). The acceleration in momentum is limited by electron-phonon scatterings [109, 112] (Fig. 6.7dC), which prevent the electronic population from being accelerated indefinitely, simply leading to an asymmetry between positive and negative k in the electronic population. Eventually, the free carriers are physically extracted from the SWCNTs, thermalizing in the metal contacts, leading to a drop in the electron and hole population and therefore a drop in the charge current (Fig. 6.8a).

The simulated THz radiation (Figs. 6.8a) and its spectrum (Figs. 6.8b) are overall in good agreement with the experimental data. The time domain experimental THz signal shows a sharp negative peak directly after the main positive one originating from the switching off of the current. Our theoretical choice of the extraction mechanism leads to a broader and therefore smaller negative peak. At this stage we cannot make a claim on the details of the extraction mechanism since this discrepancy as well as the presence of further side peaks in the experimental THz radiation can be ascribed to suppression of low and high frequency components due to a variety of factors which were not incorporated in the simulations: inherent response of detector [114–116], alignment and the effects of optical components along the THz propagation path from sample to detector [117–120]. All of these could easily distort the actual temporal and frequency profile of THz radiation from the sample. However, to verify the validity of our microscopic picture, we compare the effect of laser fluence (limited to the low fluence regime, see more in supplementary material of Ref. [83]) and bias in the simulated dynamics to the measured ones. The population of the electronic conduction bands within 2 ps after excitation is proportional to the number of absorbed photons, which explains why the THz emission amplitude shows a linear dependence on the pump power. An increase in the bias increases the induced asymmetry of the electronic distribution of both the conduction and valence bands. Since the number of autoionized free carriers is simply proportional to the laser power and not to the electric field, the induced current becomes proportional to the bias. Notice that we can exclude with certainty that the exciton break-up happens through field ionization, as the THz amplitude would, in that case, be superlinear with the bias [121].

What remains still puzzling is the superlinear behavior of the photocurrent with

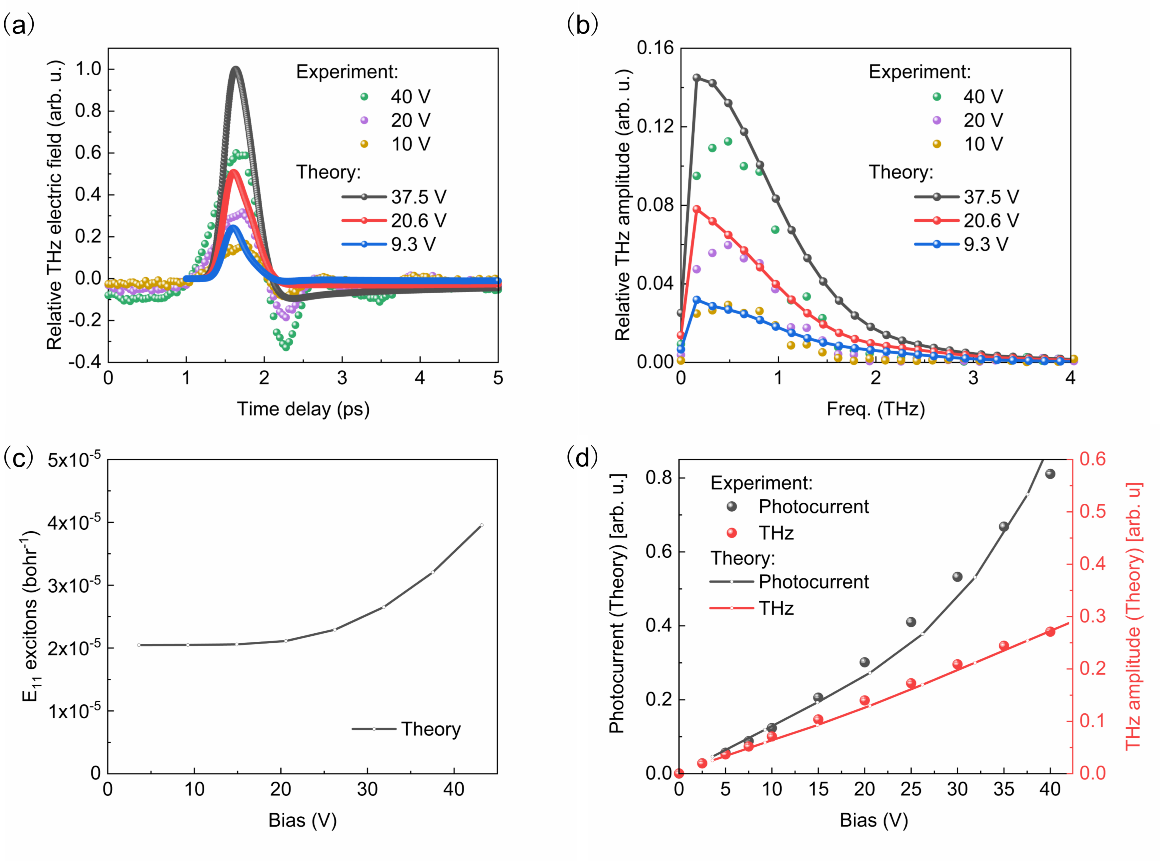

Figure 6.8: Theoretical THz emission in (a) time and (b) frequency domain, compared to experimental measurements for two biases. (c) Number of excitons left in the system at the last simulated time. (d) Comparison the computed peak amplitude of the THz emission and photocurrent with experimental results.

the applied voltage. One is usually tempted to assume the photocurrent and the THz emission to be simply different measurements of the same current, as our LT-GaAs control experiment seems to suggest (see inset in Fig. 6.6c). However, there is a subtle difference between the two measurements: while the photocurrent is able to time integrate all the current generated in the PCA, only high-frequency components are emitted and measured as THz radiation. Therefore, the two techniques provide insight into different timescales. By oversimplifying, one could say that the difference between the photocurrent and THz radiation is the amplitude of low-frequency currents.

The low energy excitons that are left in the system after the dynamics explained above (Fig. 6.7dE) are not subject to the applied bias due to their zero net charge and therefore not accelerated and not subject to an important extraction from the SWCNTs.

They survive at the bottom of the band and require longer times to annihilate through radiative or non-radiative processes (not included in the model). During this time, their high-energy tails will, due to the high temperature, slowly autoionize into free carriers (Fig. 6.7b). These will generate a slow (i.e., low-frequency) electric current, which will not contribute to the THz emission, but will be measured at the electrodes as photocurrent. Such current will be proportional to the product of the number of excitons present in the system at the end of the initial thermalization (time E in Fig. 6.7) and the bias.

At a first sight, such current is expected to be simply linear in the bias. However, a careful analysis of all possible scatterings shows that an important four-leg scattering channel becomes active for electrons with an energy above a certain threshold: exciton impact generation (Fig. 6.8c). An electron can scatter with an impurity (which provides momentum), lose energy, and generate an exciton in the process. Due to energy conservation, this scattering is allowed only for electrons with an energy larger than 1.2 eV above the band bottom. At low electric fields, only a small number of electrons can occupy such high energies. However, as the bias increases, this number grows. These electrons have therefore the chance of creating further excitons compared to the ones generated by the original optical excitation. As a consequence, the number of generated low-energy excitons has one component that is independent of the electric field, and another that instead grows with it (see Fig.6.8c). On a longer timescale (not included in our simulations), a fraction of these eventually autoionize into free carriers, which will again be accelerated by the electric field. Therefore, the photocurrent will be the sum of the picosecond current pulse and a low-frequency current generated by these autoionizing excitons. The low-frequency component of the photocurrent will be proportional to the product of the bias and the number of residual excitons at the end of the thermalization process (which depends partially on the bias itself). This explains the observed superlinear dependence of the amplitude of the photocurrent on the bias (see Fig.6.8d).

Concluding, against expectations because of the large exciton binding energy, we produced a prototype SWCNT-based THz emitter with an efficiency already comparable to commercially available THz emitters. We further performed an unprecedentedly accurate theoretical analysis of the thermalization dynamics in these SWCNTs and explained the microscopic mechanisms behind the dissociation of both high and low energy excitons, free carriers dynamics in an applied electric field, and the conversion mechanisms between different quasiparticles. We identified the critical role of exciton impact generation in the ultrafast dynamics of SWCNTs causing a superlinear dependence of the photocurrent on the bias voltage. Last but not least, our work shows that large-area films of aligned SWCNTs provide an exciting and promising playground for the study and use of the coexistence of positively and negatively charged as well as uncharged quasiparticles, as well as for the development of THz excitonics.

Chapter 7

Conclusion and outlook

The aim of this thesis was to take one step towards a better understanding of non-equilibrium dynamics in solids. Due to the involved nature of thermalization problems, where a complicated interplay of scattering and transport dictates the time-evolution, it is particularly difficult to interpret experimental results. For that purpose one needs microscopic models and numerical simulations of non-equilibrium electron dynamics.

In chapter 2 a brief introduction to the Boltzmann transport equation (BTE) was given. The BTE is seen as one of the standard methods to describe transport and thermalization in solids. We explained the main difficulties of the numerical solution of the BTE, how arbitrary scatterings are described within the Boltzmann framework and the most popular approximations.

In the following chapter 3 a special version of the electron-electron collision operator without momentum conservation was introduced. The predicted thermalization dynamics of a photo-doped Mott-insulator was compared to results of non-equilibrium DMFT. The dynamics predicted by both methods was almost identical. Additionally, the modified Boltzmann method allowed to access the whole thermalization timescale, revealing a transient state. In this intermediate state the two Hubbard bands are occupied according to Fermi-Dirac distributions with the same temperature but different chemical potentials. The numerical implementation of the modified collision operator also served as a first step towards solving the full Boltzmann collision operators.

Chapter 4 was dedicated to the transport part of the BTE. We have introduced the so-called discontinuous Galerkin finite-element method and applied it to the transport problem of a one-dimensional material without scatterings as a test case.

Chapter 5 constitutes the main part of this thesis. A novel numerical method capable of solving the fully momentum, particle and energy conserving collision operator was developed. The collision operator was projected onto a special basis that strongly improves the scaling with the number of basis-functions. Special emphasis was given to the exact conservation of energy, momentum and particle density which is necessary for long-time thermalization simulations. We found, that the exact conservation of these quantities is linked to symmetries in the discretized collision operator. The numerical method enforces these symmetries, leading to a conservation of momentum, energy and particle density up to machine precision. The developed method was implemented and the code was used to simulate the thermalization dynamics of metallic and semi-conducting two-dimensional materials. The method for solving the collision operators was also joined with the code that solves the transport part of the BTE for one-dimensional systems. The spatial resolution and transport in the spatial dimension was neglected for simplicity.

In the final chapter 6 the unified transport-plus-collision code was used to describe a real non-equilibrium experiment with semi-conducting carbon-nanotubes. In the experiment a sample of aligned nanotubes was irradiated with a femtosecond laser pulse while a voltage was applied simultaneously. It was found that this setup emits terahertz radiation. Its amplitude increased linearly with the voltage while the measured photocurrent increased super-linearly. Due to the simulations performed with the developed code we were able to understand the experimental findings on a microscopical level. The microscopic current can be split into two parts, a quick impulsive current responsible for the terahertz emission and a slow long-term current generated by thermally dissociating excitons. We found that the super-linear dependence of the photocurrent on the voltage originates from additional excitons generated by free carriers through impact excitation.

Several future projects are planned based on the findings in this thesis: (i) So far, only the transport code without spatial transport was joined with the scattering code. The theoretical method to join the full transport code with scattering was introduced in this work but not yet implemented. (ii) It is planned to compare the scattering rates obtained by Boltzmann without momentum conservation and Boltzmann with momentum conservation to the scattering rates obtained by DMFT for model systems in order to get a deeper understanding of the fundamental approximations the methods are based on. (iii) The non-equilibrium experiment with aligned carbon-nanotubes was also performed with non-aligned carbon-nanotubes where the results differ from the aligned case. We plan to use the code to understand the fundamental processes leading to the difference. (iv) The long-term goal is to make non-equilibrium simulations possible in three-dimensional systems as well. Further methodological development is needed to achieve this goal.

Appendices

Appendix A

Scattering amplitude for the Hubbard model

The scattering amplitude for electron-electron scattering is defined (Eq. (2.10)) as

$$w_{0123}^{\text{e-e}} \equiv \frac{V^2}{(2\pi)^{2d-1}\hbar}\left|\langle 2,3|\, \hat{H}_{\text{e-e}}\, |0,1\rangle\right|^2 \tag{A.1}$$

with the initial electron state $|0,1\rangle = \hat{\Psi}^\dagger_{\mathbf{k}_0\sigma_0}\hat{\Psi}^\dagger_{\mathbf{k}_1\sigma_1}|\emptyset\rangle$ and the final electron state $|2,3\rangle = \hat{\Psi}^\dagger_{\mathbf{k}_2\sigma_2}\hat{\Psi}^\dagger_{\mathbf{k}_3\sigma_3}|\emptyset\rangle$ ($|\emptyset\rangle$ denotes the state without electrons). The creation-operator for an electron in state $(\mathbf{k},\sigma)$ reads

$$\hat{\Psi}^\dagger_{\mathbf{k}\sigma} \equiv \frac{1}{\sqrt{N}}\sum_j e^{-i\mathbf{R}_j\cdot\mathbf{k}}\hat{a}^\dagger_{j\sigma}\ , \tag{A.2}$$

with the creation-operator $\hat{a}^\dagger_{j\sigma}$ of an electron with spin σ at lattice-site j and the total number of lattice sites N. The operator $\hat{a}^\dagger_{j\sigma}$ and its hermitian conjugate are fermionic creation and annihilation operators, hence they fulfill the relations

$$\left[\hat{a}_{i\sigma}, \hat{a}^\dagger_{j\sigma'}\right]_+ = \delta_{ij}\delta_{\sigma\sigma'} \tag{A.3a}$$

$$\left[\hat{a}_{i\sigma}, \hat{a}_{j\sigma'}\right]_+ = 0 \tag{A.3b}$$

$$\left[\hat{a}^\dagger_{i\sigma}, \hat{a}^\dagger_{j\sigma'}\right]_+ = 0 \tag{A.3c}$$

$$\hat{a}_{i\sigma}\,|\emptyset\rangle = 0 \tag{A.3d}$$

$$\langle\emptyset|\,\hat{a}^\dagger_{i\sigma} = 0 \tag{A.3e}$$

with $[A,B]_+ \equiv AB + BA$. The effective interaction potential operator $\hat{H}_{\text{e-e}}$ for a Hubbard model reads

$$\hat{H}_{\text{e-e}} = U\sum_i \hat{a}^\dagger_{i\uparrow}\hat{a}_{i\uparrow}\hat{a}^\dagger_{i\downarrow}\hat{a}_{i\downarrow} \tag{A.4}$$

with the on-site interaction U. With the above definitions, the transition-matrix element in Eq. (A.1) reads

$$\begin{aligned}\langle 2,3|\,\hat{H}_{\text{e-e}}\,|0,1\rangle = \frac{U}{N^2}\sum_{p,j,l,s,m}\Big[&e^{i\mathbf{R}_m\cdot\mathbf{k}_3}e^{i\mathbf{R}_s\cdot\mathbf{k}_2}e^{-i\mathbf{R}_j\cdot\mathbf{k}_0}e^{-i\mathbf{R}_l\cdot\mathbf{k}_1}\\ &\langle\emptyset|\,\hat{a}_{m\sigma_3}\hat{a}_{s\sigma_2}\hat{a}^\dagger_{p\uparrow}\hat{a}_{p\uparrow}\hat{a}^\dagger_{p\downarrow}\hat{a}_{p\downarrow}\hat{a}^\dagger_{j\sigma_0}\hat{a}^\dagger_{l\sigma_1}\,|\emptyset\rangle\Big]\,.\end{aligned}\tag{A.5}$$

We can calculate the matrix-element in the above equation with Eqs. (A.3) as

$$\langle\emptyset|\,\hat{a}_{m\sigma_3}\hat{a}_{s\sigma_2}\hat{a}^\dagger_{p\uparrow}\hat{a}_{p\uparrow}\hat{a}^\dagger_{p\downarrow}\hat{a}_{p\downarrow}\hat{a}^\dagger_{j\sigma_0}\hat{a}^\dagger_{l\sigma_1}\,|\emptyset\rangle = \delta_{pl}\delta_{pj}\delta_{pm}\delta_{ps}\delta_{\sigma_0\bar{\sigma}_1}\delta_{\sigma_2\bar{\sigma}_3}\left(2\delta_{\sigma_0\sigma_2}-1\right)\tag{A.6}$$

with the short notation $\bar{\sigma}_i \equiv -\sigma_i$. This result was expected as it tells us that the electrons can only interact (i) if they are at the same orbital with the position index p, and (ii) if the two initial electrons have opposite spin (which is necessary for (i) to be possible). Additionally the total spin is conserved in the scattering event which makes sense as the interaction potential $\hat{H}_{\text{e-e}}$ commutes with the spin operators. The term $(2\delta_{\sigma_0\sigma_2}-1)$ on the right-hand side of Eq. (A.6) is equal to ±1 and therefore it vanishes if we take the absolute square.

With Eq. (A.6) the transition matrix-element Eq. (A.5) becomes

$$\langle 2,3|\,\hat{H}_{\text{e-e}}\,|0,1\rangle = \delta_{\sigma_0\bar{\sigma}_1}\delta_{\sigma_2\bar{\sigma}_3}\left(2\delta_{\sigma_0\sigma_2}-1\right)\frac{U}{N}\underbrace{\frac{1}{N}\sum_{j=1}^{N}\left[e^{-i\mathbf{R}_j\cdot(\mathbf{k}_0+\mathbf{k}_1-\mathbf{k}_2-\mathbf{k}_3)}\right]}_{\equiv\sum_{\mathbf{G}}\delta_{(\mathbf{k}_0+\mathbf{k}_1-\mathbf{k}_2-\mathbf{k}_3),\mathbf{G}}}\tag{A.7}$$

where we have introduced the sum over all reciprocal lattice vectors $\mathbf{G}$ which are all vectors that fulfill $\mathbf{G}\cdot\mathbf{R}_j = 2\pi n$ with an arbitrary integer $n \in \mathbb{Z}_0$. Note that in Eq. (A.7) we have used a Kronecker-Delta assuming discrete momentum vectors stemming from periodic boundary conditions of the lattice.

With Eq. (A.7) the scattering amplitude becomes

$$\begin{aligned}w^{\text{e-e}}_{0123} &= \frac{V^2}{(2\pi)^{2d-1}\hbar}\frac{U^2}{N^2}\delta_{\sigma_0\bar{\sigma}_1}\delta_{\sigma_2\bar{\sigma}_3}\sum_{\mathbf{G}}\delta_{(\mathbf{k}_0+\mathbf{k}_1-\mathbf{k}_2-\mathbf{k}_3),\mathbf{G}} &\text{(A.8)}\\ &= \frac{2\pi}{\hbar}\frac{U^2}{{V_{BZ}}^2}\delta_{\sigma_0\bar{\sigma}_1}\delta_{\sigma_2\bar{\sigma}_3}\sum_{\mathbf{G}}\delta_{(\mathbf{k}_0+\mathbf{k}_1-\mathbf{k}_2-\mathbf{k}_3),\mathbf{G}} &\text{(A.9)}\end{aligned}$$

where we have used the fact that a Kronecker-Delta squared gives the same Kronecker-Delta[1] and the relations $V = NV_{UC}$, $V_{UC}V_{BZ} = (2\pi)^d$. Due to the momentum-conserving delta-distribution in the collision-operator Eq. (3.3) we may write $\sum_{\mathbf{G}}\delta_{(\mathbf{k}_0+\mathbf{k}_1-\mathbf{k}_2-\mathbf{k}_3),\mathbf{G}} = 1$ here. Eventually we can write the scattering amplitude for the Hubbard-model in d-dimensions as

$$w^{\text{e-e}}_{0123} = \frac{2\pi}{\hbar}\frac{U^2}{{V_{BZ}}^2}\delta_{\sigma_0\bar{\sigma}_1}\delta_{\sigma_2\bar{\sigma}_3}\,.\tag{A.10}$$

---

[1] The mixed terms from squaring the sum of Deltas are all zero.

Die approbierte gedruckte Originalversion dieser Dissertation ist an der TU Wien Bibliothek verfügbar.
The approved original version of this doctoral thesis is available in print at TU Wien Bibliothek.
TU Bibliothek WIEN Your knowledge hub

Appendix B

Applicability of the scattering rate equation

In section 5.3 we have re-written the collision integral as

$$\frac{\partial(\delta f_0)}{\partial t} = \ -\delta f_0\ \lambda_0 + \mathcal{R}_0\ , \tag{B.1}$$

for some deviation from the Fermi-Dirac distribution, $\delta f(t,\mathbf{k}_0) = f(t,\mathbf{k}_0) - f_{\mathrm{FD}}(\epsilon(\mathbf{k}_0),\mu,\beta)$. If the term $\mathcal{R}_0$ gives a negligible contribution, the above equation describes an exponential decay of the excitation δf and we may interpret λ_0 as scattering rate at $\mathbf{k}_0$. Here we will discuss under which conditions this requirement is fulfilled. Note that for the following derivation we will assume that δf is strictly positive in the whole domain (i.e. $\delta f(\mathbf{k}_0) \geq 0 \quad \forall \mathbf{k}_0$) which represents the creation of particles (the whole proof also works with strictly negative excitations, representing the annihilation of particles).

In order to understand the structure of $\mathcal{R}_0$ we will study its first term (all other contributions may be treated equivalently) that we call $\mathcal{R}_{01}$,

$$\mathcal{R}_{01} = w^{\text{e-e}}_{0123}\ \frac{1}{2}\sum_{\mathbf{G}} \iiint \mathrm{d}^d k_1 \mathrm{d}^d k_2 \mathrm{d}^d k_3\ \delta_{\mathbf{k}}\delta_\epsilon \delta f_1 \Big((1-f_{FD_0}) f_{FD_2} f_{FD_3} + f_{FD_0}(1-f_{FD_2})(1-f_{FD_3}) \Big). \tag{B.2}$$

We may rewrite this term as

$$\mathcal{R}_{01} = \frac{1}{V_{BZ}} \int \mathrm{d}^d k_1 \delta f(\mathbf{k}_1)\ F_{\mathbf{k}_0}(\mathbf{k}_1). \tag{B.3}$$

with the function $F_{\mathbf{k}_0}(\mathbf{k}_1)$ that is defined as,

$$F_{\mathbf{k}_0}(\mathbf{k}_1) \equiv w^{\text{e-e}}_{0123}\ \frac{1}{2}\sum_{\mathbf{G}} V_{BZ} \iint \mathrm{d}^d k_2 \mathrm{d}^d k_3\ \delta_{\mathbf{k}}\delta_\epsilon \Big((1-f_{FD_0}) f_{FD_2} f_{FD_3} + f_{FD_0}(1-f_{FD_2})(1-f_{FD_3}) \Big)\ . \tag{B.4}$$

As defined, $F_{\mathbf{k}_0}(\mathbf{k}_1)$ has the same unit and a similar order of magnitude as the scattering rate $\lambda(\mathbf{k}_0)$. It is also strictly positive in the whole domain. Furthermore, we can write the inequality relation

$$\frac{1}{V_{BZ}}\int \mathrm{d}^d k_1 \delta f(\mathbf{k}_1)\ F_{\mathbf{k}_0}(\mathbf{k}_1) \leq \max_{\mathbf{k}_1}(F_{\mathbf{k}_0}(\mathbf{k}_1))\frac{1}{V_{BZ}}\int \mathrm{d}^d k_1 \delta f(\mathbf{k}_1)\ . \tag{B.5}$$

In order for $\mathcal{R}_{01}$ to have negligible impact on the scattering, it must be much smaller than $\delta f_0 \lambda_0$ which is fulfilled if

$$\max_{\mathbf{k}_1}(F_{\mathbf{k}_0}(\mathbf{k}_1))\frac{1}{V_{BZ}}\int \mathrm{d}^d k_1 \delta f(\mathbf{k}_1) \ll \delta f(\mathbf{k}_0)\lambda(\mathbf{k}_0)\ . \tag{B.6}$$

Assuming that $\max_{\mathbf{k}_1}(F_{\mathbf{k}_0}(\mathbf{k}_1))$ and $\lambda(\mathbf{k}_0)$ have comparable orders of magnitudes, Eq. (B.6) reduces to

$$\frac{1}{V_{BZ}}\int \mathrm{d}^d k_1 \delta f(\mathbf{k}_1) \ll \delta f(\mathbf{k}_0)\ . \tag{B.7}$$

Eq. (B.7) shows that the mean value of the excitation (left-hand side of Eq. (B.7)) must be much smaller than the value at the momentum $\mathbf{k}_0$ (i.e. the maximum value of δf) where we probe the system. This is plausible as we need a particle that is localized in momentum space for the concept of a momentum dependent scattering rate (or lifetime vice versa).

We can easily construct an excitation for which Eq. (B.7) holds; we take $\delta f(0, \mathbf{k}) = A \times \exp\left(-\frac{(\mathbf{k}-\mathbf{k}_0)^2}{2\sigma^2}\right)$. We want to add only a single particle in order to probe the system, i.e.

$$1 = \frac{V}{(2\pi)^d}\int \mathrm{d}^d k\ \delta f(\mathbf{k}) = \frac{V}{(\sqrt{2\pi})^d}\sigma^d A\ . \tag{B.8}$$

With the above relation Eq. (B.7) becomes

$$\frac{(2\pi)^d}{V_{BZ}V} = \frac{1}{N} \ll A\ , \tag{B.9}$$

with the number of particles N in the system. This relation is always fulfilled for macroscopic systems where $N \to \infty$. By integration of the left-hand side of Eq. (B.7) we furthermore get the requirement

$$\frac{(\sqrt{2\pi})^d}{V_{BZ}}\sigma^d \ll 1 \quad \to \quad \sigma^d \ll \frac{V_{BZ}}{(\sqrt{2\pi})^d} \tag{B.10}$$

that is independent of A. Eq. (B.10) again shows that the probe-particle must be strongly localized in the Brillouin-zone. If this is the case, the terms in $\mathcal{R}_0$ that are $\propto \delta f$ vanish compared to the actual scattering rate contribution. Furthermore, in order for the higher order terms $\propto \delta f^2$ and $\propto \delta f^3$ to vanish, the amplitude of the excitation must be sufficiently small.

An interesting result of the above derivation is that it is not sufficient to require the excitation to be small, but it must also be strongly localized within the Brillouin-zone for the collision integral to become the easy shape

$$\frac{\partial(\delta f_0)}{\partial t} = \; - \, \delta f_0 \; \lambda_0 \; , \tag{B.11}$$

when thermalization is studied.

Bibliography

[1] E. Manousakis. *Photovoltaic effect for narrow-gap Mott insulators.* Phys. Rev. B **82**, 125109 (2010).

[2] E. Assmann, P. Blaha, R. Laskowski, K. Held, S. Okamoto, and G. Sangiovanni. *Oxide Heterostructures for Efficient Solar Cells.* Phys. Rev. Lett. **110**, 078701 (2013).

[3] M. Battiato and K. Held. *Ultrafast and Gigantic Spin Injection in Semiconductors.* Phys. Rev. Lett. **116**, 196601 (2016).

[4] L. Cheng, X. Wang, W. Yang, J. Chai, M. Yang, M. Chen, Y. Wu, X. Chen, D. Chi, K. E. J. Goh, J.-X. Zhu, H. Sun, S. Wang, J. C. W. Song, M. Battiato, H. Yang, and E. E. M. Chia. *Far out-of-equilibrium spin populations trigger giant spin injection into atomically thin MoS2.* Nature Physics **15**, 347 (2019).

[5] E. Beaurepaire, J.-C. Merle, A. Daunois, and J.-Y. Bigot. *Ultrafast Spin Dynamics in Ferromagnetic Nickel.* Phys. Rev. Lett. **76**, 4250 (1996).

[6] K. Vahaplar, A. M. Kalashnikova, A. V. Kimel, D. Hinzke, U. Nowak, R. Chantrell, A. Tsukamoto, A. Itoh, A. Kirilyuk, and T. Rasing. *Ultrafast Path for Optical Magnetization Reversal via a Strongly Nonequilibrium State.* Phys. Rev. Lett. **103**, 117201 (2009).

[7] M. Battiato, K. Carva, and P. M. Oppeneer. *Superdiffusive Spin Transport as a Mechanism of Ultrafast Demagnetization.* Phys. Rev. Lett. **105**, 027203 (2010).

[8] R. R. Hartmann, J. Kono, and M. E. Portnoi. *Terahertz Science and Technology of Carbon Nanomaterials.* Nanotechnology **25**, 322001 (2014).

[9] L. V. Titova, C. L. Pint, Q. Zhang, R. H. Hauge, J. Kono, and F. A. Hegmann. *Generation of Terahertz Radiation by Optical Excitation of Aligned Carbon Nanotubes.* Nano Lett. **15**, 3267 (2015).

[10] J. G. Fujimoto, J. M. Liu, E. P. Ippen, and N. Bloembergen. *Femtosecond Laser Interaction with Metallic Tungsten and Nonequilibrium Electron and Lattice Temperatures*. Phys. Rev. Lett. **53**, 1837 (1984).

[11] H. E. Elsayed-Ali, T. B. Norris, M. A. Pessot, and G. A. Mourou. *Time-resolved observation of electron-phonon relaxation in copper*. Phys. Rev. Lett. **58**, 1212 (1987).

[12] R. W. Schoenlein, W. Z. Lin, J. G. Fujimoto, and G. L. Eesley. *Femtosecond studies of nonequilibrium electronic processes in metals*. Phys. Rev. Lett. **58**, 1680 (1987).

[13] S. D. Brorson, A. Kazeroonian, J. S. Moodera, D. W. Face, T. K. Cheng, E. P. Ippen, M. S. Dresselhaus, and G. Dresselhaus. *Femtosecond room-temperature measurement of the electron-phonon coupling constant γ in metallic superconductors*. Phys. Rev. Lett. **64**, 2172 (1990).

[14] W. S. Fann, R. Storz, H. W. K. Tom, and J. Bokor. *Electron thermalization in gold*. Phys. Rev. B **46**, 13592 (1992).

[15] T. Hertel, E. Knoesel, M. Wolf, and G. Ertl. *Ultrafast Electron Dynamics at Cu(111): Response of an Electron Gas to Optical Excitation*. Phys. Rev. Lett. **76**, 535 (1996).

[16] N. Del Fatti, C. Voisin, M. Achermann, S. Tzortzakis, D. Christofilos, and F. Vallée. *Nonequilibrium electron dynamics in noble metals*. Phys. Rev. B **61**, 16956 (2000).

[17] C. Stamm, T. Kachel, N. Pontius, R. Mitzner, T. Quast, K. Holldack, S. Khan, C. Lupulescu, E. F. Aziz, M. Wietstruk, H. A. Dürr, and W. Eberhardt. *Femtosecond modification of electron localization and transfer of angular momentum in nickel*. Nature Materials **6**, 740 (2007).

[18] Y. Terada, S. Yoshida, A. Okubo, K. Kanazawa, M. Xu, O. Takeuchi, and H. Shigekawa. *Optical Doping: Active Control of MetalâĹŠInsulator Transition in Nanowire*. Nano Lett. **8**, 3577 (2008).

[19] A. Crepaldi, B. Ressel, F. Cilento, M. Zacchigna, C. Grazioli, H. Berger, P. Bugnon, K. Kern, M. Grioni, and F. Parmigiani. *Ultrafast photodoping and effective Fermi-Dirac distribution of the Dirac particles in* Bi_2Se_3. Phys. Rev. B **86**, 205133 (2012).

[20] G. Garcia, R. Buonsanti, E. L. Runnerstrom, R. J. Mendelsberg, A. Llordes, A. Anders, T. J. Richardson, and D. J. Milliron. *Dynamically Modulating the Surface Plasmon Resonance of DopedSemiconductor Nanocrystals*. Nano Lett. **11**, 4415 (2011).

[21] G. Malinowski, F. Dalla Longa, J. H. H. Rietjens, P. V. Paluskar, R. Huijink, H. J. M. Swagten, and B. Koopmans. *Control of speed and efficiency of ultrafast demagnetization by direct transfer of spin angular momentum.* Nature Physics **4**, 855 (2008).

[22] T. Kampfrath, M. Battiato, P. Maldonado, G. Eilers, J. Nötzold, S. Mährlein, V. Zbarsky, F. Freimuth, Y. Mokrousov, S. Blügel, M. Wolf, I. Radu, P. M. Oppeneer, and M. Münzenberg. *Terahertz spin current pulses controlled by magnetic heterostructures.* Nature Nanotechnology **8**, 256 (2013).

[23] F. Freyse, M. Battiato, L. V. Yashina, and J. Sánchez-Barriga. *Impact of ultrafast transport on the high-energy states of a photoexcited topological insulator.* Phys. Rev. B **98**, 115132 (2018).

[24] J. Rammer and H. Smith. *Quantum field-theoretical methods in transport theory of metals.* Rev. Mod. Phys. **58**, 323 (1986).

[25] L. V. Keldysh. *Diagram technique for nonequilibrium processes.* Zh. Eksp. Teor. Fiz. **47**, 1515 (1964). Sov. Phys. – JETP 20, 1018 (1965).

[26] L. Boltzmann. *Weitere Studien über das Wärmegleichgewicht unter Gasmolekülen.* Sitzungsberichte der Kaiserlichen Akademie der Wissenschaften. **66**, 275 (1872).

[27] J. Ziman. *Electrons and phonons: the theory of transport phenomena in solids.* Oxford university press (1960).

[28] D. W. Snoke. *Solid State Physics Essential Concepts.* Pearson Education, 1 edition (2007).

[29] D. W. Snoke. *The quantum Boltzmann equation in semiconductor physics.* Annalen der Physik **523**, 87 (2011).

[30] L. Erdös, M. Salmhofer, and H.-T. Yau. *On the Quantum Boltzmann Equation.* Journal of Statistical Physics **116**, 376 (2004).

[31] G. D. Mahan. *Many-Particle Physics.* Kluwer Academic/Plenum Publishers, New York (2000).

[32] L.-Y. Chen and Z.-B. Su. *Quantum Boltzmann equation and Kubo formula for electronic transport in solids.* Phys. Rev. B **40**, 9309 (1989).

[33] M. Bonitz. *Quantum Kinetic Theory.* Springer, Cham (2016).

[34] B. V. Alexeev. *Unified Non-Local Theory of Transport Processes.* Elsevier, 2 edition (2015).

[35] J. K. Freericks, V. M. Turkowski, and V. Zlatić. *Nonequilibrium Dynamical Mean-Field Theory.* Phys. Rev. Lett. **97**, 266408 (2006).

[36] H. Aoki, N. Tsuji, M. Eckstein, M. Kollar, T. Oka, and P. Werner. *Nonequilibrium dynamical mean-field theory and its applications.* Rev. Mod. Phys. **86**, 779 (2014).

[37] N. Ashcroft and N. Mermin. *Solid State Physics.* Hartcourt College Publishers, New York (1976).

[38] R. G. Chambers. *Electrons in Metals and Semiconductors.* Chapman and Hall (1990).

[39] S. M. Sze and K. K. Ng. *Physics of Semiconductor Devices.* Wiley-Interscience (1969).

[40] M. Battiato, V. Zlatic, and K. Held. *Boltzmann approach to high-order transport: The nonlinear and nonlocal responses.* Phys. Rev. B **95**, 235137 (2017).

[41] G. K. Madsen and D. J. Singh. *BoltzTraP. A code for calculating band-structure dependent quantities.* Computer Physics Communications **175**, 67 (2006).

[42] B. Rethfeld, A. Kaiser, M. Vicanek, and G. Simon. *Ultrafast dynamics of nonequilibrium electrons in metals under femtosecond laser irradiation.* Phys. Rev. B **65**, 214303 (2002).

[43] P. Maldonado, K. Carva, M. Flammer, and P. M. Oppeneer. *Theory of out-of-equilibrium ultrafast relaxation dynamics in metals.* Phys. Rev. B **96**, 174439 (2017).

[44] V. A. Jhalani, J.-J. Zhou, and M. Bernardi. *Ultrafast Hot Carrier Dynamics in GaN and Its Impact on the Efficiency Droop.* Nano Lett. **17**, 5012 (2017).

[45] S. Sadasivam, M. K. Y. Chan, and P. Darancet. *Theory of Thermal Relaxation of Electrons in Semiconductors.* Phys. Rev. Lett. **119**, 136602 (2017).

[46] T. Kurosawa and H. Maeda. *Monte Carlo Calculation of Hot Electron Phenomena. I. Streaming in the Absence of a Magnetic Field.* Journal of the Physical Society of Japan **31**, 668 (1971).

[47] C. Jacoboni and L. Reggiani. *The Monte Carlo method for the solution of charge transport in semiconductors with applications to covalent materials.* Rev. Mod. Phys. **55**, 645 (1983).

[48] M. V. Fischetti and S. E. Laux. *Monte carlo analysis of electron transport in small semiconductor devices including band-structure and space-charge effects.* Phys. Rev. B **38**, 9721 (1988).

[49] N. Medvedev, U. Zastrau, E. Förster, D. O. Gericke, and B. Rethfeld. *Short-Time Electron Dynamics in Aluminum Excited by Femtosecond Extreme Ultraviolet Radiation.* Phys. Rev. Lett. **107**, 165003 (2011).

[50] S. Mattei, K. Nishida, M. Onai, J. Lettry, M. Tran, and A. Hatayama. *A fully-implicit Particle-In-Cell Monte Carlo Collision code for the simulation of inductively coupled plasmas.* Journal of Computational Physics **350**, 891 (2017).

[51] D. M. Nenno, B. Rethfeld, and H. C. Schneider. *Particle-in-cell simulation of ultrafast hot-carrier transport in Fe/Au heterostructures.* Phys. Rev. B **98**, 224416 (2018).

[52] J. Sánchez-Barriga, M. Battiato, M. Krivenkov, E. Golias, A. Varykhalov, A. Romualdi, L. V. Yashina, J. Minár, O. Kornilov, H. Ebert, K. Held, and J. Braun. *Subpicosecond spin dynamics of excited states in the topological insulator* $\mathrm{Bi_2Te_3}$. Phys. Rev. B **95**, 125405 (2017).

[53] M. Battiato, J. Minár, W. Wang, W. Ndiaye, M. C. Richter, O. Heckmann, J.-M. Mariot, F. Parmigiani, K. Hricovini, and C. Cacho. *Distinctive Picosecond Spin Polarization Dynamics in Bulk Half Metals.* Phys. Rev. Lett. **121**, 077205 (2018).

[54] N. N. Bogoliubov and K. P. Gurov. *Kinetic Equations in Quantum Mechanics.* Journal of Experimental and Theoretical Physics (in Russian) **17**, 614 (1947).

[55] J. Yvon. *La thÃľorie statistique des fluides et l'Ãľquation d'Ãľtat (in French).* Actual. Sci. & Indust. **203** (1935).

[56] J. G. Kirkwood. *The Statistical Mechanical Theory of Transport Processes I. General Theory.* The Journal of Chemical Physics **14**, 180 (1946).

[57] J. G. Kirkwood. *The Statistical Mechanical Theory of Transport Processes II. Transport in Gases.* The Journal of Chemical Physics **15**, 72 (1947).

[58] M. Born and H. S. Green. *A General Kinetic Theory of Liquids I. The Molecular Distribution Functions.* Proc. Roy. Soc. A **188**, 10 (1946).

[59] D. Xiao, M.-C. Chang, and Q. Niu. *Berry phase effects on electronic properties.* Rev. Mod. Phys. **82**, 1959 (2010).

[60] A. A. Vlasov. *On Vibration Properties of Electron Gas*. J. Exp. Theor. Phys. **8**, 291 (1938).

[61] A. A. Vlasov. *The Vibrational Properties of an Electron Gas*. Soviet Physics Uspekhi. **10**, 721 (1968).

[62] P. A. Dirac. *The quantum theory of the emission and absorption of radiation*. Proc. R. Soc. Lond. A **114**, 243 (1927).

[63] E. Fermi. *Nuclear physics: a course given by Enrico Fermi at the University of Chicago*. University of Chicago Press (1950).

[64] H. Fröhlich, H. Pelzer, and S. Zienau. *XX. Properties of slow electrons in polar materials*. The London, Edinburgh, and Dublin Philosophical Magazine and Journal of Science **41**, 221 (1950).

[65] H. Fröhlich. *Electrons in lattice fields*. Advances in Physics **3**, 325 (1954).

[66] M. Wais, M. Eckstein, R. Fischer, P. Werner, M. Battiato, and K. Held. *Quantum Boltzmann equation for strongly correlated systems: Comparison to dynamical mean field theory*. Phys. Rev. B **98**, 134312 (2018).

[67] J. Hubbard. *Electron Correlations in Narrow Energy Bands*. Proceedings of the Royal Society of London. Series A, Mathematical and Physical Sciences **276**, 238 (1963).

[68] A. A. Abrikosov, L. P. Gorkov, and I. E. Dzyaloshinski. *Methods of Quantum Field Theory in Statistical Physics*. Dover Publications (1975).

[69] W. Nolting. *Grundkurs Theoretische Physik 7: Viel-Teilchen-Theorie*. Springer Spektrum (2015).

[70] A. Kamenev. *Field Theory of Non-Equilibrium Systems*. Cambridge University Press (2011).

[71] P. Werner, K. Held, and M. Eckstein. *Role of impact ionization in the thermalization of photoexcited Mott insulators*. Phys. Rev. B **90**, 235102 (2014).

[72] M. E. Sorantin, A. Dorda, K. Held, and E. Arrigoni. *Impact ionization processes in the steady state of a driven Mott-insulating layer coupled to metallic leads*. Phys. Rev. B **97**, 115113 (2018).

[73] S.-K. Mo, H.-D. Kim, J. W. Allen, G.-H. Gweon, J. D. Denlinger, J.-H. Park, A. Sekiyama, A. Yamasaki, S. Suga, P. Metcalf, and K. Held. *Filling of the Mott-Hubbard Gap in the High Temperature Photoemission Spectrum of* $(V_{0.972}Cr_{0.028})_2O_3$. Phys. Rev. Lett. **93**, 076404 (2004).

[74] A. Kauch *et al.* (2018). (unpublished).

[75] M. Eckstein, M. Kollar, and P. Werner. *Thermalization after an Interaction Quench in the Hubbard Model.* Phys. Rev. Lett. **103**, 056403 (2009).

[76] N. Dasari and M. Eckstein. *Photo-excited states in correlated band insulators.* ArXiv e-prints (2018).

[77] C. Johnson. *Numerical solutions of partial differential equations by the finite element method.* Cambridge University Press (1987).

[78] B. Cockburn and C.-W. Shu. *Runge-Kutta Discontinuous Galerkin Methods for Convection-Dominated Problems.* Journal of Scientific Computing **16**, 173 (2001).

[79] M. Wais, K. Held, and M. Battiato. *Deterministic solver for the time-dependent far-from-equilibrium quantum Boltzmann equation.* arXiv:2004.02683 (2020).

[80] L. Lindsay and D. A. Broido. *Three-phonon phase space and lattice thermal conductivity in semiconductors.* Journal of Physics: Condensed Matter **20**, 165209 (2008).

[81] E. Schmidt. *Zur Theorie der linearen und nichtlinearen Integralgleichungen I. Teil: Entwicklung willkürlicher Funktionen nach Systemen vorgeschriebener.* Mathematische Annalen **63**, 433 (1907).

[82] S. Leon, A. Bjorck, and W. Gander. *Gram-Schmidt orthogonalization: 100 years and more.* Numerical Linear Algebra with Applications **20** (2013).

[83] F. R. G. Bagsican, M. Wais, N. Komatsu, W. Gao, L. W. Weber, K. Serita, H. Murakami, K. Held, F. A. Hegmann, M. Tonouchi, J. Kono, I. Kawayama, and M. Battiato. *Terahertz Excitonics in Carbon Nanotubes: Exciton Autoionization and Multiplication.* Nano Letters **20**, 3098 (2020). PMID: 32227963.

[84] J.-C. Charlier, X. Blase, and S. Roche. *Electronic and transport properties of nanotubes.* Rev. Mod. Phys. **79**, 677 (2007).

[85] E. A. Laird, F. Kuemmeth, G. A. Steele, K. Grove-Rasmussen, J. Nygård, K. Flensberg, and L. P. Kouwenhoven. *Quantum transport in carbon nanotubes.* Rev. Mod. Phys. **87**, 703 (2015).

[86] G. G. Samsonidze, R. Saito, A. Jorio, M. A. Pimenta, A. G. Souza Filho, A. Grüneis, G. Dresselhaus, and M. S. Dresselhaus. *The Concept of Cutting Lines in Carbon Nanotube Science.* Journal of Nanoscience and Nanotechnology **3**, 431 (2003).

[87] T. Ando. *Theory of Electronic States and Transport in Carbon Nanotubes.* Journal of the Physical Society of Japan **74**, 777 (2005).

[88] K. S. Novoselov, A. K. Geim, S. V. Morozov, D. Jiang, Y. Zhang, S. V. Dubonos, I. V. Grigorieva, and A. A. Firsov. *Electric Field Effect in Atomically Thin Carbon Films.* Science **306**, 666 (2004).

[89] K. S. Novoselov, A. K. Geim, S. V. Morozov, D. Jiang, M. I. Katsnelson, I. V. Grigorieva, S. V. Dubonos, and A. A. Firsov. *Two-dimensional gas of massless Dirac fermions in graphene.* Nature **438**, 197 (2005).

[90] E. Gerstner. *Nobel Prize 2010: Andre Geim & Konstantin Novoselov.* Nature Physics **6**, 836 (2010).

[91] S.-i. Tomonaga. *Remarks on Bloch's Method of Sound Waves applied to Many-Fermion Problems.* Progress of Theoretical Physics **5**, 544 (1950).

[92] J. M. Luttinger. *An Exactly Soluble Model of a Many-Fermion System.* Journal of Mathematical Physics **4**, 1154 (1963).

[93] T. Vuković, I. Milošević, and M. Damnjanović. *Carbon nanotubes band assignation, topology, Bloch states, and selection rules.* Phys. Rev. B **65**, 045418 (2002).

[94] M. S. Dresselhaus, G. Dresselhaus, R. Saito, and A. Jorio. *Exciton Photophysics of Carbon Nanotubes.* Annual Review of Physical Chemistry **58**, 719 (2007).

[95] J. Maultzsch, R. Pomraenke, S. Reich, E. Chang, D. Prezzi, A. Ruini, E. Molinari, M. S. Strano, C. Thomsen, and C. Lienau. *Exciton binding energies in carbon nanotubes from two-photon photoluminescence.* Phys. Rev. B **72**, 241402 (2005).

[96] J. Jiang, R. Saito, G. G. Samsonidze, A. Jorio, S. G. Chou, G. Dresselhaus, and M. S. Dresselhaus. *Chirality dependence of exciton effects in single-wall carbon nanotubes: Tight-binding model.* Phys. Rev. B **75**, 035407 (2007).

[97] R. B. Weisman and J. Kono (eds.). *Optical Properties of Carbon Nanotubes: A Volume Dedicated to the Memory of Professor Mildred Dresselhaus.* World Scientific, Singapore (2019).

[98] M. Zheng. *Sorting Carbon Nanotubes.* Top. Curr. Chem. **375**, 1 (2017).

[99] W. Gao and J. Kono. *Science and Applications of Wafer-Scale Crystalline Carbon Nanotube Films Prepared through Controlled Vacuum Filtration.* R. Soc. open sci. **6**, 181605 (2019).

[100] F. Wang, G. Dukovic, L. E. Brus, and T. F. Heinz. *The Optical Resonances in Carbon Nanotubes Arise from Excitons.* Science **308**, 838 (2005).

[101] G. Dukovic, F. Wang, D. Song, M. Y. Sfeir, T. F. Heinz, and L. E. Brus. *Structural Dependence of Excitonic Optical Transitions and Band-Gap Energies in Carbon Nanotubes.* Nano Letters **5**, 2314 (2005).

[102] E. Malic and A. Knorr. *Graphene and Carbon Nanotubes: Ultrafast Relaxation Dynamics and Optics.* WILEY-VCH, Cambridge (2013).

[103] M. Hirtschulz, F. Milde, E. Mailic, C. Thomsen, and S. Reich. *Theory of ultrafast intraband relaxation in carbon nanotubes.* Phys. Stat. Sol. B **245**, 2164 (2008).

[104] M. Hirtschulz, E. Malic, F. Milde, and A. Knorr. *Excitation-induced dephasing and ultrafast intrasubband relaxation in carbon nanotubes.* Phys. Rev. B **80**, 085405 (2009).

[105] C. Köhler, T. Watermann, and E. Malic. *Time- and momentum-resolved phonon-induced relaxation dynamics in carbon nanotubes.* J. Phys.: Condens. Matter **25**, 105301 (2013).

[106] Y.-S. Lim, A. R. T. Nugraha, S.-J. Cho, M.-Y. Noh, E.-J. Yoon, H. Liu, J.-H. Kim, H. Telg, E. H. Hároz, G. D. Sanders, S.-H. Baik, H. Kataura, S. K. Doorn, C. J. Stanton, R. Saito, J. Kono, and T. Joo. *Ultrafast Generation of Fundamental and Multiple-Order Phonon Excitations in Highly Enriched (6,5) Single-Wall Carbon Nanotubes.* Nano Lett. **14**, 1426 (2014).

[107] J.-C. Charlier, X. Blase, and S. Roche. *Electronic and transport properties of nanotubes.* Rev. Mod. Phys. **79**, 677 (2007).

[108] J. Park, O. G. Reid, J. L. Blackburn, and G. Rumbles. *Photoinduced spontaneous free-carrier generation in semiconducting single-walled carbon nanotubes.* Nature Communications **6** (2015).

[109] J.-Y. Park, S. Rosenblatt, Y. Yaish, V. Sazonova, H. Üstünel, S. Graig, T. A. Arias, P. W. Brouwer, and P. L. McEuen. *Electron-Phonon Scattering in Metallic Single-Walled Carbon Nanotubes.* Nano Lett. **4**, 517 (2004).

[110] S. Reich, M. Dworzak, A. Hoffmann, C. Thomsen, and M. S. Strano. *Excited-State Carrier Lifetime in Single-Walled Carbon Nanotubes.* Phys. Rev. B **71**, 033402 (2005).

[111] J. S. Lauret, C. Voisin, G. Cassabois, C. Delalande, P. Roussignol, O. Jost, and L. Capes. *Ultrafast Carrier Dynamics in Single-Wall Carbon Nanotubes.* Phys. Rev. Lett. **90**, 057404 (2003).

[112] C. Manzoni, A. Gambetta, E. Menna, M. Meneghetti, G. Lanzani, and G. Cerullo. *Intersubband Exciton Relaxation Dynamics in Single-Walled Carbon Nanotubes.* Phys. Rev. Lett. **94**, 207401 (2005).

[113] R. Baer and E. Rabani. *Can Impact Excitation Explain Efficient Carrier Multiplication in Carbon Nanotube Photodiodes?* Nano Letters **10**, 3277 (2010).

[114] M. Tani, K. Sakai, and H. Mimura. *Ultrafast Photoconductive Detectors Based on Semi-Insulating GaAs and InP.* Japanese Journal of Applied Physics **36**, L1175 (1997).

[115] S. G. Park, M. R. Melloch, and A. M. Weiner. *Analysis of terahertz waveforms measured by photoconductive and electrooptic sampling.* IEEE J. Quantum Electron. **35**, 810 (1999).

[116] L. Duvillaret, F. Garet, J. Roux, and J. Coutaz. *Analytical modeling and optimization of terahertz time-domain spectroscopy experiments, using photoswitches as antennas.* IEEE Journal of Selected Topics in Quantum Electronics **7**, 615 (2001).

[117] P. Kužel, M. A. Khazan, and J. Kroupa. *Spatiotemporal transformations of ultrashort terahertz pulses.* J. Opt. Soc. Am. B **16**, 1795 (1999).

[118] P. U. Jepsen, R. H. Jacobsen, and S. R. Keiding. *Generation and detection of terahertz pulses from biased semiconductor antennas.* J. Opt. Soc. Am. B **13**, 2424 (1996).

[119] T. Hattori, R. Rungsawang, K. Ohta, and K. Tukamoto. *Gaussian Beam Analysis of Temporal Waveform of Focused Terahertz Pulses.* Japanese Journal of Applied Physics **41**, 5198 (2002).

[120] J. V. Rudd and D. M. Mittleman. *Influence of substrate-lens design in terahertz time-domain spectroscopy.* J. Opt. Soc. Am. B **19**, 319 (2002).

[121] Y. Kumamoto, M. Yoshida, A. Ishii, A. Yokoyama, T. Shimada, and Y. Kato. *Spontaneous Exciton Dissociation in Carbon Nanotubes.* Phys. Rev. Lett. **112**, 117401 (2014).

Curriculum Vitae

Personal Information

Name:	Michael Wais
Date of Birth:	24 May 1990
Place of Birth:	Waidhofen an der Thaya, Austria

Education

2016-present:	Ph.D. in Physics, member of the interdisciplinary FWF doctoral school Building Solids for Function (Solids4Fun), Vienna University of Technology, Austria
2014-2016:	M.Sc. in Technical Physics (with distinction), Vienna University of Technology, Austria
2010-2014:	B.Sc. in Technical Physics (with distinction), Vienna University of Technology, Austria
2004-2009:	Higher technical school for electronics with specialization on technical informatics (with distinction), HTBL Hollabrunn, Austria

Academic Employment

11/2016-present:	Project Assistant (FWF), Vienna University of Technology, Austria
10/2015-01/2016:	Tutor for Quantum Mechanics 1, Vienna University of Technology, Austria
03/2015-06/2015:	Tutor for Electrodynamics 1, Vienna University of Technology, Austria
10/2012-01/2013:	Tutor for Mathematical Methods in theoretical Physics, Vienna University of Technology, Austria

Conferences and Research Visits

2019: Research visit (2 weeks) at Nanyang Technological University in the group of Prof. Marco Battiato, Singapore (Singapore)

Building Solids for Function (Solids4Fun) summer school (poster presentation), Waidhofen an der Ybbs (Austria)

2018: Research visit (6 months) at Nanyang Technological University in the group of Prof. Marco Battiato, Singapore (Singapore)

2017: Spin, charge and energy transport in novel materials conference (poster presentation), Hvar (Croatia)

Building Solids for Function (Solids4Fun) summer school (talk), Waidhofen an der Ybbs (Austria)

IFF spring school on topological insulators, Jülich (Germany)

Publication List

Peer-reviewed journal publications:

F. R. G. Bagsican*, M. Wais*, N. Komatsu, W. Gao, L. W. Weber, K. Serita, H. Murakami, K. Held, F. A. Hegmann, M. Tonouchi, J. Kono, I. Kawayama and M. Battiato; Terahertz Excitonics in Carbon Nanotubes: Exciton Autoionization and Multiplication. Nano Letters 20(5), 3098 (2020)

M. Wais, M. Eckstein, R. Fischer, P. Werner, M. Battiato and K.Held; Quantum Boltzmann equation for strongly correlated systems: Comparison to dynamical mean field theory. Phys. Rev. B 98, 134312 (2018)

M. Wais, K. Held and M. Battiato; Importance of Schottky barriers for wide-bandgap thermoelectric devices. Phys. Rev. Materials 2, 045402 (2018)

G. Wachter, S. Nagele, S.A. Sato, R. Pazourek, M. Wais, C. Lemell, XM. Tong, K. Yabana and J. Burgdörfer; Protocol for observing molecular dipole excitations by attosecond self-streaking. Phys. Rev. A 92, 061403(R) (2015)

* These authors contributed equally

Preprints:

M. Wais, K. Held and M. Battiato; Deterministic solver for the time-dependent far-from-equilibrium quantum Boltzmann equation. arXiv:2004.02683 (2020)